DYNAMIC COMPACTION OF POWDERS AND SPALL FRACTURE IN SOLIDS

A thesis submitted to the

Victoria University of Manchester

as part of the requirements for the degree of

DOCTOR OF PHILOSOPHY

in the Faculty of Technology

by

Mohammed Sarumi

Department of Mechanical Engineering

University of Manchester Institute of

Science and Technology

Manchester, England

October 1994

DEDICATION

I dedicate this work to all those who take genuine interest in the plight of others, with intent to give a helping hand.

Be they rewarded in kind.

ACKNOWLEDGEMENTS

The departmental photographer, Mr. John Howe, said: "Do not worry, I have already been told by Professor Al-Hassani that you are coming to have some photographs done for your thesis". This is only a small illustration of the help, assistance and encouragement I received from Professor Al-Hassani. I am privileged to have worked under his supervision.

Special thanks to Professor Chen Danian who was very helpful during his visit to UMIST. My appreciation to all members of Applied Mechanics Academic staff and all my colleagues in the High Energy Rate Engineering Group, UMIST. The author would like to mention Messrs. D. Mortimer, K. Mitchell and J. Howe for their help. Thanks also to Mr. A. De joode and Mr A R Wahono.

My gratitude to K. Mathews and S. Barter for typing this thesis, Doctor A. S. Kaddour for his assistance, and Susan Ody-Obiora for proof reading this work.

ABSTRACT

This thesis presents analytical and numerical models, backed up with experiments, on the subjects of Dynamic Compaction of Powders and Spall Fracture in Solids. The subjects are presented in two parts.

Part one covers the subject of Dynamic Compaction of Powders. Two models are presented to describe the compaction process. One of the methodologies is based on the triaxial testing of powders, the results of which are used in the numerical simulation of the compaction process. The design and development of a new split cell triaxial test system is presented. The details of the analytical model, "Staircase Method", on which the numerical analysis is based, is also covered.

Good comparisons were obtained between the theoretical simulation and experimental results of the die compaction of di-pac sugar.

The second methodology is a wholly analytical model in which equations are derived to describe different stages of the compaction process. Experimental work was carried out to illustrate how some of the parameters required for the equation can be obtained, and how the method is related to experimental data.

Details of the adaptation of a stress wave technique based on the Split Hopkinson Pressure Bar is presented. This is aimed at obtaining some mechanical properties of powder compacts in tension and compression. Results of the experiments on di-pac sugar are compared with those obtained by other methods.

In the subject of Spall Fracture in Solids, both microscopic and macroscopic models to describe ductile and brittle spallation processes are proposed. Also a simple unified model to describe both brittle and ductile spallation is presented. All the models are incorporated into a one dimensional hydrocode, and the practical spallation events were modelled. There is very good agreement between the result of the simulations and experimental data.

Finally, the simple unified model is incorporated into a two dimensional hydrocode, AUTODYN. Practical two dimensional spallation events are modelled and the results compared with experiments. The details of a gas gun experiment of the plane impact of plates is also described.

CONTENTS

DYNAMIC COMPACTION OF POWDERS AND SPALL FRACTURE IN SOLIDS

GENERAL INTRODUCTION

Consider the following question: What is the parallel between the powder compaction process and the phenomenon of spallation in solids? There will be no surprise if one is baffled by the question, and a possible response might be that both mechanisms are time dependent. However, if one considers that the main feature of a powder mass is porosity, and that spallation in its early stages involves the evolution of pores, a parallel between the two might become more obvious. It is possible to see the compaction process, involving pore shrinkage and densification, as an inverse of the spallation process, which involves void nucleation, growth and eventual separation of a previously solid material. Now the parallel is a lot clearer. Although the subject matter of this thesis, "Dynamic compaction of Powders and Spall Fracture in Solids", sounds incompatible at first, they are not so irreconcilable after all.

There is, therefore, logically two parts of this work. Part one is the compaction of powders and part two deals with the spall fracture in solid materials. Different methodologies have been advanced in both parts and these are presented as the subject matter of the various chapters.

Part One - Dynamic Compaction of Powders

In literature, there have been numerous approaches to the theoretical description of the

compaction process. However, these can be divided into two broad categories. Namely, macroscopic or bulk approach and the micro-mathematical and numerical approach.

The bulk approach has been largely empirical and has been measurably successful. The mean feature of the method is to relate applied compaction pressure with the density of the compact. Many relationships between pressure and density (or porosity) have been proposed, the most widely used of which are the Heckel and Kawakita equations. However, none of the proposed equations can describe the compaction process over a wide range of pressure, and the variety of powders. Furthermore, they do not take into account the obvious time dependent nature of the compaction process. Attempts have also been made to treat granular materials with viscosity type equations, in order to account for the time dependent nature of the process. These have not been altogether successful.

In this work, we propose two methodologies. The first is "closed form solution" involving triaxial tests to obtain variation of elastic moduli with volumetric strains, and these are fed into a numerical program for the analysis of the compaction process. The second is an analytical approach, proposing relationships to describe different stages of the compaction process, the constants required in these equations are shown to be obtainable by experimental test.

After a general introduction and background, the design of a new Split Cell triaxial test system is presented together with some preliminary, traditional triaxial tests on di-pac sugar. Details of a new method, staircase method, was then presented along with experimental results based on the method. The use of these results in a numerical analysis was presented in another chapter.

The stress-wave technique of the Split Hopkinson Pressure Bar to obtain the mechanical properties of compacts was presented along with some experimental results. Finally, the new analytical approach yielding equations to describe different stages of the compaction process was derived. Experimental work to obtain the necessary parameters was presented along with some test results.

Part Two : Spall Fracture in Solids

The subject of spallation in solid materials has been widely studied, and many advances have been made. Numerical and analytical methods have been put forward to describe both ductile and brittle spallation. One common problem to most of the methodologies proposed is that they are necessarily complicated and require large numbers of parameters, most of which are simply not obtainable for practical engineering materials.

In Chapters seven to ten of this thesis, we proposed simplified microscopic and

macroscopic methods to describe the phenomenon of ductile and brittle spallation. One of these chapters presents a simple unified spallation failure model to describe both ductile and brittle spallation. All the models presented were incorporated into a one dimensional numerical program. Plane impact of plates were simulated and the results compared with experimental data.

The last chapter presents the details of the spallation experiments. Also covered is the extension of the unified model to two dimensions. The simulation of two further practical spallation events were discussed and compared with experiments.

PART ONE

DYNAMIC COMPACTION OF POWDERS

CHAPTER ONE

COMPACTION OF POWDERS

1.1 SUMMARY

In this work, we present two main methodologies for the study of the compaction of powders. The first is a "closed form solution" involving a new type of triaxial testing of powders to determine some material parameters, and using those parameters in a numerical analysis of the compaction process. A new split cell triaxial test system was designed and commissioned, and some traditional triaxial tests were carried out. A special loading path, staircase test, was devised to obtain non-linearly varying hypoelastic properties of powders as a function of deformation.These properties were used in numerical modelling of die compaction using ABAQUS finite element package, and more successfully using the AUTODYN finite difference code.

The second method is a rigorous analytical approach. Some relationships were derived to describe four different stages in the compaction of powders. Further to the two methods described above, the Split Hopkinson Pressure Bar was used to characterise the strength of compacts.

After an introduction and a general background covering some of the previous work in this field, the subjects mentioned above are presented in the next five Chapters. The last Chapter in this first part of the thesis offers general discussion and conclusion of the work on the "Dynamic Compaction of Powders."

1.2 A STATEMENT OF THE PROBLEM

There have been two main approaches to research into powder compaction. Namely, the bulk method and the micro-mathematical approach. The bulk approach is one in which pressure-density behaviour of powder under compaction is studied. This has been a mainly empirical approach, drawing from long experience of researchers and large experimental data. Useful and reasonably workable relationship between pressure and density (or porosity) have been developed over the years. These have proved very useful indeed, but these relationships are not applicable over the whole range of pressure, powder materials or loading rates.

In the second approach, compaction is investigated through the study of the interaction of the primary particles with a view to developing a mathematical model. This has not been as successful, and has found more use in other areas of powder technology, such as rheology. This method is sometimes used as the analytical basis for a numerical approach. The problem has been that there is very little input of physical material parameters into the development of these models, and no general correlation with experimental work.

The questions posed in this work are two fold. Is it possible to identify, and measure, some parameters attributable to the powder mass, as a continuum, thereby enabling us to develop a methodology that combines experimental and numerical analysis as a means of describing the compaction process? On the other hand, is it possible to find an analytical equation or equations to describe the whole compaction process?

The first attempt, in this work, was to find a "closed form solution" involving experimental data and numerical simulation. Later, a rigorous analytical approach is described.

1.3 INTRODUCTION

Compression techniques, exemplified by pelleting and tabletting, produce agglomeration when applying a suitable external pressure to a multi-particulate system held in a confined space (eg a die). This technique is of fundamental importance to a wide variety of interests, eg metallurgy, ceramics industry, explosive filling, catalyst manufacture and in the production of pharmaceutical tablets.

Despite diversification into capsules, intravenous and other forms of administering medication, medicine in the form of tablets is by far the most popular. Owing to such advantages as; ease of administering, dissolvability, accuracy of dose, simple means of mass production, and convenient storage, package and dispensation etc., it accounts for at least fifty per cent of all forms of medication.

The demand for high speed mass production of medicinal tablets have meant that the process of powder compaction has to be closely studied. Early approaches have concentrated on re-evaluation of, and improvement to various mechanical means of tabletting, such as reciprocation and rotary punch tabletting machines. Considerable improvements were made in the design of such machines and consequently to the tabletting process. This met with the early boom in the demand for mass production of medicants.

The emergence of ever increasing varieties of pharmaceutical products, the need to simplify and reduce the period of pre-formulation and demand for higher quality products have resulted in the careful study of the mechanism of powder compaction itself. This roughly coincided with demand for better products in the field of powder metallurgy, the rapidly expanding plastic industry, and the emerging need for "dry-pressing" in the ceramic industry. There was therefore much stimulus for functional research into the compaction of powders, with contribution from all the above industries.

In the particular field of the compaction of pharmaceutical powders (as in other fields) empirical techniques and relationships were developed. A great majority of work published on this subject has been directed towards the evaluation of excipients such a binders, lubricants and disintegrants. Only relatively recently have systematic efforts been made to define the mechanism of compression, and obtain constitutive equation(s)

for the process.

Researches were carried out on various aspects of powder compaction including; transmission of forces through compacting mass, moisture content of compacts, interparticulate cohesive forces, theory of yield of powders, and empirical equations of compaction etc. These various researches can be classed into two broad categories. Namely; the empirical bulk approach, and the micro-mathematical and numerical method.

The bulk approach is based on one simple truism. That is; the compaction pressure more than any other factor largely controls the densification of powders and the resulting mechanical properties of the compact. Since the usually desired result of any compaction process is a densified and mechanically sound product, a knowledge of the relationship between the compaction pressure and the corresponding density of the powder is very important. The bulk approach has its roots in the vast experience of many industrial and academic researchers and the numerous experimental data of pressure versus density (or porosity) for a large number of powders. With contributions from metallurgy, pharmaceutical industry, chemical engineering, ceramics etc., the results are a set of well tried and trusted empirical relationships between basically, pressure and density (or porosity).

These empirical relations have been very useful and contributed a great deal to the

study of powder compaction and the resulting industrial processes. However, these pressure-density empirical relations are limited. They cannot be applied across the whole range of practical compaction pressures, loading rates and the wide spectrum of powder materials with widely differing properties.

The micro-mathematical and numerical approach has been applied to powder compaction. This usually involves the study of force interaction between the primary particles that make up the powder mass. This has not been hugely successful, largely because no intrinsic material parameters have been identified. Such parameter that are measurable for any particulate in a simple experiment, and can be used in an analytical or numerical model. The absence of such a link between a quantifiable practical material parameter and many of the analytical and numerical models have made such models seem unreal and inaccessible. As a result industrialists have opted for the "safe" and well tried empirical methods.

In this work we present a methodology which includes experimental testing of a powder mass and using the data obtained in a numerical analysis based on a simple analytical model. The experimental work is based on the triaxial testing of the powder mass. To this end, a new triaxial cell system was developed and commissioned. Some traditional triaxial tests were carried out as preliminary tests. Further triaxial tests were carried out, following a new loading cycle. The staircase loading was designed so that non-linearly varying hypoelastic properties as a function of deformation are obtained.

This is fed as input into a finite-element program to simulate die compaction, and the result is compared with experiments.

The data obtained from the "staircase cycle" test were also used to construct a polynomial model for the compaction process. These were included into a finite difference program to simulate die compaction of powder.

The stress-wave technique of the Split Hopkinson pressure bar was adapted to test the strength of compacts. The result of this technique was compared with those obtained by other methods. This stress-wave technique was also used to obtain the acoustic speed in powder compacts of different densities. The result was used to try the "porous model" in a finite difference code.

In literature, the physical processes that take place during the compaction of powders have been well understood. The compaction process can be divided into three main stages; transitional restacking, elastic-plastic deformation; and cold working. The widely used Heckel equation is known to have been successful in describing Stage II of the process, for a wide range of powders. Remarkably the Heckel equation, which has an empirical background, is similar to the pore collapse equation of Carroll and Holt (Chapter 9). But the Heckel equation fails to describe Stages I and III of the compaction process and does not take into account the time dependent nature of the compaction process.

We present an analytical model, based on the Carroll and Holt model, to describe the four stages of the compaction process. Each stage requires a material parameter than can easily be determined from experimental data. Instead of using pressure, we use pressure as a function of time, thereby accounting for the time dependent nature of the compaction process.

This section of the thesis ends with a general discussion of the work presented and a brief conclusion.

1.4 Historical Background

The earliest record of an attempt to mould substances in the form of tablets was recorded in the manuscripts of Al-Zahrawi in the late tenth century [1]) (1970). He described the making of medicinal tablets by using moulds made from wood, ivory or grinding stone, and even suggested ways of controlling the weight of the tablets.

However, it was not until the early 1800's, in the field now known as powder metallurgy, that the first published description of powder compaction was encountered. This was because early furnaces could not achieve the required temperature to melt metals. Grains of iron and copper were compacted under pressure and then heated to produce desired refractory metals. Development of superior furnaces meant that popular metals could be melted, but the temperatures achieved were still not high enough to melt platinum. Up to the early nineteenth century platinum was still made by compaction and sintering. The early advances in powder compaction were therefore

made in this field.

Wollaston [2] (1829) was the first acknowledged scientific worker in this field. In about 1812 he realised that considerable pressure has to be exerted to compact a mass of platinum granules. To produce this pressure mechanically, he developed his famous toggle press and described his powder compaction process for the production of pure aluminium. One of the earliest works published describing the pressing of dry powders was by Burel [3] (1922).

Osann [4] (1841) developed a process for making impressions for medals by compacting copper powders in a die followed by sintering. It was Brockendon [5] (1844) who first patented a machine for manufacturing pills and medicated lozenges by causing granular materials or powders to be made into form and solidified by pressure in dies. Brockendon claimed that his products were then in their final state, not requiring further treatment such as heat.

While interest in Brockendon's invention was maintained by the production of medicinal tablets, on a small scale, Woolaston's method fell into virtual disuse because of the development of fusion techniques for the production of platinum. There is no evidence that further advances were made in this field for at least twenty years.

In the early 1860's demand for new types of medicaments led Dunton [6] to patent his

"tablet" machine based on Brockendon's principles. This was closely followed by the invention of the automatic single punch machine [7] and two types of rotary machines [8-9] (1914).

In the 1870's attention was beginning to focus on the quality of powder compacts produced by the various methods available. In 1872 Burroughs [10] reported on the superiority of the disintegration rate of compressed tablets compared with pills made by conventional methods, and containing the same medicaments. For almost half a century, developments in powder compaction have been spearheaded by the tabletting of medicants. The late 1800's and early 1900's saw a resurgence of activity in metallic powder compaction and sintering, with greater emphasis on quality. Detailed scientific study of powder compaction had begun.

In 1880 a publication by Spring [11] (1880) reported on properties of solid bodies and their welding under pressure. A series of papers followed in which the effects of compressing powders (mainly metallic) in dies were studied. Shortly afterwards Hagen [12] (1919) published his work in which he attempted to classify a wide range of powders according to their "compressional behaviour". By the 1920's the correlation between applied pressure, transmitted pressure and material deformation had been studied, as presented in the papers by Shaxby and Evans [13] (1923), and by Walker [14] (1923).

Meanwhile, in the field of pharmaceutical powder compaction, the techniques for making medicinal tablets were, empirically, well established, reciprocating and rotary punch tabletting machines were widely in use. Apart from a drive for an increased rate of output there was little incentive for changes to be made.

However, in the late 1930's, when Berry [15] (1939) focused attention on the possible shortcomings of tablets as a method of administering medicants, serious functional research into the process of powder compaction started. The publication "Principles of Powder Metallurgy" by Jones [16] (1937), and Balshin's [17] (1938) classical paper which appeared later, made considerable impact on the process of powder compaction. Balshin proposed an equation describing the compaction of a powder mass under pressure to be

$$lnF = A(V/V_0) + B \tag{1.1}$$

Jones, on the other hand, proposed

$$lnp = D(V/V_0)^2 + C \tag{1.2}$$

where V is the volume of powder under applied force F, V_0 is the net volume of powder and A,B,C and D are constants.

As in most other scientific fields, the second world war provided a sharp stimulus to

research and development in powder compaction. Many important papers were published in the field of powder metallurgy, pharmaceutical tabletting and contributions were made from the rapidly expanding plastics industry and the ceramic industry, which was then showing increasing interest in "dry-pressing." Amongst the notable works of the early post-war years was Bowden and Tabor's explanations for the friction phenomenon encountered in powder compaction [18] (1954), throwing more light on die wall and inter-particulate friction.

This period of intense activity, in all spheres of powder compaction, lead to greater understanding of the factors involved. Developments in plant design [19] (1960) have been made possible and roll pressing, isostatic pressing and impact compaction have all become practical realities. A new era in the compaction of powders had begun.

1.5 RECENT WORKS AND DEVELOPMENTS

The intense activity in the years after the second world war led to considerable developments in the field of powder compaction. Much of the scientific studies carried out in this field can be broadly classified into two broad categories, namely; macroscopic and microscopic approach.

The macroscopic approach centres mainly on the attempt to obtain a correlation between applied pressure and material deformation (ie volume changes), thus

establishing constitutive equation(s) for powder compaction. The work of Balshin [17] (1958) in 1958, and that of Jones [16] (1937), mentioned earlier, falls into this category. Later in the 1940's and 1950's several papers were published in which many pressure-volume relationships were proposed. These include works by Smith, Murray, Tanimoto,Terzahi and Nishihara to mention only a few.

Notably, Konopicky [20] (1948), Shapiro [21] (1947) and Heckel [22] (1961), arrived at similar constitutive equations using different assumptions. The Heckel equation is:

$$\ln(1/1-D) = C_1 p + C_2 \qquad (1.3)$$

where p is the applied pressure, D is relative density (ie ratio of apparent density to true density), and C_1 and C_2 are constants. This equation implies a linear relationship between ln(1/1-D) and pressure p. However, this is only true over a limited range of compaction pressure.

A review of various constitutive equations put forward over the years was carried out by Kawakita and Tsutsumui [23] (1966) and more recently by Kawakita and Ludde [24] (1971). These equations were compared with Kawakita's own equation which is of the form:

$$C = \frac{(V_0 - V)}{V_0} = \frac{ABp}{(1 + Bp)} \qquad (1.4)$$

Where C is the degree of volume reduction (often referred to as degree of compaction), V_0 is initial apparent volume, V is the powder volume under applied pressure p, and A and B are constants characteristic of the particular powder being compacted. This widely accepted equation, in the field of powder compaction, is notable for its accuracy for many pharmaceutical products, furthermore it can be applied to piston compression and, with slight modifications, to tapping and vibration compressions.

Hersey and Rees [25] (1970) and later Cole and Rees [26] (1972) carried out a study of Kawakita and Heckel equations comparing their applicability to various pharmaceutical compounds. The above and similar equations are only valid over a limited range of compacting pressure and of rate of compaction.

It was Cooper and Eaton [27] (1962), working in the field of ceramic dry-pressing, who derived a constitutive equation to cover a much wider range of compacting pressure. They divided the compaction process into two broad events namely; the filling of porous holes of the same order of size as the powder particles, by sliding past one another, and the filling of voids that are considerably smaller than the original powder particles, by plastic flow and fragmentation. They came up with the following expression for the progressive compaction of a mass of powder;

$$(V_0 - V)/(V_0 - V_\infty) = C_1 Exp\ -(K_1/p) + C_2.Exp-(K_2/p) + \ldots \qquad (1.5)$$

Where V_0 is the initial volume, V_0 is bulk volume, V is the current volume of the compact under pressure p. C_1 is a dimensionless coefficient for the fraction of theoretical compaction possible at infinite pressure, by the first stage of the compaction process; and C_2 is a similar coefficient for the second stage. K_1 and K_2 are factors indicating the pressure at which pore filling is occurring, by each process, with maximum probability. Thus if the whole compaction process can be described by the two processes only, then $(K_1 + K_2)$ is unity. If some other process is involved, $(K_1 + K_2)$ is less than unity.

Cooper and Eaton [27] (1962) determined the coefficients C_1, C_2, K_1 and K_2 for different ceramic powders of various hardness. The compaction curve they predicted with their equation was reasonably close to the experimental data they obtained.

Although the various constitutive equations put forward, especially those of Heckel, Kawakita, and Cooper and Eaton are empirical, they have nonetheless proved very useful in quantitatively describing the compaction process and allowing comparative experiments to be carried out, albeit over limited ranges of pressure and compaction speed. These equations also help in the selection of optimum compaction conditions.

Work on specific aspects of powder compaction was carried out almost hand in hand with the evolution of various constitutive equations. These include investigations into

the effects of die wall friction, radial pressure, strain rate, effects and into the broader region of dynamic compaction. Though some of these works yielded constitutive equations for the compaction process, most fall into the second category of research referred to earlier, ie the microscopic aspect.

The microscopic aspect is concerned mainly with the observation of the distribution of internal stresses and density, and investigation into the process of compaction as opposed to the quasi-equilibrium pressure-volume behaviour, which is the concern of the macroscopic approach.

Since the time of Balshin [17] (1938), and later contributions from Walker [28] (1943) etc., it was generally accepted that compaction may be visualised as a composite of several processes: Particle diffusion into void space, fracture, elastic deformation, plastic deformation and cohesion between particle surfaces. It is possible that these processes occur simultaneously, although not necessarily to the same degree, at any stage in the compression cycle.

One of the most notable of the early works in this aspect of research, is the work of Seeling and Wulff [29] (1946) published in 1947. They proposed three, though not totally distinct, stages for the compression process during uniaxial consolidation; Stage one of the process involves the rearrangement and packing of the powder particles. Here the particles flow past one another into new positions. The important variables

at this stage are; particle size, size distribution, particle shape and surface properties such as inter-particle friction etc. The second stage of the process is the elastic-plastic deformation and fragmentation of the particles. This includes inter-particle bonding, mechanical interlocking of the particles and various particle interactions; such as interfacial forces due to capillary action, electrostatic forces, adhesive and cohesive forces etc. The final (third) stage is the cold working of the almost solid compact, with or without particle attrition.

As mentioned earlier, these three stages are not distinct and need not follow the above sequence. They may overlap and one of the stages may be absent under certain circumstances. The importance of each stage depends on the properties of the particular powder under consideration.

A number of other works were carried out, throughout the 1950's, on all aspects of research into the compaction of powders. These include the work on variation of the coefficient of friction along die wall, by Kamm, Steinberg and Wulff [30] (1949), the effect of particle size by Heckel, and time-dependent behaviour of powders by Shlanta and Milosovich [31] (1964), and many more.

However, the work of Train [32] (1956), in the particular field of pharmaceutical powders, carried out in the 1950's deserves a mention. Train established a good correlation between pressure and density variation within pharmaceutical compacts.

This he achieved experimentally by the use of manganin wire-resistant gauges embedded in the powder. He presented a theoretical analysis of the relationship between the force required to eject the compact, the maximum pressure applied and the final surface area of the compact. He also discussed, in general terms, the possible causes of "capping", which is the name given to the phenomenon of lamination of the compact on ejection from the die.

Also important is Train's hypothesis on the mechanisms involved in tablet formation. He divided the consolidation process into four stages instead of three as proposed by Seeling and Wulff. Stage one takes into account the interparticulate slippage of the powder particles, which leads to a decrease in relative volume of the compact. The formation of temporary struts, columns and vaults due to the increased resistance of the powder to compression is manifested in stage two. Failure of these structures, brought about by increasing the compression force on the powder material, is obtained in stage three. Here the structure failure is a result of crushing or plastic-flow. In stage four, rebonding is taking place more quickly than particle fracture, and the decrease in the relative volume of the compact becomes quite small as compared to the former stages. There are more refined classifications of the physical mechanisms involved in powder compaction processes; eg Van de Zwan and Siskens [39] (1982) proposed a four stage process,and Duberg and Nystron [34] (1985) proposed seven stages. These will be referred to later in this work.

In UMIST, Es-Saheb [35} (1984) carried out some work primarily aimed at determining the influence of compression rate on the residual resilience, strength, forms of pressure-density relationships including the Heckel and Kawakita diagrams, and the relationship between axial and radial pressures during uniaxial straining. His work covers a wide range of compression strain rates ($1\sigma^{-3}$ to 10^5 per sec.), and he used various powders including di-pac sugar, sodium chloride, potassium bromide, paracetamol DC, copper sulphate, avicel, lactose and calcium phosphate.

His results show that the materials he tested exhibit varying degrees of strain rate sensitivity (ie increased resistance to compaction as the speed is increased). By observing the decay of both axial and radial pressures, under constant volume condition, during successive compression and decompression cycles at various speeds, Es-Saheb arrived at certain conclusions about the relative elastic-plastic behaviour of the materials; he found that the use of linear visco-elastic theory could be useful in predicting the general trend of the compaction process but insufficient to model the response of various powders to the different loading conditions.

This survey of the historical background and recent developments, is by no means a complete one. It is, however, an attempt to highlight some of the important achievements in the field of powder compaction, especially those with particular relevance to the present work. A more thorough survey was recently carried out by Es-Saheb [35] (1985).

The great advance in computer technology heralded another approach to the powder compaction study. Namely, micro-mathematical and numerical approach. This usually involves the study of force interaction between the primary particles that make up the powder mass, Morrison and Richmond [36] (1976). Al-Khattat and Al-Hassani used an approach based on continuum mechanics and numerical analysis [37-39] (1987).

1.6 THE PRESENT WORK

Part one of this thesis covers the work done on compaction of powders. This is laid out in the next few Chapters as follows:

1.6.1 The Triaxial Cell

A new split cell triaxial test system was designed and commissioned. The new cell is capable of high pressure and has a control system which enables sophisticated loading paths. Some preliminary tests of di-pac sugar based on the traditional triaxial testing were carried out.

The theory underpinning the "staircase method" is presented. The results of the "staircase cycle" for di-pac sugar is presented and discussed.

1.6.2 Simulations

The results of the staircase cycle were used for numerical simulations. The first simulation carried out was with the ABAQUS finite element package. Using a polynomial model, the triaxial test results were used in a finite difference simulation of die compaction using AUTODYN.

1.6.3 Stress-wave Technique

The stress-wave technique of the Split Hopkinson Pressure Bar has been used to measure the dynamic properties of metals in the past. We adapt this technique to measure the strength of compacts in tension and compression.

1.6.4 Analytical Method

This has recently been extended to model the spallation phenomenon (Chapter 9). This model is remarkably similar to the empirical equation of Heckel. We present an analytical model based on the Carroll and Holt model to describe the four identifiable stages of the compaction process. We show how relevant parameters can be obtained - experimentally and take into account, the time-dependent nature of the compaction process.

A general discussion of the methodologies presented and conclusions round up this part of the thesis.

1.7 REFERENCES

1 R E King, Remington Pharmaceutical Sciences, 14th Edition, Published by Mack Printing Co. (1970), pp 11649 - 1696

2 W H Woolaston, Phil. Trans, 1829, 119, 1

3 M Bruel, Quarterly Journal of Literature, Science and Arts of the Royal Society of Great Britain, 1882, 12, 246

4 G Osann, Ann. Phys., Lpz., 1841, 128, 406

5 Brockedon, Pharm. J., 1844, 3, 544, (Report on English Patent 9977)

6 J Dunton, US Patent 174790/1876

7 T J Young, US Patent 156398/1874

8 J Wyeth through L F Kebler, J. Amer.Pharm. Ass. 1914, 3, 820; Idem, Ibid., 1062

9 J A McFerran, US Patent 152666/1874

10 S M Burroughs, "An Inaugural Essay on the Compression of Medicinal Powders," Presented to the Philadelphia College of Pharmacy, 1877

11 W Spring, Bull. Acad. Belg. C1. Sci. 1880, 49, 323

12 T Z Hagen, Elektrochem, 1919, 25, 375

13 J H Shaxby and J C Evans, Trans. Faraday Soc., 1923, 19, 60

14 E E Walker, Trans. Faraday Soc., 1923, 19, 73

15 H Berry, Quat. J. Pharm., 1939, 12, 501

16 W D Jones, "Principles of Powder Metallurgy", 1937 (London: Edward

Arnold Publishers Ltd)

17 M Y Balshin, Vestnik Metallopromishiennosti, 1938, 18, 124

18 F P Bowden and D Tabor, "Friction and Lubrication of Solids", 1954 (Oxford: Clarendon Press)

19 W D Jones, "Fundamental Principles of Powder Metallurgy", 1960, a 323, b 928, and c 343, (London, Edward Arnold Publishers)

20 K Konopicky, "Parallelitat der Gesetzma Big Keiten in Keramik und Pulvermetallurgie", Radex-Rundschan, 3, (1948) Hefdt 7/8, 141-148

21 I Shapiro and I M Kolthoff, "Studies on the Ageing of Precipitates and Co-precipitation XXXVIII; The Compressibility of Silver Bromide Powders." The Journal of Physical Chemistry, Vol. 51, (1947), 483-493

22 R W Heckel, "Density Pressure Relationships for Powder Compaction," Trans. of the Metallurgical Society of AIME, Vol. 221, Aug. 1961, 671-675

23 K Kawakita and Y Tsutsumi, "A comparison of Equations for Powder Compression", Bull. Chem. Soc. Japan, 39, 1364-1368, (1966)

24 K Kawakita and K H Ludde, "Some Consideration on Powder Compression Equations", Powder Technology, 4, (1970/71), 61-68

25 J A Hersey and J E Rees, "The Effect of Particle Size on the Consolidation of Powder during Compaction", Proc. of a Conf. organised by the Society for Analytical Chem. on Particle Size Analysis, 9-11 September, Bradford, (1970), 33-41

26 J A Hersey, E T Cole and J E Rees, "Powder Consolidation during Compaction" Proc. 1st Int. Conf. on the Compaction and Consolidation of Particulate Matter, Brighton, October 1972, p 165-172, Editor: Goldberg A S London Power Advisory Centre

27 A R Cooper Jr., and L E Easton, "Compaction Behaviour of Several Ceramic Powders",J. Amer. Ceram. Soc., Vol. 45, no.1, (1962), p97

28 E E Walker, "The Properties of Powders. Part VI: The Compressibility of Powders.", Trans. Faraday Soc. 19, (1923), 73-82

29 R P Seeling and J Wulff, "The Pressing Operation in the Fabrication of Articles by Powder Metallurgy", Trans. Am. Inst. Mining Met. Engrs., 166, (1946), 492-505

30 R Kamm, M A Steinburg and J Wulff, "Leadgrid Study of Metal Powder Compaction" et. Tech. Tech. Pap. No. 2487, Dec. 1948, Trans. AIME, 180; 694-706 (1949)

31 S Shlanta and G Milosovich, "Compression of Pharmaceutical Powders. I Theory and Instrumentation," J. Pharm. Sci., 53 (1964); 562

32 D Train, "An Investigation into the Compaction of Powders", J. Pharm. Pharmac. 8, (1956), 745-761

33 I Van der Zwan and C A M Siskens, Powder Technology, 33 1982) 43

34 M Duberg and C Nystrom, Powder Technology, 46 1986), 67

35 M H H Es-Saheb, PhD thesis, UMIST, (1985)

36 H L Morrison and O Richmond, Powder Technology, 14 1976), 153

37 I M Khattat and S T S Al-Hassani, "Towards a Computer Aided Analysis and Design of Tablet Compaction," Chemical Engineering Science, Vol. 42, No. 4, (1987), 707-712

38 I M Al-Khattat and S T S Al-Hassani, "A Continuum and Finite Element Model for Compressible Solids" (Part I: Conceptual Experimental and Computational Aspects), UMIST, (1987)

39 I M Al-Khattat and S T S Al-Hassani, "A Continuum and Finite Element Model for Compressible Solids" (Part II: Analysis of a Test Problem in Powder Compaction), UMIST (1987)

CHAPTER TWO

HIGH PRESSURE TRIAXIAL CELL

2.1 INTRODUCTION

The stress-strain response of "natural" particulate materials, such as clay and sand, has been studied for many years by civil engineers. In soil mechanics, it was realised that an ideal soil testing apparatus is one which is able to impose a completely general state of stress in which principal planes may rotate. Developing such an ideal apparatus will involve a great number of technical difficulties and consequently the strategy adopted in soil mechanics has been to involve several different kinds of apparatus each loading soil samples in a special way. This gave rise to two broad categories of tests:

(i) tests in which the sample boundaries are principal planes of stress and strain

(ii) shear tests

The first category of tests involve apparatus with smooth, non-rotating rigid platens and/or flexible membrane. An apparatus of this kind immediately imposes two conditions on the behaviour of the sample; principal planes of stress and strain coincide and cannot rotate.

The kinds of tests available in this class of apparatus are:

(a) Uniaxial compression

(b) Isotropic compression

(c) Plane stress

(d) Plane strain or biaxial

(e) The "triaxial" test or cylindrical compression

(f) True triaxial.

On one extreme is the true triaxial test in which all three principal stresses may differ and each may be varied independently. Whilst on the other extreme, in the isotropic compression test, all principal stresses are equal (See Figure 2.1). There are various other kinds of tests between these two extremes and the most important one is the triaxial test. Strictly speaking, the triaxial test in which $\sigma_2 = \sigma_3 = \sigma_r$ would be better described as the cylindrical compression test or axially symmetric test, but the word "triaxial" is firmly established in soil mechanics technology.

The triaxial tests have been adopted in powder technology [1] (1970). In recent years some investigators have employed this kind of test in studying the compaction properties of ceramic and metal powders at very high stress, for example Masuda and Sakai [2] (1972).

In Chapter One, an elaborate discussion on the various works carried out in the field of powder compaction were presented. Extensive empirical data relating axial pressure and overall average density have been obtained in the past and various pressure-density equations were developed. However, these equations cover only a limited range of the compaction process. Although they are useful in classifying the average deformation behaviour of powders, they do not provide any information about local stress distribution. A complete stress analysis of the compaction process is necessary if we are to be able to predict the behaviour of powder compacts more accurately and to explain the phenomena encountered in powder compaction, such as the "capping" phenomenon. This might involve the development of constitutive stress-strain relations which allow for three dimensional stress systems involving large changes in density.

Hope now rests with the use of experimentally based finite element method to carry out a complete stress analysis of the process. An attempt in this direction was made by Loo [3] (1984), but his contribution was limited by the lack of experimental data. It was for this reason that the high pressure triaxial cell was proposed for application to the compaction of pharmaceutical powders.

After some background work, a prototype triaxial cell was developed and built, it was later tested by Asghar [4] (1984). The attempt was successful but some further improvements were required. This led to the development and construction of a new triaxial cell, which is the subject of this chapter.

This chapter covers the development and construction of the new triaxial cell, and the problems encountered in both testing and using it. A brief look at a new high pressure intensifier unit and a new pumping system. Transparent membranes were manufactured for ease of examination after testing, and the chapter gives a brief mention to other auxiliary equipment. The results of preliminary tests carried out with the new set up are presented and discussed.

2.2 THE OLD TRIAXIAL CELL

The old triaxial cell broadly consists of a one-piece pressure vessel and a lower and upper punch. The pressure vessel has an inner bore of 0.784 ins (20.0 mm) in diameter, and is 3.25 ins (92.55 mm) in diameter and a length of 4.125 ins (104.8 mm). It is made from EN30B (nickel-chromium molybdenum) tool steel having a tensile strength of 100 tonf/in^2 (1544.0 MN/m^2).

The lower punch is fixed to the cell body with a screw and carries an end cap, whilst the upper punch has a hole drilled and tapped for pressure transducer housing.

This triaxial cell was used with a Tangyer two speed hydropac pump having a maximum pressure of 8000 psi (55.16 MN/m^2). The full details of this cell and its auxiliary equipment are given by Asghar [4] (1984), and an assembly drawing can be seen in Figure 2.2.

As mentioned in the introduction, this triaxial cell requires some major improvements. These include:

(a) Locating the specimen properly; In the old cell, the sample was attached to the upper punch and then located into the end cup sitting on the lower punch. The sample was located by measuring the length of the specimen and then determining the gap between the flange of the upper punch and the top of the cell body such that the sample sits exactly in the cup, without being pre-compressed. This was clumsy and the sample might not exactly sit in the cup or be pre-compressed. Furthermore, though the end cup was supposed to fit exactly, fluid pressure can act on the end of the specimen in the end cup. To remedy this, the specimen is to be fastened to both the upper and lower punch in the new triaxial cell.

(b) The lower punch of the old cell was fixed, this means that the density distribution in the specimen was much less uniform than would be the case if double action compression was allowed. The lower punch should therefore be free to move, compressing the powder from the bottom.

(c) There was no means of attaching any transducer to the sample with the old cell design.

(d) A high pressure is required and the new triaxial cell will be capable of up to 30,000 psi (206.84 MN/m^2) operating pressure.

2.3 THE NEW TRIAXIAL CELL

For the reasons enumerated above, a new triaxial cell was developed and built. The new cell is a split cell, ie it is constructed in two parts and held together by a nut. This means that the specimen can be attached to both the lower and upper punches, thus eliminating the sample location problems encountered with the old cell, and there is no risk of fluid pressure acting on the lower end of the specimen. A split cell also means that transducers can be attached to the specimen for the measurement of change in dimension or other desired measurements.

The lower punch is free axially, so that double action compression is possible, allowing more uniform distribution of density along the length of the specimen. The lower punch has holes drilled in it, allowing strain gauge leads or leads from other devices to be fed through the inside of the high pressure cell. Like the old cell, the upper punch is able to house a pressure transducer for measuring the pore pressure.

The new cell has several other features that allow easier handling of the cell, including a re-usable high pressure centre sealing ring, and its own supporting system. It is designed to a working pressure of 30,000 psi (206.84 MN/m^2) and subjected to a test pressure of 40,000 psi (275.8 MN/m^2).

2.4 THE NEW CELL DESIGN

As mentioned earlier the new cell is a split cell, which was constructed in two halves.

The top and bottom halves are similar except that the lower half has the inlet port drilled through its side and has two holes near its top for pins to support the nut during cell assembly. The upper half has the bleed port drilled through its side and has two holes for pins which can be hooked to pins on the upper pinch, so that the upper half of the cell and the punch can be lifted together during dis-assembly. Both the inlet and the bleed ports are similar. The lower half has a recess of 2.5 ins (63.4 mm) in diameter and 0.124 ins (3.15 mm) deep, a similar but protruding profile, is on the upper half so that they match accurately. In addition, the upper half of the cell is threaded so that the two halves can be held together by a nut. Figure 2.3 shows the assembly drawing of the two halves of the cell body.

In designing the new triaxial cell there is very little leeway in the choice of size of the bore. The following governed the size of the bore:

(a) The dimensions of the sample need to be kept close to the tabletting dimensions used in the industry.
(b) The upper punch, which has a hole drilled through to house a pressure transducer, should be able to withstand the axial load it is to be subjected to during testing.
(c) A reasonable space is required around the specimen to allow an adequate supply of hydraulic fluid which pressurises the specimen uniformly during testing.

In the final analysis, the choice of commercially available industrial high pressure seals

whose diameter will permit the above constraints, determined the adopted bore diameter ie 20.0 mm (0.789 in).

The next step is the determination of the minimum allowable thickness of the high pressure vessel, having an internal diameter of 20.0 mm and to be tested to a pressure of 40,000 psi (275.8 MN/m^2). This is certainly a case of a thick wall cylinder under high internal pressure. Therefore, Lame's thick cylinder equation was applied in conjunction with the more conservative, Tresca criterion. Figure 2.3 shows the drawing of the upper and lower body. Also Figure 2.4 shows a picture of the cell dis-assembled.

2.4.1 THE NUT

The two halves of the high pressure triaxial cell are held together with a nut made from 316-S16 stainless steel. During assembly the nut is supported by two pins attached to the periphery of the lower half of the cell near the top. When the specimen has been properly positioned, the nut is screwed on to the upper half holding the two halves of the cell together. There are three untapped holes on the periphery of the nut so that the nut can be tightened or untightened with its specially made "spanner". Also the nut is knurled on its circumference to aid in hand-gripping during screwing and unscrewing. A drawing of the nut can be seen in Figure 2.5 and pictured in Figure 2.6.

The input and the bleed ports are fitted with high pressure Sno-trik valves capable of

60,0000 psi (413.7 MN/m^2).

2.4.2 PLUNGERS (PUNCHES)

The upper punch is very much similar to the upper plunger of the old triaxial cell, except that it is longer and has two pins screwed into the periphery of the flange so that the punch can be hooked to the upper half of the cell and can be lifted together when dis-assembling the cell. A hole is drilled through the punch to house the pressure transducer unit for measuring air pressure. This comprises of a filter fitted to the end face bordering the sample, followed by piezo-resistive pressure transducer. The top of the flange has a slot so that leads can be fed through from the transducer. Finally there is a threaded adaptor to enable the upper punch to fit the spigot of the intended testing machine - the RDP Howden.

An alternative upper punch was made for use in trials with the new cell. This was to avoid using the punch which can house the air pressure measuring device in case of any possible damage. Figure 2.6 shows the drawing of this alternative punch.

The lower punch on the other hand is different from the lower punch of the old cell. The profile of the new lower punch is similar to that of the upper punch, but it is longer and has four tiny holes through its "shoulder" converging in a central hole drilled along the vertical axis of the punch. These holes will enable leads to be fed through from any

transducer which might be attached to the specimen. A high pressure seal is used to seal off the end of the hole. The end of the lower punch is shaped like a long hexagon nut and rests on a horizontal plate instead of being attached to the cell body, as was the case with the old cell. Both the upper and lower punches can be clearly identified in the assembly drawing, Figure 2.7.

2.3 HIGH PRESSURE SEALS

Three different sizes of high pressure seals were used with the new triaxial cell, these include: The 2.5 ins (63.5 mm) diameter ring seal placed between the two halves of the triaxial cell, the seals at the punches, and that used to seal the lead through hole of the lower punch.

All the seals are polypak seals, they are type B molythane shell with a nitrate 0-spring energiser and are capable of withstanding up to 60,000 psi (414 MN/m^2).

2.5 PRESSURE TESTING OF THE NEW TRIAXIAL CELL

A testing rig was made to test the new triaxial cell. The cell, designed to a working pressure of 30,000 psi (207 MN/m^2), was pressurised to a test pressure of 40,000 psi (276 MN/m^2). No leaks or distortion was noticed during the test. The outline assembly of the cell complete with the testing rig can be seen in Figure 2.8.

2.6 TRANSDUCERS

The most important measurements in the triaxial cell system are: accurate measurement of the cell pressure and direct axial load measure. The cell is designed so that it is easy to add various devices for measuring the response of the specimen being tested. In the case of powders, pore pressure can be measured by a very sensitive pressure gauge housed in the upper punch as described earlier. A clip gauge was also designed to measure the change in diameter of the specimen. Solid specimens, such as glass fibre composites, can be strain gauged. Some of these devices are briefly described below.

2.6.1 PRESSURE TRANSDUCER

A high pressure gauge is mounted on the hydraulic circuit after the high pressure intensifier unit, just before the cell. This measures, very accurately, the pressure in the cell. It is a very high response electronic pressure gauge whose output is fed into the control unit. Its signal is used to provide direct pressure reading which shows up on a meter on the control unit. Sockets are also provided for its output to be fed into a data logger for continuous recording. Its signal is also used in the feedback system and to calculate the pressure component of the total load recorded by the load cell on the testing machine.

2.6.2 AIR PRESSURE GAUGE

A miniature air pressure gauge is housed in the upper punch to measure the pore pressure. A very small chamber was created near the tip of the upper punch, which

is separated from the perforated PTFE on top of the specimen by a metal filter. The tiny gauge is mounted at the top of the small chamber in its housing. In this way, any air squeezed out of the powder under compaction is trapped in the small chamber and the increasing pressure in the chamber is measured by the air pressure gauge. The recorded pore pressure can be used to calculate the volumetric strain of the powder mass being tested. This device can be seen in its housing in Figure 2.9, along with the devices used to prepare the specimen.

2.6.3 CLIP GAUGE

A strain gauge device was developed for use in measuring the change in the diameter of the powder mass contained in a flexible neoprene membrane, as described earlier. The device, made out of spring steel, has a circular shape such that it can be clipped round the specimen. It is equipped with a full bridge strain gauge, two hoop and two axial, and calibrated to measure small changes in the diameter of the specimen. Figure 2.10 shows a sketch of the device.

2.6.4 AXIAL DISPLACEMENT MEASUREMENT

We could not rely on the axial displacement device on the testing machine. This was because, at high loads when the specimen is almost fully compacted, the change in length of the specimen is of the order of the rigidity of the system, ie deflection of the testing machine itself and the combined displacement in the two plungers. A very sensitive LVDT was mounted between the shoulder of the upper punch and the top half

of the cell. This was calibrated in such a way as to take into account the axial deflection of the plungers, thereby providing an accurate measure of axial displacement.

2.6.5 DIRECT AXIAL LOAD

This is one of the most important measurements in the triaxial test system. This could be seen as being fairly straightforward, but in fact it proved very problematic and required a drastic solution.

Both the upper and the lower punches stepped from the dimension of the bore down to the intended dimension of the specimen. As a result, a substantial component of the axial load, measured by the testing machine, is due to the pressure acting on the shoulder of the plungers. The pressure component was subtracted electronically in the control unit to provide us with a true load reading, as explained later.

However, the high pressure seals at the bore affect the load reading as the pressure is increased. This effect, we discovered, is not linear and cannot easily be accounted for. This has been a longstanding problem in the design of such high pressure triaxial cell systems. Usually such cells are designed without any seals but with tight fitting of the plungers to the bore. Very good finish is provided to reduce sticking and the whole cell assembly is continuously rotated to-and-fro to avoid sticking. This limits the pressure capacity of such cells because of leakage and, therefore, the flow rate required

from the pump.

In our design of the new cell, we deliberately used seals to ensure high pressure capacity. The seals were carefully chosen so that their effect can easily be calibrated. However, we demanded high accuracy, and the non-linearity in the response of the seal meant a radical solution had to be considered. A load cell internal to the cell chamber is the only practical solution and this meant a re-design of the lower punch.

There is no room inside the cell for any kind of miniature load cell to be considered, and it is hard to think of a load cell that is not going to be affected by the very high pressure environment in the cell. We therefore opted to build the load cell into the lower punch. Figure 2.11 shows the evolution of a workable lower plunger/load cell design.

The first design was a modification of the existing lower punch so that a strain gauge bridge could be mounted onto it, above the shoulder. Because of the short length of the punch above the shoulder, there is stress concentration at corners worsened by the high pressure in the cell.

Figure 2.12 shows the drawing of an old design. The top part of the cell is a cap housing a small cylindrical load cell. A picture of this, with the cap on the side is shown in Figure 2.11 This was only relatively successful. The copper sheems used

to seal the load cell from the high pressure environment flattened slowly with repeated use. As a result the calibration changes by a small amount after several uses.

A drawing of the successful design is shown in Figure 2.13 and also in the picture, Figure 2.11. The design was simple and it worked very well. The design was aided by the use of ABAQUS finite element program. The top part of the punch above the shoulder was simplified. The result is a solid cylindrical portion long enough to mount a full bridge strain gauge set, see Figure 2.14. The design was modelled numerically to ensure that the area where the strain gauge bridge was mounted sustains only uniform stresses. Contours showing the result of the modelling are shown in Figure 2.15, and a listing of the ABAQUS input file is in Appendix Three.

The new load cell is affected by pressure but this is linear and very small. The strain reading due to pressure is negligible, compared to that due to axial loading. The pressure effect was subtracted electronically so that a direct axial load reading could be monitored and recorded continuously by a data logger.

2.7 AUXILIARY EQUIPMENT

Various other equipment form an essential part of the triaxial cell system. Some of these are described below.

2.7.1 THE CELL SUPPORT SYSTEM

Unlike the old cell assembly in which the lower punch is directly screwed into the spigot of the RDP Howden testing machine, the new cell assembly is equipped with a support system which supports it's base. The support system comprises of four 20 mm diameter and 343 mm long screwed rods, a 10 mm by 163.5 mm mild steel plate, a 31.75 mm by 163.5 mm mild steel plate, four 10 mm nut and washers and four 10 mm knurled nuts.

The cell rests on the thinner plate, and the lower punch, and the whole assembly rests on the thicker plate. This plate has a 10 mm stud firmly fixed to its base so that the whole assembly can be screwed down to the spigot of the RDP testing machine. The knurled nuts can be turned to adjust the cell to the required height. An outline assembly drawing of the triaxial cell and the support system is shown in Figure 2.16 and the cell is pictured on its support system in Figure 2.17.

2.7.2 HYDRAULIC SYSTEM

In the old triaxial system, a Tangyer two speed hydraulic hand pump was used. The unit was capable of 8,000 psi (55 MN/m^2). However, the triaxial cell requires a hydraulic system capable of sustaining a pressure of up to 30,000 psi (207 MN/m^2) in the cell.

The new hydraulic system is made up of a pumping unit and a high pressure intensifier unit operated through a servo-control unit.

2.7.2 (a) THE PUMPING UNIT

The first pump used with the high pressure intensifier unit was the SC hydraulic pump model 10-500, driven by an Airmaster air pump. But the flow rate was not enough to catch up with the leak across the servo-valve of the high pressure intensifier unit. A hydraulic power pack was therefore substituted in place of the pump.

The power pack is capable of a maximum pressure of 31.5 MPa (4,750 psi) and a maximum flow rate of 8 litres per second at a minimum pressure of 0.1 MPa. The operating pressure is set by hand operated pressure relief valve equipped with a pressure gauge and situated on top of the tank. The unit can be controlled locally or via a remote control located on the high pressure intensifier unit.

Start/stop and a high/low pressure mode can be selected at both the local and remote control levels. However, the motor can only start in the low pressure mode regardless of the setting of the pressure mode switch.

The hydraulic fluid used in the power pack unit and the triaxial cell system is the Shell Tellus R37 oil. The unit has a reservoir of fifty litres and the same oil is used for topping-up purposes. Figure 2.18 shows some details of the hydraulic power pack connected to the hydraulic circuit of the triaxial cell. The picture in Figure 2.19 also shows the power pack with the rest of the hydraulic system.

2.7.2 (b) HIGH PRESSURE INTENSIFIER UNIT

The high pressure intensifier unit consists mainly of a 15 μm pressure filter, a 2 litre accumulator, a servo-valve and the 1:10 intensifier.

A flexible high pressure hose from the power pack is connected to the 15 μm, 40 MPa (6000 psi) pressure filter via a 0.05 MPa non-return valve. The filter itself is equipped with an electrical indicator and a switch. The 2 litres accumulator, to store 31 MPa (4,500 psi), and a 6 ins gauge, reading up to 40 MPa are positioned on the pipe leading from the filter to the servo-valve. The servo-valve is controlled from the control unit and operates the 1:10 intensifier which maintains the high pressure required in the triaxial cell. There is a pressure transducer which measures the pressure output from the intensifier, this is routed to a pressure signal amplifier in the control unit. There is also a piping which by-passes the intensifier, via a hand controlled valve, to pre-fill and bleed the triaxial cell. The system is equipped with a 24 Mpa (35,000 psi) burst disc which ensures that the pressure into the triaxial cell is below 240 MPa. Finally, there is a hand valve to let down the system by bypassing fluid through a flexible nylon hose to the return line of the power pack unit. Both Figures 2.18 and 2.19 show some details of the high pressure intensifier unit and its position in the hydraulic system of the triaxial cell.

2.7.2 (c) SERVO-CONTROL UNIT

The essential components of the control unit include a pressure signal amplifier, load

cell signal amplifier, a signal processor and a servo-valve to maintain the pressure demand. This unit monitors the actual axial load on the specimen in the triaxial cell and the confining pressure. The true load is worked out by subtracting the axial load, exerted on the annulus of the punch by the hydraulic fluid, from the total axial load registered by the RDP load cell, see figure 2.20.

$A_1 = 111.782\ mm^2$

$A_2 = 314.788\ mm^2$

$A_2 - A_1) = 203.006\ mm^2$

Apparent axial load = load indicated by the load cell

True axial load = Indicated load - $(A_2 - A_1)p$.

Where p is the radial (confining) pressure.

This true load measure provides a back-up and a check on the direct load measure described in Section 3.5.

Part of the control unit is illustrated in Figure 2.18 which shows the schematic layout of the triaxial system. It is also pictured in Figure 2.21.

2.8 CONTROL MODES

At least three different control modes are available to the triaxial cell system. These include; independent pressure and load control, independent close loop pressure and load control, and dependent control mode.

Figure 2.22 shows an example of pressure against load pattern for independent pressure and load control mode. The load is controlled by manually operating the cross head control on the RDP testing machine to achieve the desired axial load, and the pressure is controlled from the pressure demand dial in the servo-control unit. In this case axial load can be increased at constant pressure, but increase in pressure is accompanied by a change in axial load due to the effect of the pressure on the specimen.

In Figure 2.23, a typical pattern of pressure against load is shown for independent close-loop pressure and load control. Here axial load can be increased at constant pressure and the pressure can also be increased at constant axial load.

Figure 2.24 shows the dependent control mode in which the confining pressure and the true axial load on the specimen were increased in constant proportion to one another. In this case both the maximum load and the maximum pressure to be achieved were set on the servo-control unit, the RDP was then started on the automatic mode, and the demand signal was gradually increased until the maximum load and pressure had been achieved.

Plans are being advanced to introduce computer control in the near future. This will enable a more complex loading pattern to be generated, and smoothly and efficiently operated. Such a modification will require axial load demand signal to be incorporated.

2.9 TRIALS AND FAILURES WITH THE NEW TRIAXIAL CELL

After the pressure testing of the cell to 40,000 psi an attempt was made to try out some tests by incorporating it into the hydraulic circuit. During this test some leakage of oil was noticed. It was quickly

realised that the high pressure seal between the two halves of the triaxial cell has failed. When the cell was decoupled and examined, it was noted that the seat of the high pressure seal had been slightly distorted and the base of the nut had bowed out. This failure might have been initiated during the 4,000 psi pressure testing and plastic deformation of the critical part of the nut might have progressed due to subsequent loading. A possible reason for the failure of the nut could have been that the critical part of the nut on which the lower half of the cell rests was not thick enough, resulting in an over-estimation of the yield stress of the nut material. The material is stainless steel 316-S16. Its stress-strain characteristics show no particular yield point and about 0.2 percent proof stress was used in the calculations.

The profile of the seat of the high pressure seal was re-machined and a new nut was made using tool steel EN24T. Also some dimensions of the nut were modified.

The new nut performed adequately in the first few tests and then the confining pressure was raised up to 25,000psi. When an attempt was made to undo the nut after the test, the nut would not unscrew. Various methods were used, including differential heating and cooling, but the nut would still not unscrew. Eventually the nut had to be sawn

off to separate the two halves of the cell. The damaged nut and the cell bodies can be seen in Figure 2.25.

It was not immediately clear why the nut had seized up but one or more of the following may account for the mishap;

(i) Though the cell and the nut were cleaned by air blast, it is possible that some particles of metal dust or dirt might remain. This might weld the threads together at high pressure.

(ii) It could be due to a very tight tolerance on the threads. The effect of this could also be to weld the threads together at very high pressure.

(iii) It might be due to dissimilar material. The cell body was made from stainless steel 431-S29 whilst the nut was made from tool steel EN24T as mentioned above.

The proposed solution to the latest mishap was to build a new nut using Copper-Nickel Silicon alloy steel. It is a stronger material with a proof stress of 500 MN/m^2 and an ultimate tensile strength of 670 MN/m^2 and has some lubricating properties. Though both the upper and the lower halves of the cell survived, they need to be touched off on the lathe.

2.10 TRANSPARENT NEOPRENE LATEX BAGS

In triaxial testing, the specimen is enclosed in cylindrical flexible membrane which allows the application of confining pressure to the specimen and prevents the hydraulic

fluid from mixing with it. In the work of Asghar [4] (1984), black (opaque) neoprene latex membrane was used. This meant that the specimen cannot be examined after the test is over. The specimen normally breaks up during removal from the membrane.

To overcome this difficulty, transparent membranes were made instead. The method of manufacture of neoprene latex bag and the associated equipment are meticulously detailed in Asghar's work [4]. The only difference is that a different type of latex and coagulant were used in the present work. Some of the apparatus used are pictured in Figure 2.9.

The latex used was: AL330 pre-vulcanised Dunlop latex compound.

The coagulant used was: 20 percent calcium nitrate solution in methanol.

2.11 PRELIMINARY TRIAXIAL TESTS

The stress-strain behaviour of a material can be studied by controlling the stress and recording the strain, or vice-versa. The triaxial system developed is particularly suited to stress-controlled triaxial tests, permitting independent (and dependent) control of axial and radial stresses. Various types of stress controlled tests, depending on the stress path used, can be carried out. This can be explained with the aid of a q-p diagram, where q is the deviatoric stress and p is the mean normal stress. $q = \sigma_1 - \sigma_3$ and $p = 1/3(\sigma_1 + \sigma_3)$.

Figure 2.26 shows three possible stress paths; (1) represents the case where σ_1/σ_2 is kept constant, curve (2) applies when $p = 1/3(\sigma_1 + 2\sigma_3)$ is kept constant, and curve (3) when $\sigma_2 = \sigma_3$.

Tests carried out in accordance with such stress paths will produce stress-strain characteristics of the material being studied, and a failure line such as shown in Figure 2.26 can be determined.

Two categories of tests were carried out. These include:

(a) Tests in which the confining pressure was kept constant and the axial pressure is gradually increase, ie σ_3 is constant. This is in agreement with curve (3) in Figure 2.26.

(b) Tests in which both the confining pressure and the axial pressure were increased together in a constant proportion to one another: σ_1/σ_3 = constant. This is in agreement with curve (1) in Figure 2.26.

2.12 RESULTS

The results of the tests carried out are presented in the following forms:

(1) Mohr Stress Circles: this shows shear stress against the direct stress. It is drawn by plotting the principal stresses σ_1 and σ_3 on the direct stress axis, and drawing a circle through the two points. The middle of the circle being $(\sigma_1 + \sigma_3)/2$. Figures

2.27(a) to 2.31(a) show the Mohr circles for the various tests. Figures 2.27 to 2.30 (a to h) are results for the different constant radial pressures, and Figures 2.31 and 2.32 (a to h) are for the two σ_1/σ_3 = constant.

(2) Axial Stress, σ_1 Against Radial Stress, σ_3: These are shown in Figures 2.27(b) to 2.32(b) for each of the tests.

(3) Deviatoric Stress, q Against Mean Stress, p: Figures 2.27(c) to 2.32(c).

(4) Stress Ratio, R, Against Change In Height, DH: Figures 2.27(d) to 2.32(d).

(5) Axial Stress, σ_1, Against Axial Strain, : Figures 2.27(e) to 2.32(e).

(6) Stress Ratio, R, Against Axial Strain, : Figures 2.27(f) to 2.32(f).

(7) Axial Stress Against Change In Height: Figures 2.27(g) to 2.32(g).

(8) Deviatoric Stress Against Axial Strain: Figures 2.27(h) to 2.32(h).

2.13 DISCUSSIONS

The tests carried out with the old cell in the new hydraulic circuit yielded some interesting results. In the case of the tests in which the radial pressure was kept constant, Figures 2.27(c) and 2.30(c) show that in each case the respective constant radial pressure was achieved with remarkable stability. This is further illustrated by Figures 2.27(a) to 2.30(a), showing Mohr stress circles all of which pass through one common point. Figures 2.27(b) to 2.30(b show the stress path followed on a q-p diagram and these are as predicted in Figure 2.26). Where q is deviatoric stress (σ1 -

σ_3) and p is mean stress, $2/3(\sigma_1 + 2\sigma_3)$.

Figures 2.27(d) to 2.30(d) show that a similar pattern of stress ratio, R, against change in height, dh, was obtained for all the cases of constant radial pressure. The stress ratio remained almost constant at between 1.3 and 1.4 before a distinct transition into a steep rise at about 20 to 25 percent compression. The tests were stopped after about 40 to 50 percent compression for safety reasons, but if the test had continued further these curves would have terminated at failure. Although failure is not observed in the curves presented here, most of the specimens were observed to have failed after removal from the cell, this is most likely due to unloading stresses.

The rest of the graphs σ_1 against strain, q against strain etc. look very much like the curve of R against dh as expected.

In the cases of σ_1/σ_3 = constant, Figures 2.31(c) and 2.32(c) show that a constant stress ratio was maintained and the q-p diagrams in Figures 2.31(b) and 2.32(b) are as predicted in Figure 2.26. However, Figure 2.31(d) and 2.32(d) show some apparent variation of the stress ratio, R. A close examination of the curves will reveal that the stress ratio was constant to between 4 and 7 percent, this accounts for the scatter observed in these two Figures.

Figures 2.31(a) and 2.32(a) show the Mohr circles of stress. Interestingly, a very good

straight line is produced by the linkage of the circumferences of the circles. It is the slope and Y-intercept of these straight lines which give the values of angle of internal friction and cohesion respectively.

The curves for σ_1 against strain and that of q against strain etc. look similar to one another, an exponential rise of stress against strain. But the curves of R against strain are similar to those of R against dh as might be expected, since R is more or less constant.

The experiments were highly satisfactory and very much repeatable. This fact is proven by comparing the results for the constant radial pressure of 137 MN/m^2 (20,000 psi approx.) as shown in Figures 2.29 and 2.30 (a to h). These are results of two separate tests but are virtually the same in all respects.

3.14 CONCLUSIONS

A new high pressure split triaxial test system is designed and constructed. Tests carried out with it show that it is operating satisfactorily.

An important feature of the system is the flexibility built into it to accommodate transducers within the cell. This proved to be very successful.

Preliminary tests carried out show that the system is reliable and the experiments are repeatable.

2.15 REFERENCES

(1) R L Brown and J C Richards, "Principles of Powder Mechanics", Pergoman Press, OXFORD, 1970.

(2) Y Masuda and N Sakai, J. Jpn. Soc. Powder Metall., 19 (1972), 1

(3) W Y Loo, PhD Thesis, UMIST, 1984

(4) H Asghar, MSc Dissertation, UMIST, 1984.

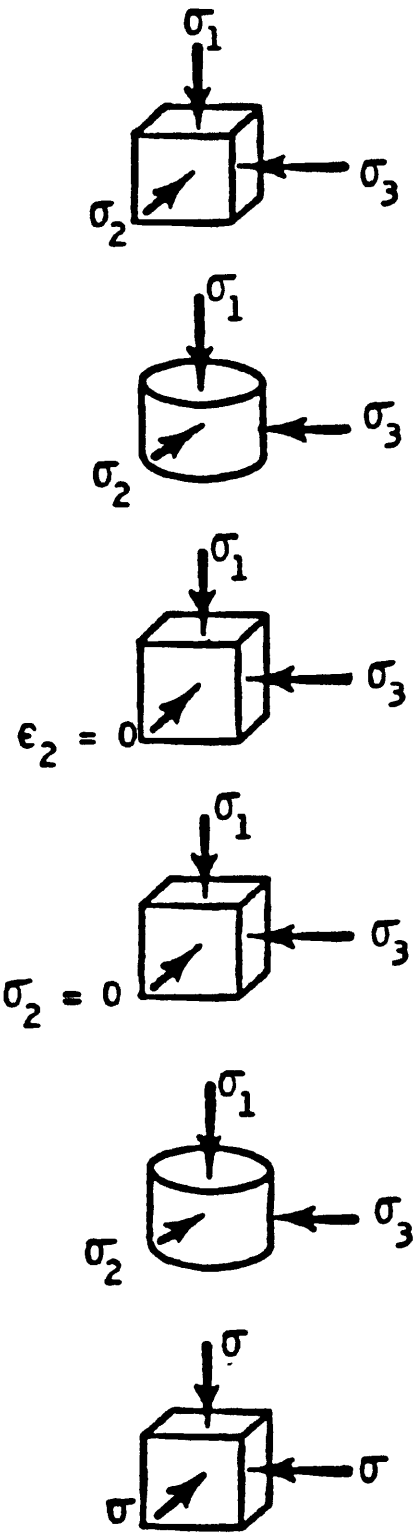

True Triaxial Test
$\sigma_1 \neq \sigma_2 \neq \sigma_3$
$\varepsilon_1 \neq \varepsilon_2 \neq \varepsilon_3$

The 'Triaxial Test'
(Cylindrical Compression)
$\sigma_1 = \sigma_2 = \sigma_3$
$\varepsilon_1 = \varepsilon_2 = \varepsilon_3$

Plane Strain or Bi-Axial
$\varepsilon_2 = 0$

Plane Stress
$\sigma_1 = 0$

Uniaxial Confined Compression
$\sigma_2 = \sigma_3 = 0$

Isotropic Compression
$\sigma_1 = \sigma_2 = \sigma_3 = 0$
$\varepsilon_1 = \varepsilon_2 = \varepsilon_3 = 0$

Fig 2.1 Common Types of Multi-Axial Tests

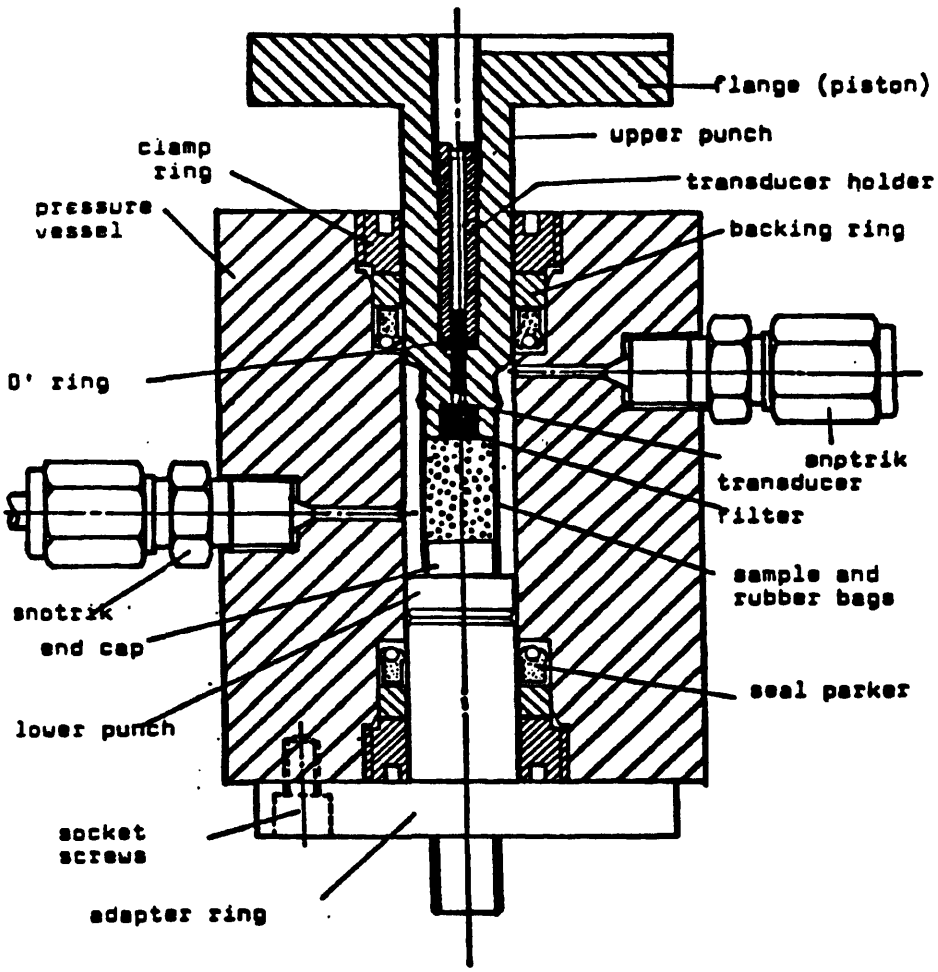

Fig 2.2 The Old Triaxial Cell

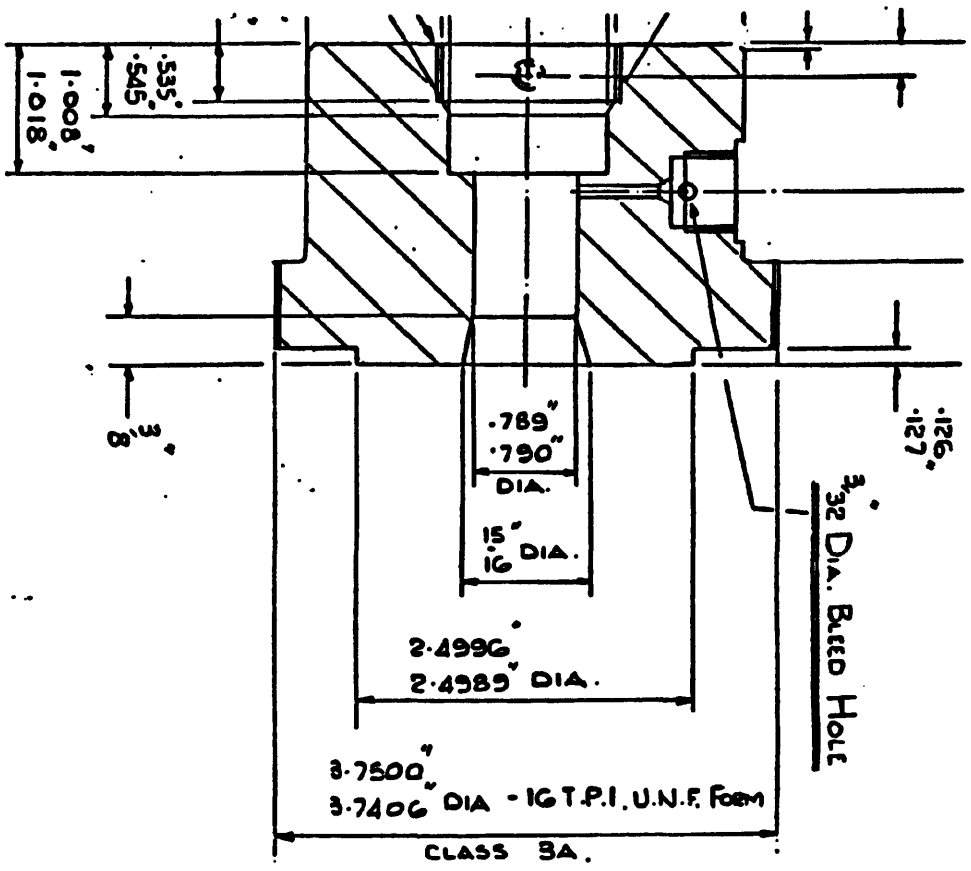

Fig 2.3 (a) Upper Triaxial Cell Body

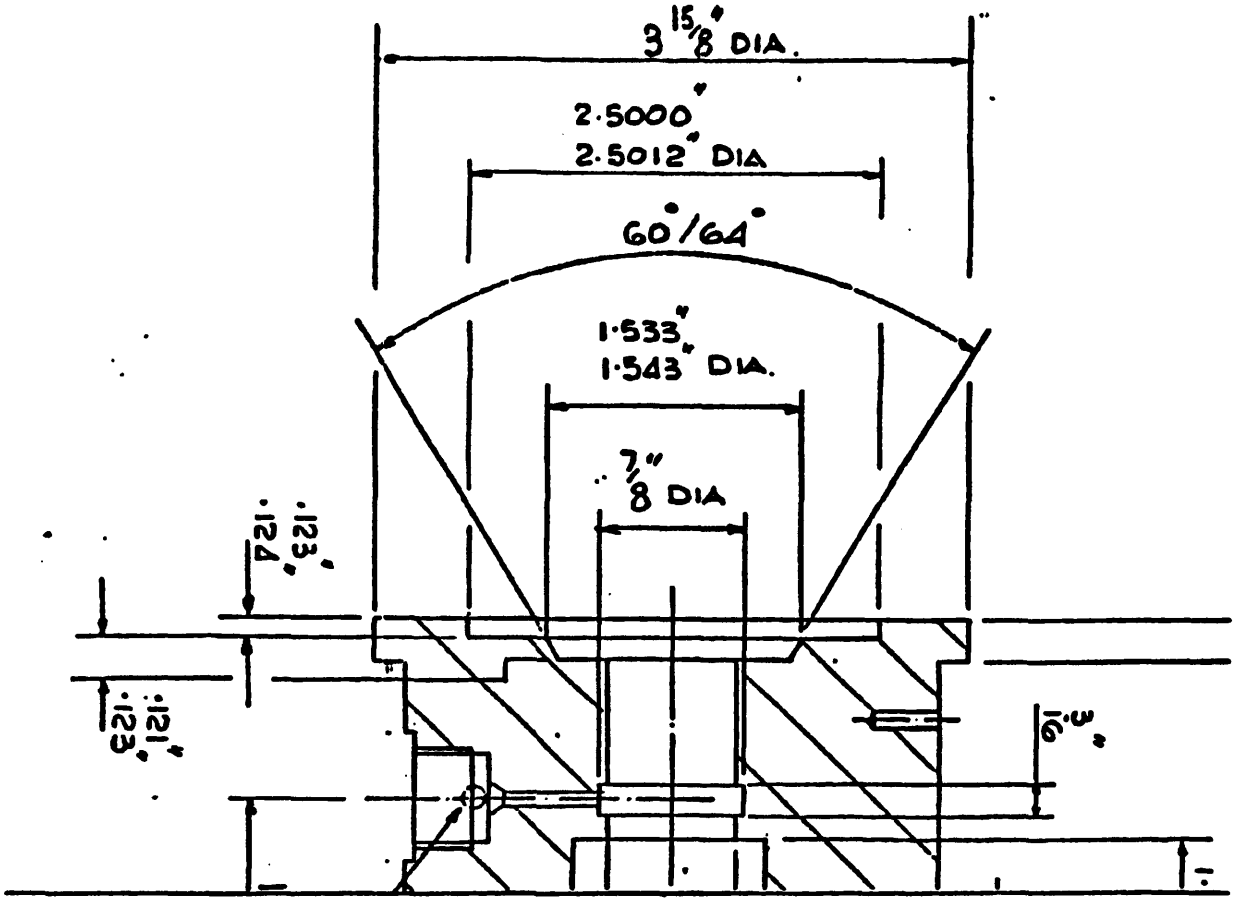

Fig 2.3 (b) Lower Triaxial Cell Body

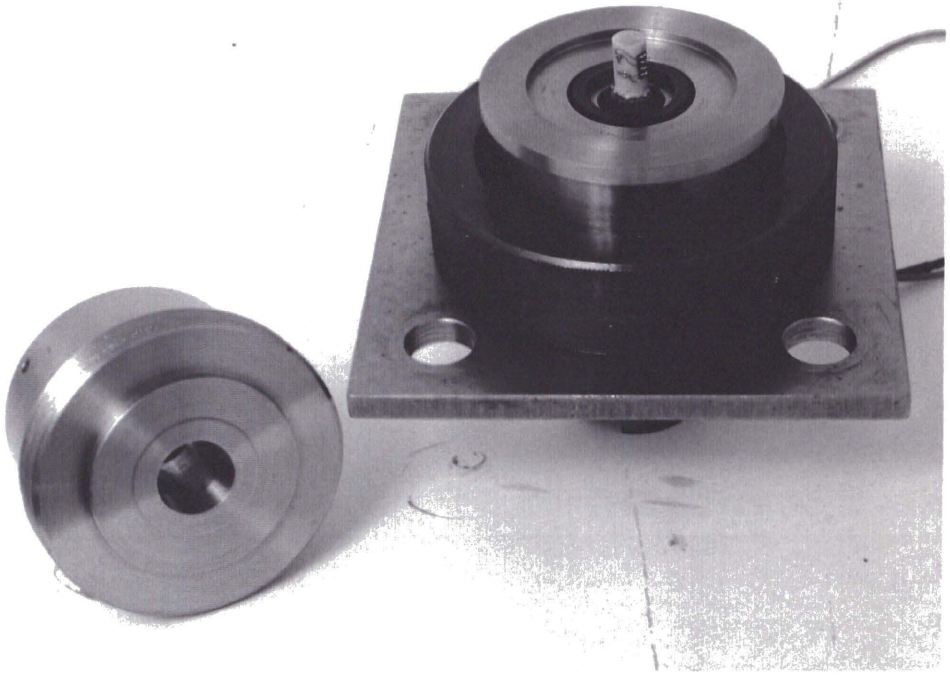

Fig 2.4 Triaxial Cell Disassembled

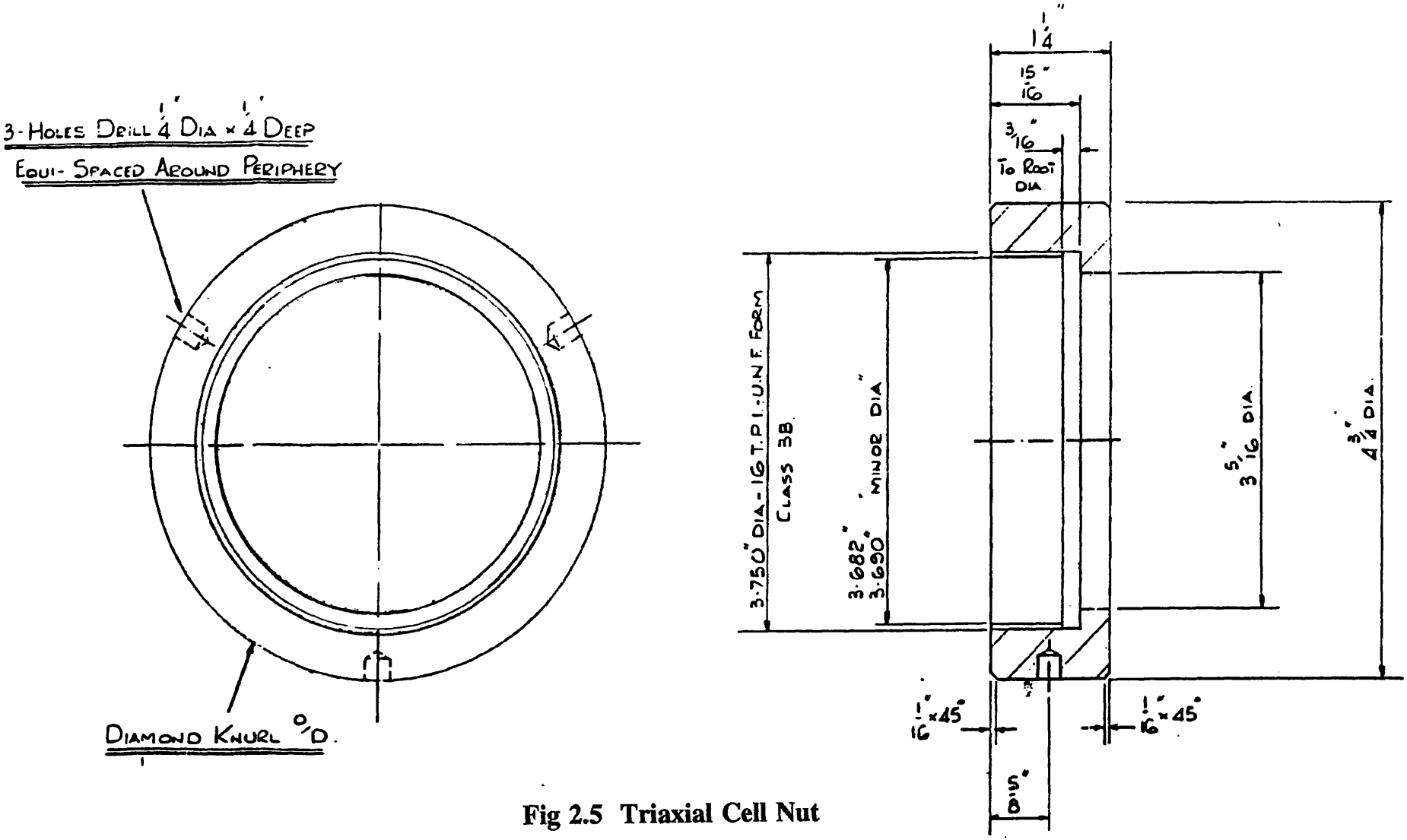

Fig 2.5 Triaxial Cell Nut

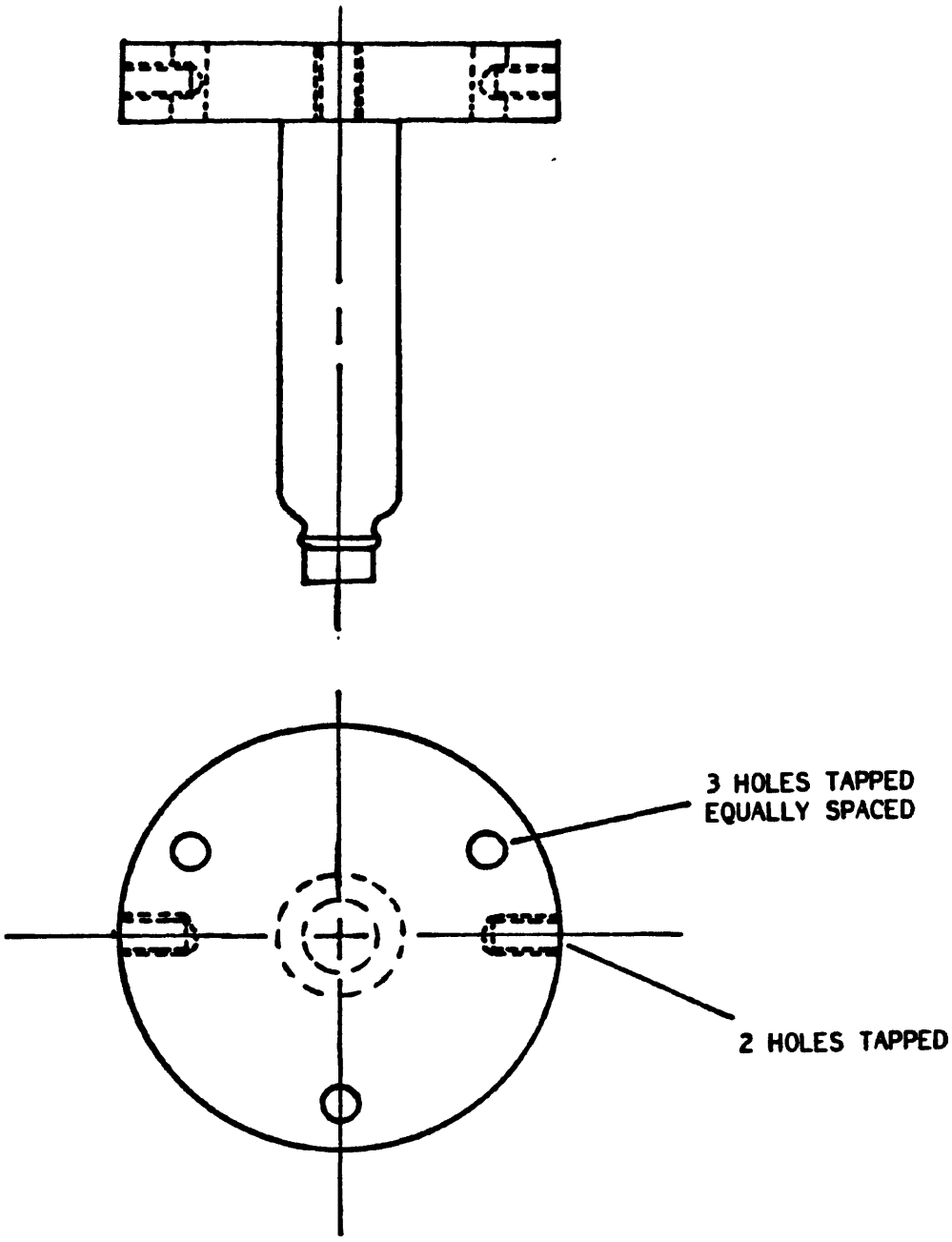

Fig 2.6 Alternative Upper Plunger

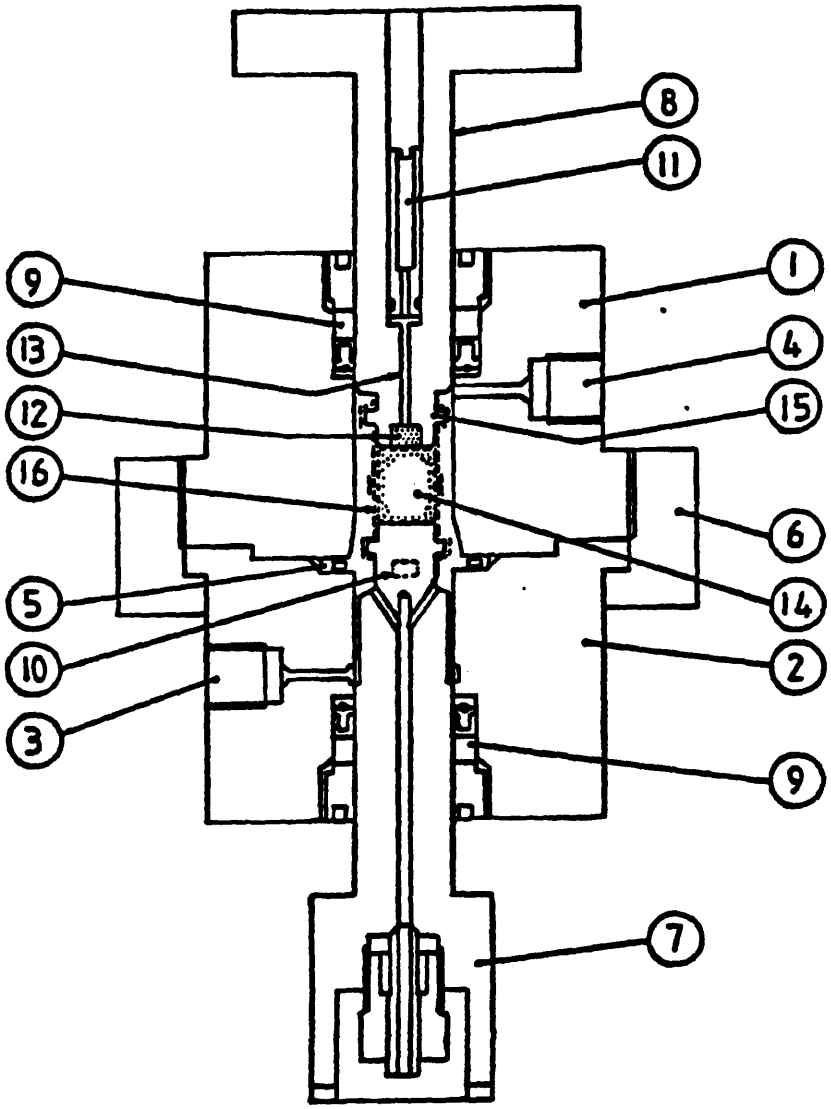

Figure 2.7 The Triaxial Cell Assembly

(1). Upper Body (2). Lower Body (3). Input Port
(4). Servo Valve (5). 1:10 Intensifier (6). Pressure Amplifier
(7). Load Amplifier (8). Upper Punch (9). Seal
(10). Load Cell (11). Air Pressure Transducer
(12). Porous Plug (13). Air Chamber (14). Powder Specimen
(15). Depth Stop (16). Bag

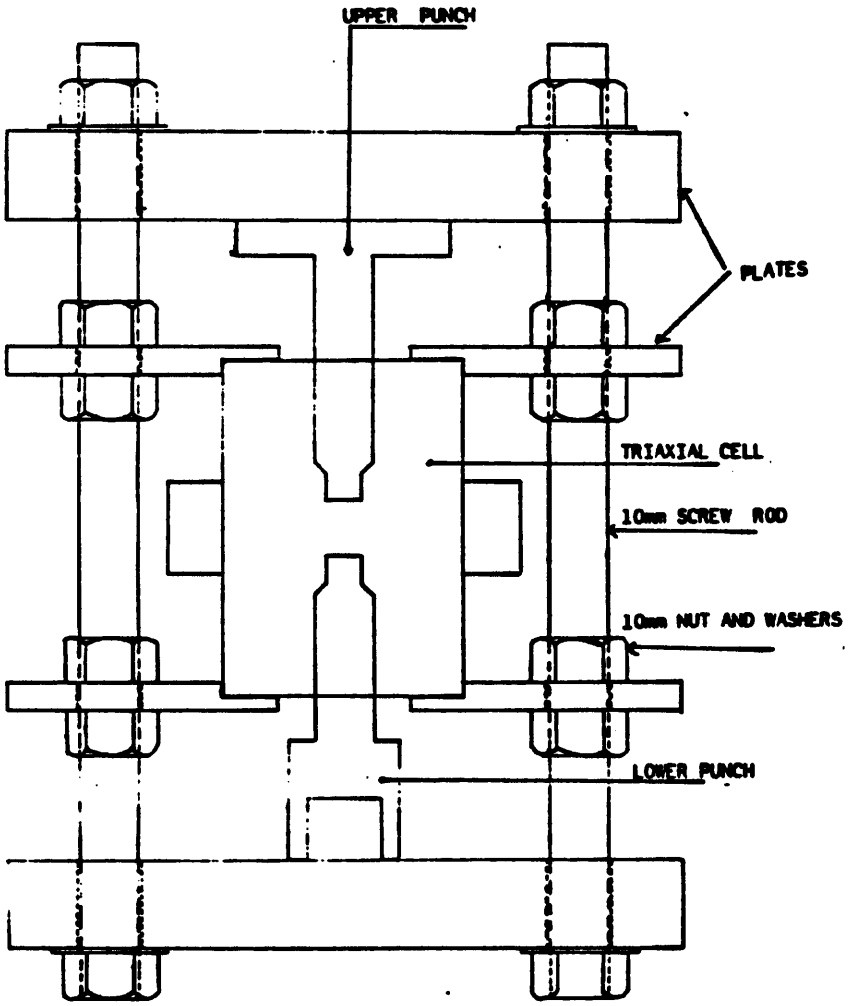

Fig 2.8 Outline Drawing of Cell and Testing Rig

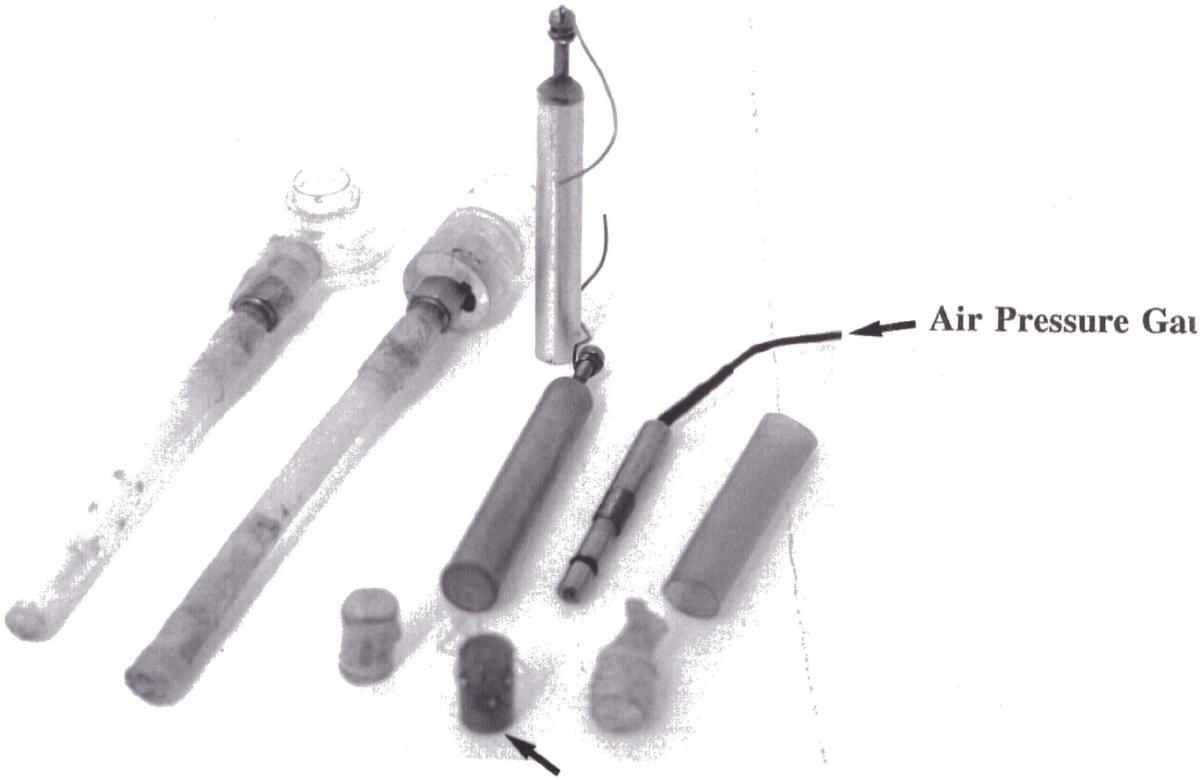

Fig 2.9 Auxilliary Equipment

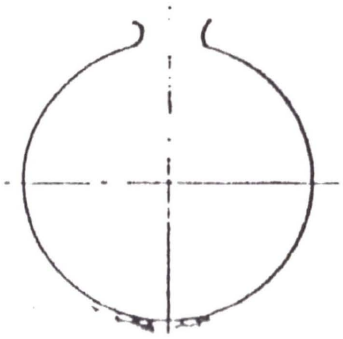

Fig 2.10 Clip Gauge

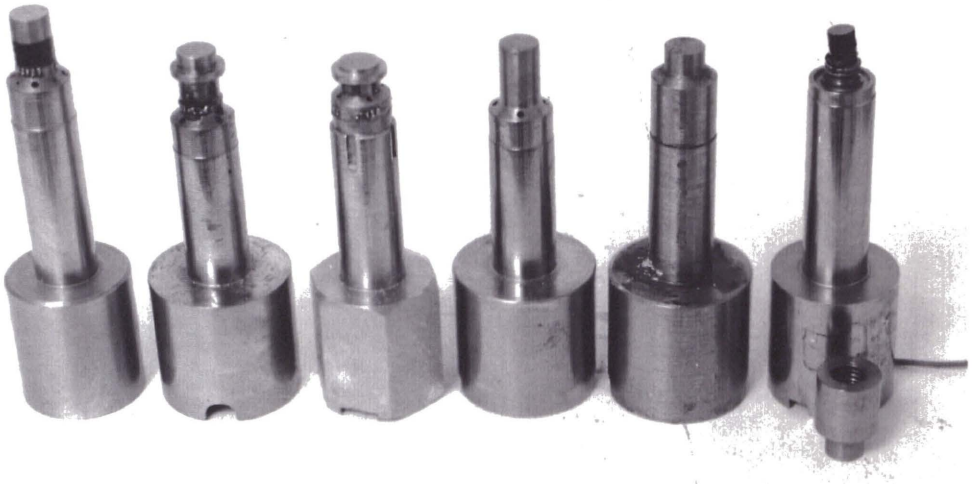

Fig 2.11 Various Lower Punch - Load Cell

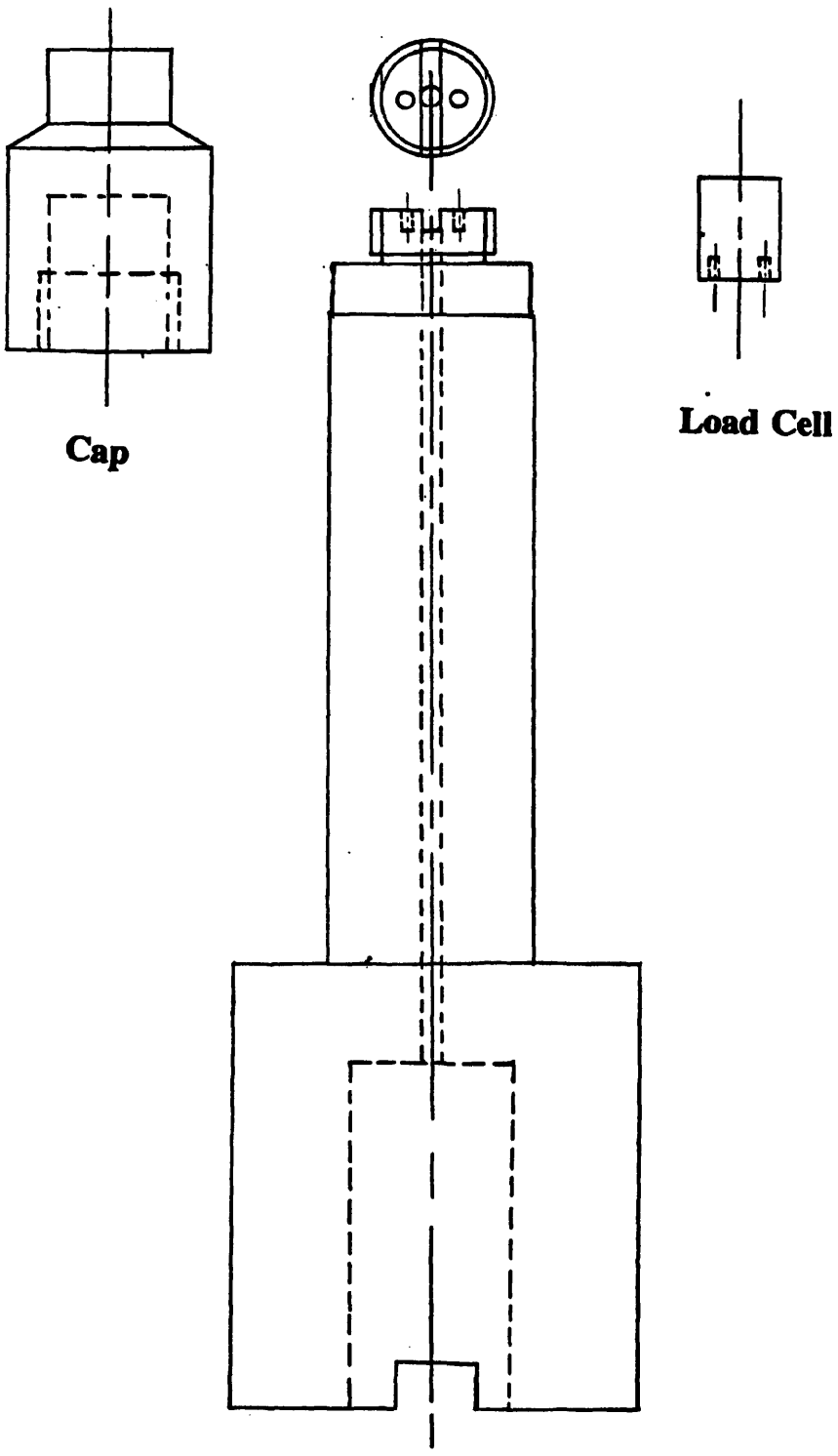

Fig 2.12 Old Punch Design With Internalised Load Cell

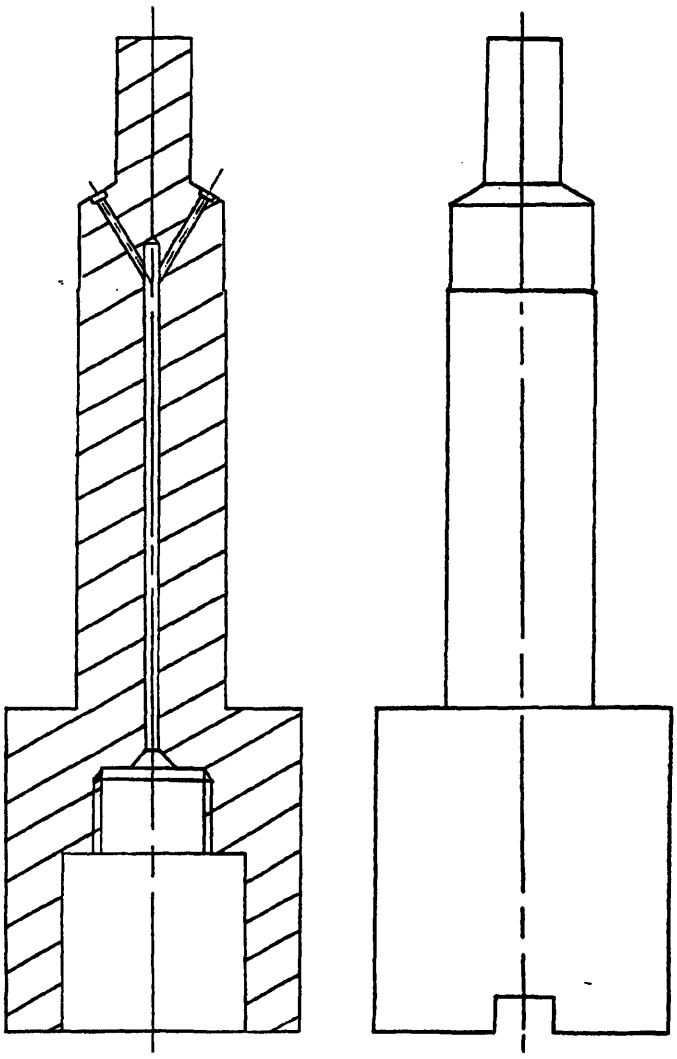

Fig 2.13 Successful Lower Punch

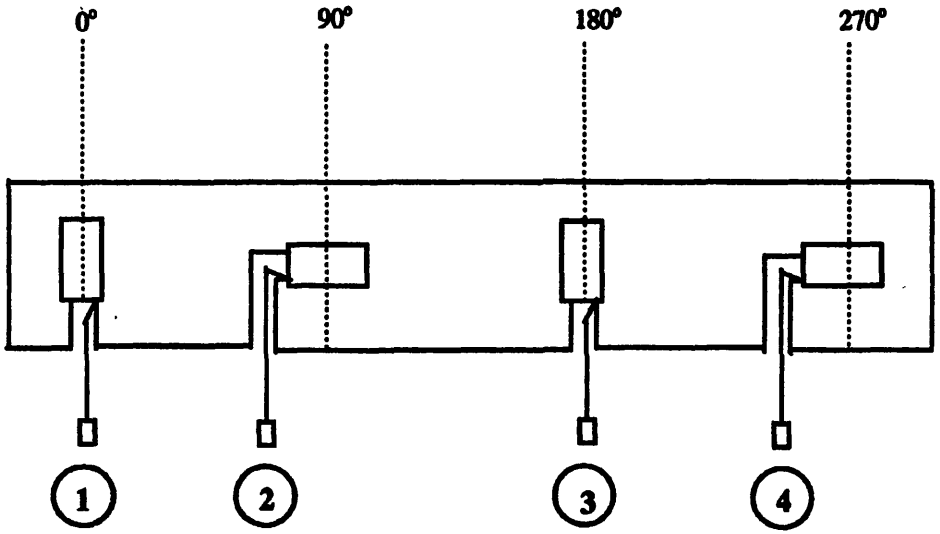

Fig 2.14 Strain Gauge Position and Orientation for Load Cell Construction

Fig 2.15 ABAQUS Simulation of Lower Punch

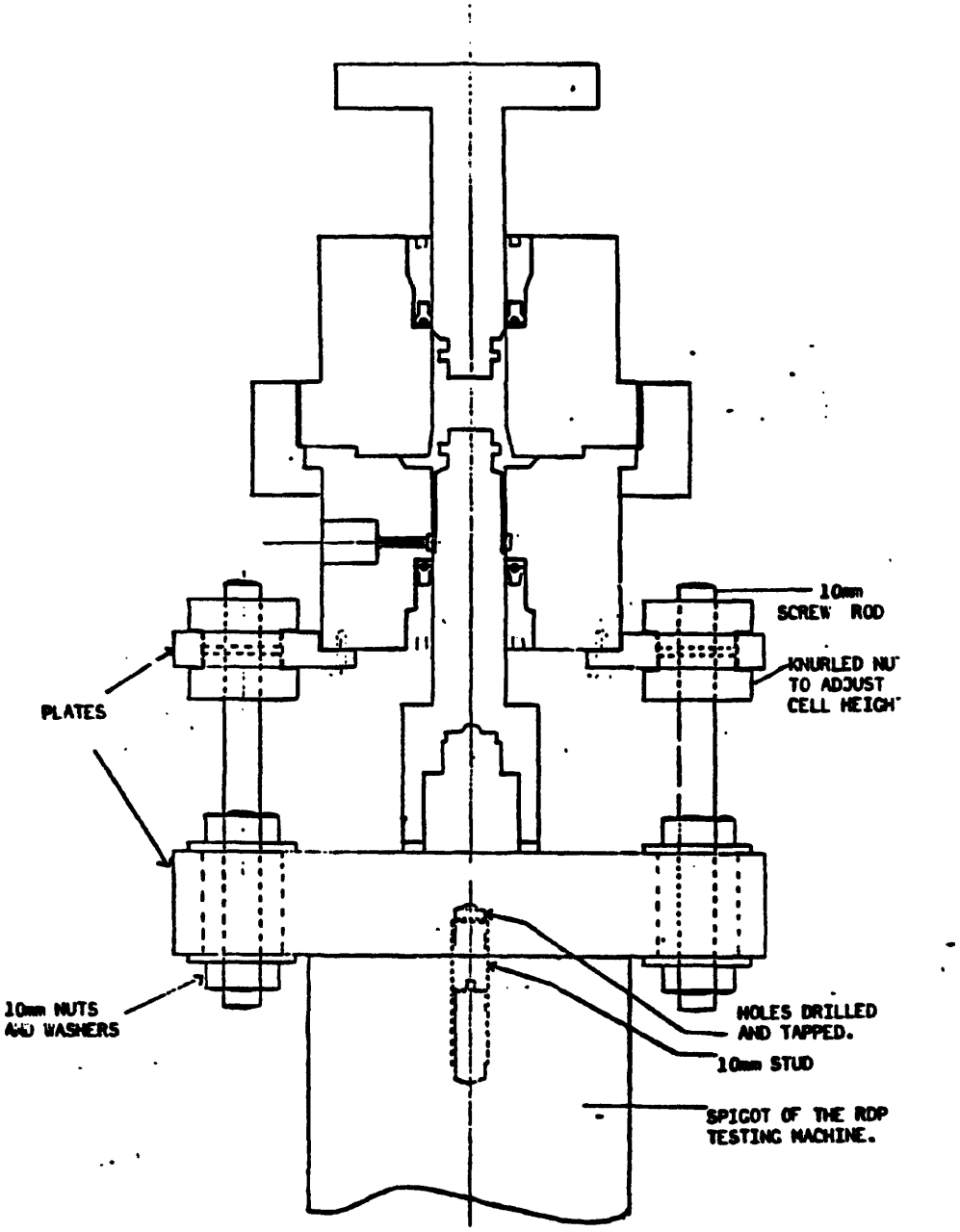

Fig 2.16 Triaxial Cell on its Support

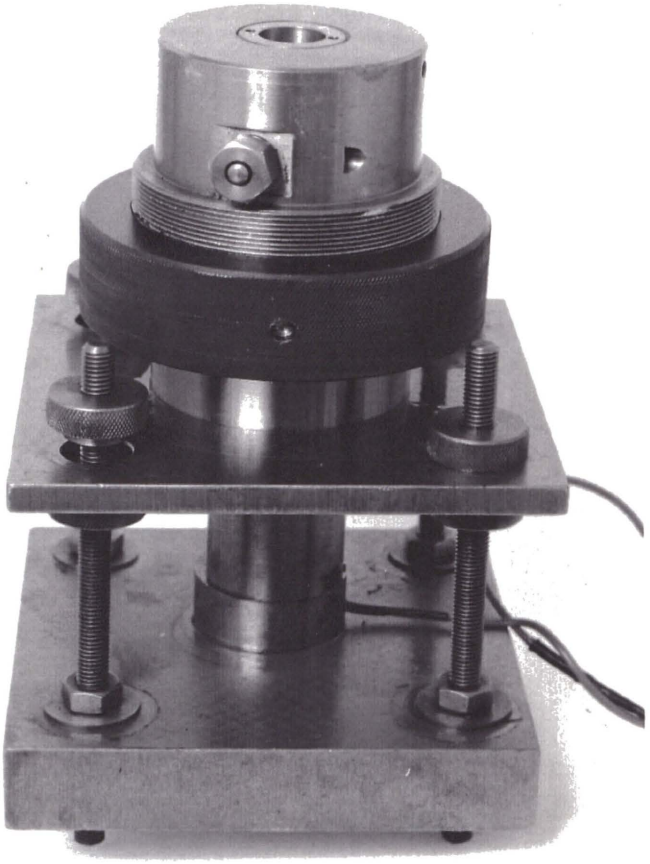

Fig 2.17 Assembled Triaxial Cell

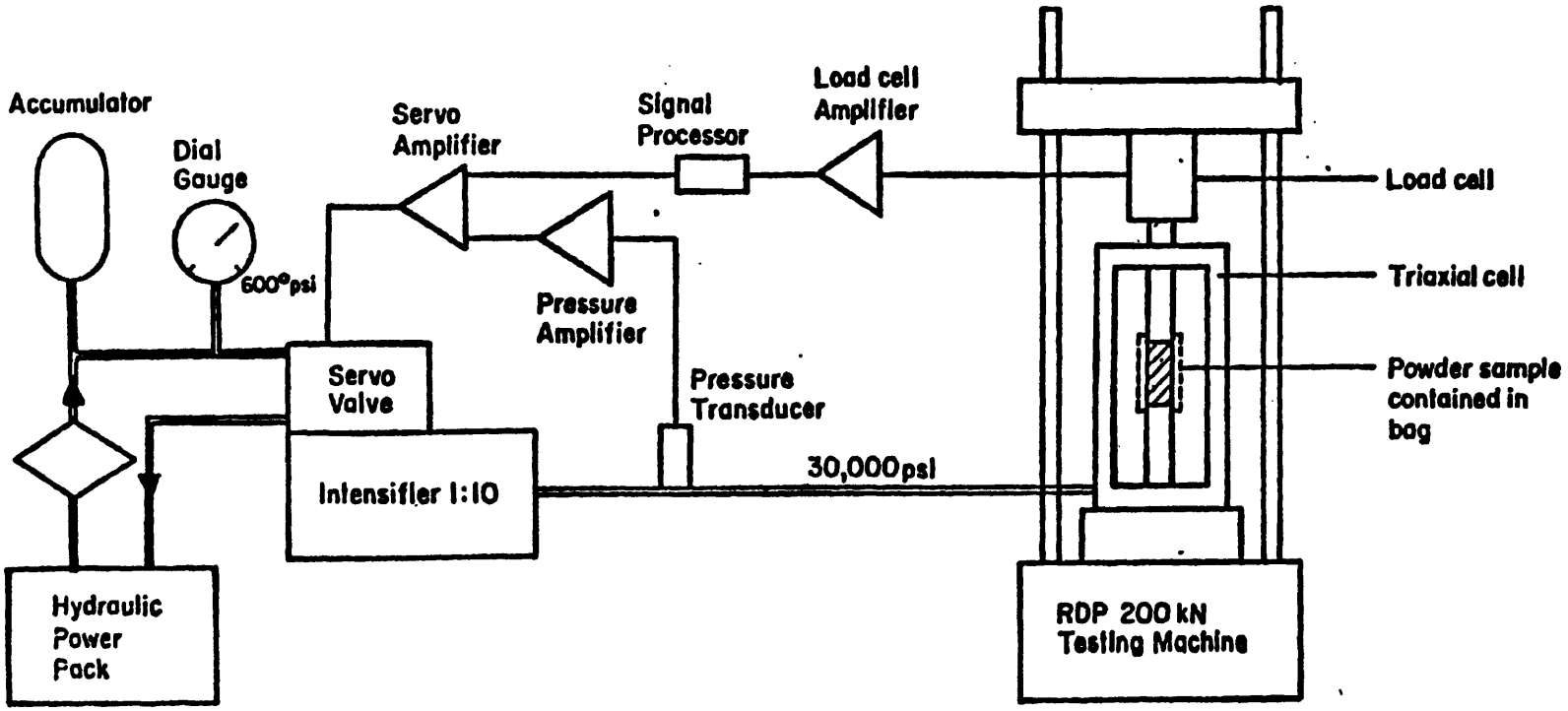

Fig 2.18 Schematic Layout of the Hydraulic Circuit for the Triaxial Test System

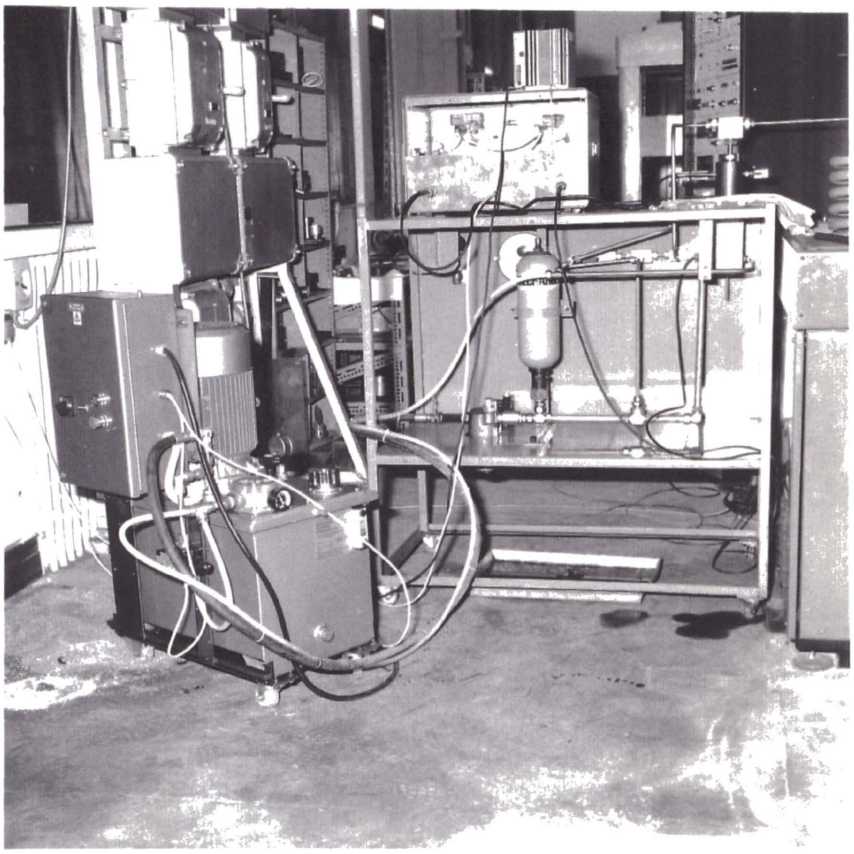

Fig 2.19 Hydraulic Circuit

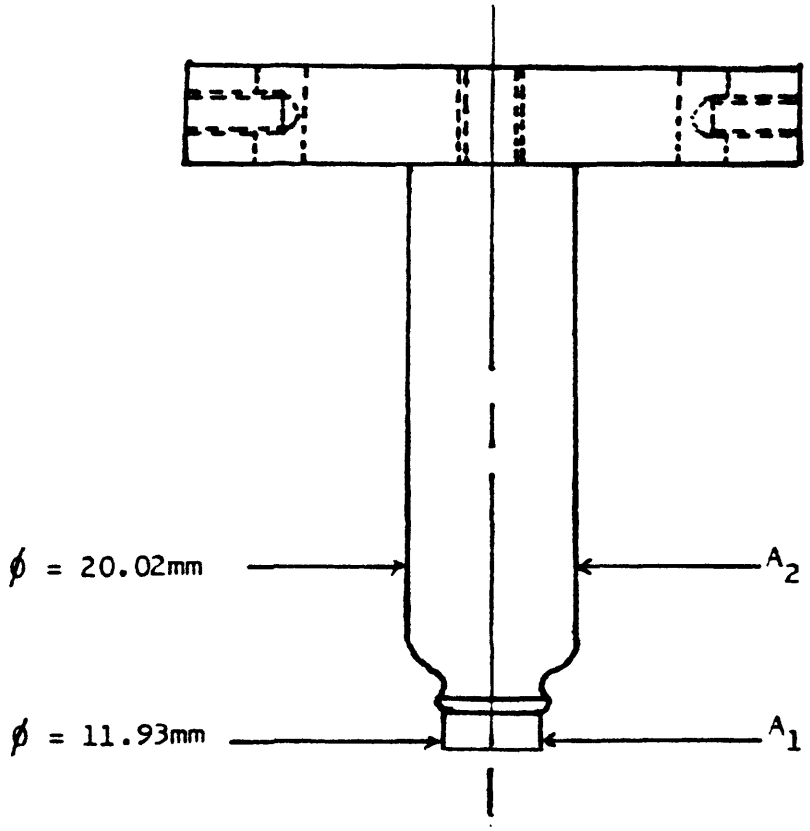

$A_1 = 111.782\ mm^2$

$A_2 = 314.788\ mm^2$

$(A_2 - A_1) = 203.006\ mm^2$

FIGURE 2.20: TRUE LOAD CALCULATION.

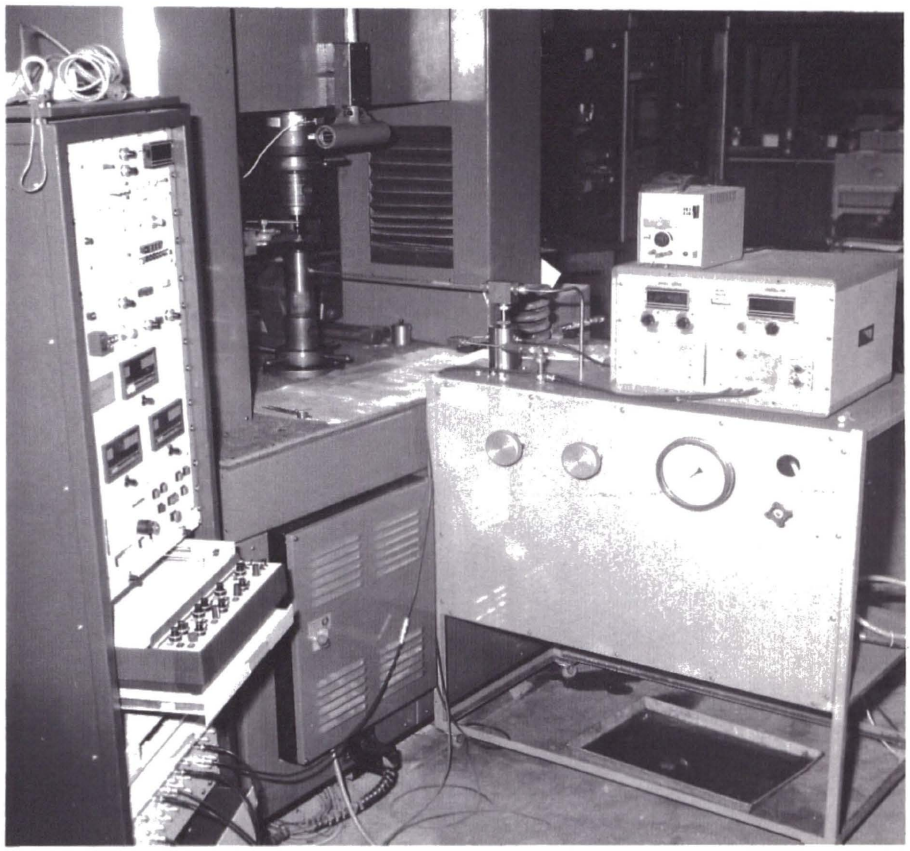

Fig 2.21 Triaxial Test System

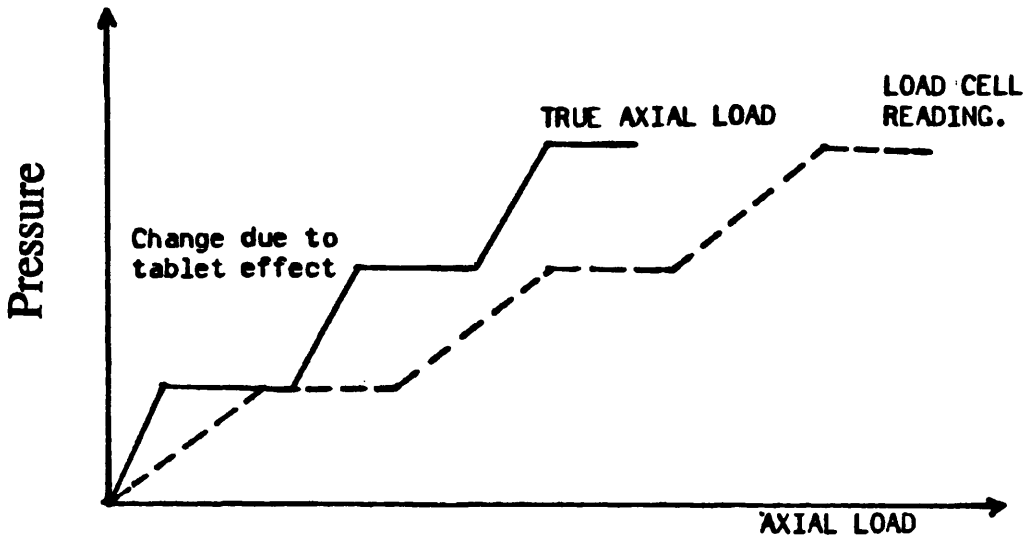

Fig 2.22 Independent Pressure/Load Control

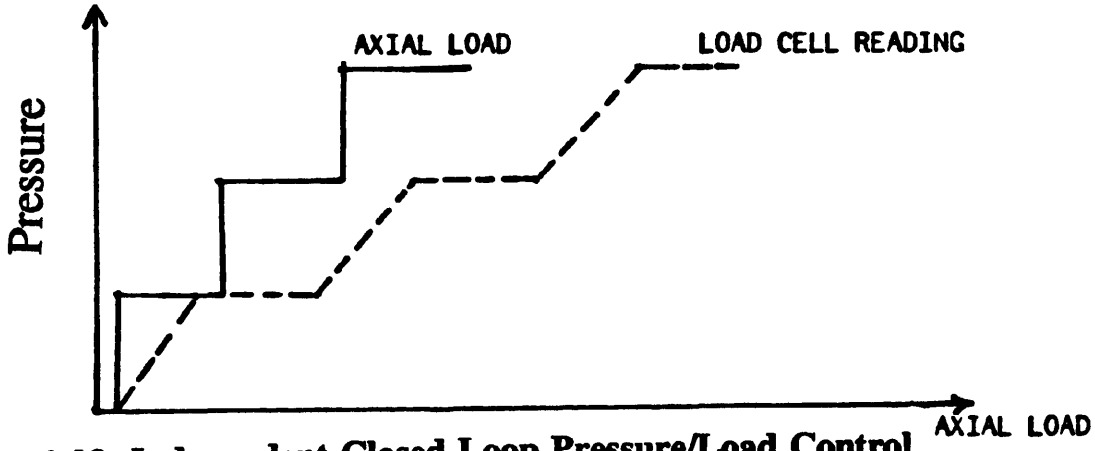

Fig 2.23 Independent Closed Loop Pressure/Load Control

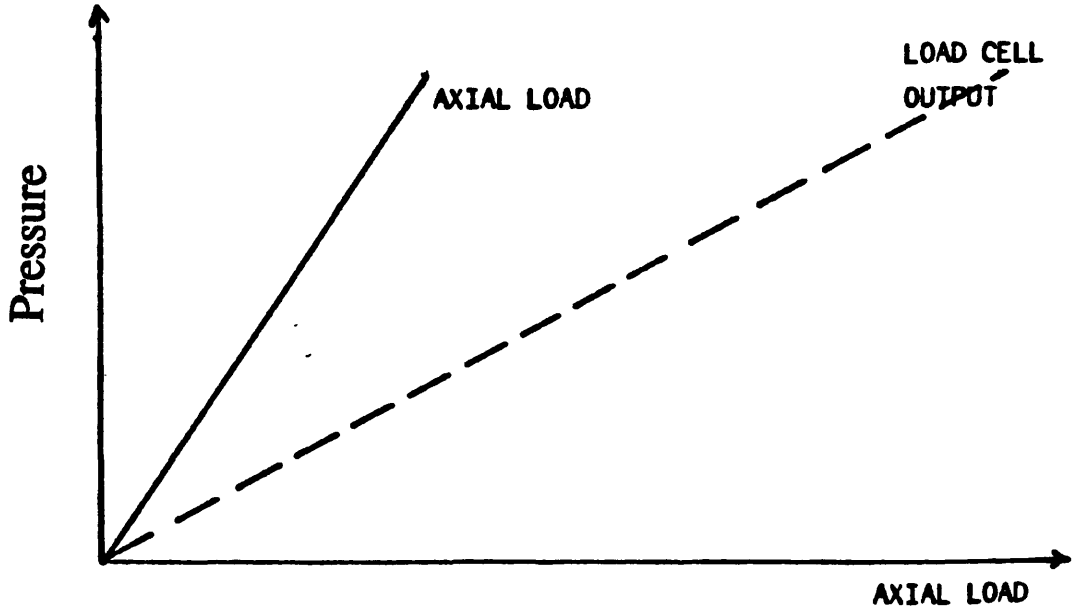

Fig 2.24 Dependent Control Mode

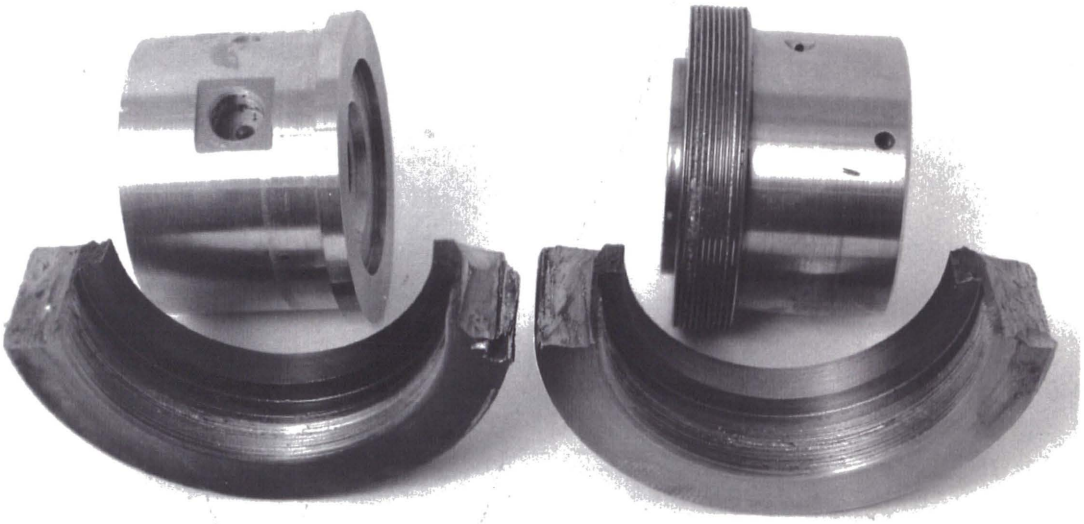

Fig 2.25 Damaged Nut

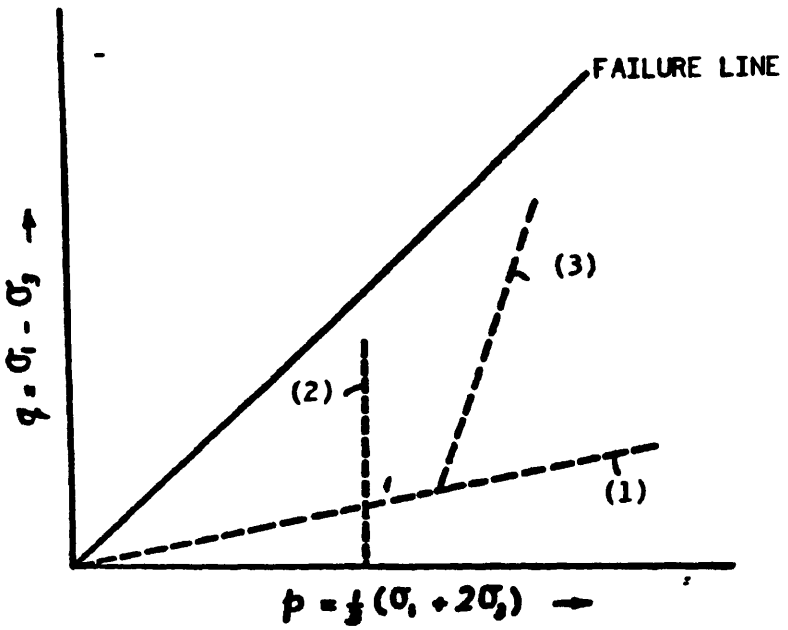

Fig 2.26 q-p Diagram (Loading Paths)

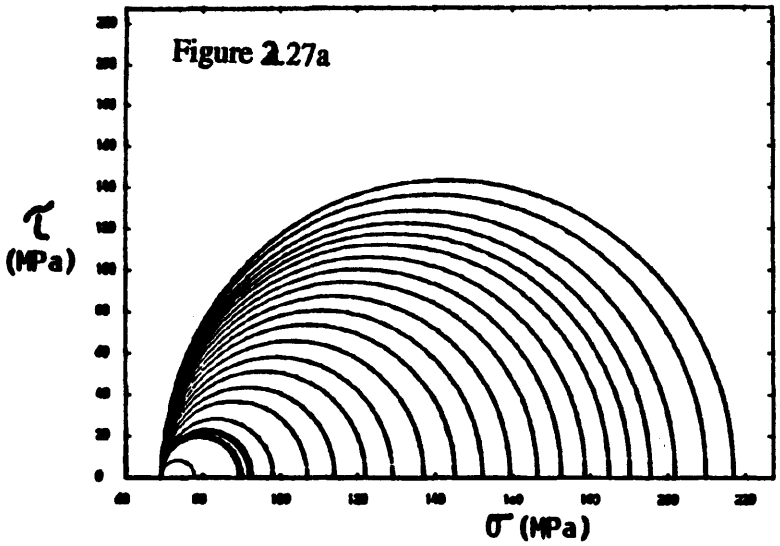

Figure 2.27a

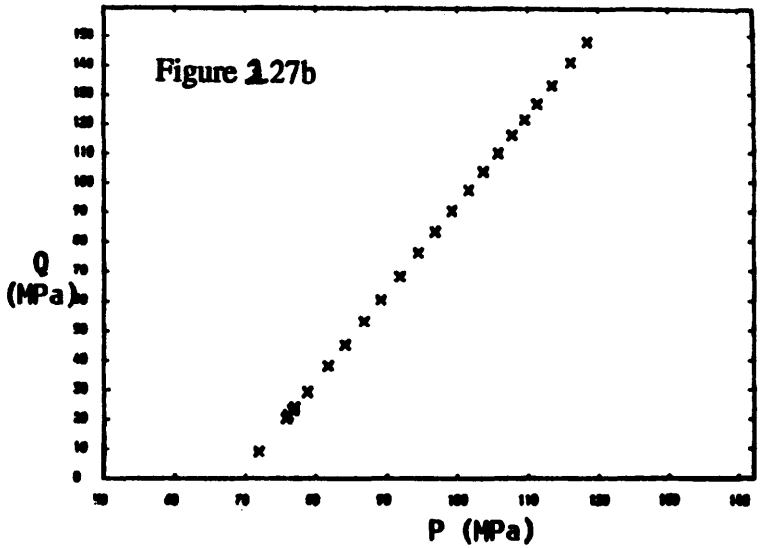

Figure 2.27b

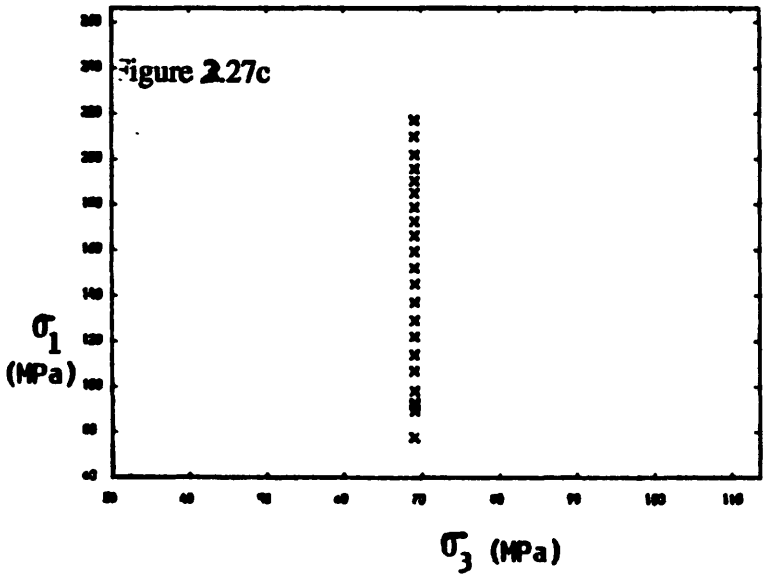

Figure 2.27c

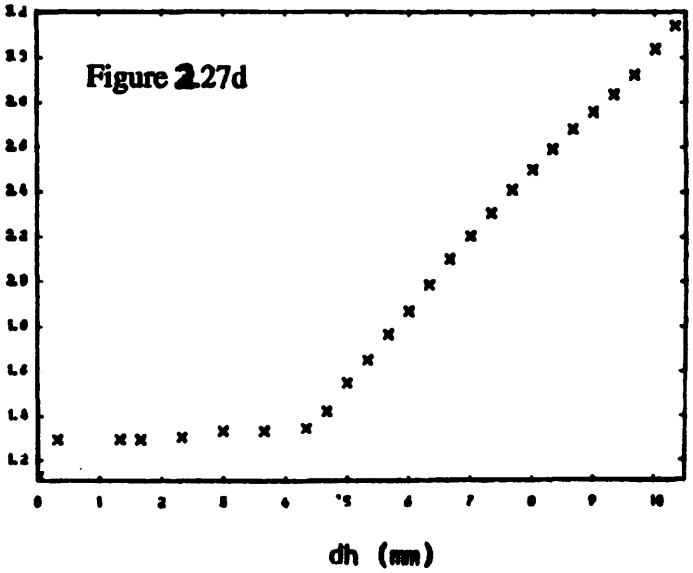

Figure 2.27d

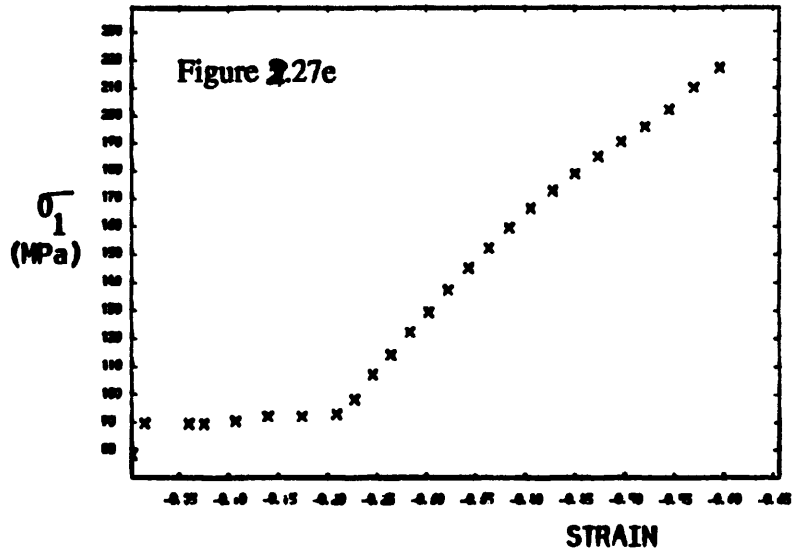

Figure 2.27e

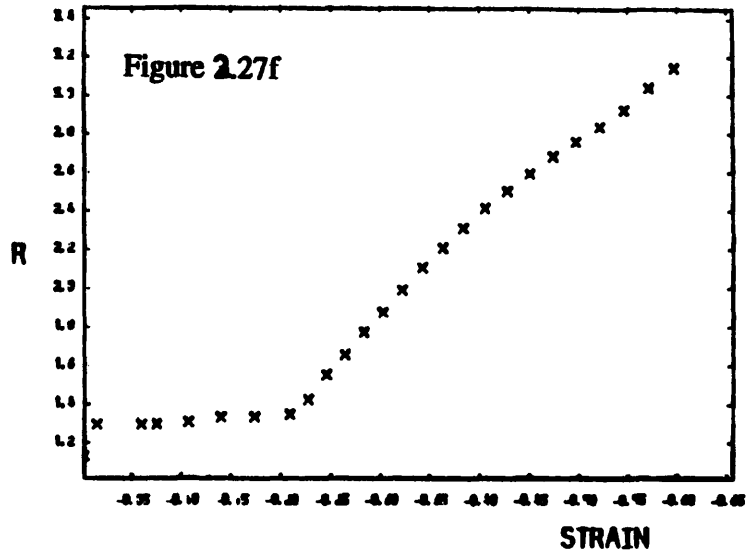

Figure 2.27f

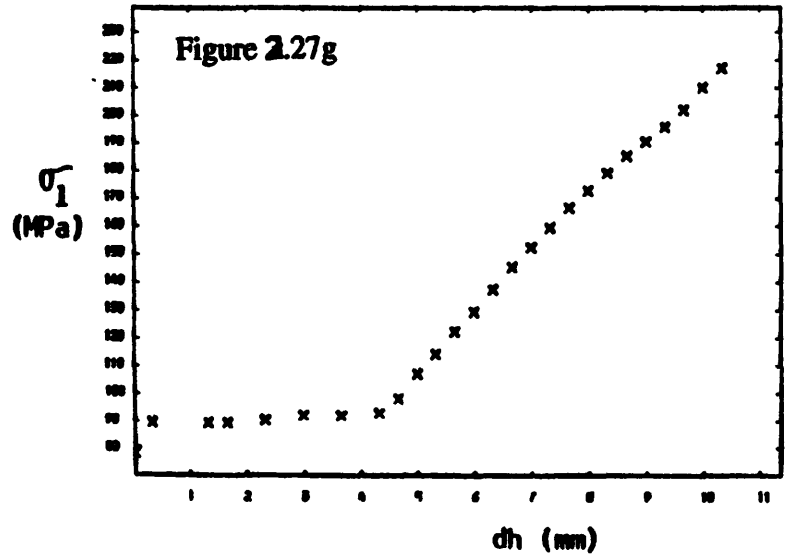

Figure 2.27g

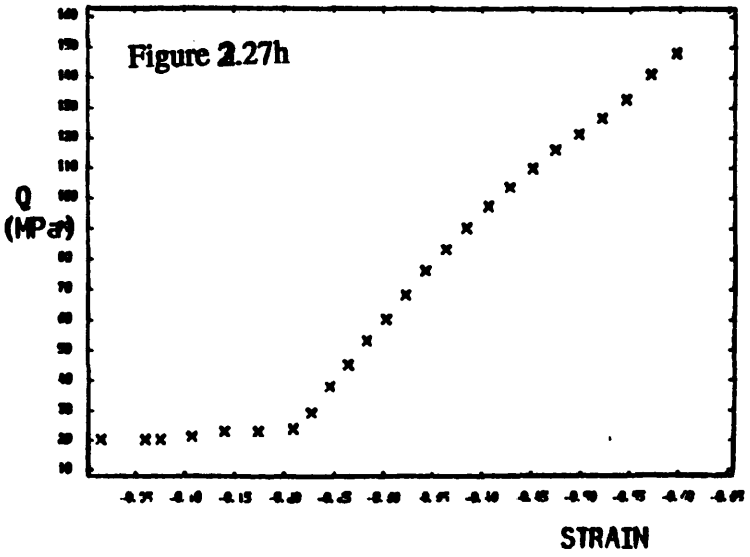

Figure 2.27h

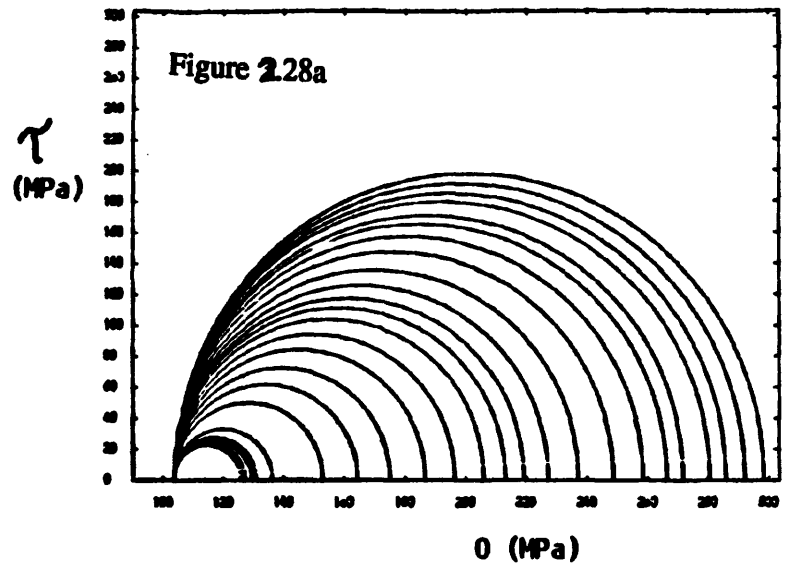

Figure 2.28a

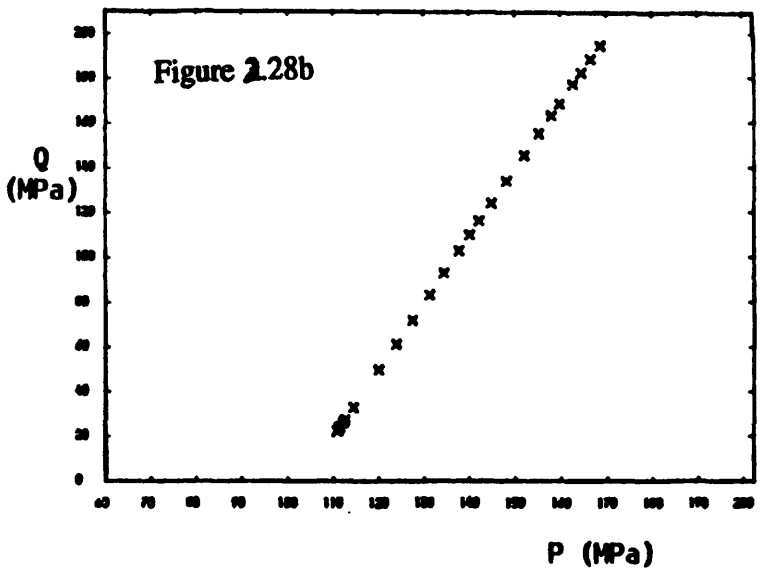

Figure 2.28b

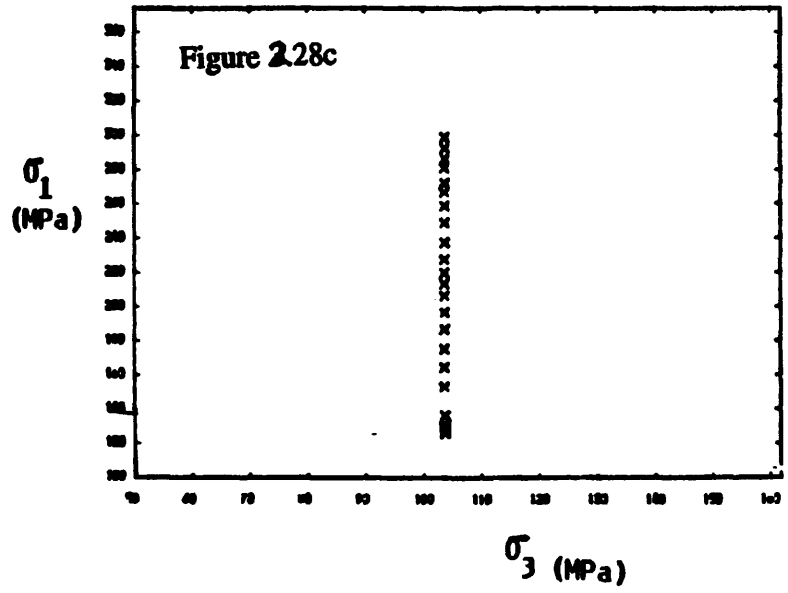

Figure 2.28c

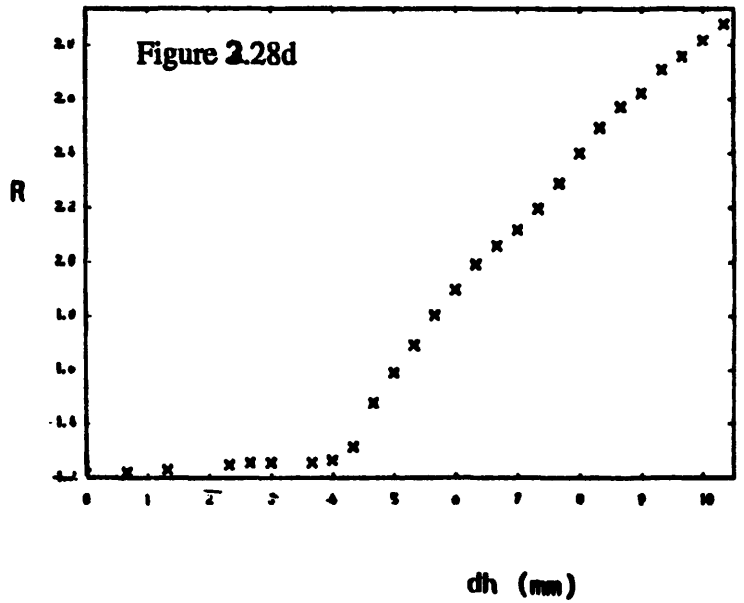

Figure 2.28d

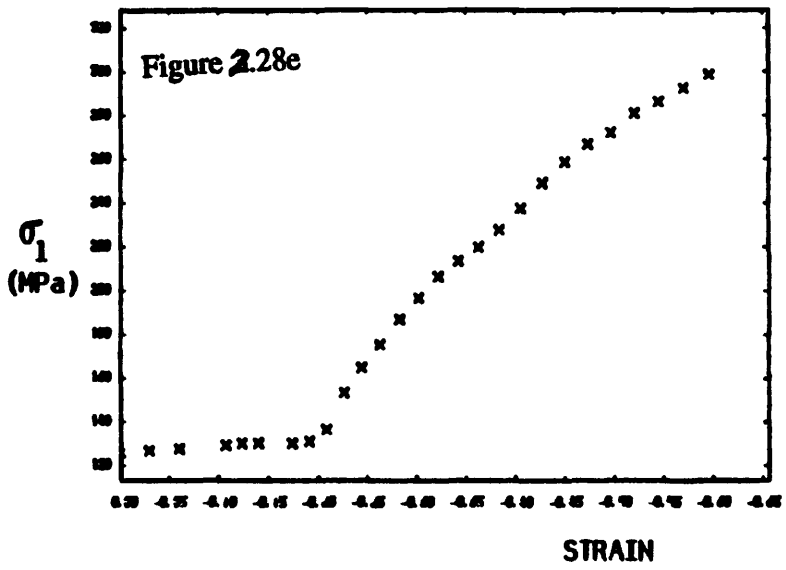
Figure 2.28e
σ_1
(MPa)
STRAIN

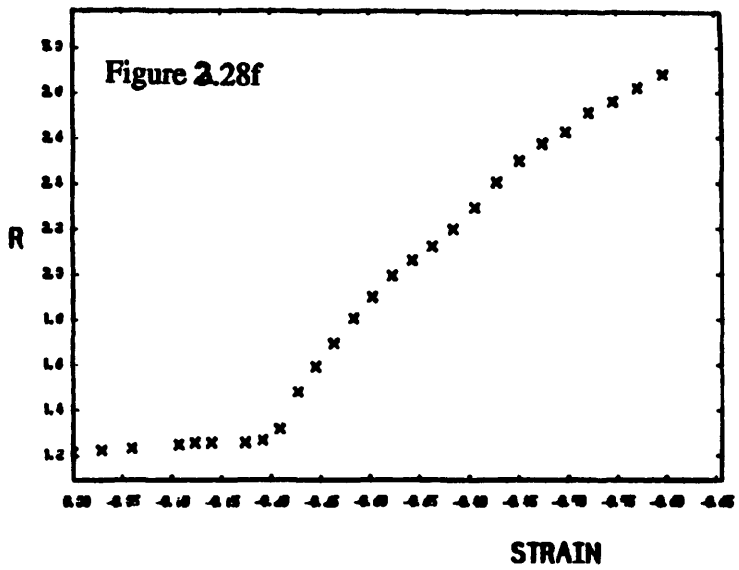
Figure 2.28f
R
STRAIN

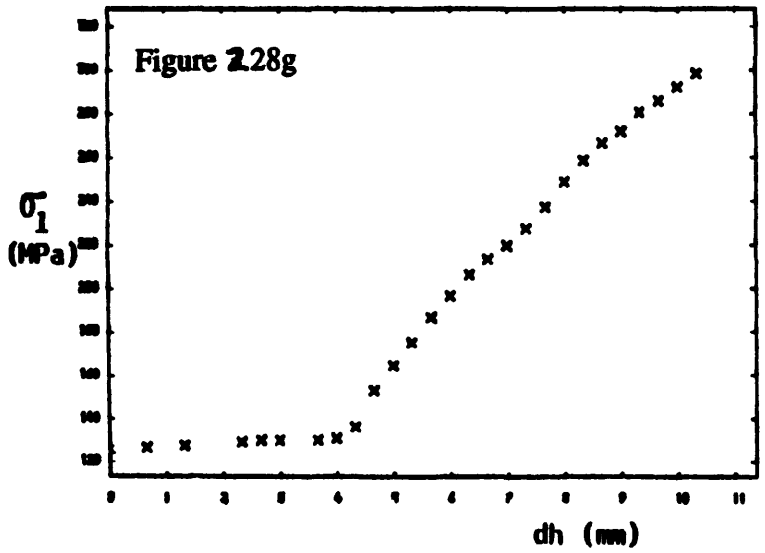
Figure 2.28g
σ_1
(MPa)
dh (mm)

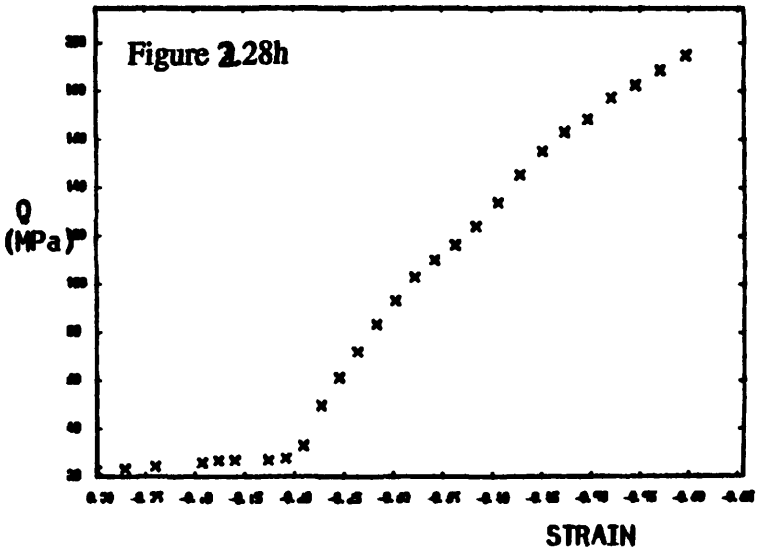
Figure 2.28h
Q
(MPa)
STRAIN

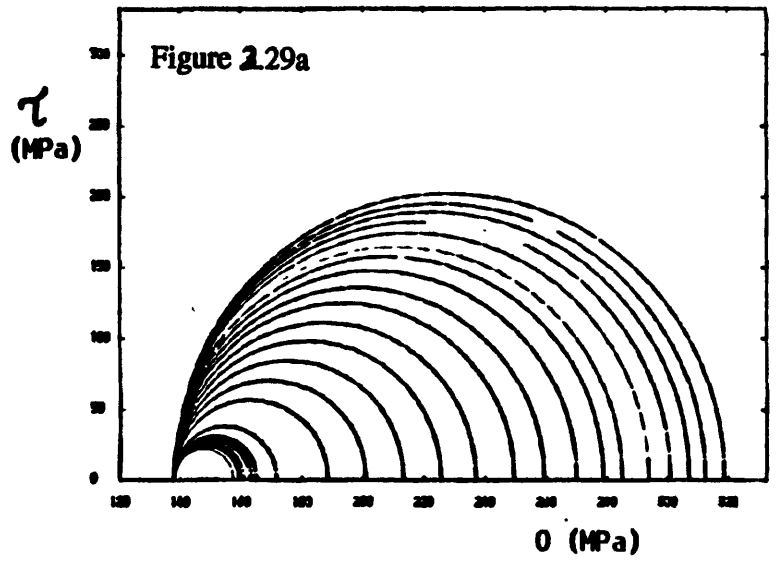

Figure 2.29a

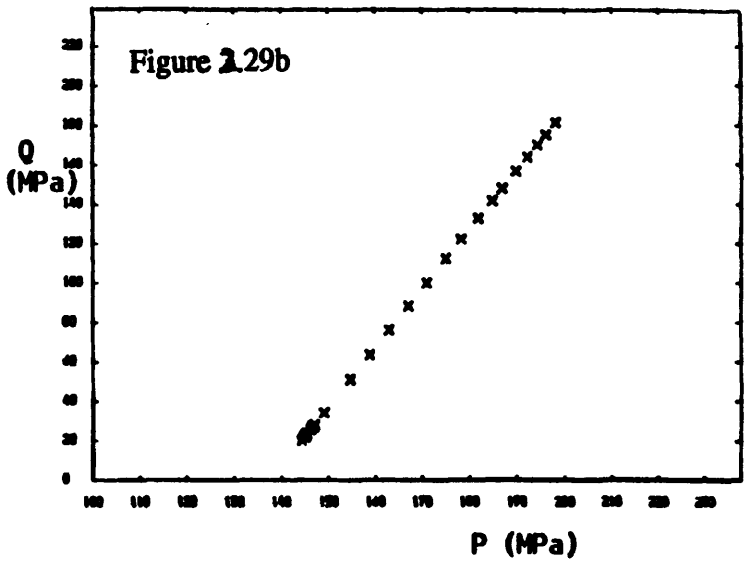

Figure 2.29b

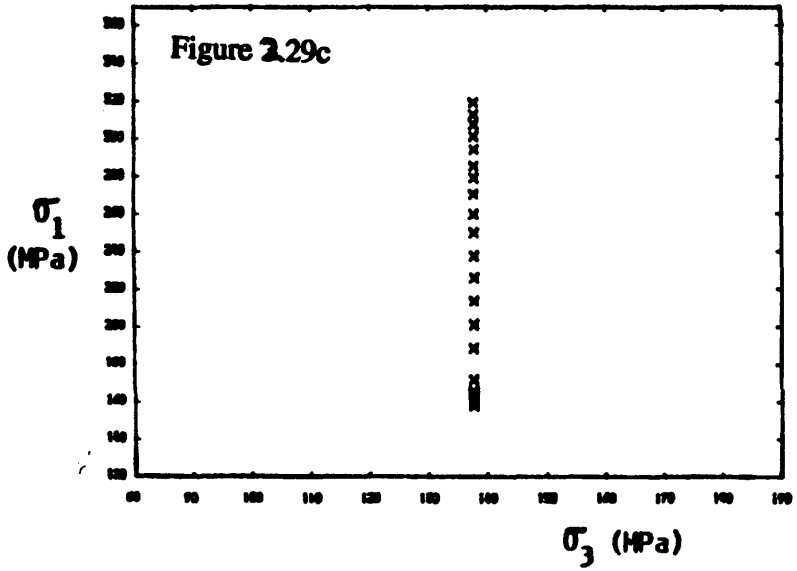

Figure 2.29c

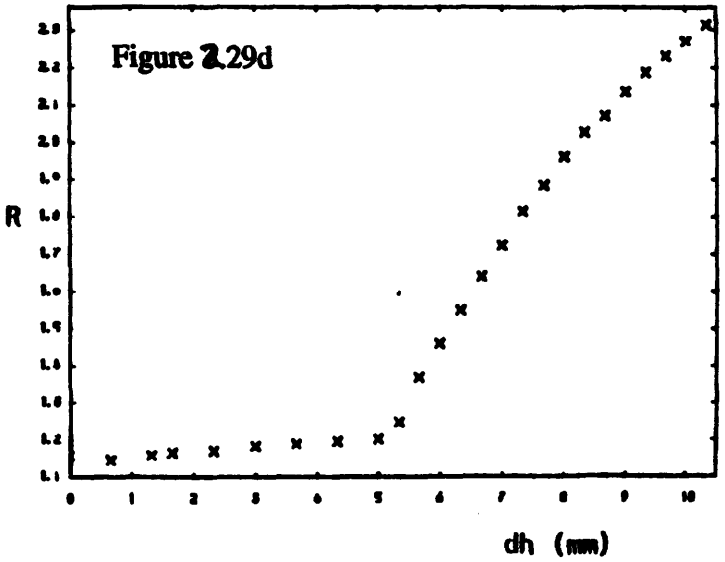

Figure 2.29d

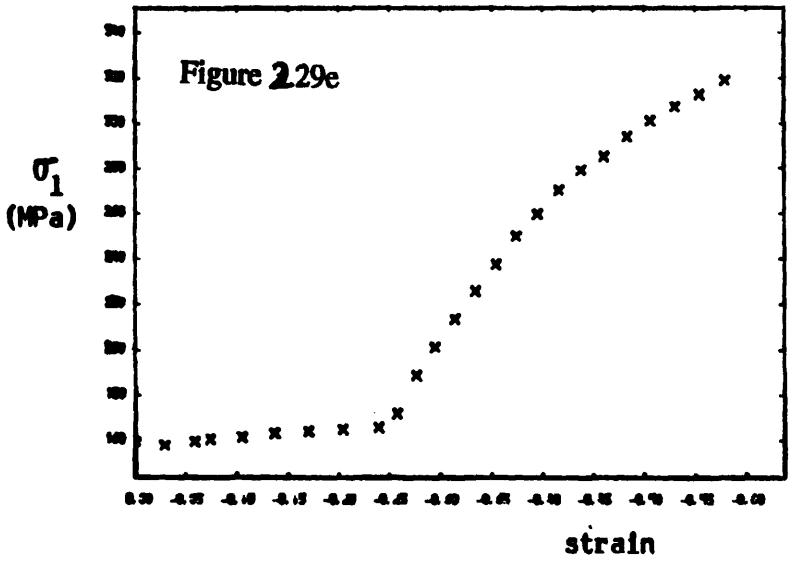
Figure 2.29e
σ1
(MPa)
strain

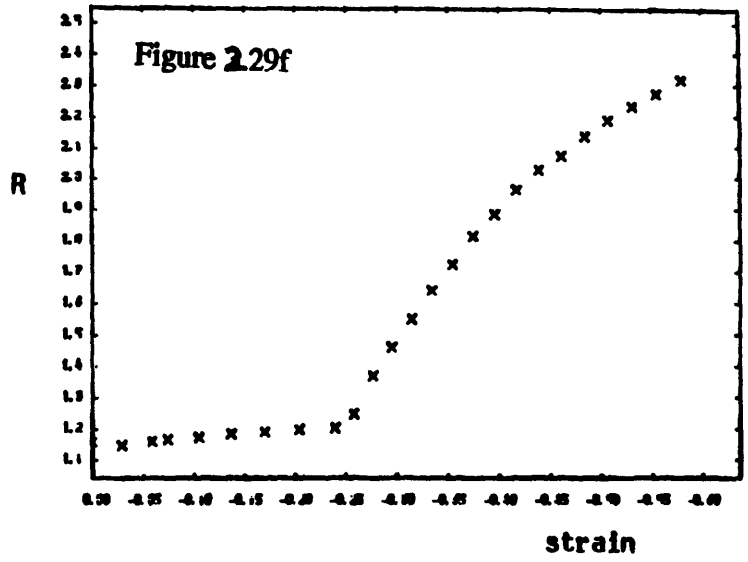
Figure 2.29f
R
strain

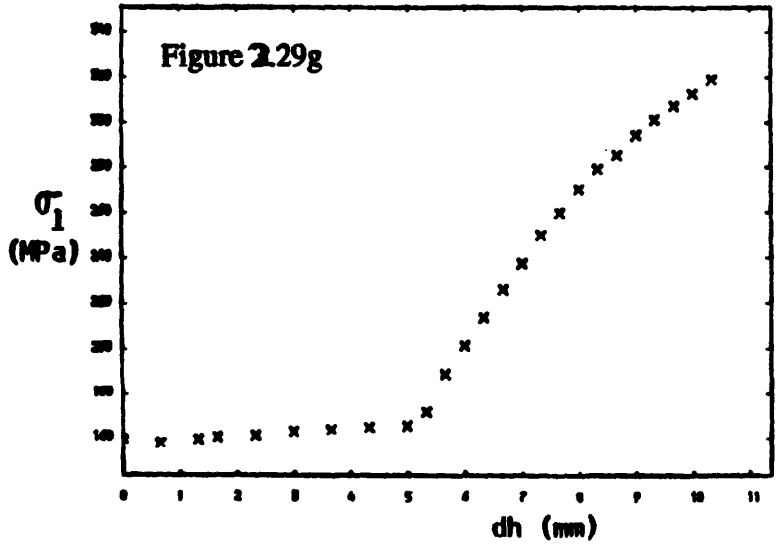
Figure 2.29g
σ1
(MPa)
dh (mm)

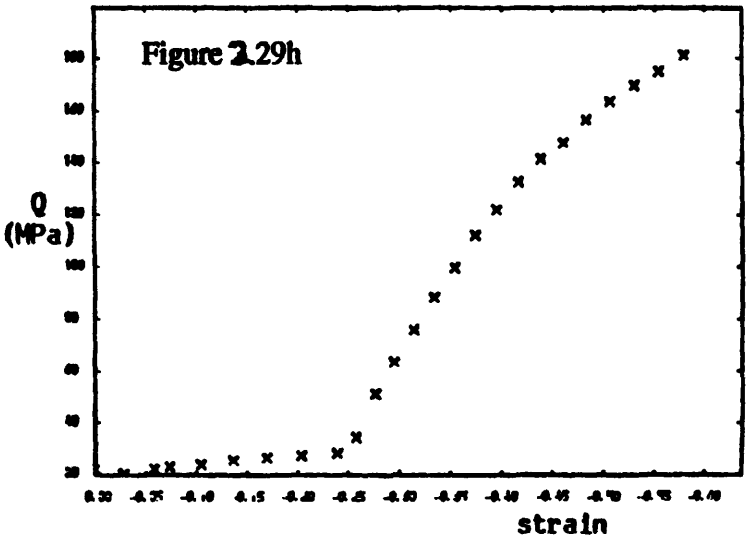
Figure 2.29h
Q
(MPa)
strain

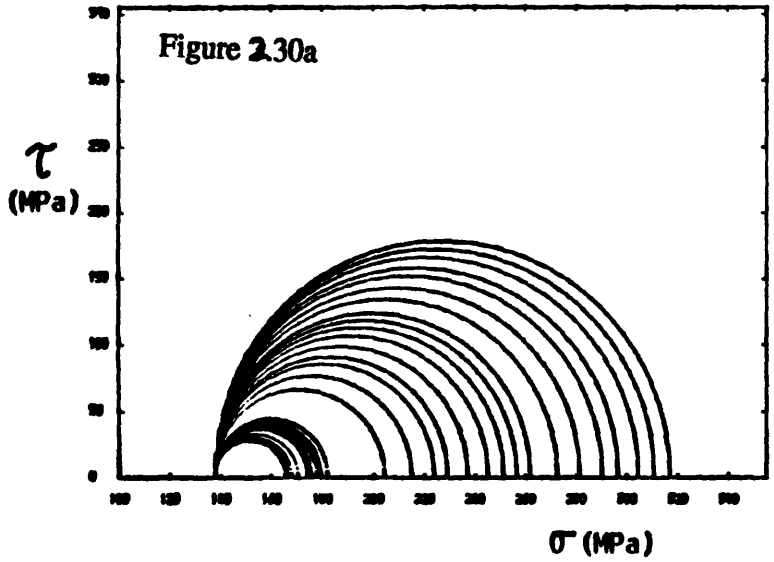

Figure 2.30a

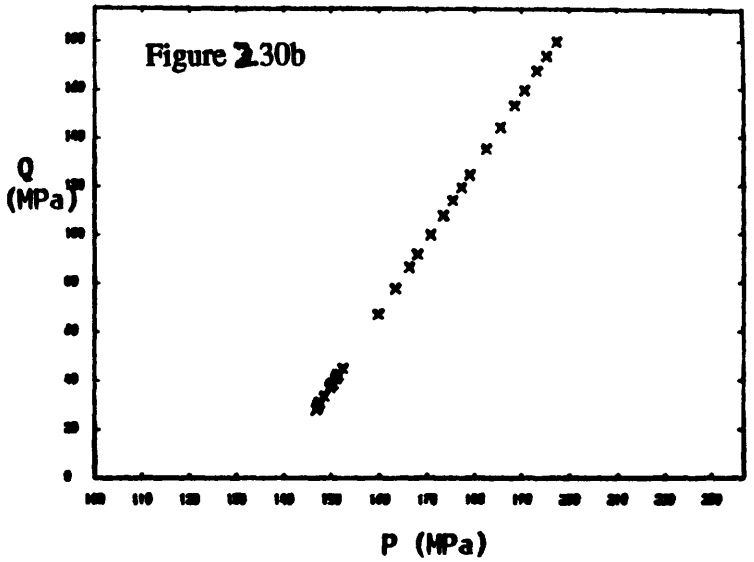

Figure 2.30b

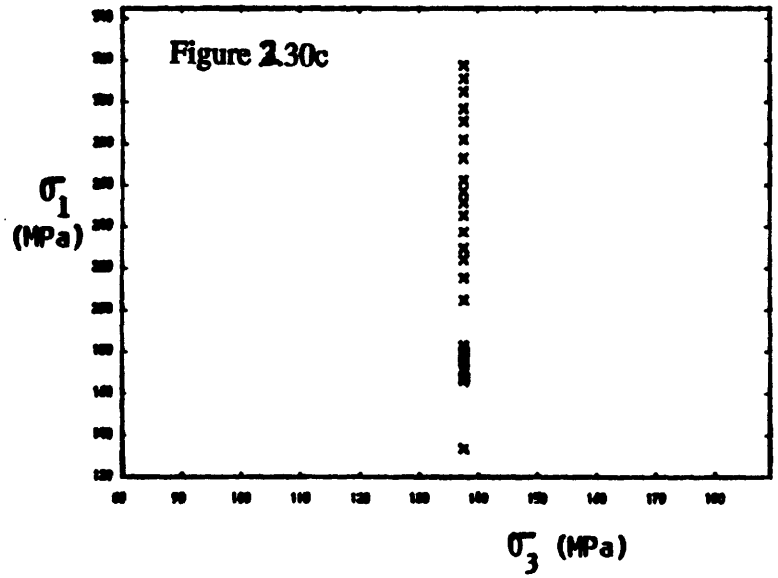

Figure 2.30c

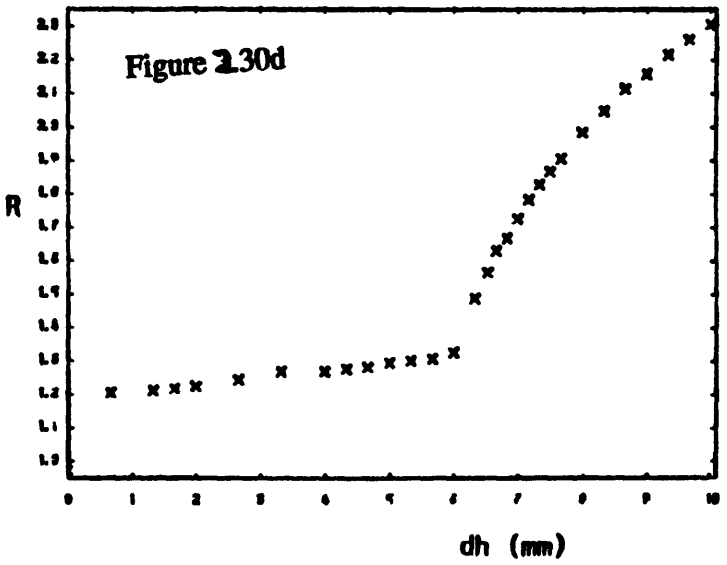

Figure 2.30d

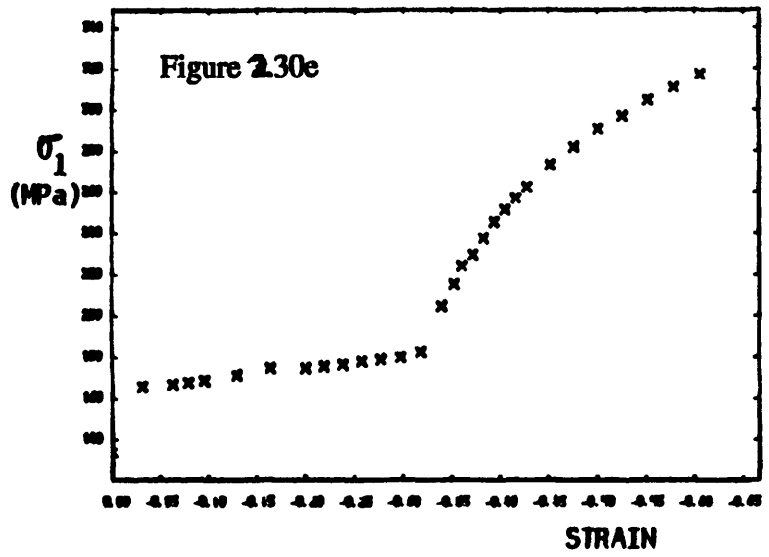

Figure 2.30e

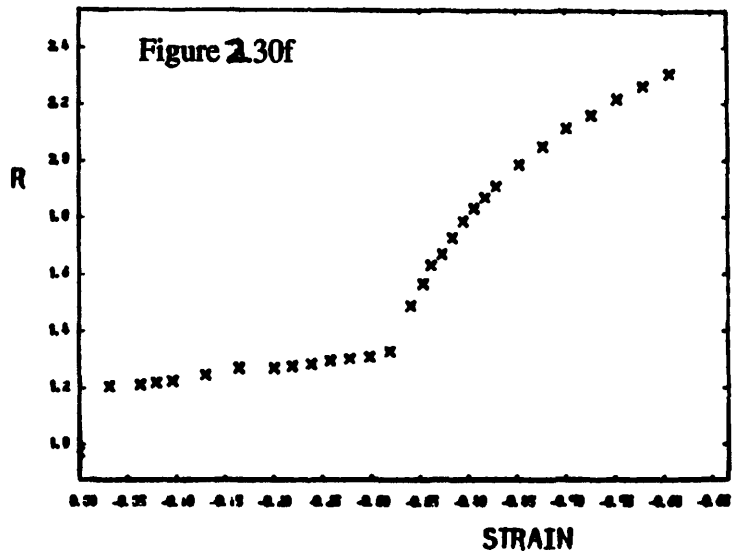

Figure 2.30f

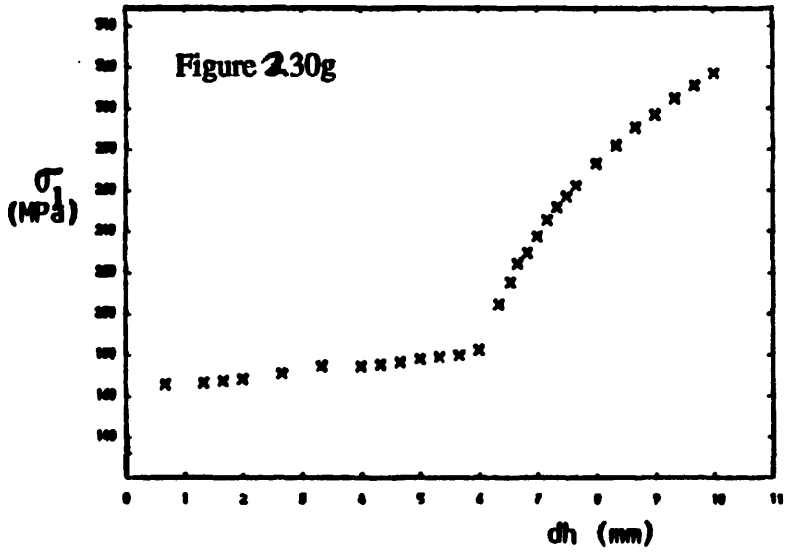

Figure 2.30g

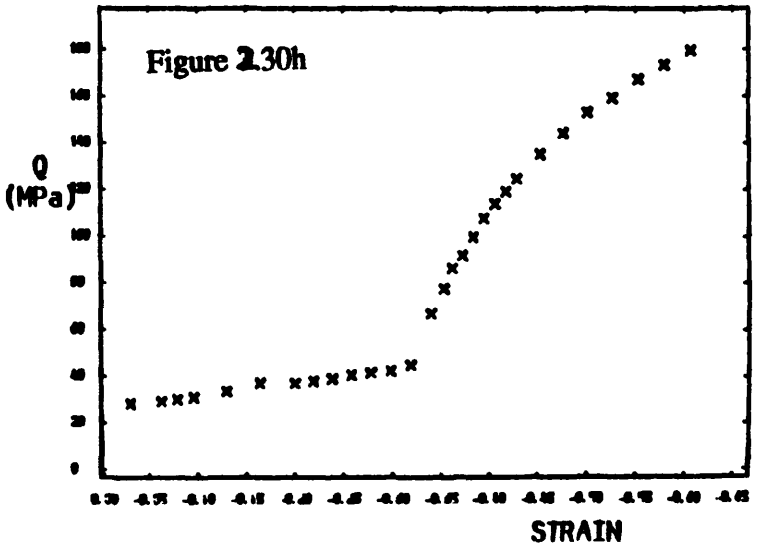

Figure 2.30h

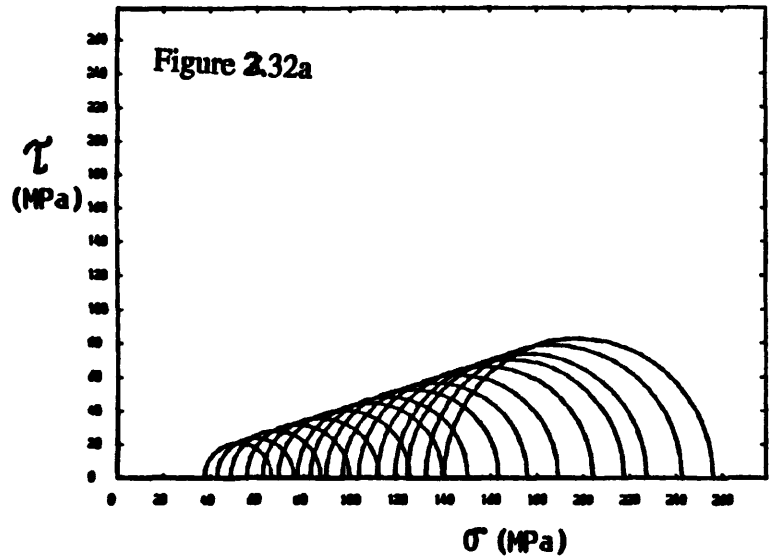

Figure 2.32a

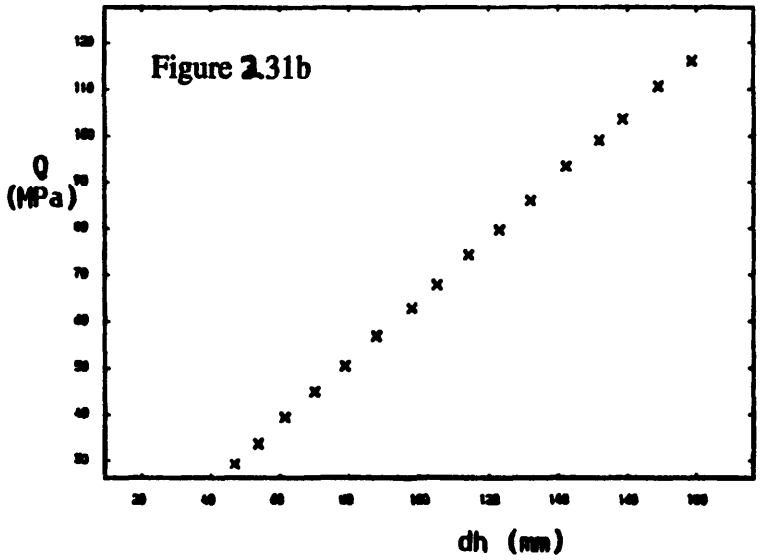

Figure 2.31b

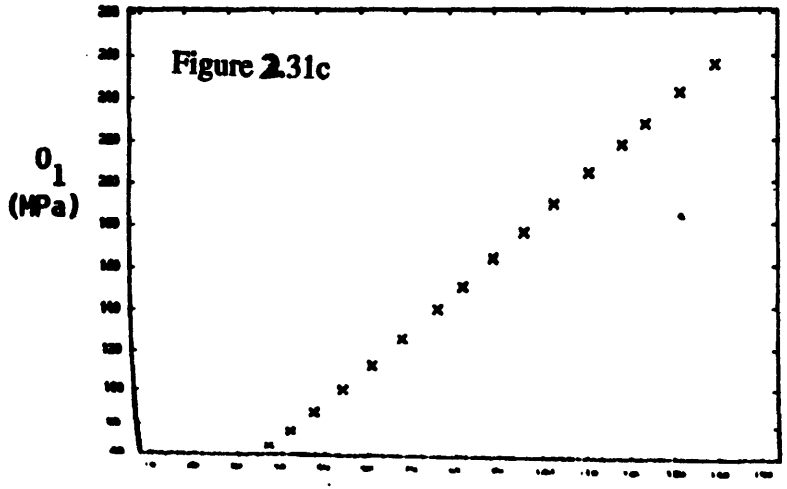

Figure 2.31c

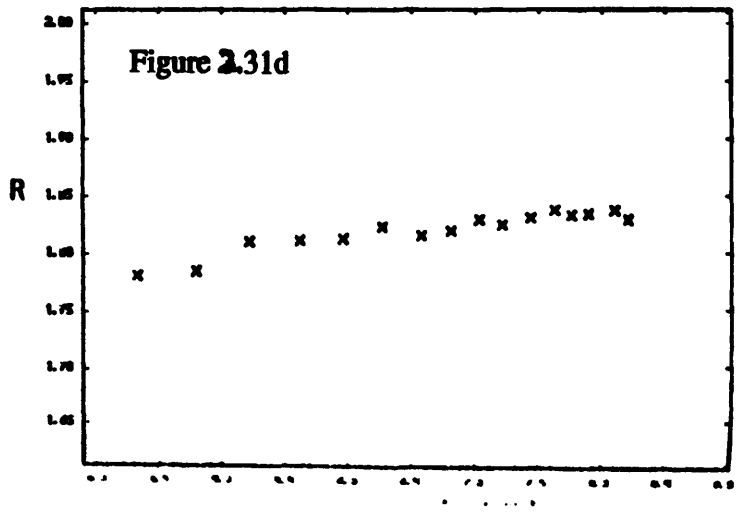

Figure 2.31d

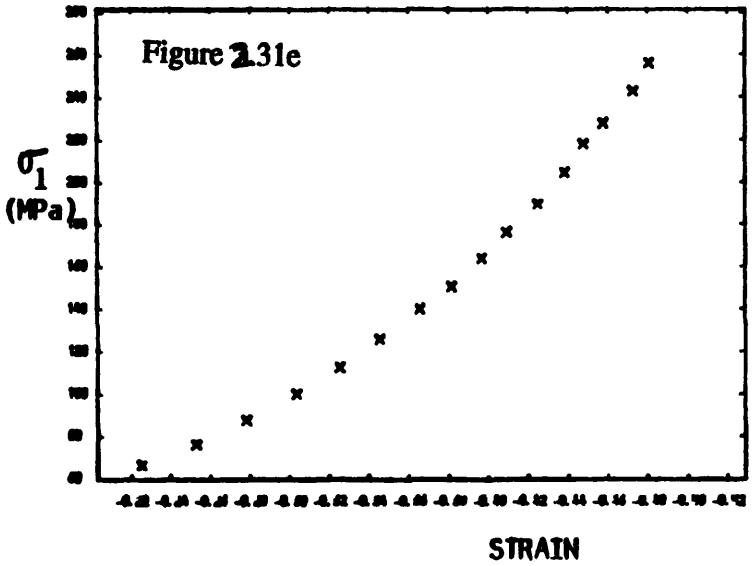
Figure 2.31e
σ_1 (MPa)
STRAIN

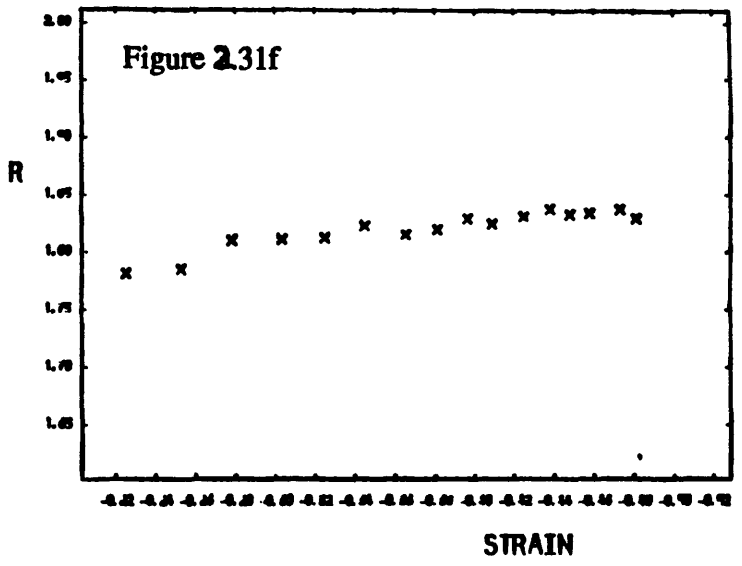
Figure 2.31f
R
STRAIN

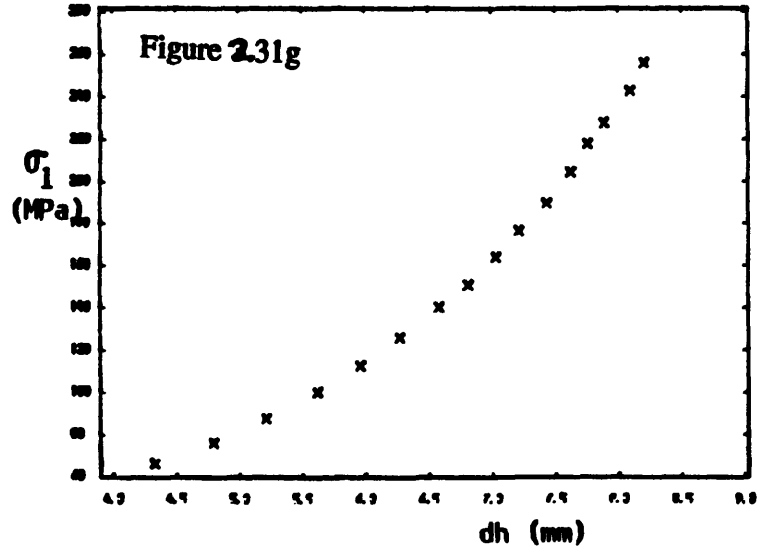
Figure 2.31g
σ_1 (MPa)
dh (mm)

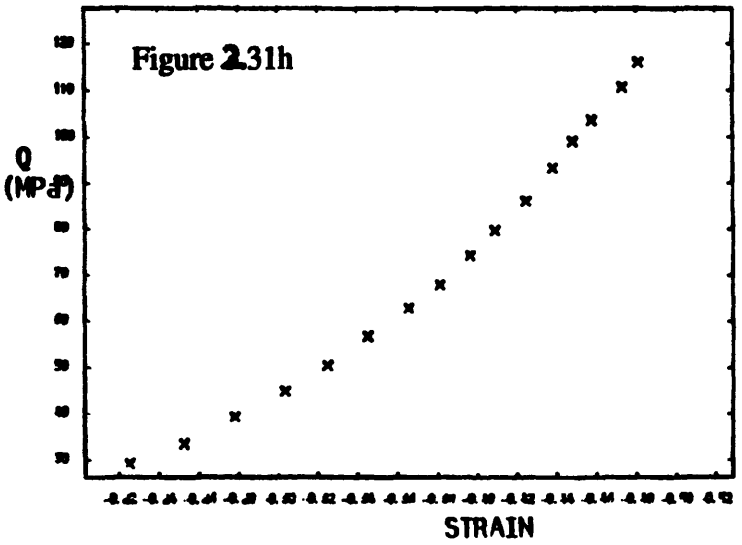
Figure 2.31h
Q (MPa)
STRAIN

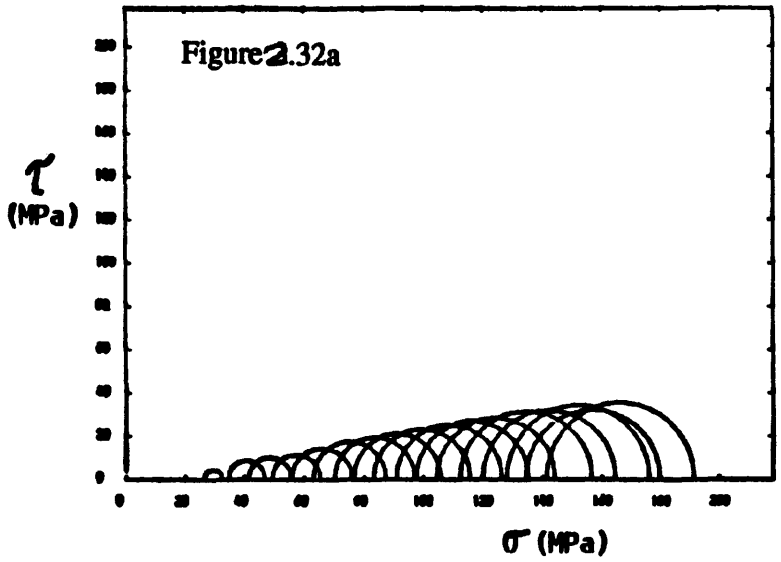

Figure 2.32a

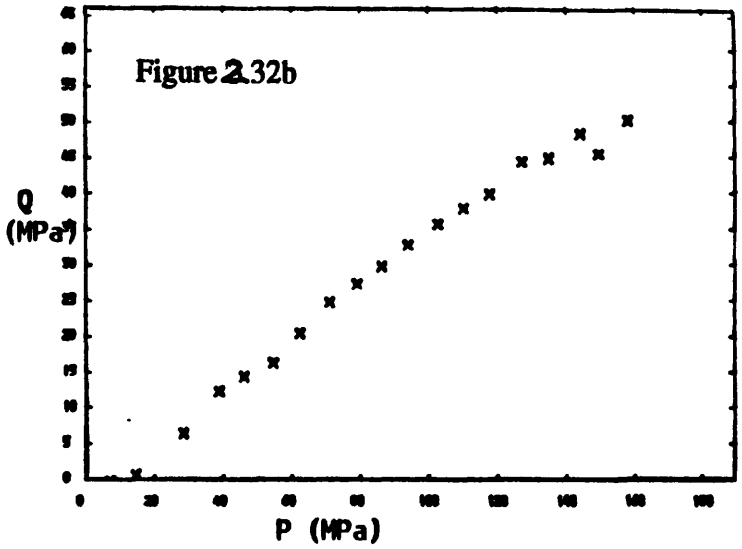

Figure 2.32b

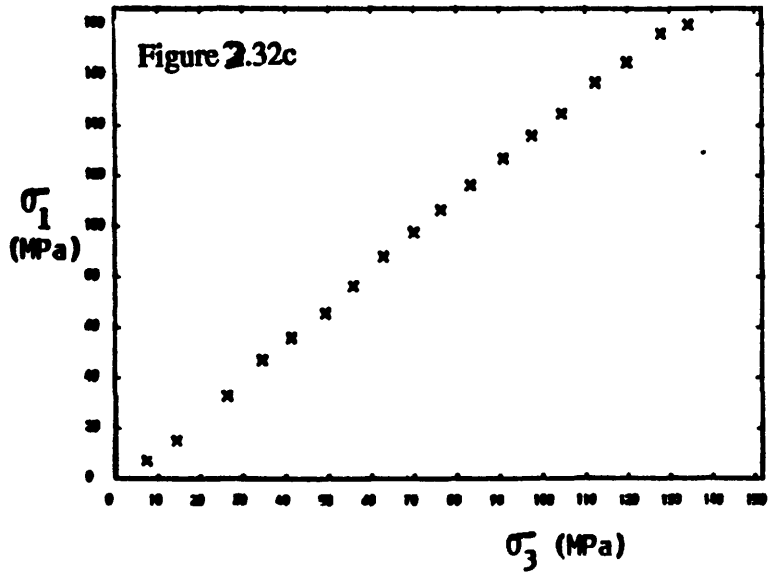

Figure 2.32c

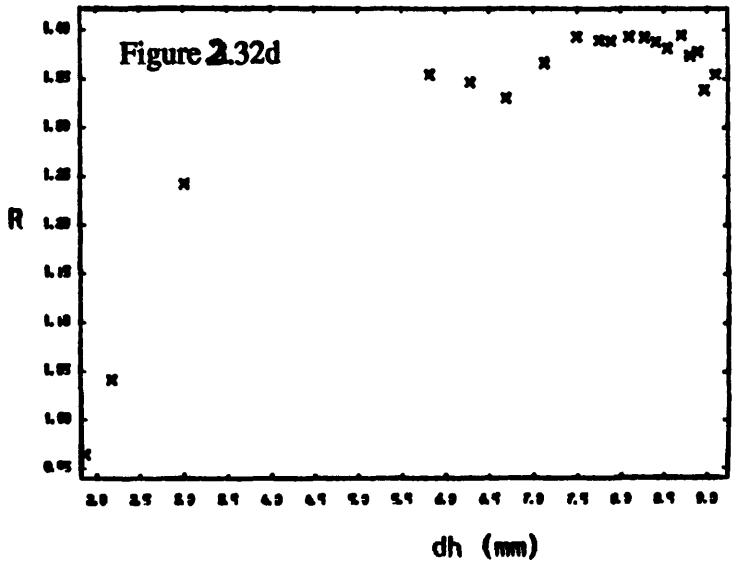

Figure 2.32d

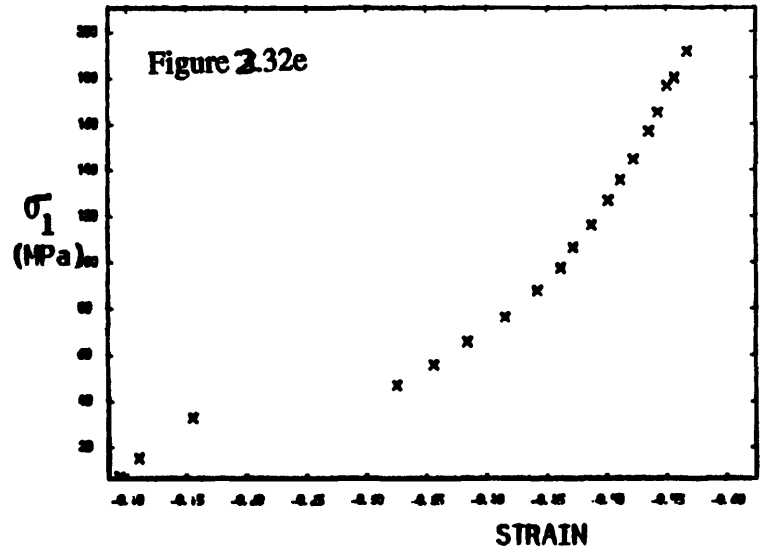
Figure 2.32e
σ1
(MPa)
STRAIN

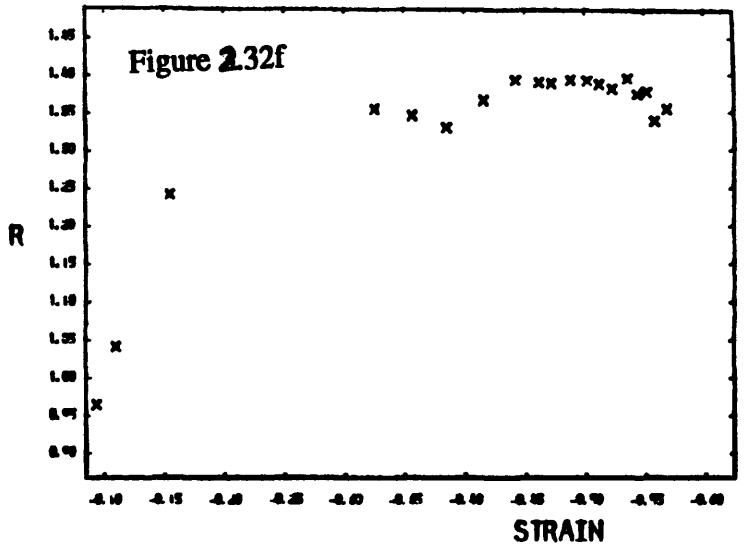
Figure 2.32f
R
STRAIN

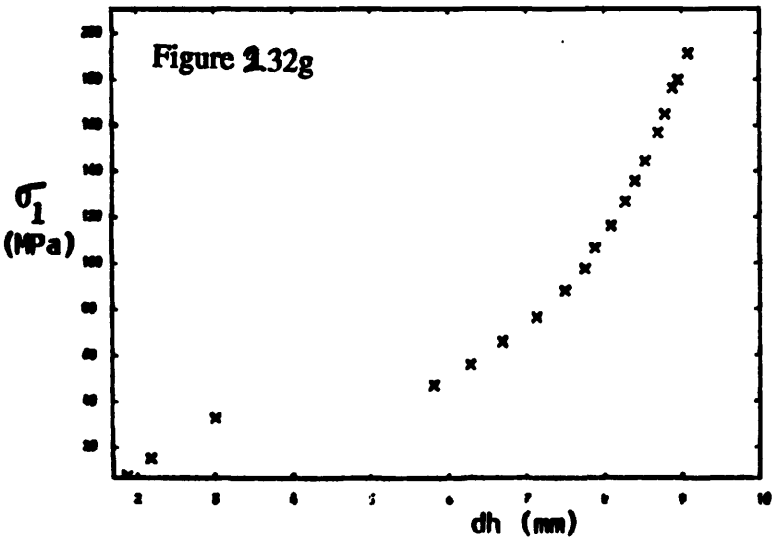
Figure 2.32g
σ1
(MPa)
dh (mm)

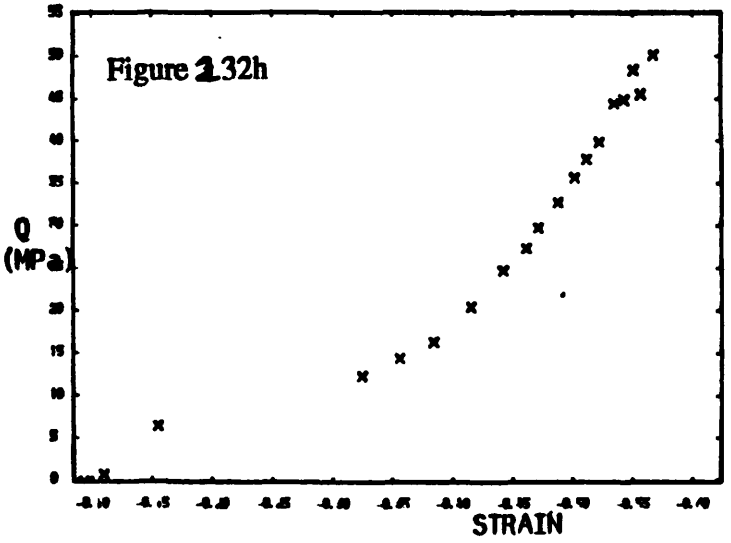
Figure 2.32h
Q
(MPa)
STRAIN

CHAPTER THREE

THE STAIRCASE METHOD

3.1 INTRODUCTION

The design and construction of a new split cell triaxial test system was presented in Chapter Two. Apart from the traditional triaxial tests, some of which are presented in Chapter Two, a new test cycle to provide data for a polynomial hypo-elastic modelling of the compaction process, is now presented.

The theoretical basis for this test method is discussed in this Chapter, and the results of a typical test on di-pac sugar are presented.

3.2 THEORY

Figure 3.1 shows a sketch of a triaxial test specimen. The powder is contained in a cylindrical flexible membrane. With this type of geometry, and the nature of the

triaxial cell, the boundaries of the specimen are the principal planes of stress and strain. In other words, the nature of the apparatus is such that it imposes the condition whereby principal planes of stress and strain coincide and cannot relate, a fact which is very important in this theoretical model.

Figure 3.2 shows one cycle of the proposed loading path. The cycle starts with an isostatic stress state at (0); the isostatic stress is then increased to p_1 bringing it to point (1), and the corresponding axial strain $\Delta\varepsilon_{z1}$ is recorded. The specimen is then taken through a pure shearing phase by reducing the radial pressure by an amount $\Delta\sigma$, point (2), and the axial load increased by $2\Delta\sigma$, point (3). The corresponding axial strain $\Delta\varepsilon_{z(1,3)}$ is recorded. During this stage, the basic hydrostatic stress remains constant. The specimen is then returned to a new isostatic stress state at point (4). The cycle can then be repeated until the desired degree of compaction is attained.

In straining the specimen from state (0) to (1), the stress state remains purely hydrostatic, that is $\sigma_r = \sigma_\phi = \sigma_2 = \sigma$; where σ_r is radial stress, σ_ϕ is circumferential stress, and σ_z is axial stress.

At this stage, the global stress state is equal to the spherical stress state. The deviatoric component is zero. The stress state at this stage can be written as:

From Hooke's law, we can write;

$$\begin{pmatrix} \sigma & 0 & 0 \\ 0 & \sigma & 0 \\ 0 & 0 & \sigma \end{pmatrix} = \begin{pmatrix} \sigma & 0 & 0 \\ 0 & \sigma & 0 \\ 0 & 0 & \sigma \end{pmatrix} + \begin{pmatrix} 0 & 0 & 0 \\ 0 & 0 & 0 \\ 0 & 0 & 0 \end{pmatrix} \tag{3.1}$$

General stress state *Spherical stress state* *Deviatoric stress state*
GSS *SSS* *DSS*

$$\Delta\epsilon_{21} = \frac{\sigma_2}{E} - \frac{\upsilon}{E}(\sigma_r + \sigma_\theta)$$

$$= \frac{\sigma}{E}(1 - 2\upsilon) \tag{3.2}$$

This can be re-arranged as;

$$\Delta\epsilon_{21} = \frac{\sigma}{3} \cdot \frac{3(1 - 2\upsilon)}{E}$$

Bulk modulus K is ;

$$K = \frac{E}{3(1 - 2\upsilon)} \tag{3.3}$$

Therefore,

$$\Delta\epsilon_{z1} = \frac{\sigma}{3K}$$

or

$$K = \frac{\sigma}{3\Delta\epsilon_{z1}} \tag{3.4}$$

Thus the applied pressure σ and the corresponding measured value of $\Delta\varepsilon_{21}$ from the triaxial test provide an average value of K over the range $\Delta\varepsilon_{21}$,

Now, in the next stage, the confining pressure was reduced by $\Delta\sigma$ and the axial stress by $2\Delta\sigma$, corresponding to a measured strain, $\Delta\varepsilon_{z(1,3)}$. The prevailing state of stress can now be written in a general form as;

$$\underset{GSS}{\begin{pmatrix} \sigma+2\Delta\sigma & 0 & 0 \\ 0 & \sigma-\Delta\sigma & 0 \\ 0 & 0 & \sigma-\Delta\sigma \end{pmatrix}} = \underset{SSS}{\begin{pmatrix} \sigma & 0 & 0 \\ 0 & \sigma & 0 \\ 0 & 0 & \sigma \end{pmatrix}} + \underset{DSS}{\begin{pmatrix} 2\Delta\sigma & 0 & 0 \\ 0 & -\Delta\sigma & 0 \\ 0 & 0 & -\Delta\sigma \end{pmatrix}} \tag{3.5}$$

Since the spherical stress state remains unchanged from the previous state, the value of K is not affected. The deviatoric components, however, are no longer zero, and therefore the observed change in $\Delta\varepsilon_z$ is related only to the shear modulus G. Hence,

$$\Delta\epsilon_{z(1,3)} = \frac{2\Delta\sigma}{E}(1 + \upsilon) \tag{3.6}$$

The shear modulus G is given by:

$$G = \frac{E}{2(1 + \upsilon)} \tag{3.7}$$

therefore

$$\Delta\epsilon_{z(1,3)} = \frac{\Delta\sigma}{G}$$

or

$$G = \frac{\Delta\sigma}{\Delta\epsilon_{z(1,3)}} \tag{3.8}$$

This provides an average value of G corresponding to this stage of loading.

The cycle can then be repeated from point (4) and a second set of K and G values are obtained. In this way a complete set of K and G values are obtained up to the desired degree of compaction. A convenient way of representing the qualitative variation of K's and G's is by normalising them with respect to their initial values and plot them against axial strain.

Having computed the values of K's and G's equations (3.3) and (3.7) can be used to obtain Young's modulus and Poisson's ratio.

$$E = \frac{9Gk}{G + 3k} \tag{3.9}$$

and

$$\upsilon = \left(\frac{3K - 2G}{6K + 2G}\right) \tag{3.10}$$

The material characteristics derived above may be considered as unique for a given granular material, and should be applicable to any general deformation process. These non-linearly varying hypoelastic properties of the particulate as a function of deformation can be used in the numerical simulation of the compaction process. This is the subject of the next chapter.

3.3 EXPERIMENT

The compaction cycle described above (Section 3.2) in the triaxial cell was carried out. The material tested was Avicel and the actual cycle followed is presented in Figure 3.3. Figure (3.4) presents the variation of the normalised values of K,G, E and υ with ε_z.

3.4 CONCLUSION

In this chapter, the theoretical basis for the staircase method is presented. It shows that non-linearly varying hypoelastic properties can be obtained or a given powder mass using the split cell triaxial system.

Experimental results obtained for Avicel are presented.

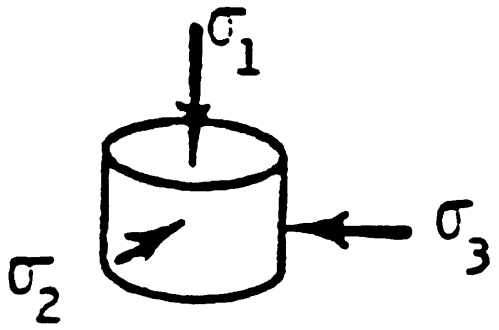

Fig. 3.1 A Sketch of the Test Specimen

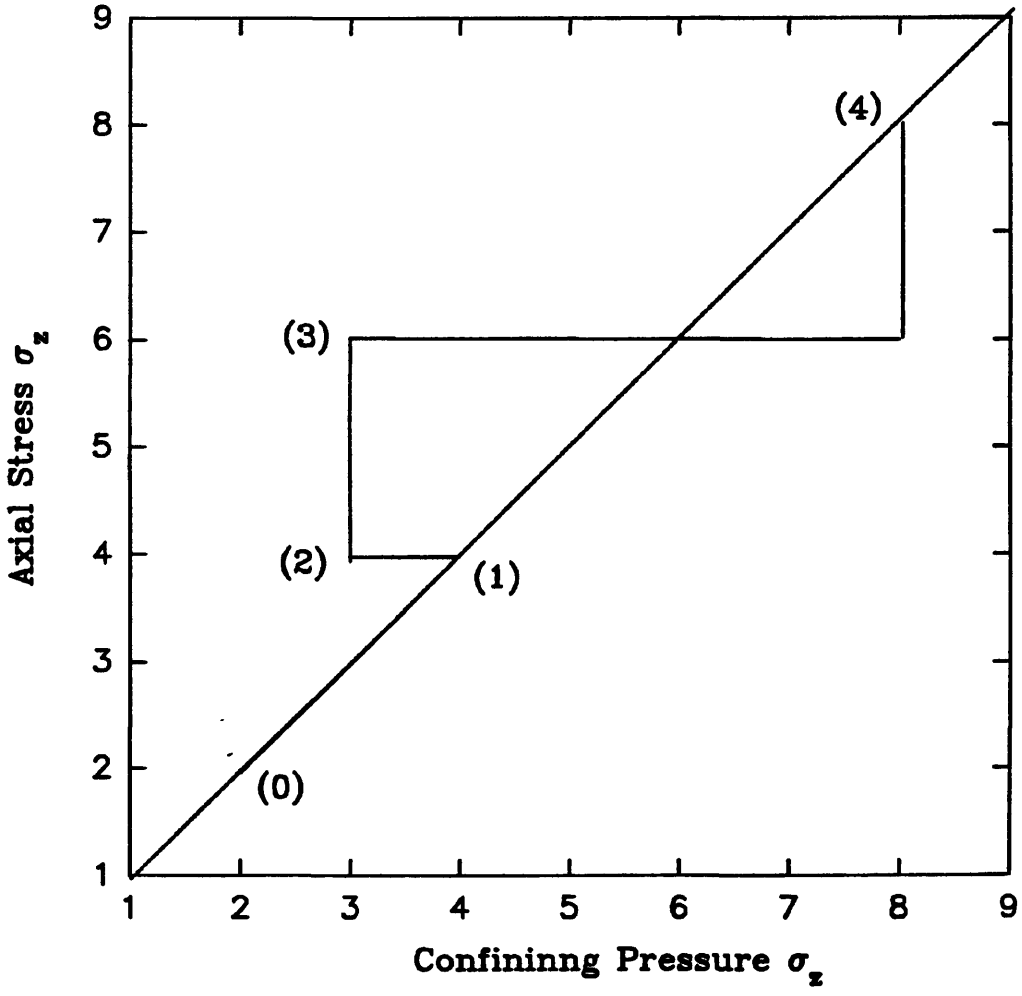

Fig. 3.2 The Staircase Cycle

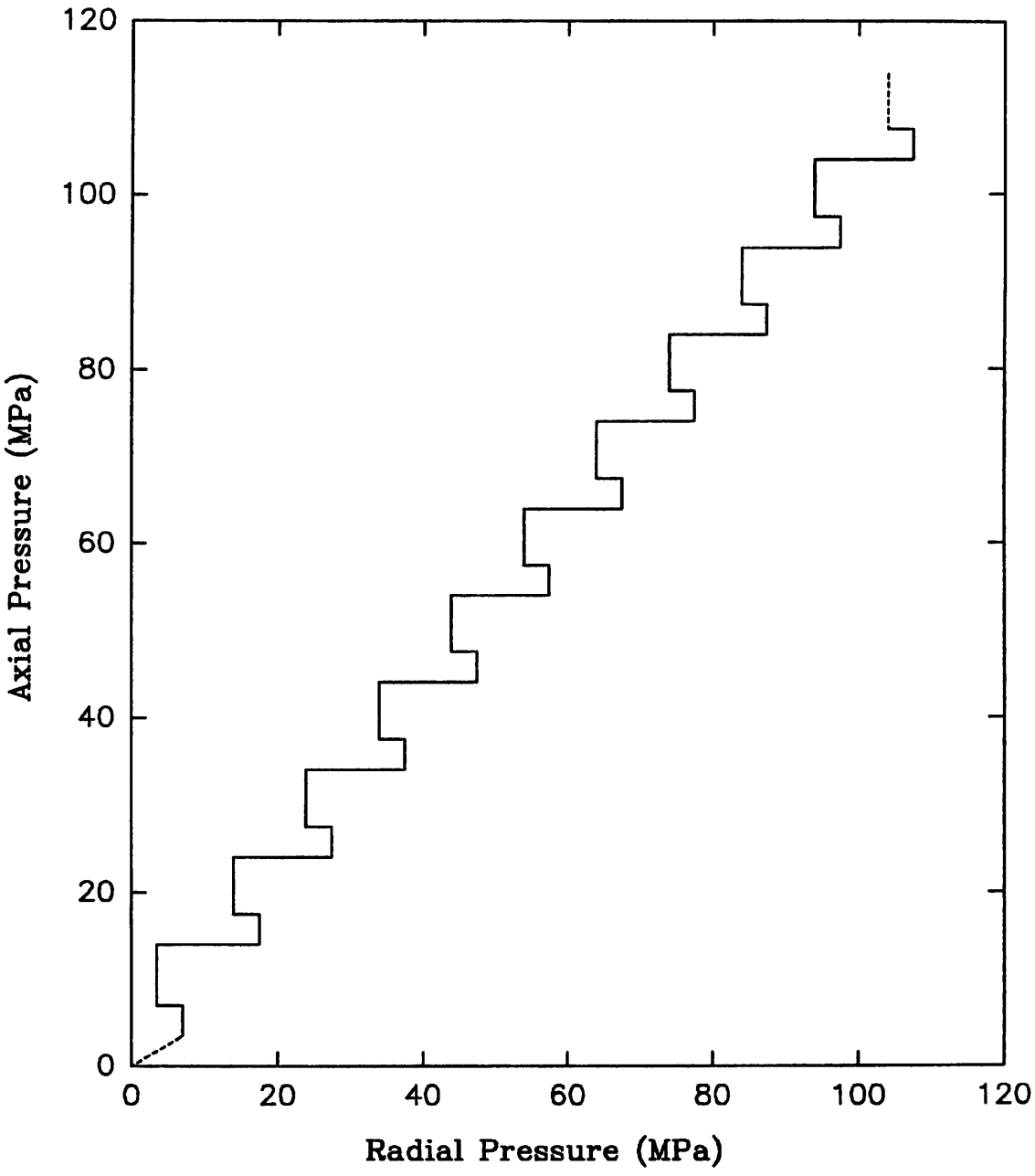

Fig. 33 Loading Cycle

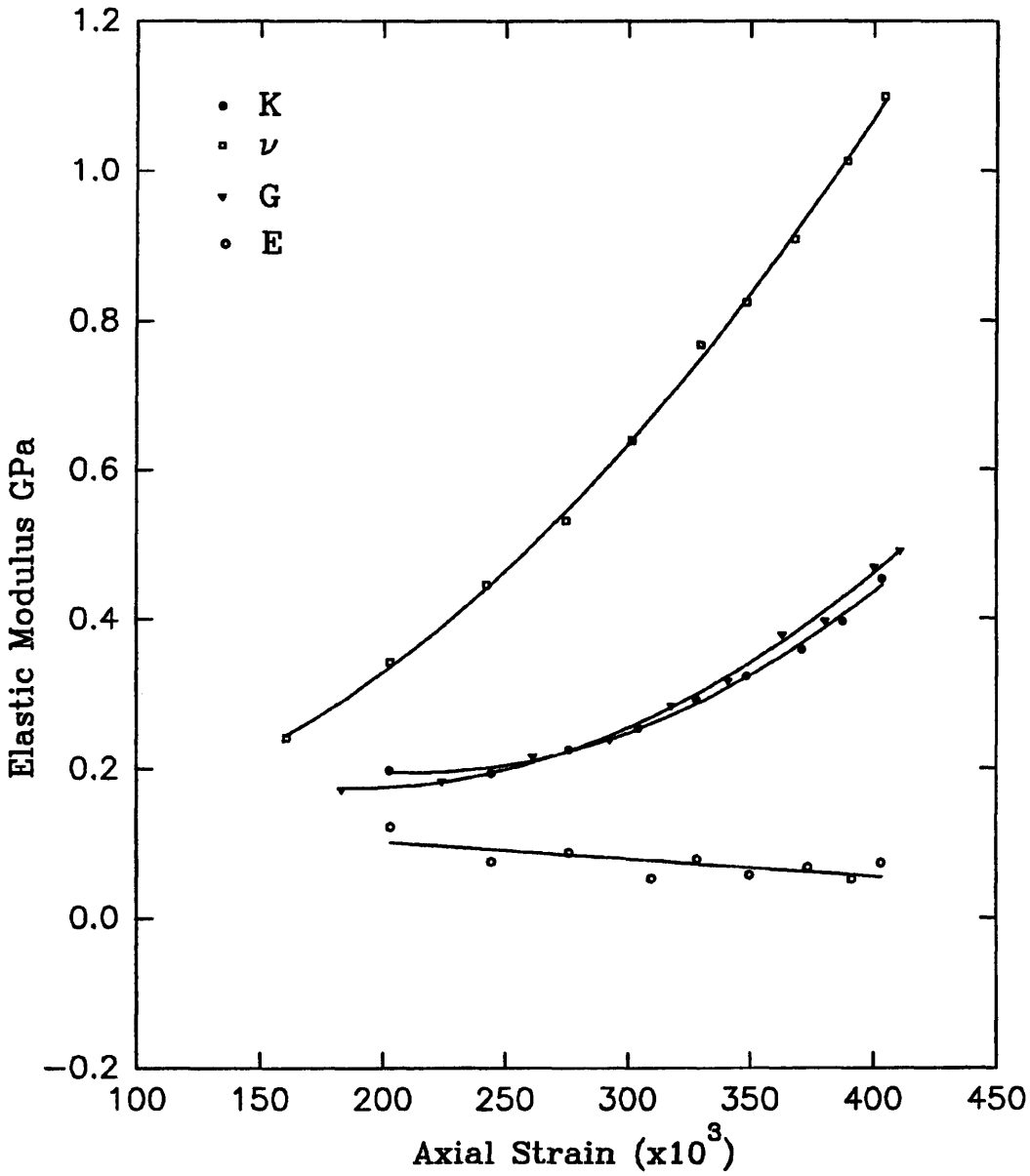

Fig. 3.4 Non−Linear Hypo−elastic Properties

CHAPTER FOUR

NUMERICAL SIMULATION

4.1 INTRODUCTION

In Chapter Three, the Staircase Model was presented. The non-linear hypoelastic properties obtained can be used in numerical simulation of the compaction process.

During the course of this work, three different methods to simulate the compaction process based on the data from the triaxial tests, presented in Chapters Two and Three were attempted. This chapter describes the three methods and typical results obtained from the most promising of them are presented.

4.2 MULTILAYER FINITE ELEMENT METHOD

One of the most prominent finite element packages in use is the ABAQUS code. One way of incorporating such material behaviour into the code would be to write a material sub-routine. This is no trivial task, and instead a multi-layer mesh approach was undertaken [1].

For the proposed finite element modelling of the compaction process the E's and υ's curves similar to those presented in Chapter Three, are discsretized to N horizontal segments (in E, υ - plane) which may or may not be equal, over each of which the corresponding average values of these parameters are considered to be constant. Clearly, the length of each segment and hence the number N of the segments depend on previously prescribed upper permissible variation in starting and finishing values of E's and υ's over them.

The initial geometry of the billet is also suitably discretized using appropriate type of finite elements, and N number of geometrically similar layers, superimposed onto one another are created. Using multiple constraints and boundary conditions, appropriate to the process being modelled, on the relevant set of superimposed nodal points, all the layers are made to follow deformation patterns prevailing in the actual compaction. Each consecutive layer is assigned material properties obtained from the incremental value of E's and actual value of υ's in the corresponding segment of Fig. 4.1. Thus the (N - m)th layer has incremental value of E' and actual value of υ' obtained from the (N-m)th segment of Fig. 4.1 and so on.

To start the compaction process, all but the first layers of the discsretized billet are removed, appropriate boundary conditions are introduced and loading is applied from initial point of pre-defined pressure - normalized time histories (static analysis). The first stage of compaction is completed when ε_z reaches $\Delta\varepsilon_{z1}$ (See Fig. 4.1). During this

stage, because of the global definition of the multiple constraints, all the layers deform together geometrically, but because only layer 1 is active materially, the rest offer no resistance to such deformation. At the end of the first stage, layer 2 with its appropriate material properties is activated in the analysis with already active layer 1. Boundary conditions, appropriate for this situation are introduced and loading applied from the relevant point on the pressure-time histories to initiate the second stage of compaction. This is allowed to proceed up to $\varepsilon_z = \Delta\varepsilon_{z2}$ whence layer 3 is activated in a similar way. The process is completed when the Nth layer has been activated, compaction allowed to continue until ε_z reaches its final desired value. It should be noted here that, once activated, each layer retains its respective incremental physical value of material properties to the end of the analysis.

Fig. 4.2 depicts the experimentally observed loading and unloading paths in a typical compaction test. For this particular material, the difference in displacement (loading) and corresponding displacement (unloading) = dr_j for a given load value is due mainly to the fact that the imposition of compaction has resulted in the change of material physical composition and hence response characteristics.

If unloading behaviour at the end of loading is also to be simulated, then as for loading, the unloading response of displacement recovery must also be measured. The unloading part is discretized into a number of segments in such a way that the slope of a segment is as close as possible to that of one of the segments in the loading path.

This is shown in Fig. 4.2 for a model having four layers, where segment FG is approximately parallel to segment 4 and segment GH is parallel to segment 3 and so on. In order to simulate the experimentally observed unloading path an additional (N+1)th layer, having material properties $E = \{E'_N + \Delta E'_{(N+1)-N}\}$ and $\upsilon' = \upsilon'_{(N+1)}$, is attached to the model at the end of the compaction process, and then unloading is initiated which follows the path EF. When point F is reached layer 4 is "deactivated" from the model and recovery takes place along segment FG. When point G is reached layer 3 is "deactivated" from the model and recovery takes place along segment GH and so on. It may be mentioned here that if unloading is initiated without attaching the (N+1)th layer then the unloading takes place along the dotted line also shown in Fig. 4.2 In the event that the pairing of parallel segments in the two paths is not sequential in the sense mentioned earlier, the same unloading procedure may be applied, but now the global constraints appropriate to the particular problem at hand must be incorporated in the beginning of simulation process.

The finite element modelling technique described above was developed using ABAQUS finite element code. During the development of the input data coding, appropriate checks were carried out carefully using relatively few layers and nine elements per layer of the billet to ascertain the validity of the proposed simulation technique. In practice, however, many more layers and elements would usually be necessary to obtain reasonably accurate results. See Appendix Two for the input file for the ABAQUS finite element simulation. Fig. 4.3 shows the compaction curve,

obtained with four layers, with experimental data.

4.3 THE POLYNOMIAL MATERIAL MODEL

Evidently the finite element method described above is cumbersome. Even with nine elements per layer and only four layers, which was the trial coding carried out, the complexity of the model was evident. To properly model a compaction process one would require in excess of thirty layers and over fifty elements per layer.

Instead a representation of the triaxial test data was undertaken. The pressures at the spherical stress states, explained in Chapter Three, were plotted against the corresponding values of compression, μ.

$$\mu = 1 - \frac{\rho}{\rho_0} \tag{4.1}$$

Figure 4.4 shows a typical result obtained for dipac sugar.

A polynomial of the type:

$$p = A_1\mu + A_2\mu^2 + A_3\mu^3 + [B_0 + B_1\mu]\rho_0 e \tag{4.2}$$

was fitted to the experimental data and the values of the parameters (A_1, A_2, A_3, B_0,

and B_1) were obtained; μ is compression, ρ_0 is initial density and e is energy. Figure 4.3 shows that a very good fit can be obtained.

In AUTODYN finite difference code, a polynomial equation of state represented by Equation (4.2) was used. All that is required is to choose that equation of state for the powder material and supply the values of the parameters obtained from the experimental curve.

Some simulations of die compaction of dipac sugar were carried out and reasonable results were obtained. The major problem with the method was that the shear modulus was a constant. As we saw in Chapter Three, the shear modulus has a non-linear variation with deformation. Several different statistical averages of the shear modulus were used before a reasonable result was obtained for dipac sugar. Although the method was simple and straightforward as compared to the multi-layer method, it is clearly unsatisfactory. It transpired that the only way we can have the varying shear modulus recognised is by writing a separate material subroutine which is then coupled with the program. This was something we tried to avoid with the ABAQUS finite element code.

4.4 AUTODYN MATERIAL SUBROUTINE

For the reasons mentioned in Section 4.3 above, we wrote two material subroutines for

the AUTODYN finite difference code. One of the subroutines is for the non-linearly varying bulk modulus and the other was for the shear modulus.

In both cases, the experimental values were fitted to a third order polynomial and the appropriate constants were obtained. These were then written into the subroutines. The new approach was tested by carrying out a simulation of the die compaction of dipac sugar. The pressure versus axial displacement curve from the simulation was compared with experimental values. The results obtained were very encouraging. Figure 4.5 shows the experimental points and the simulated curve.

The only disadvantage of this method is that the subroutine has to be altered for different powders, recompiled and linked to the main program.

4.5 CONCLUSIONS

Three different attempts to simulate the compaction process, using the experimental results from triaxial tests, were presented. Although these were successful to different extent, they demonstrated that such an approach is feasible.

Results obtained for the simulation of die compaction of dipac sugar showed very good agreement.

4.6 REFERENCES

1 Dr. R. Kormi, Leeds Metropolitan University, Private Communication.

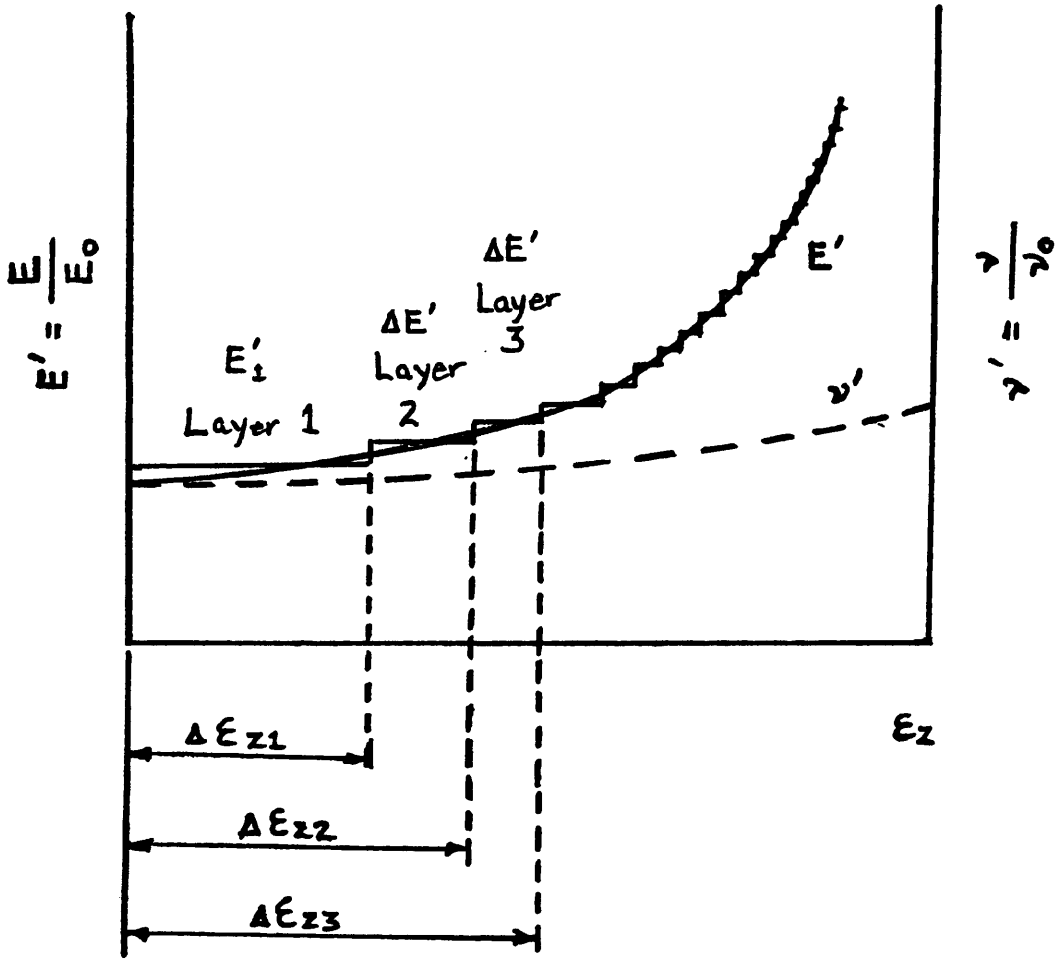

Fig. 4.1 Discretized Hypo-elastic Modulus

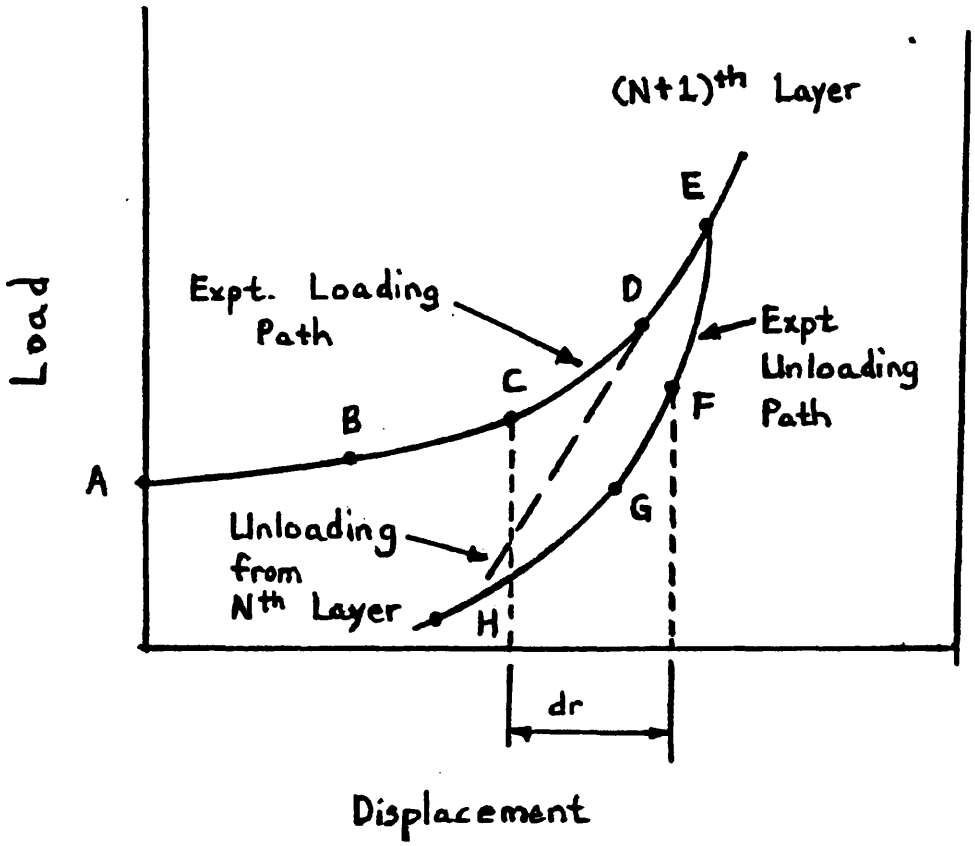

Fig. 4.2 Load Displacement Curve

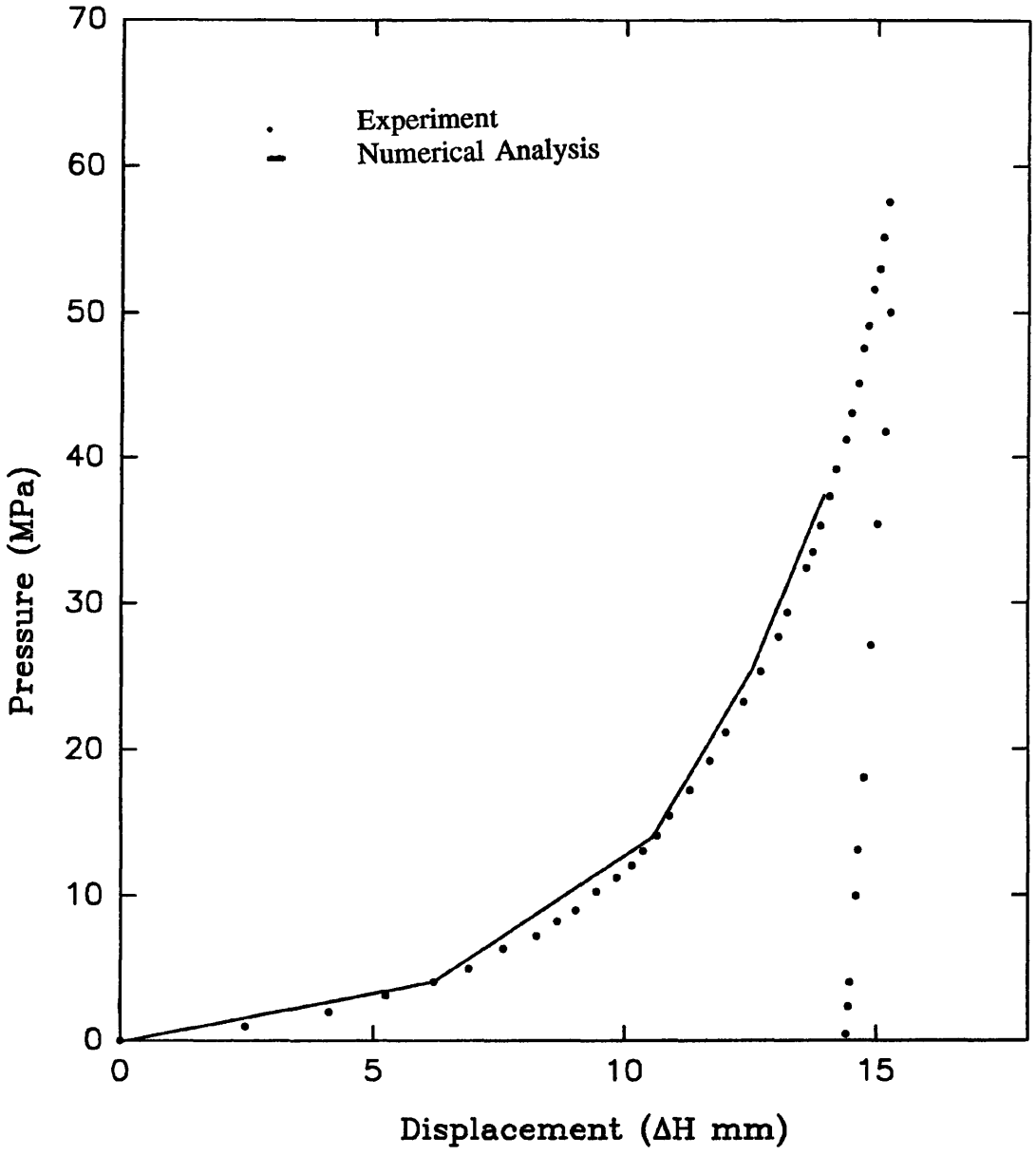

Fig. 4.3

Compaction Curve Showing Experimental Data Along With the Result of the Staircase Method

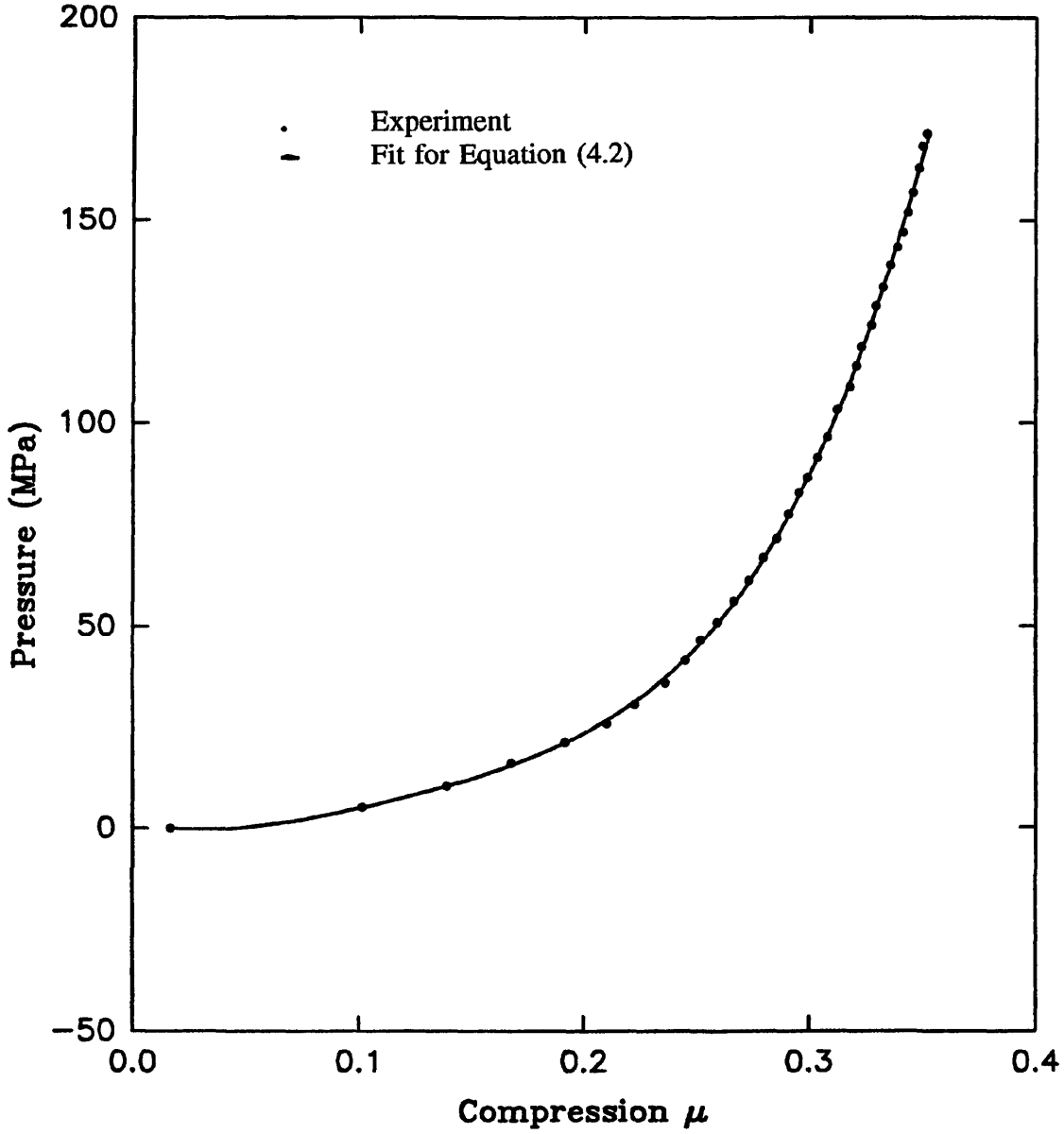

Fig. 4.4

Pressure vs μ (For AUTODYN input)

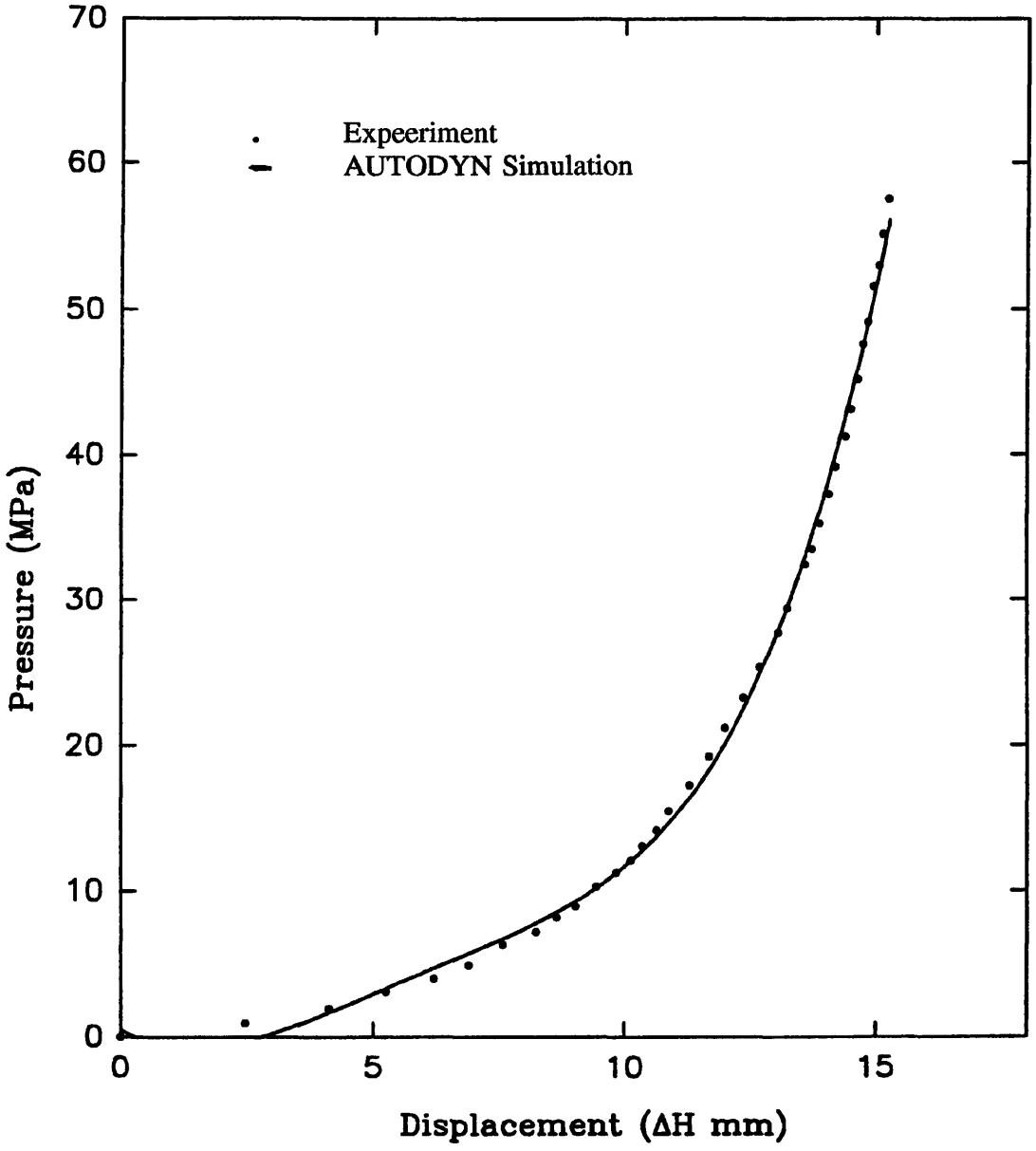

Fig. 4.5

Compaction Curve Showing Experimental Data Along With the Result From AUTODYN

CHAPTER FIVE

STRESS-WAVE TECHNIQUE OF THE SPLIT HOPKINSON PRESSURE BAR

5.1 INTRODUCTION

Various industrial requirements, such as the need to assess resilience and toughness of pellets, leads to the necessity of determining mechanical properties for powder compacts. Finite element analysis of the powder compaction process [1], (1987), [2] (1984), for example, requires data such as elastic modulus in tension and compression at several representative average densities throughout the compaction cycle. To date, such information has been traditionally obtained through the diametral compression "Brazilian" test [3-4] (1984) which measures tensile strength of compacts, or by direct tensile testing [5] (1987). Due to the difference in Young's modulus in tension and compression, the results from the Brazilian test are subject to error. This is because the formula used in relating the applied radial in-plane compressive load to the tensile stress at the centre of the tablet assumes full isotropy and identical properties in tension and compression [6](1980).

The direct tensile and compression testing was earlier used to obtain elastic modulus

and fracture strength of di-pac sugar compacts [5] (1987). This involved the making and machining of large cylindrical specimens. The machining operations required were complicated and delicate, the prepared specimens were then strain gauged with up to eight gauges each. The picture in figure(5.1) shows some of the specimens used. The method is cumbersome and delicate because of the fragility of the compacts.

Later, some thought was given to the possibility of adapting the stress-wave technique of the Split Hopkinson Pressure Bar to the testing of powder compacts. The method proved effective, and offered a simple means of determining some mechanical properties of compacts in tension and compression, using specimens that are easy to produce and handle.

5.2 BACKGROUND

In 1914 Hopkinson devised what was perhaps the first method of measuring transient impulsive stresses. The Hopkinson's method consists simply of an elastic bar of appreciable length which is subjected to dynamic loading on one end. This pressure-time loading is transmitted to the other end of the bar, usually, it is assumed, without significant distortion or attenuation. By suitable measurement techniques, either on the unloaded end of the bar or at a point on the radial surface, and by application of elastic wave theory, the details of the applied disturbance can be reconstructed. Since the bar remains elastic, it can be used to measure either loads or displacements.

The method, now known as the Hopkinson pressure bar, was later developed by Landon and Quinney [7] in 1923. In 1948 R.M. Davies made a critical study of the method and described a modified form of the apparatus in which the measurements are made electrically. Davies's work entitled "A Critical Study of the Hopkinson Pressure Bar" [8] (1923), amounts to a complete experimental and theoretical study of the Hopkinson pressure bar and clearly defines its limits of application.

The Hopkinson pressure bar has found useful application in the study of the transient response of materials to dynamic loading. In these applications the specimen is placed in series with the bar and an impulse is applied either by an accelerated mass or by detonation of explosive charge. Measurements made on the bar then yield the load transmitted by the specimen and/or displacement of the face of the specimen in contact with the bar. Various arrangements of bar, specimen and loading mechanism have been employed in the past. These include firing the specimen directly at one end of the bar, and impacting the bar itself to transmit the load to the specimen.

Unquestionably, the most versatile use of the Hopkinson pressure bar resides in the widely used split Hopkinson pressure bar arrangement, devised by Kolsky [9] in 1949 for tests on the basic compression properties at high strain rates. Kolsky's arrangement involves a short compression specimen sandwiched between two pressure bars and loaded by a single compression pulse applied to the end of one of the bars, and is transmitted through the system. The pressure bars, in this arrangement, are used both

to apply the load to the specimen and as transducers to measure the displacements and applied loads at the faces of the specimen in contact with the bars.

The split Hopkinson pressure bar arrangement became widely used and was applied to material testing by Ripperger in 1952, Campbell in 1953, Bell in 1956 to 1961. More recently Hauser et al 1961, and Tardiff and Marquis 1963 have, amongst others, applied the technique successfully. Davies and Huner [10] (1963) carried out a review of the split Hopkinson bar in 1963 and Lindholm, [11] (1964) used the system in the dynamic testing of materials in 1964.

Although the method has traditionally been used for tests on the basic compression properties of materials (mostly metals and ceramics) at high strain rate, it is now being applied to tablets made from pharmaceutical powders.

5.3 THEORY

The elastic stress wave technique of the Hopkinson pressure bar is accurate within the framework of a number of assumptions. Foremost of these assumptions are that: The Hopkinson pressure bar behaviour can be identified by one-dimensional wave mechanics, a condition of uniform spacial distribution of all the state variables (eg. stress) exists in the specimen during loading, and the pulse is propagated down the bar without appreciable change in form (ie. without distortion).

Kolsky's [9] (1949) split Hopkinson pressure bar arrangement involves sandwiching a short cylindrical specimen between two long rods of high strength steel, so that they are coaxially aligned. A rectangular stress pulse is initiated at the face of one of the elastic rods (ie. the input bar) by the longitudinal impact of a striker. The stress wave thus transmitted through the bar, dynamically loads the specimen. At the specimen's interface with the input bar, part of the incident wave is reflected and the rest transmitted through the second elastic rod (ie. the output bar) - see figure 5.2.

By using strain gauges to measure the incident, reflected and the transmitted waves, it is possible to derive the stress-strain relation for the specimen. The displacement of face (1) of the specimen, the face bordering the input bar, is a result of the incident strain pulse, ε_i travelling in the positive X-direction and the reflected strain pulse, ε_r travelling in the negative X-direction (see figure 5.3).

The passage of the plane longitudinal stress waves along a bar is described by the one dimensional form of the standard wave equation as follows,

$$\frac{\partial^2 u}{\partial x^2} = \frac{1}{c^2} \frac{\partial^2 u}{\partial t^2} \qquad (5.1)$$

where x denotes position along the bar, t refers to time, u is the particle displacement and c the longitudinal stress wave speed in the bar.

This equation has a general solution $u = f(x-ct) + g(x+ct)$. Functions $f(x-ct)$ and $g(x+ct)$ represent arbitrary wave shapes moving in the forward and backward directions respectively.

The general conditions for plane propagation are:

a) the pulse length is long compared with the lateral dimensions of the bar, preferably greater than 10:1. This leads to virtually no dispersion due to lateral deformation and a travelling pulse should retain its shape as it propagates along the bar.

b) The bar is long compared with its lateral dimensions to ensure that the stress distribution across any plane section may be considered uniform.

c) The strain monitoring station is far enough away from any discontinuity in geometry or material.

These conditions fulfilled, the simple theory may be used to predict accurately the effects produced by a stress pulse meeting discontinuities [12] (1972).

Whenever a wave encounters a discontinuity, it divides into reflected and transmitted components whose sign and amplitude depend upon comparison of the physical

features either side of the discontinuity. At any such interface, a wave moving into a region of lower mechanical impedance generates a reflected wave of opposite sign and a transmitted wave with the same sign as itself. The free ends of a bar represent an extreme condition where total reflection occurs. It is the first strain reflected tensile wave in the output bar which provides the tensile loading on specimen. The thin specimen presents two discontinuity interfaces and from strain measurements of the incident, reflected and transmitted pulses, the specimen's stress-strain relationship can be found.

Referring to Fig.5.3 the simple theory for finding the elastic modulus is readily derived. The displacement, u_1 of the input bar at face 1 is the sum of the incident and reflected pulses and can be written as:-

$$u_1 = f(x_1 - ct) + g(x_1 + ct) \tag{5.2}$$

where f() and g() are the incident and reflected pulses respectively.

The strain at any point is simply

$$\epsilon = \frac{\partial u}{\partial x} \tag{5.3}$$

Let

$$x_1 - ct = \theta$$

and

$$x_1 + ct = \phi$$

Thus

$$\epsilon_1 = \frac{\partial u}{\partial x_1} \tag{5.3}$$

and from equation (5.2) we get,

$$\epsilon_1 = \frac{\partial f}{\partial x_1} + \frac{\partial g}{\partial x_1}$$
$$= \epsilon_i + \epsilon_r$$

Hence

$$\epsilon_1 = \frac{\partial f}{\partial \theta}\frac{\partial \theta}{\partial x_1} + \frac{\partial g}{\partial \phi}\frac{\partial \phi}{\partial x_1} \tag{5.4}$$
$$= f' + g'$$

since $\partial\theta/\partial x_1 = 1$ and $\partial\phi/\partial x_1 = 1$ and $f' = \partial f/\partial\theta$ and $g' = \partial g/\partial\phi$

The functions f' and g' have known forms, represented by the recorded incident and

reflected strain waves ε_i and ε_r respectively.

From a consideration of the particle velocity

$$\dot{\epsilon}=\frac{\partial u}{\partial t}=\frac{\partial f}{\partial t}+\frac{\partial g}{\partial t}$$
$$=\dot{\theta}f'+\dot{\phi}g'$$

or

$$\dot{u}=-cf'+cg' \qquad (5.5)$$
$$=-c\epsilon_i+c\epsilon_r$$

Hence the total displacement of a point over the period of a pulse is,

$$u=\int_0^t \dot{u}dt \qquad (5.6)$$

Applying to face 1, equation (5.5) gives

$$u_1= c\int_0^t(-\epsilon_i+\epsilon_r)dt \qquad (5.7)$$

Similarly for face 2 of the output bar, we have a transmitted pulse ε_t only, thus

$$u_2 = h(x_2\text{-}ct)$$

and

$$\epsilon_2 = \frac{\partial u_2}{\partial x_2} = \frac{\partial h}{\partial x_2}$$

giving

$$\epsilon = \dot{h} = \epsilon_t \tag{5.8}$$

and

$$u_2 = \int_0^t -\epsilon_t \, dt \tag{5.9}$$

The specimen strain, ϵ_s, assumed 'uniform' along the specimen is therefore

$$\epsilon_s = \frac{u_2 - u_1}{l_s}$$

where l_s denotes the specimen length.

By substitution form (5.7) and (5.8) we obtain,

$$\epsilon_s = \frac{c}{l_s} \int_0^t (\epsilon_i - \epsilon_r - \epsilon_t) dt \tag{5.10}$$

The forces P_1 and P_2 acting on the specimen faces 1 and 2 are:-

$$P_1 = AE(\epsilon_i + \epsilon_r) \tag{5.11}$$

and

$$P_2 = A\ E\ \epsilon_t \tag{5.12}$$

where A is the cross-sectional area and E the Young's modulus of the bars.

By neglecting the inertial effects of the thin specimen, it follows that P_1 can be equated to P_2 and hence

$$\epsilon_i + \epsilon_r = \epsilon_t \tag{5.13}$$

which combines with equation (5.10) to give:-

$$\epsilon_s = -2\frac{c}{l_s}\int_0^t \epsilon_r dt \tag{5.14}$$

where $\int_o^t \epsilon_r dt$ is simply the area under the reflected strain curve.

The average specimen stress is given by

$$\sigma_s = \frac{P_1}{A_s} = \frac{P_2}{A_s}$$

which, using equation (5.11) and (5.12)becomes

$$\sigma_s = \frac{E\,\epsilon_t\,A}{A_s} \tag{5.15}$$

where A_s is the specimen cross-sectional area. It may be worthwhile to note that by adjustment of the diameter of the specimen a significant amplification of the stress may be achieved. In our experiments care was taken to keep σ_s low in the compression cycle to avoid crushing.

The elastic modulus, E_s, for the specimen can now be found from

$$E_s = \frac{\sigma_s}{\epsilon_s} \tag{5.16}$$

This would require the experimental set up to measure ϵ_r and ϵ_t separately. It is interesting to note that equation (5.14) shows that ϵ_r gives a direct measure of the strain rate in the specimen.

Appropriate strain signals are selected for determining the compressive Young's modulus from equation (5.16) with ϵ_r and ϵ_t values taken from the first passage of the compressive pulse. The tensile Young's modulus is obtained in the same way except that this time ϵ_r and ϵ_t values are taken from the passage of the pulse, ϵ_t, reflected as a tensile wave from the free end.

The minimum tensile fracture stress can be calculated from the transmitted strain pulse

of the tension loading cycle in those cases where the specimen is fractured. The strain pulse associated with the stress level reached up to fracture continues to propagate unambiguously through to the other bar being cut off at the instant the free surface has been created.

5.4 APPARATUS AND INSTRUMENTATION

The arrangement of the instrumentation is seen diagrammatically in Fig.5.3 and an overall view of the complete system is shown in the photograph, Fig.5.4 and a close up of the tablet zone in figure 5.5. The input and output bar dimensions and the strain monitoring points have been chosen to satisfy conditions for one dimensional wave theory and to separate the incident and reflected pulses on the time scale, making it practicable to apply and measure effects of compression and tensile loading separately.

The two cylindrical bars, made from 10mm diameter high strength steel, are supported on four adjustable Vee slot knife edges rigidly mounted on an I-beam and accurately aligned axially. The knife edge supports minimise frictional effects to prevent disturbance of the passing waveforms., All four bar ends are smooth perpendicular to their axes.

The specimen under test, approximately 5mm long and 10mm diameter, is sandwiched between the bars and glued co-axially in position using standard strain gauge adhesive,

type M Bond 200. This adhesive will transmit both compressive and tensile stresses through the specimen, without depreciation or distortion.

In these experiments, a short compressive loading pulse is initiated by striking the free end of the input bar co-axially with a short, 10mm diameter, Aluminium rod. At the specimen interface, this pulse divided into transmitted and reflected components which are compressive and tensile respectively in this case. The transmitted wave travels on to the free end of the output bar reflecting back as a tensile wave to load the specimen in tension. Further subdivision occurs at the interface.

Because the duration of the loading pulse is long compared with the wave transit time through the specimen, numerous internal reflections occur in the short specimen during the passage of the loading pulse. For this reason, the stress distribution in short specimens becomes smoothed out very rapidly and internal wave transversal can be safely neglected.

Eventually, the multiple division of waves at the specimen interfaces form complex waveforms of no special interest. The first compression and tensile loading cycles provide all the information necessary to calculate the elastic constants.

5.5 TEST PROCEDURE and CALIBRATION

The test tablets are made in the laboratory, drawings of the die and punch set used are shown in Fig 5.6. These are glued into position taking care to maintain axial alignment. Light pressure is maintained on the specimen for about 30 to 60 seconds allowing the adhesive to cure. The energising levels and balance of the strain gauge bridges are checked. Triggering which is initiated from the input bar bridge circuit, is also checked prior to arming the storage oscilloscope for a test. It is usual to set the controls for 10-20% pre-trigger information to ensure all the incident peak is recorded.

The input bar is struck by the striker. The captured signals, displayed on screen, are transferred to floppy disk for permanent storage. Accurate time and voltage measurements can be taken from the screen display using the cursor and expansion controls available on the Nicolet 4094. It is easy therefore to measure to stress wave velocity, c, in steel by choosing two convenient strain peaks a known distance apart and measuring their separation interval.

Areas (under the curve) are also very easily found by selecting appropriate sections of the waveforms with the cursor system and carrying out a numerical integration using a standard Nicolet software package.

Voltage levels are converted to strains by calculation from a knowledge of the bridge constants and amplifier gain. Confirmation of strain levels is readily achieved through direct calibration by injecting known strain step changes into the system.

The stress waves travelling along the bars are detected by measuring their associated strains. At each strain monitoring location, four strain gauges are attached and connected in the form of a full bridge, refer to Fig.5.5. Two axial and diametrically opposite gauges form two bridge arms with two circumferential and diametrically opposite gauges completing the bridge. This configuration increases sensitivity by including Poisson strains, improves measurement stability, eliminates bending strain effects and measures axial strains only.

The monitoring locations were chosen with some prior knowledge of pulse lengths and wave speeds in the bars. In the present system, this lead to selection of gauge positions as indicated in Fig. 5.7. This figure shows a space-time diagram which represents the length of the bar system (input bar 2.2m and output bar 1m) on the horizontal axis. It also shows the position of the wave fronts along the bars with time plotted along the vertical axis. The input compressive pulse is reflected as a tensile pulse of a different amplitude from the first interface. Fig. 5.7. clearly illustrates the time separation of pulses at the measuring stations.

The strain gauge bridges are energised at 5 volts dc and their signals conditioned by Fylde Transducer Amplifiers with gain levels set at 1000. The output waveforms are captured on a two channel Nicolet 4094 digital storage oscilloscope and permanently stored on floppy disc. Digitisation rates of 1μs per point are chosen to provide adequate resolution and recording time.

5.6 VERIFICATION TESTS

Figure 5.8 shows the result of a single compressive pulse reflecting within the input bar alone. Peak amplitude measurements for a pulse travelling several meters along the bar indicate an attenuation of around 1%. Observation of the first few peaks also shows little distortion suggesting no significant dispersion.

To test the effect of the adhesive, the input and output bars were glued together without a specimen. The traces obtained when a single compressive pulse passes through the two bars is shown in Figure 5.9. Reflections do not occur at the adhesive interface which is seen to support both the compressive and tensile stresses. Again, peak height measurements over a passage of several meters shows a decay of about 3% slightly more than would be expected from a continuous bar. However, the decay attributable to the adhesive is still small enough to be ignored.

To assess the accuracy of the measuring technique, an aluminium disk, identical in size to the powder tablets, was glued in position and tested in the same manner. A typical aluminium result is shown in Figure 5.10 measurements on peaks A, B and C give the compressive elastic modulus and on peaks D, E & F the tensile modulus. Values obtained were 69.4 GPa and 71.4 GPa respectively, which compare favourably with the tabulated value of 70 GPa. Although different, it is significant that the two modulus values are fairly close in keeping with the expected isotropy of aluminium.

It should be noted here, that in addition to the accuracy of the electrical measurements, the accuracy of measuring the specimen and bar geometries as well as the value chosen for Young's modulus of the bar, contributes to the accuracy of the calculated modulus of the specimen.

5.7 POWDER COMPACTION TESTS AND RESULTS

Sets of di-pac Sugar and paracetamol tablets covering a range of densities were made in the laboratory with a punch and die system, shown in figures 5.6, using powders having a measured particle size distribution shown in Table 6.1. Initially, a calibration for the powder type is carried out by plotting the load/displacement curve for a known mass of powder within the die holder. Displacement is readily converted to density from the punch dimensions. By adjusting the initial mass of powder and compacting to the appropriate load, tablets of different density, approximately 5mm thick, can be produced.

The tablets were each tested in the manner described earlier producing traces typical of those shown in Figure 5.11. Peaks A, B and C are utilised to calculate the compression modulus and peaks D, E and F to calculate the tensile modulus. The minimum tensile fracture stress is determined from the amplitude of peak F, in Fig.5.11 when fracture occurs. Fig.5.12 shows a close up view of a typical fractured tablet.

It is important to note that the imposed level of compressive stress should not be high enough to produce permanent compressive deformation or crushing damage. It is well worth subjecting a similar tablet specimen to compressive loadings to ascertain the crushing strength before a decision is made on the severity of the impact in the stress wave bar test.

The variation of the Young's modulus in compression E_c and that in tension E_t for the Di-pac sugar tablets with tablet compaction formation pressure is shown in Fig. 5.13 as determined by the present stress wave technique and by the conventional uniaxial compression and tensile tests. The use of the tablet compaction pressure instead of its density is a usual practice in the palletizing industry. A similar plot is given in Fig.13 for paracetamol D.C tablets as obtained from the stress wave technique.

The fracture stress of di-pac sugar has been measured in this laboratory using the Diametral "Brazilian" test, in which a tablet, of similar size to those used above, is loaded edgewise between two flat punch faces in a testing machine. Uniaxial tests have also been undertaken on a series of large di-pac sugar tablets over a similar range of densities. These were formed and machined to a suitable shape then loaded in a standard testing machine, see ref.6 and figure 5.1. Fig.5.14 shows that for the sugar and paracetamol, there is a marked difference between compressive and tensile values of Young's modulus. There is also a reasonable agreement between the results of the stress wave technique and uniaxial tests.

The fracture stress values obtained from the present stress wave technique and those produced by the other two methods are compared in Fig.5.14 for di-pac sugar. The stress wave technique gives higher values whilst the Brazilian test gives lower values than those obtained from the uniaxial tension tests. However, at higher compaction pressures they tend to be closer. This is not surprising since tablets formed at high compaction pressures tend to be more consistent and have similar properties.

This chapter is intended to outline the principles of this new technique and to discuss the mechanics of deformation and fracture. This would clearly be of immediate future interest in view of the fact that there is a degree of inaccuracy in each of the available measuring techniques. It is hoped that the simplicity and cost effectiveness of this technique would make it widely used in powder metallurgy and pharmaceutical industries.

5.8 CONCLUSION

An objective of this work was to devise a simple but cost effective and acceptable method of measuring the elastic tension and compression moduli for powder compacts and their tensile fracture strength. Specimen tablets have proved easy to make, handle and install in the stress wave bar system. This technique requires further refinement by controlling the input pulse, positioning the strain gauges and alignment of the bars and bonding the tablet to the bars.

REFERENCES

1. I.M. Al-Khattat and S.T.S. Al-Hassani

   "Towards a Computer Aided Analysis and Design of Tablet Compaction". Chemical Engineering Science,

   Vol.42, No.4, 1987 (707-712)

2. W.T. Loo, "Analysis of Powder Compaction Process using Non-Linear Finite Element Method", Ph.D Thesis, UMIST, 1984.

3. M.H.H. Es-Saheb, "An Investigation into the Mechanics of Dynamic Compaction of Pharmaceutical Powders" Ph.D Thesis", UMIST, 1985.

4. H. Asghar, "Triaxial Compaction of Pharmaceutical Powders", MSc Dissertation, UMIST, 1984.

5. M. Sarumi, "Compaction of Pharmaceutical Powders", MSc Dissertation, UMIST, 1987.

6. P N Sundram and J M Corrales, Int J rock Mech, Min Sci & Geomech. Abstr., 17, (1980), 131.

7. Landon, J.W., and Quinney, H.,

   Proc. Roy. Soc. A, 103, 622 91923).

8. R.M. Davies,

A "Critical Study of the Hopkinson Pressure bar.", Phil. Trans. Roy. Soc., A240, 375.

9. Kolsky, H.,

"An Investigation of the Mechanical Properties of Materials at Very High Strain Rate.", Proc. Phys. Soc., B62, (1949) 676.

10. E.D.H. Davies, and S.C. Hunter,

"The Dynamic Compression Testing of Solids by the Split Hopkinson Pressure Bar.", J. Mech. Phys. Solids, Vol.11, 91963; P155-179.

11. U.S. Lindholm

"Some Experiments with the Split Hopkinson Pressure Bar.", J. Mech. Phys. Solids, Vol. 12, (1964), P317-335.

12. W. Johnson, "Impact Strength of Materials" Edward Arnold, 1972.

TABLE 5.1

Aperture (μm)	Fractional percentage Di-pac Sugar	Fractional percentage Paracetamol D C
1000	0	0
710	0.2	0.4
500	0.2	0.2
355	13.6	0.8
250	40.4	2.6
180	23.4	14.2
125	19.0	28.0
90	1.2	24.6
63	0.4	16.2
< 63	1.6	13.0

Di-pac Sugar True Density = 1580 kg/m^3

Paracetamol D C True Density = 1288 kg/m^3

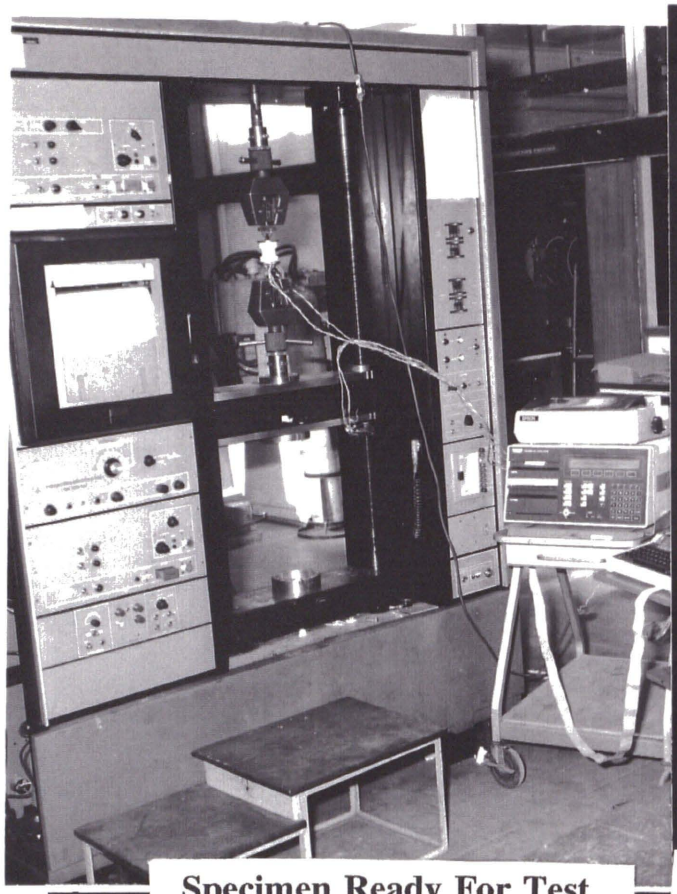

Specimen Ready For Test

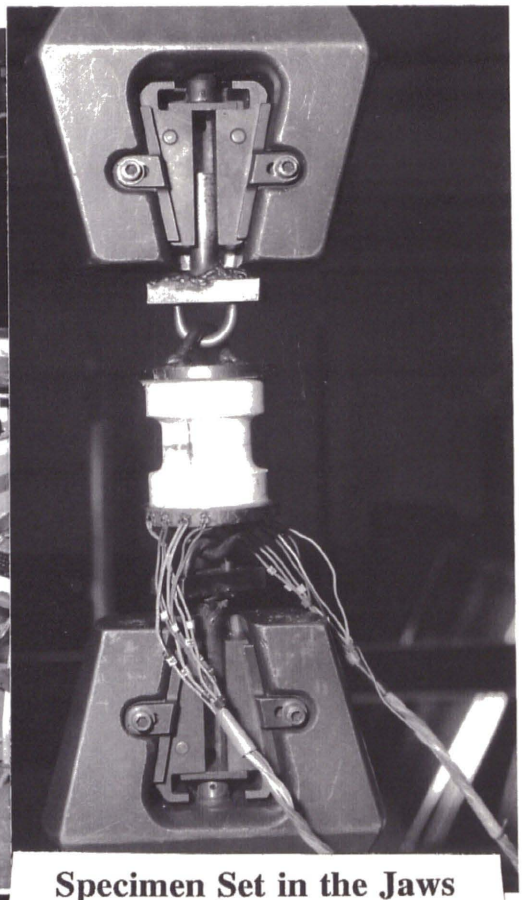

Specimen Set in the Jaws

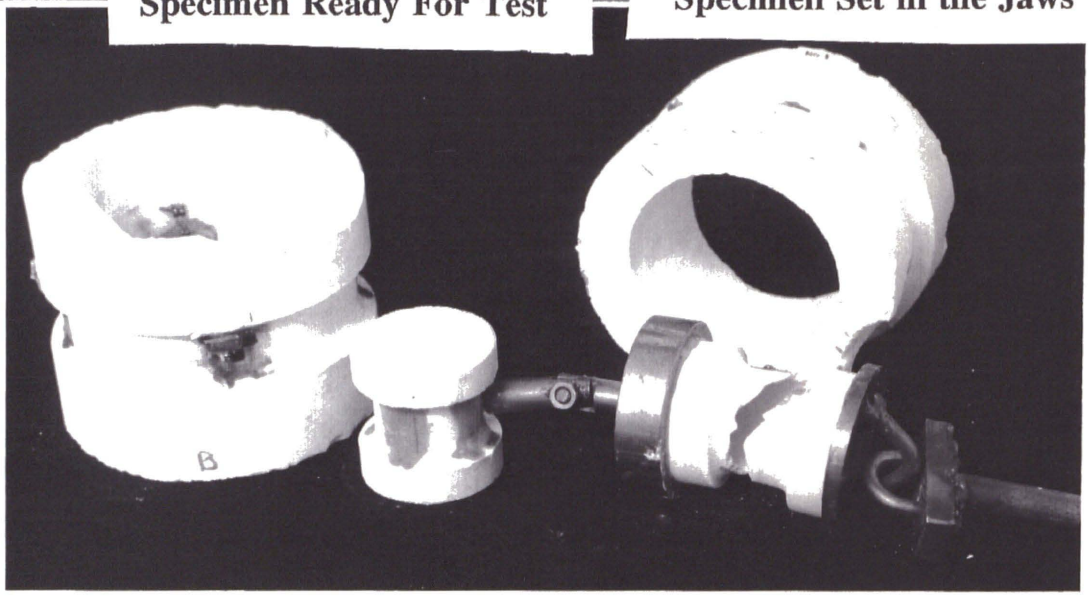

Typical Test Specimens

Fig. 5.1 Direct Compact Testing

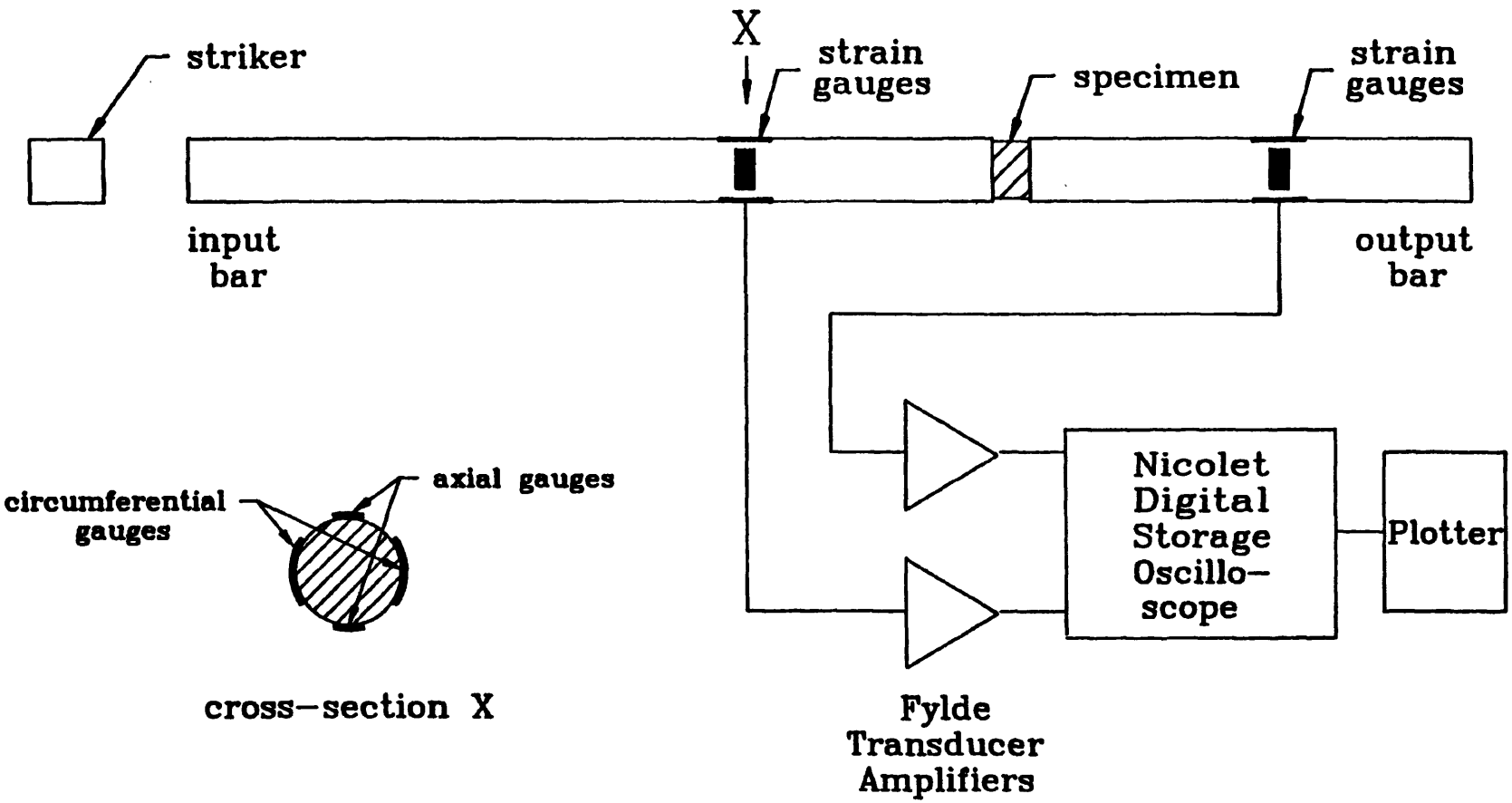

Fig. 5.2 Layout of the Split Hopkinson Pressure Bar with Instrumentation

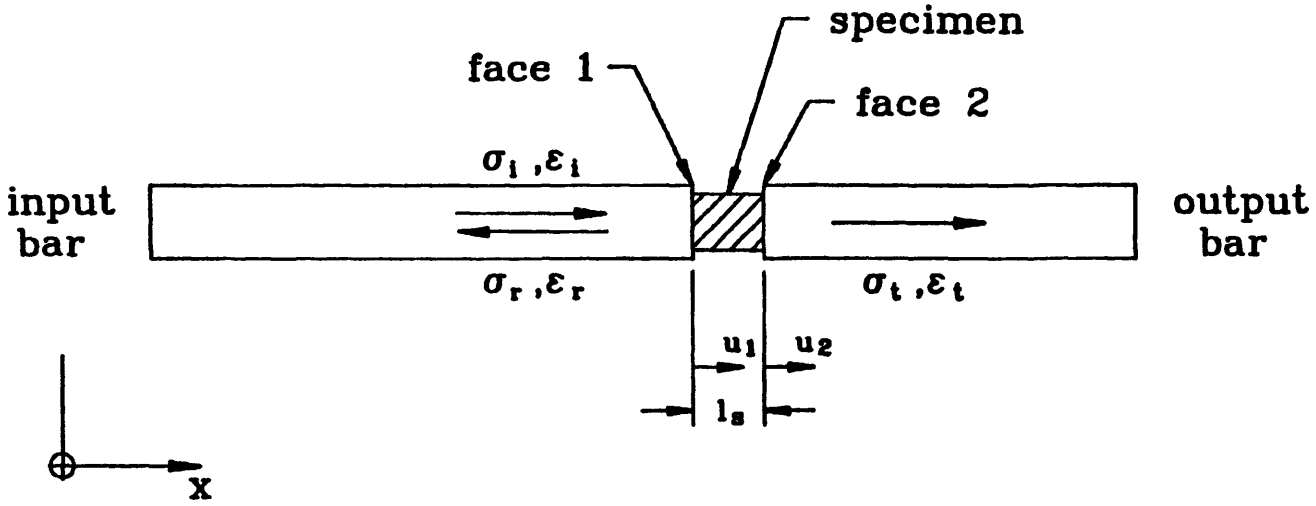

Fig. 5.3 Pulse Reflection and Transmission at Tablet Interfaces

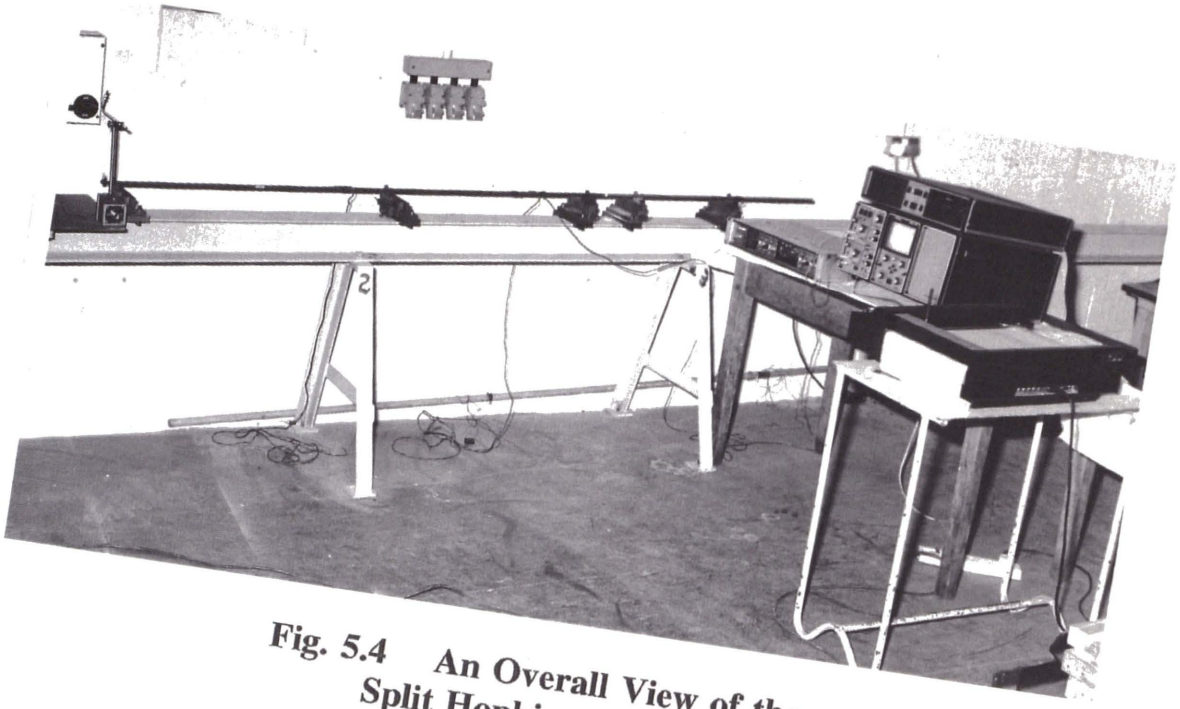

Fig. 5.4 An Overall View of the Split Hopkinson Pressure Bar

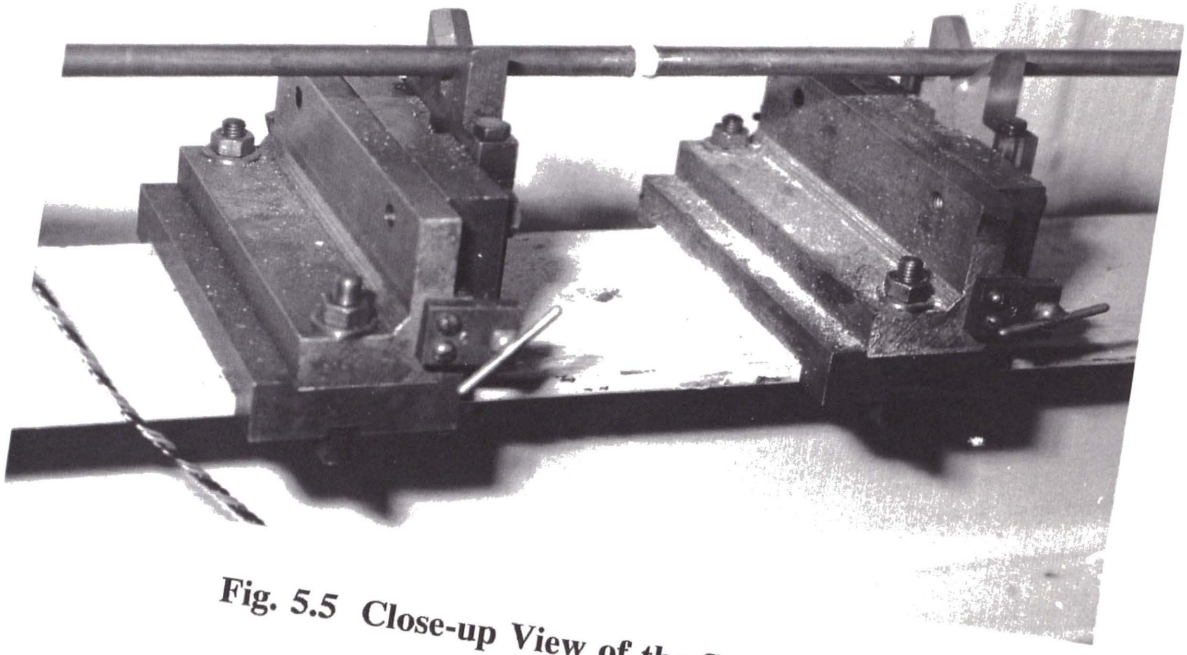

Fig. 5.5 Close-up View of the Specimen

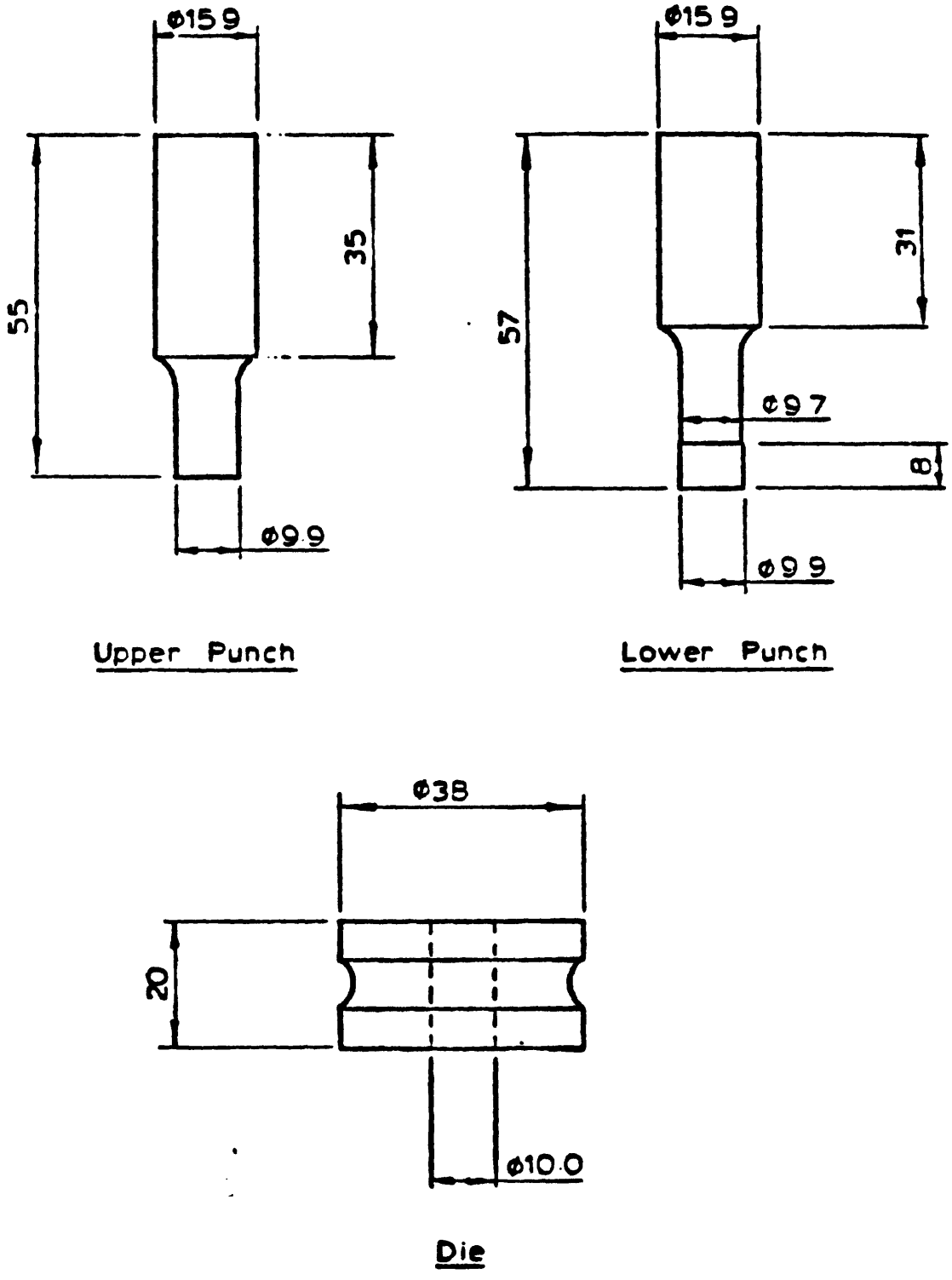

Fig. 5.6 Punch and Die Set

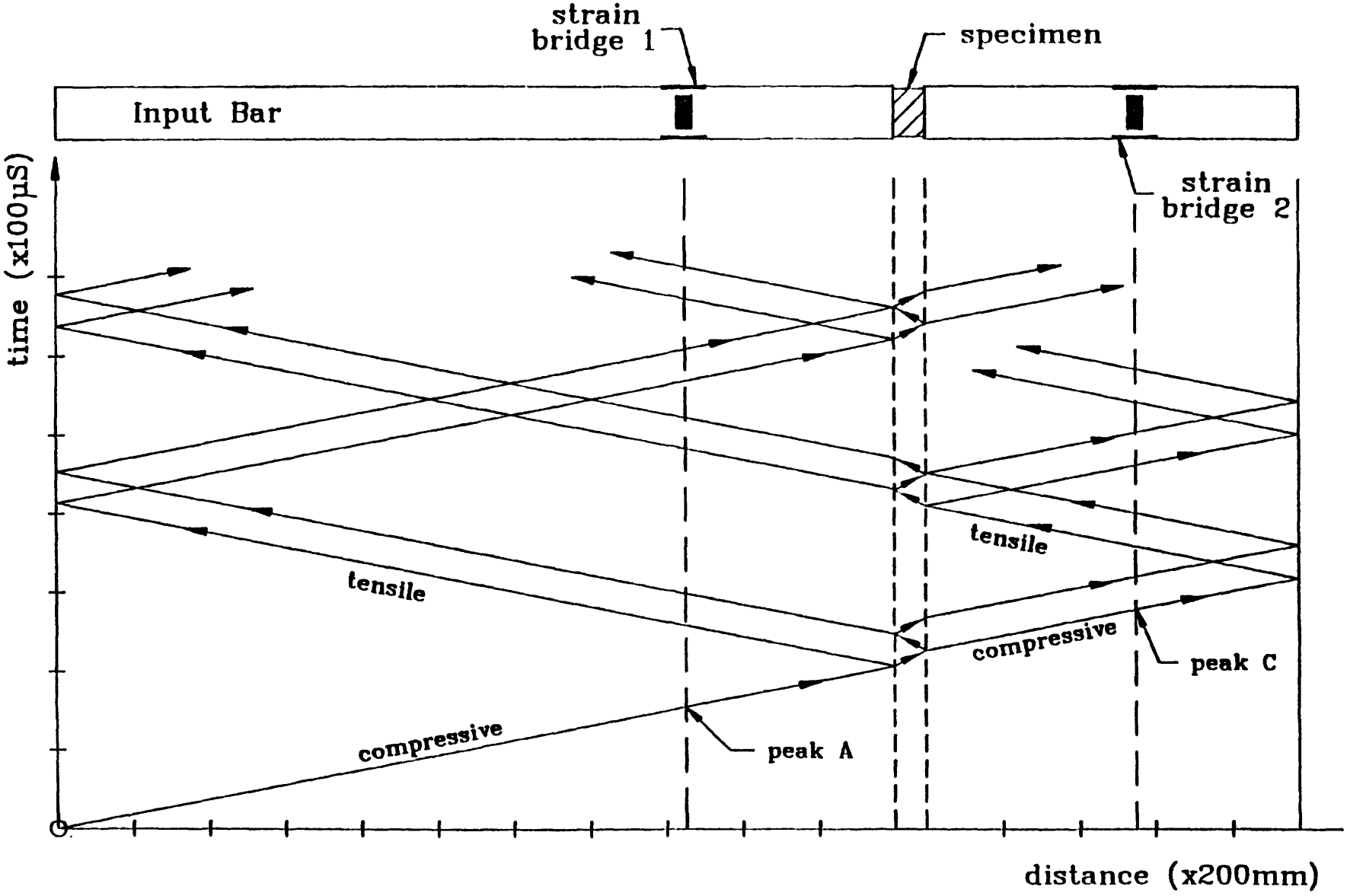

Fig. 5.7 Space - Time Diagram for the Split Hopkinson Pressure Bar Showing Partition at the Discontinuities

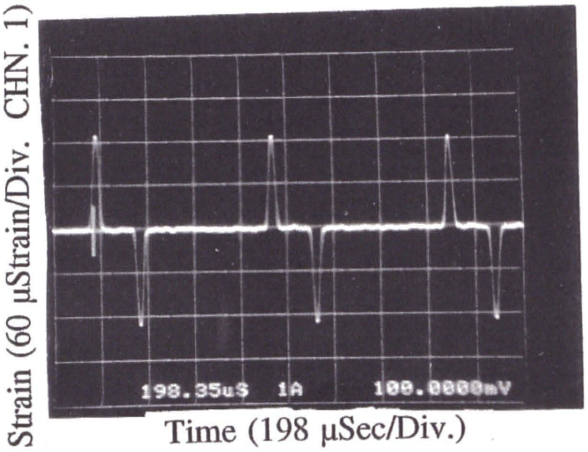

Fig. 5.8 Reflecting Wave Forms Within a Single Bar

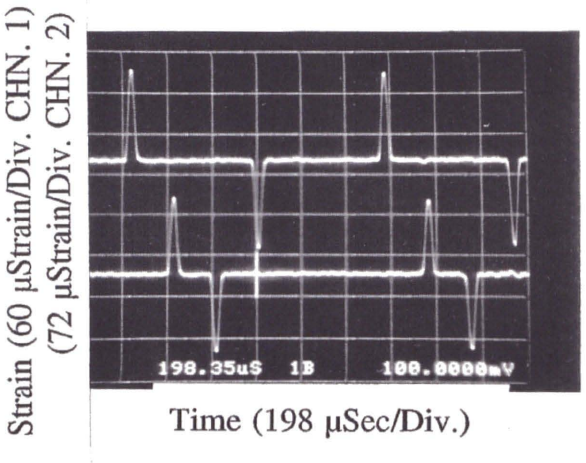

Fig. 5.9 Glue Test Input (upper Trace) and Output (Lower Trace) Gled Together

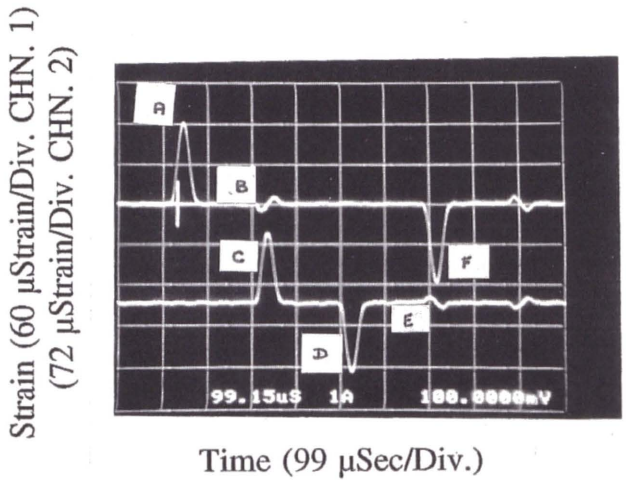

Fig. 5.10 Typical Output Traces For Aluminium Tablet

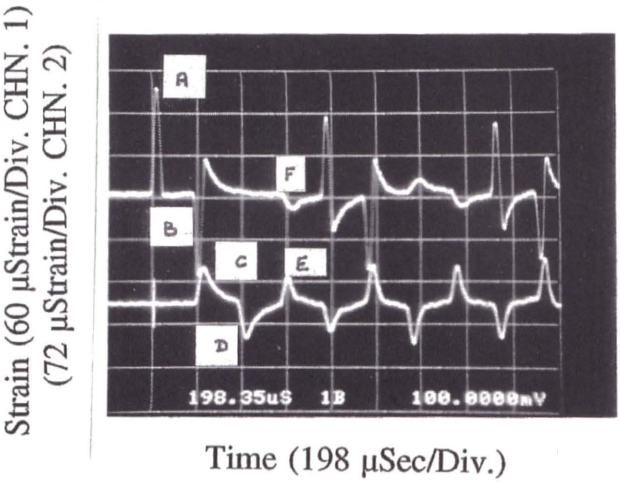

Fig. 5.11 Typical Traces For Paracetamol Tablet

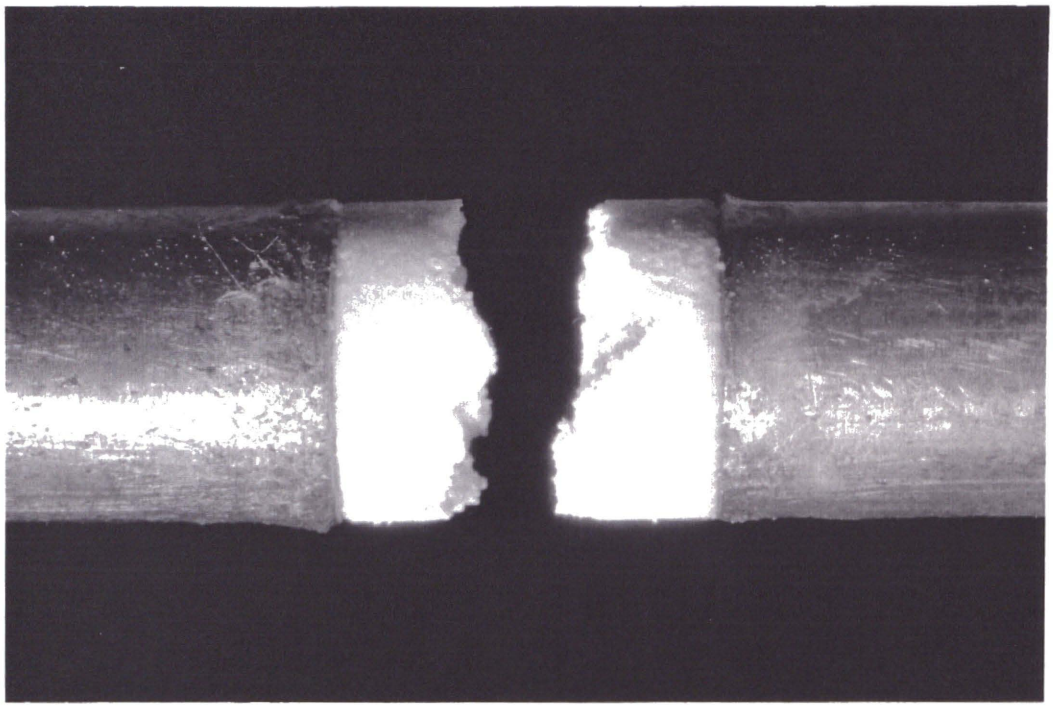

Fig. 5.12 Fractured Tablet

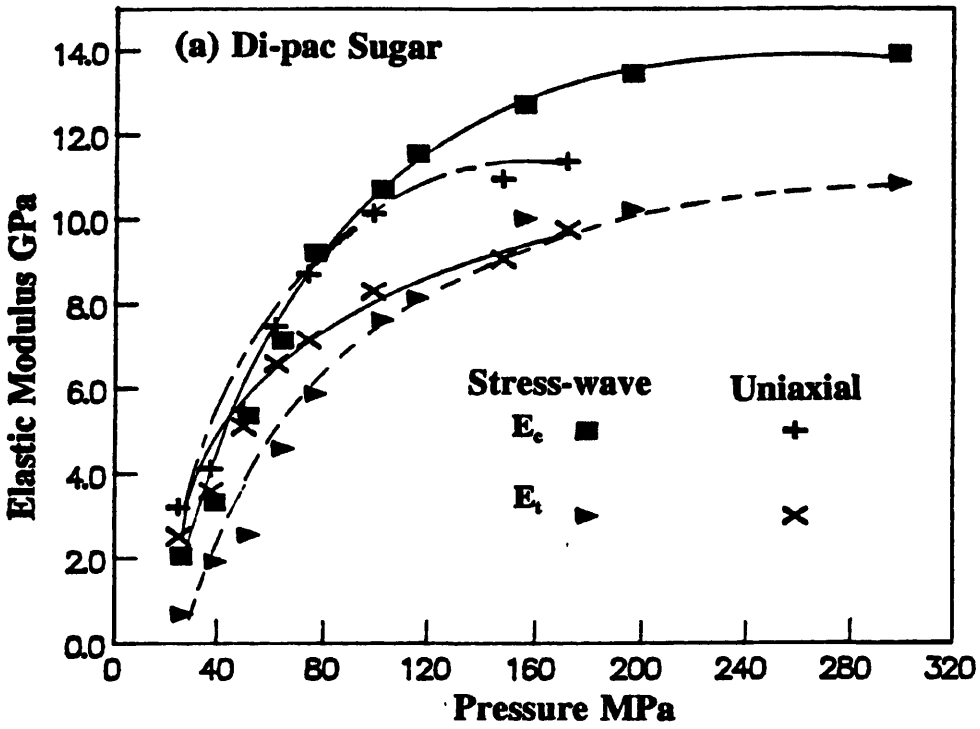

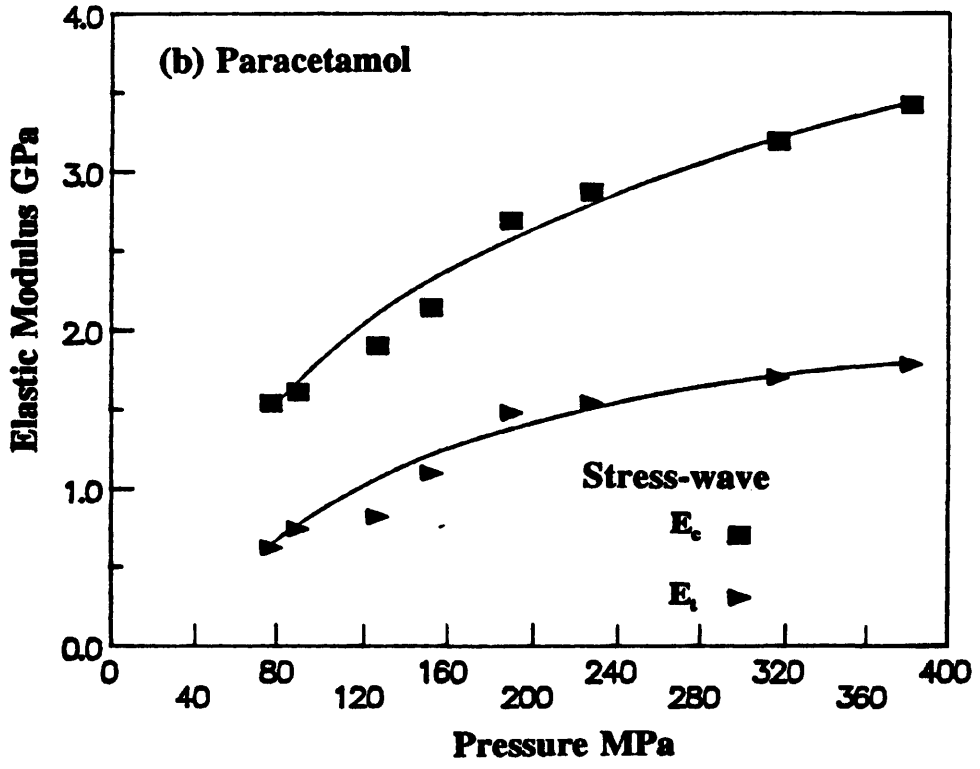

Fig. 5.13 Young's Modulus in Compression E_c and in Tension E_t Versus Compaction Pressure as Obtained by the Stress-wave Technique and Uniaxial Tests

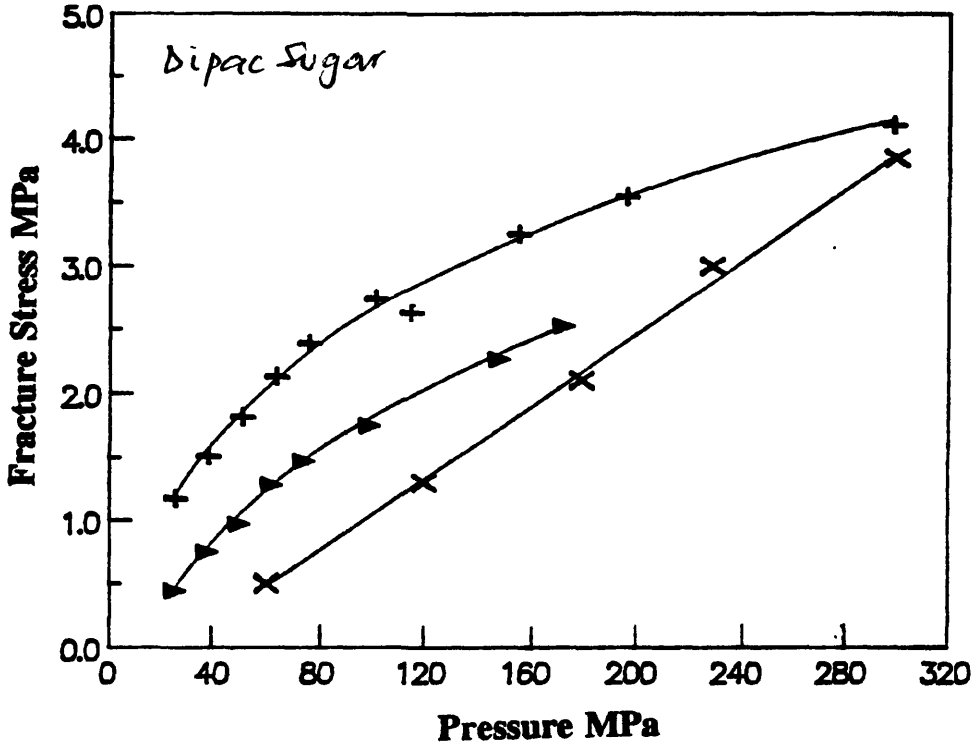

Fig. 5.14 Tensile Fracture Stress Versus Compaction Pressure from Stress-wave Technique +, Uniaxial Test , and Brazilian Test x.

CHAPTER SIX

ANALYTICAL APPROACH TO THE COMPACTION PROCESS

6.1 SUMMARY

Four equations, 'material models', were derived, each to describe the different stages in the compaction process. Experiments were carried out to show how some of the parameters and constants required in these equations could be obtained, and to relate the method to experimental data.

6.2 INTRODUCTION

There have been several equations, 'material models', proposed, to relate the compaction pressure to the compact density or porosity. A comprehensive review of nine of the more popular ones was carried out by Kawakita and Ludde [1] (1969). The Kawakita equation is one of the most commonly used equations, and is as follows;

$$\frac{P}{C} = \frac{1}{ab} + \frac{P}{a} \qquad (6.1)$$

where, $C = \frac{V_o - V}{V}$ referred to as the degree of compaction,

V_o is initial apparent volume

V is powder volume under applied pressure, p, and

a and b are constants.

The other most popularly used equation is that of Heckel [2-3] (1961), which was not reviewed by Kawakita. This equation, like Kawakita's equation and most of the others, is empirical. Heckel based his equation on that of Konopicky [4] (1948) which assumes the rate of change of density to be proportional to the void fraction. Heckel likened the compaction process to the first order "chemical reaction" in which the pores are the "reactant" and the densification of the bulk of the products to be the "kinetics" of the process.

By integrating Konopicky's relation, Heckel found that;

$$\ln\left(\frac{1}{1-D}\right) = Kp + \ln\left(\frac{1}{1-D_o}\right) \qquad (6.2)$$

where,

D_o is the relative apparent density of the powder

p is applied pressure

D is the relative density of the powder

K is a constant.

He replaced, $\ln\left(\frac{1}{1-D_o}\right)$ with a constant A yielding,

$$\ln\left(\frac{1}{1-D}\right) = Kp + A \tag{6.3}$$

Heckel himself and many researchers, subsequently found that the linear relation between $\ln\left(\frac{1}{1-D}\right)$ and p does not hold at low pressures. Although Heckel assumed that it should hold at higher pressures, this has been found to be untrue as Fig 6.1, for typical organic powder and Fig 6.2 for typical metallic powder illustrates. Similarly, many researchers using Kawakita's equation, including Kawakita himself, recognised that the equation cannot represent the complete range of compaction pressures. Furthermore, neither equation takes rate effects into account, as many researchers have found out, including Es-Saheb [5] (1984), the powder compaction process is a time dependent process.

The empirically based equation presented by Heckel bears a close resemblance to the pore collapse relation presented by Carroll and Holt [6-7] (1972) for ductile solids. This equation is;

$$p = \frac{2}{3}\,\sigma_o \ln\left(\frac{\alpha}{\alpha-1}\right) \tag{6.4}$$

where,

p is pressure

σ_o is yield stress

α is the distention ratio given by;

$$\alpha = \frac{V}{V_s} \tag{6.5}$$

V is the apparent volume

V_s is the volume of the solid constituent.

α has the same meaning as D in the Heckel's equation. In fact the Carroll and Holt equation is the same as the empirical equation presented by Ballhausen [8] (1951), who offered the following relationship;

$$\ln\left(\frac{D}{1-D}\right) \alpha\, p \tag{6.6}$$

Which can be rewritten as

$$p = A \ln\left(\frac{D}{1-D}\right) \tag{6.7}$$

If we replace $2/3\sigma_o$ with a constant in the Carroll and Holt equation (6.4) and knowing that D has the same definition as α, the two equations are the same. In fact, Heckel confirmed that Ballhausen's equation is just as valid as that of Konopicky, on which he based his own equation. Heckel preferred Konopicky's equation because it is applicable to slightly lower pressures than Ballhausen's.

So, how is it that an equation derived analytically for ductile solid metals with

spherical voids, by Carroll and Holt, is identical to empirical relations of Ballhausen and Heckel, used to describe the compaction of powders? What is more, the empirical relation has been applied to metallic powders, Heckel [2] (1981), pharmaceutical powders, Es-Saheb [5] (1984), polymer granules, Spencer et al [9] (1950), rock granules and sand, Athy [10] (1930) and ceramic powders, Van Der Zwan and Siskens [11] (1982). It is reasonable to suggest that the reason for this is that the dominant process in this compaction stage is essentially the same as that of pore collapse in solid ductile materials. This is why neither the Ballhausen nor the Heckel equation fits the early stage of the compaction process (ie at low pressures) and the late, very high pressure stage. These two stages are not akin to the pore collapse mechanism that is the hallmark of the broad, middle stage of the compaction process.

This chapter provides a detailed theoretical basis for the empirical relation presented by Ballhausen [8] (1951) to describe the middle stage of the compaction process, based on the Carroll and Holt's model [6] (1972). We also provide equations which describe the early and the late stages of the compaction process. The threshold criteria for transition from one stage to the next stage are discussed, and how the required parameters can be obtained experimentally.

Experimental evidence is provided to show that the method is applicable to powders of different constituents, from organic to metallic powders. Based on the evidence of various researchers in a variety of fields, as cited above, it is concluded that the

methodology should be applicable to all types of granular materials.

6.3 THE COMPACTION PROCESS

The compaction pressure, more than any other factor, largely controls the density of the final product. Therefore, a knowledge of the relationship between compaction pressure and the material properties of the power mass is very important. The physical processes that takes place during the compaction process have been thoroughly researched, and there is now a consensus on the basic processes amongst researchers in powder technology.

The compaction process have been classified into two broad stages [11-14] (1962-1972):

The first stage is the filling of holes of the same order of size as the original particles: This occurs primarily by particles sliding past one another.

The second state is the filling of voids which are substantially smaller in size, compared with the particles. This takes place by plastic flow and fragmentation.

Lukasiewicz [17] (1978), proposed a three stage process for the compaction process by making a distinction between porous and non-porous agglomerates. On this basis,

Van Der Zwan and Siskens [14](1982) proposed a four stage and further subdivided into a seven stage process.

It is not necessary to keep subdividing the stages. The comprehensive review of literature by Es-Saheb [5] (1984), shows that a three stage process command the widest consensus. Many of the further subdivision of these three stages are based on attempts to explain the deviation from the traditional empirical relations, especially at low and very high pressures.

The curves shown in figures 6.1 and 6.2 are typical of all the organic and metallic powders tested. These are plots of the Ballhausen equation and show four distinct stages. The initial stage, on this plot is concave downwards, the second stage being a straight line obeying the Ballhausen's equation, a third stage which is concave upwards and the fourth is a straight line. These stages were found in many different powders. We conclude that these stages are described by the processes explained by Es-Saheb [5] (1984).

Stage I: Transitional Restacking

Transitional restacking and particle rearrangement are processes closely associated with the early stage of the compacting process. The particles slide past one another to fill spaces that are of the same order of size as themselves. Therefore the important

characteristics of the particulates during this process are particle size, size distribution, particle shape, and surface properties. Some elastic deformation takes place during the later part of this stage.

Stage II: Elastic-plastic deformation:

Elastic-plastic deformation, fragmentation and inter-particulate bond formation are the mechanisms which dominate the stage two of the compaction process. Bocksteigel [13] (1965) has shown that the onset of stage two is indicated by the ceasing of particle flow and repacking. This he attributed to powder particles being locked in situ by internal bridge stresses and frictional effects at the inter-particulate contact points.

In stage two, compaction is due first to elastic deformation at inter-particulate contact points, which as the compaction pressure increases, is followed by plastic deformation. 'Ductile' powders will deform significantly during the plastic stage, whilst more 'brittle' powders are prone to fragmentation. During this plastic deformation and fragmentation, the contact areas between adjacent particles grow and interparticulate bonding can occur.

It is generally agreed that the strength of bond between two surfaces is determined by the area over which they are in intimate contact. Thus the deformation and failure properties of the particulates are important during this stage two. The extent to which

these mechanisms (elastic plastic deformations and fragmentation) occur and which dominates the process, depends on several factors. These include the physical properties of the particulates and the rate of compression. At high compression rates, the particulates are unable to deform at a sufficient rate to accommodate the induced strain, and fragmentation is more likely to predominate.

Stage III: Cold Working

Cold working and particle attrition are the main features of the third stage in the compaction process. Hirschhorn and Grey [14] (1969) have shown that at high compaction pressures, iron powders show increases in micro-hardness. This they attributed to the fact that individual particles of the powder mass experience significance cold working during compaction.

Stage IV: Elastic Compression

It is conceivable that when compaction pressure is very high, the process can go beyond stage three. Indeed this has been suggested in the past. In discussing the relation between relative volume and applied pressure for magnesium carbonate, Train [15] (1956) suggested a further mechanism, the elastic compression of the solid

compact at very high pressures. There have not been any level of interest in compaction at very high pressures, because the compact is very likely to 'cap' delaminate) during ejection from the die. However, since we are interested in characterising the whole range of compaction pressures, we include this stage (stage IV) and will suggest a governing equation for it.

The various mechanisms discussed above will occur to varying degrees during the compaction process, depending on the mechanical and physical properties of the particulates involved and the rate of compaction. Some of the mechanism may predominate while others may be all but absent.

6.4 POWER COMPACTION LIKE PORE COLLAPSE

Now back to the question raised earlier in the introduction, section 6.2. How is it that an equation derived analytically for ductile solid metals with spherical voids, by Carroll and Holt, is identical to the empirical relation, presented by Ballhausen and Heckels, to describe the compaction of powders and applied to metallic, organic and other types of powders?

We suggest that the reason is that stage II of the powder compaction process, described

above, is similar to the case of porous solids modelled by Carroll and Holt. Certainly the main process in the materials represented by carroll and Holt type model is plastic deformation in the material matrix around the voids. In the description of stage two of the compaction process, presented above, we see that plastic deformation in the particulate is a prominent feature of the process. Furthermore we know that during this stage, the size of the voids are much smaller than the size of the powder which are by now beginning to bond together forming a material matrix similar to the porous solids represented by the Carroll and Holt model.

Figure 6.3 presents a graphic representation of the Carroll and Holt model, showing random and uniform distribution of voids surrounded by solid matrix. Figure 6.4 shows a graphical representation of spherical particulate as will be found towards the end of stage one of the compaction process. If we home in on three neighbouring particles, we can readily see the Carroll and Holt scenario of a small void surrounded by solid matrix. The picture is even more convincing if we take into account the fact that the contact area between adjacent particles will increase at higher pressure, and inter-particulate bonding will occur, as explained earlier.

However, this is a theoretical model, and we are entitled to ask if it is true of the reality. In chapter eight, of this thesis, we showed that the Carroll and Holt model is successfully applicable to the phenomenon of spallation. Micrograph of specimens during the void growth stage of the spallation process shows that the model is

physically realistic, Curran et al [16] (1987). The spheres shown in Fig 6.4 represent a powder mass towards the end of stage I. Further compaction will lead to interactions between neighbouring particles as shown in Fig 6.5. The effect of the particle deformation further reduces the pore size, which becomes more spherical as depicted in Fig 6.6. We therefore have a material matrix with relatively small pores distributed within it. Let us examine some micrographs to see if there is a physical basis for such a scenario.

The micrographs in Fig 6.7 show spherical loose powder particles for a metallic powder (a) and agglomerates for an organic powder (b). In Fig 6.8, the micrograph shows a compacted metallic powder. This illustrates the point made above, that during the compaction process a powder mass essentially becomes a material matrix with distributed micro-voids. This fact is further illustrated by micrographs of titanium alloy powders under compaction.

Fig 6.9 (b) shows the loose spherical particles of the alloy and a bigger magnification in Fig 6.9 (a). Fig 6.10 shows a low pressure compaction of the alloy (a) and almost fully compacted (b). The scenario described above is even more credible if it can be shown that particle interaction leads to bonding. Interparticulate bonding, and distributed microvoids in a plastically deforming matrix resemble very closely the case of porous solids as discussed by Carroll and Holt. No surprise therefore, that the Carroll and Holt equation is the same as the traditional pressure-density relation used

in powder compaction.

As we have seen, a good case can be made for spherical or nearly spherical particulates resembling porous solid. What about, the powder whose particles are not spherical or which are not ductile. In chapter ten, we discussed the surprising finding of Curran et al [16] (1987). They discovered that the equation derived for spherical microvoid growth in ductile solid is more applicable to microcrack growth in brittle materials than equations based on the energy method of traditional fracture mechanics. Spallation models based on the assumption of spherical microvoid growth in ductile matrix have been applied to brittle spallation with very good results. Therefore no problem is expected in applying the model described above to powders having non-spherical and brittle particles. Indeed, the fact that the Bellhausen and Heckel equations have been applied to metallic powders, organic powders (eg pharmaceutical powders), ceramic powders, soil and rock particulates, and polymer particles, further illustrate the point about the wide applicability of the model.

As discussed earlier, the Heckel equation is applicable only to stage two of the compaction process, which happens to be the dominant stage , and covers most of the range of pressure for most powder compaction application. However, the derivation presented below will provide equations for all of the four stages of the compaction process, discussed earlier.

6.5 DERIVATION

Figure 6.12 shows a small spherical void, in a porous media, surrounded by solid material matrix formed by adjacent particles. Although a powder mass is regarded as compressible, the primary particles are solid incompressible material. Also, an agglomerate particle is made up of primary particles that are themselves incompressible so this formulation will not exclude powders made up of agglomerate.

The porous element, fig 6.12 described above, has a spherical void of radius a in a sphere of elastic-plastic material matrix of radius b. It is subjected to an external, time dependent, pressure p(t).

Although the pore will have a pressure, this is negligible as compared to the imposed external pressure. The inner boundary of the sphere is therefore assumed to be unloaded.

Consider the sliced element shown in the figure, at a radius r, thickness dr and subtend an angle of $\delta\theta$ at the spherical centre. Since we assume the solid region to be incompressible, conservation of volume dictates that;

$$4\pi r^2 dr = 4\pi r_o^2 dr_o \tag{6.8}$$

The initial position of the slice is at r_o and its initial thickness dr_o. Therefore,

$$r^2 dr = r_o^2 dr_o$$

Integrating

$$\frac{r^3}{3} + C_1 = \frac{r_o^3}{3} + C_2$$

or

$$r^3 = r_o^3 - 3\,(C_1 - C_2)$$

The constants C_1 and C_2 are time dependent and can be replaced by a single constant B(t). Therefore,

$$r^3 = r_o^3 - B(t) \tag{6.9}$$

Differentiate equation (6.9) w.r.t. time,

$$\dot{r} = \frac{-\dot{B}(t)}{3r^2} \tag{6.10}$$

and

$$\ddot{r} = \frac{-3\ddot{B}(t)\, r^2 + 6\dot{B}(t)\dot{r}r}{9r^4}$$

$$= -\frac{\ddot{B}(t)}{3r^2} + \frac{2\dot{B}(t)\dot{r}}{3r^5} \tag{6.11}$$

Now, we introduce ψ such that;

$$v = \frac{\partial \psi}{\partial r} \tag{6.12}$$

Integrate

$$\psi = v\, dr$$

substitute equation (6.11), we have;

$$\psi = \left(- \frac{\ddot{B}(t)}{3r^2} - \frac{2\dot{B}(t)\dot{r}}{3r^3} \right) dr$$

Substitute from equation (6.10)

$$\psi = \left(\frac{-\ddot{B}(t)}{3r^2} - \frac{2[\dot{B}(t)]^2}{9r^5} \right) dr$$

Integrate,

$$\psi\ (r,t) = \frac{\ddot{B}(t)}{3r} + \frac{[\dot{B}(t)]^2}{18r^4} \tag{6.13}$$

We now introduce distension α;

$$\alpha = \frac{V}{V_s} \tag{6.14}$$

where V is the total volume and V_s is the solid volume.

$$\therefore \quad \alpha = \frac{b^3}{b^3 - a^3} \tag{6.15}$$

Using equation (6.9) we can write;

$$b^3 = b_o^3 - B(t) \tag{6.16}$$

$$a^3 = a_o^3 - B(t) \tag{6.17}$$

We can also write;

$$\alpha_o = \frac{b_o^3}{b_o^3 - a_o^3} \tag{6.18}$$

It can easily be shown that;

$$B(t) = a_o^3 \, (\alpha_o - \alpha)/(\alpha_o - 1) \tag{6.19}$$

$$\frac{B(t)}{a^3} = \frac{\alpha_o - \alpha}{\alpha_o - 1} \tag{6.20}$$

$$\frac{B(t)}{b^3} = \frac{\alpha_o - \alpha}{\alpha} \tag{6.21}$$

We now consider the forces on the element as shown in figure 6.12. The equation of motion;

Net force = mass x acceleration

Therefore,

$$-\sigma_r r^2 (\delta\theta)^2 + \left(\sigma_r + \frac{\partial \sigma_r}{\partial r} \delta r\right) (\delta\theta)^2 - 4\sigma_\theta \frac{\delta\theta}{2} \delta r \delta\theta = \rho \ddot{r} r^2 (\delta r) (\delta\theta)^2$$

$$2\sigma_r r + \frac{\partial \sigma_r}{\partial r} r^2 - 2\sigma_\theta r = \rho \ddot{r} r^2$$

$$\frac{\partial \sigma_r}{\partial r} + 2 \frac{\sigma_r - \sigma_\theta}{r} = \rho \ddot{r} \tag{6.22}$$

using equation (6.12).

$$\rho \frac{\partial \psi}{\partial r} = \frac{\partial \sigma_r}{\partial r} + 2 \frac{\sigma_r - \sigma_\theta}{r}$$

We integrate w.r.t. r from a to b

$$\rho[\psi_a(t) - \psi_b(t)] = - p(t) + 2\int_a^b \frac{\sigma_r - \sigma_\theta}{r} dr \tag{6.23}$$

Using equation (6.13), (6.19), (6.20), and (6.21), it can be shown that;

$$\rho [\psi_a(t) - \psi_b(t)] = \tau^2 Q(\ddot{\alpha}, \dot{\alpha}, \alpha) \tag{6.24}$$

where,

$$\tau^2 = \frac{\rho a_o^2}{3(\alpha_o - 1)^{2/3}} \tag{6.25}$$

and,

$$Q(\ddot{\alpha},\dot{\alpha},\alpha) = -\ddot{\alpha}\,[(\alpha-1)^{1/3} - \alpha^{1/3}] + 1/6\,\dot{\alpha}^2\,[(\alpha-1)^{-4/3} - \alpha^{-4/3}] \quad (6.26)$$

Therefore, equation (6.23) can be written as;

$$\tau^2 Q\,(\ddot{\alpha},\dot{\alpha},\alpha) = p(t) - 2\int_a^b \frac{\sigma_r-\sigma_\theta}{r}\,dr \quad (6.27)$$

Now, equation (6.9) can be rewritten as;

$$r^3-r_o^3 = -B(t)$$

For infinitesimal principal displacement, $r \approx r_o$.

Therefore,

$$3r^2(r-r_o) = -B(t)$$

or

$$u = \frac{-B(t)}{3r^2} \quad (6.28)$$

where $u=(r - r_o)$ the displacement.

Therefore, the principal strains are;

$$\epsilon_r = \frac{\partial u}{\partial r} = \frac{2B(t)}{3r^3} \tag{6.29}$$

$$\epsilon_\theta = \epsilon_\phi = \frac{u}{r} = \frac{-B(t)}{3r^3} \tag{6.30}$$

The principal stresses are;

$$\sigma_r = -p + S_r \tag{6.31}$$

$$\sigma_\theta = -p + S_\theta \tag{6.32}$$

$$\sigma_\phi = -p + S_\phi \tag{6.33}$$

where S is the deviatoric stress, $(\sigma_r - \sigma_\theta)$.

Therefore,

$$S_r = 2G\epsilon_r = \frac{4GB(t)}{3r^3} \tag{6.34}$$

$$S_\theta = S_\phi = 2G\,\epsilon_\theta = -\frac{2\,G\,B(t)}{3r^3} \tag{6.35}$$

using equations (6.31) to (6.35) we can write;

$$\frac{\sigma_r - \sigma_\theta}{r} = \frac{2GB(t)}{r^4} \tag{6.36}$$

Ignoring the inertia term in equation (6.27);

$$p(t) = 2\int_a^b \frac{\sigma_r - \sigma_\theta}{r}\,dr$$

substitute (6.36)

$$p(t) = 4\int_a^b \frac{GB(t)}{r^4}\,dr$$

$$= \left[\frac{4GB(t)}{3r^3}\right]_a^b$$

$$= \frac{4GB(t)}{3}\left(\frac{1}{b^3} - \frac{1}{a^3}\right)$$

Using equation (6.19), (6.20) and (6.21), we have;

$$p(t) = \frac{4G(\alpha_o - \alpha)}{3\alpha(\alpha - 1)}$$

$$p(t) = K_1 \frac{(\alpha_o - \alpha)}{\alpha(\alpha - 1)} \qquad (6.37)$$

If we consider plastic deformation as described for stage two of the compaction process;

$$\frac{\sigma_r - \sigma_\theta}{r} = \frac{\sigma_o}{r} \qquad (6.38)$$

where σ_o is the yield stress.

Ignoring the inertia term in equation (6.27);

$$p(t) = 2 \int_a^b \frac{\sigma_r - \sigma_\theta}{r} \, dr$$

Substitute (6.38);

$$p(t) = 2 \int_a^b \frac{\sigma_o}{r} \, dR$$
$$= 2 \, \sigma_o \ln \left(\frac{b}{a} \right)$$

using equations (6.19), (6.20) and (6.21) we can rewrite this as;

$$p(t) = \frac{2}{3} \, \sigma_o \ln \left(\frac{\alpha}{\alpha - 1} \right)$$

or

$$p(t) = K_2 \ln \left(\frac{\alpha}{\alpha - 1} \right) \qquad (6.39)$$

We can rewrite equation (6.23) as;

$$p(t) - P_g = - \rho \, [\psi_a(t) - \psi_b(t)]$$

where Pg is the threshold pressure given by,

$$p_g = 2 \int_a^b \frac{\sigma_r - \sigma_\theta}{r} \, dr$$

Using equations (6.24) to (6.26);

$$P(t) - Pg = \tau^2 Q \, (\ddot{\alpha}, \dot{\alpha}, \alpha)$$

or

$$p(t)-p_g = K_3\,[\ddot{\alpha}[(\alpha-1)^{-1/3} - \alpha^{-1/3}] + \frac{1}{6}\dot{\alpha}^2\,[(\alpha-1)^{-4/3} - \alpha^{-4/3}]] \qquad (6.40)$$

If we assume constant compaction rate, then $\dot{\alpha}$ = constant and $\ddot{\alpha} = 0$. therefore,

$$p(t) - p_g = K_3\left[\frac{1}{6}\,\dot{\alpha}^2\,(\alpha-1)^{-4/3} - \alpha^{-4/3}\right] \qquad (6.41)$$

STAGE I:

As discussed in section 6.3, stage one of the compaction process is dominated by inter-particle friction during rearrangement and some elastic deformation of the particles. We expect equation 6.37 to characterise this stage of the compaction process. We mentioned in section 6.3 that the most important variable at this stage included particle size, size distribution and particle shape. Obviously α_o and to some extent α in equation (6.37) are a function of these variables. The other important variable mentioned, in that section, was surface properties, such as friction. We suggest that K_1 in equation 6.1 can be linked to the limiting shear stress. The concept of limiting shear stress, angle of internal friction, angle of repose etc., used to quantify the surface properties of powder particles was discussed in detail by Es-Saheb [5] (1984). K_1 may be a function of α for some materials. This is not unexpected since different particle shapes and sizes will interact differently. For powders whose particles are agglomerates, the dependence of K_1 on α is an obvious one. For the powers we tested, we found that K_1 is either constant or has a direct, or indirect proportional relation with

α. Thus

$$K_1 = C,$$
$$K_1 \propto \alpha,$$
$$K_1 \propto 1/\alpha$$

K_1 can be obtained from the experimental data of uniaxial die compaction. First plot P against $\ln(\alpha/\alpha\text{-}1)$ as in figure 6.1. The data relevant to stage I is the lower non-linear region of this plot. By fitting equation (6.37) to this data, the value of K_1 can be obtained

Note that K_1 can have a direct or inverse proportional relation with α. So, equation (6.37) can be;

$$p(t) = K_1 \frac{\alpha_o - \alpha}{\alpha(\alpha - 1)} \qquad (6.37)$$

or

$$p(t) = A\ (\alpha_o - \alpha)/(\alpha - 1) \qquad (6.42)$$

or

$$p(t) = B\alpha\ (\alpha_o - \alpha)/(\alpha - 1) \qquad (6.43)$$

In the tests we carried out, we found that the stage of behaviour of di-pac sugar is described by equation (6.37), that of steel and copper powders is characterised by equation (6.42), and aluminium powder is described by equation (6.43).

The value of distention, $\alpha_{1,2}$ at the transition between stages I and II was used to identify the transition pressure (threshold pressure between stages I and II), p_c

$$p_c = \frac{2\sigma_o}{3\alpha_{1,2}}$$

STAGE II:

In section 6.3, we explained that plastic deformation and fragmentation are the dominant processes. This will suggest that yield stress and fracture stress are the important properties of the particle powders during this stage. Accordingly we expect equation (6.39) to describe stage II of the compaction process.

This is the most important stage in the compaction process, especially at moderate pressures and low loading rates. Under these conditions, it accounts for over 70% of the compaction process. This is why the Ballhausen, and Heckel equations, referred to above, have been reasonably successful. The equation we obtain for this stage is identical to that of Ballhausen, obtained empirically.

K_2, as we have seen, can be linked to yield stress, and it is a constant. The value of K_2 can be obtained by plotting p against $\ln(\alpha/(\alpha-1))$ from the results of uniaxial die compaction. The plot is a straight line whose slope is K_2.

The threshold pressure between stages II and III, Pg is given by

$$p_g = p_c + K_2 \ln\left(\frac{\alpha_{2,3}}{\alpha_{2,3}-1}\right)$$

STAGE III:

In section 6.3, stage three of the compaction process is said to be dominated by cold working and attrition. This is a rate dependent process and accordingly, we expect equation (6.41) to characterise this stage if compaction is at constant loading rates, and by equation (6.40) if the loading rate is not constant.

Es-Saheb [5] (1984), carried out several die compactions at different strain rates, for several materials. He represented the result by Heckel's equation plotted on the same graph for he various strain rates, and also made plots of pressure against degree of compaction. An example is shown in fig 6.13. Interestingly, the early stages, stages I and II, showed the same result for all the strain rates, and only diverge during stage III, which is the rate dependent stage.

The value of K_3 can be obtained in a similar manner as described for K_1.

STAGE IV

If a porous mass is compressed to very high pressures, the plot of pressure against

density, porosity or distention shows that the very high pressure part of the curve is linear. This has been noticed for metallic and organic type powders, indicating that a fourth stage proposed by Train [15] (1956) does exist. We suggest that this linear region is described by;

$$p(t) = K_4\alpha$$

K_4 can be linked to the bulk modulus of the powder particulates. The transition between stages III and IV is defined by a value of critical porosity appropriate for the material. Typical value of critical porosity, ϕ_c used in modelling dynamic microfracture phenomena is 0.03.

6.6 EXPERIMENTATION

In order to illustrate the applicability of the equations presented above, for the different stages of the compaction process, we carried out uniaxial die compaction of several powders. The die and punch set were designed so that double action compression takes place. The picture in fig 6.14 shows the die and punch set. Friction was avoided by lubricating the die and the top surface of the plungers with stearic acid solution in chloroform.

The compaction was at constant loading rate, and time, pressure and change in height of the powder mass were continuously recorded. All initial values, such as mass and initial height were recorded.

The graphs in figures 6.15 (a) to (d) show typical results compared with the theoretical model for each stage.

6.7 CONCLUSIONS

Four stages for the compaction process have been identified and described. Different equations to describe each stage of the process, and methods to experimentally obtain the constants were suggested. The transition points between the various stages were identified.

Stage I: Initial Stage

$$p(t) = K_1 \frac{(\alpha_o - \alpha)}{\alpha(\alpha - 1)}$$

K_1 may be constant or a simple function of α. It may be related to the limiting shear stress.

The transition pressure to stage II is:

$$p_c = \frac{2\sigma_o}{3\alpha_{1,2}}$$

Stage II: Elastic-Plastic Stage.

$$p(t) - p_c = K_2 \ln\left(\frac{\alpha}{\alpha - 1}\right)$$

K_2 is a constant and is related to the yield stress. The transition between this stage and stage III is given by:

$$p_g = p_c + K_2 \ln\left(\frac{\alpha_{2,3}}{\alpha_{2,3} - 1}\right)$$

Stage III: Rate dependent cold working

$$P(t) - Pg = F(\ddot{\alpha}, \dot{\alpha}, \alpha)$$

The transition to stage IV is marked by a critical porosity ϕ_c, appropriate for the material Typical value of ϕ_c is about 0.03.

Stage IV: Solid Stage

$$P(t) = K_4 \alpha$$

K_4 can be related to bulk modulus.

We carried out experimental tests, for several powder types, to illustrate the applicability of the above equations. We obtained very good agreement between the results and the equations.

6.8 REFERENCES

(1) K. Kawakita and K. Ludde, Powder Technol., 4 (1970/71) 61

(2) R.W. Heckel, Trans. of the Metallurgical Society of AIME, 221, (1961), 671

(3) R.W. Heckel, Trans. of the Metallurgical Society of AIME, 221, (1961), 1001

(4) K. Konopicky, "Parallelitat der Gesetzma Big Keiten in Keramik und Pulvermetallurgie". Radex-Rundsehan, 3, (1948) Heft 7/8, 141

(5) M. H. H. Es-Saheb, PhD Thesis, UMIST, 1984

(6) M. M. Carroll and A. C. Holt, J. Appl. Phys. 42 (1972) 759

(7) M. M. Carroll and A. C. Holt, J. Appl. Phys. 43 (1972) 1626

(8) C. Ballhausen: Arch. Eisenhuttenw., 22, (1951), 185

(9) R. S. Spencer, G.D. Gilmore, and R.M. Wiley, J. Appl. Phys. 21, (1950), 527

(10) L.F. Athy, Bull. Am. Assoc. Petrol. Geologists, 14;(1930), 1.

(11) J. Van Der Zwan and C.A.M. Siskens, Powder Technology, 33 (1982) 43

(13) G. Bocksteigel, "Modern Development in Powder Metallurgy", ed. H.H. Housner, Pub. Plenum Press. New York, 1, (1966), 15.

(14) J.S. Hirschhorn and M.W. Grey, Int. J. Powder Met., 5 (1), (1969), 35.

(15) D. Train, J. Pharm. Pharmac., 8, (1956), 745

(16) D.R. Curran, L. Seaman and D.A. Shockey, Physics Reports, 147 (1987) 253.

(12) P J James, Powder Metall. Int., 4(2), (1972), 82.

(17) S J Lukasiewicz and J S Reed, Am. Ceram. Soc. Bull., 57(9), (1978), 789

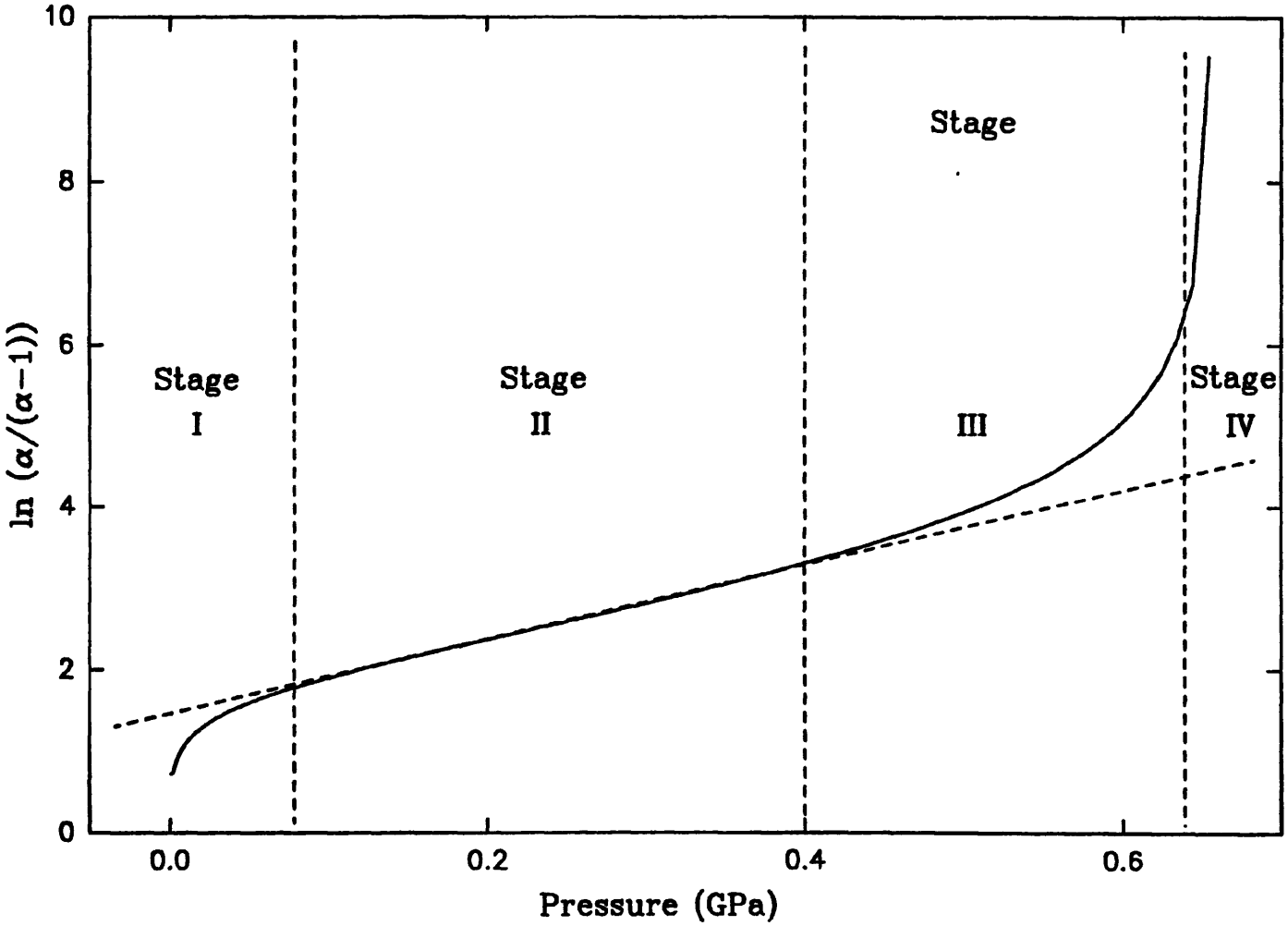

Fig. 6.1 Plot Showing Four Stages of Compaction For Di-pac Sugar

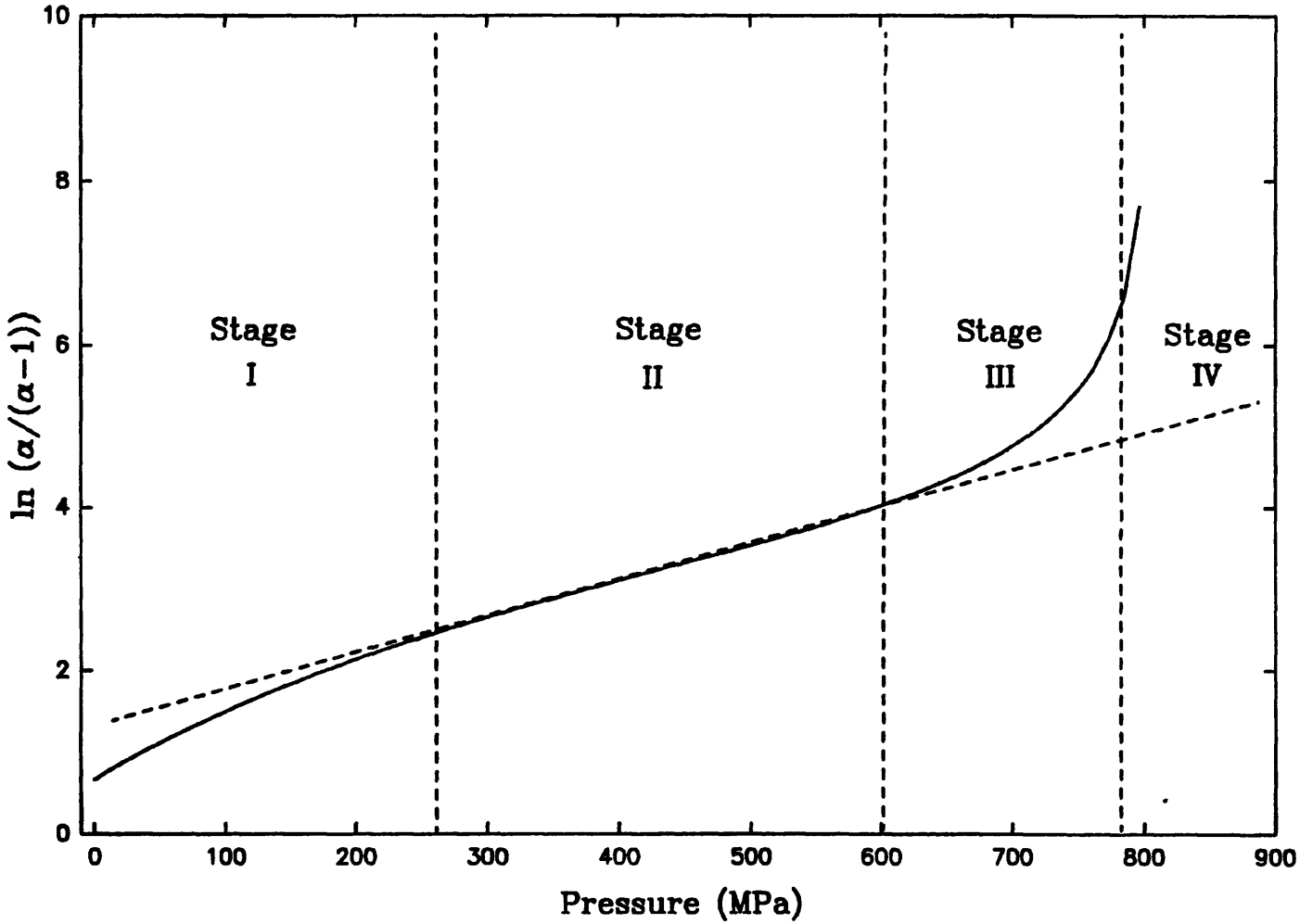

Fig. 6.2 Plot Showing Four Stages of Compaction for Aluminium Powder

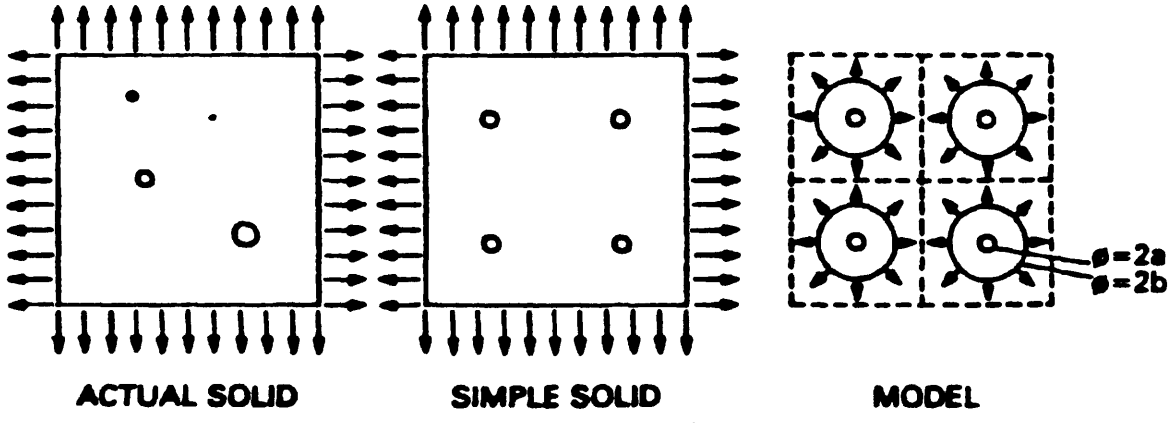

Fig 6.3 Graphical Representation of the Simplification of the Porous State.

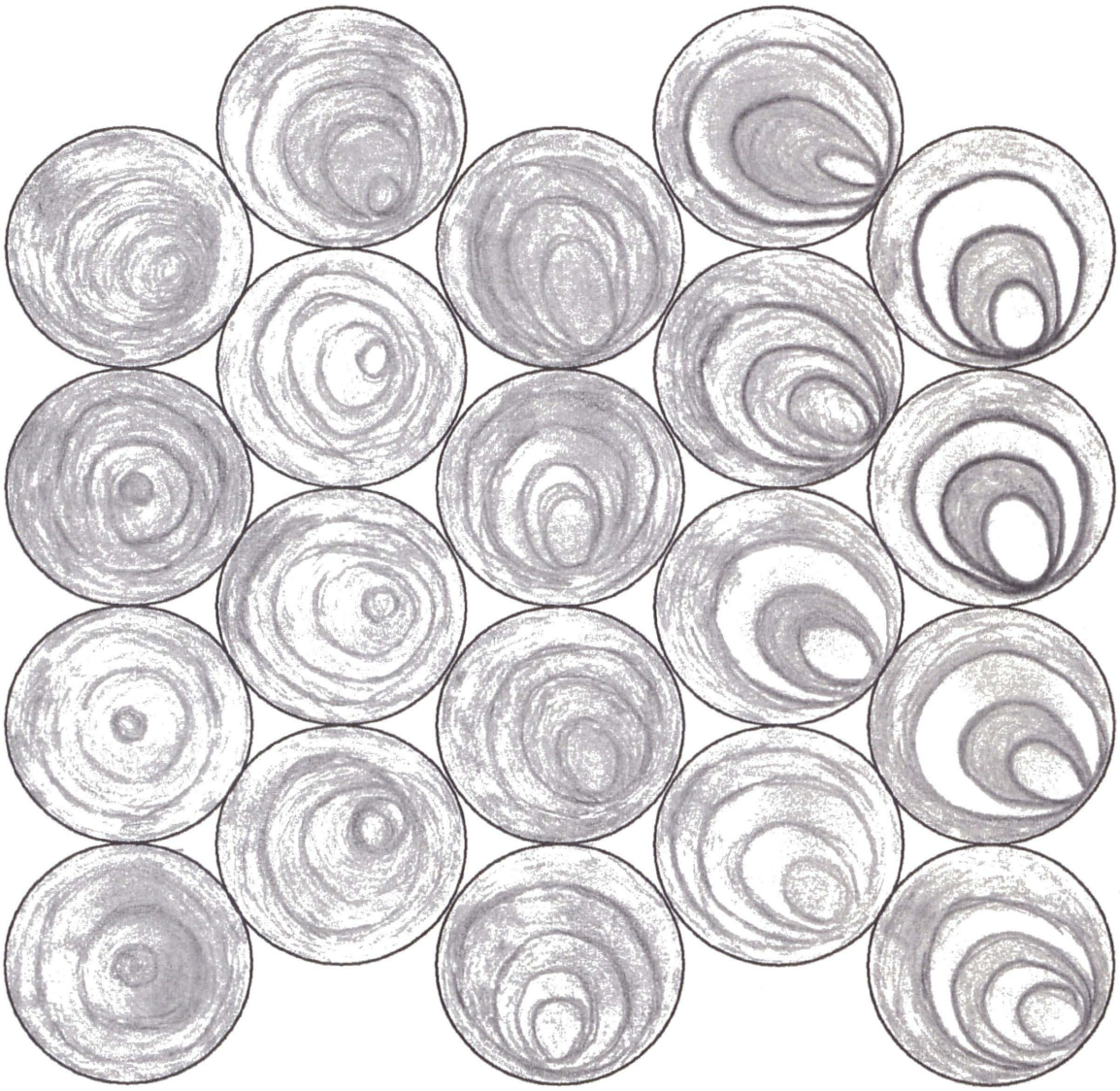

Fig 6.4 Schematic Representation of Spherical Particles.

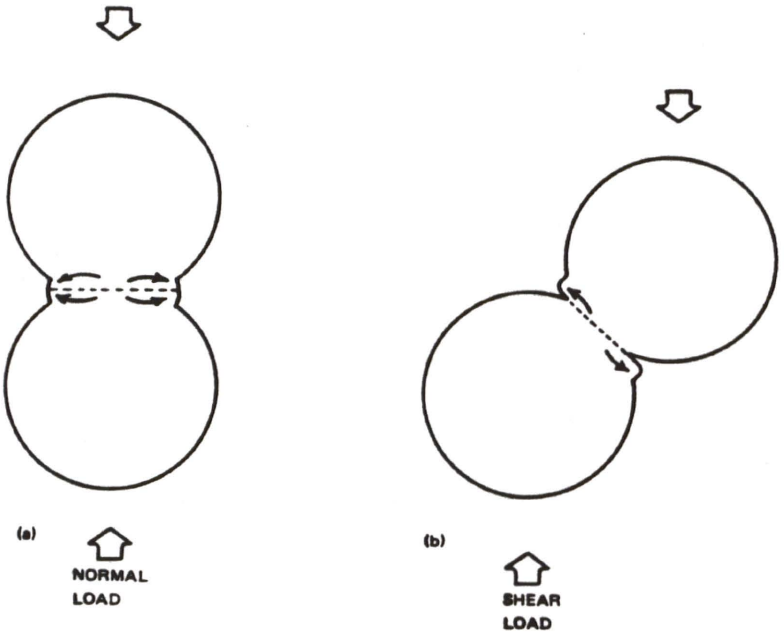

Fig 6.5 Schematic Representation of Relative Particle Interactions.

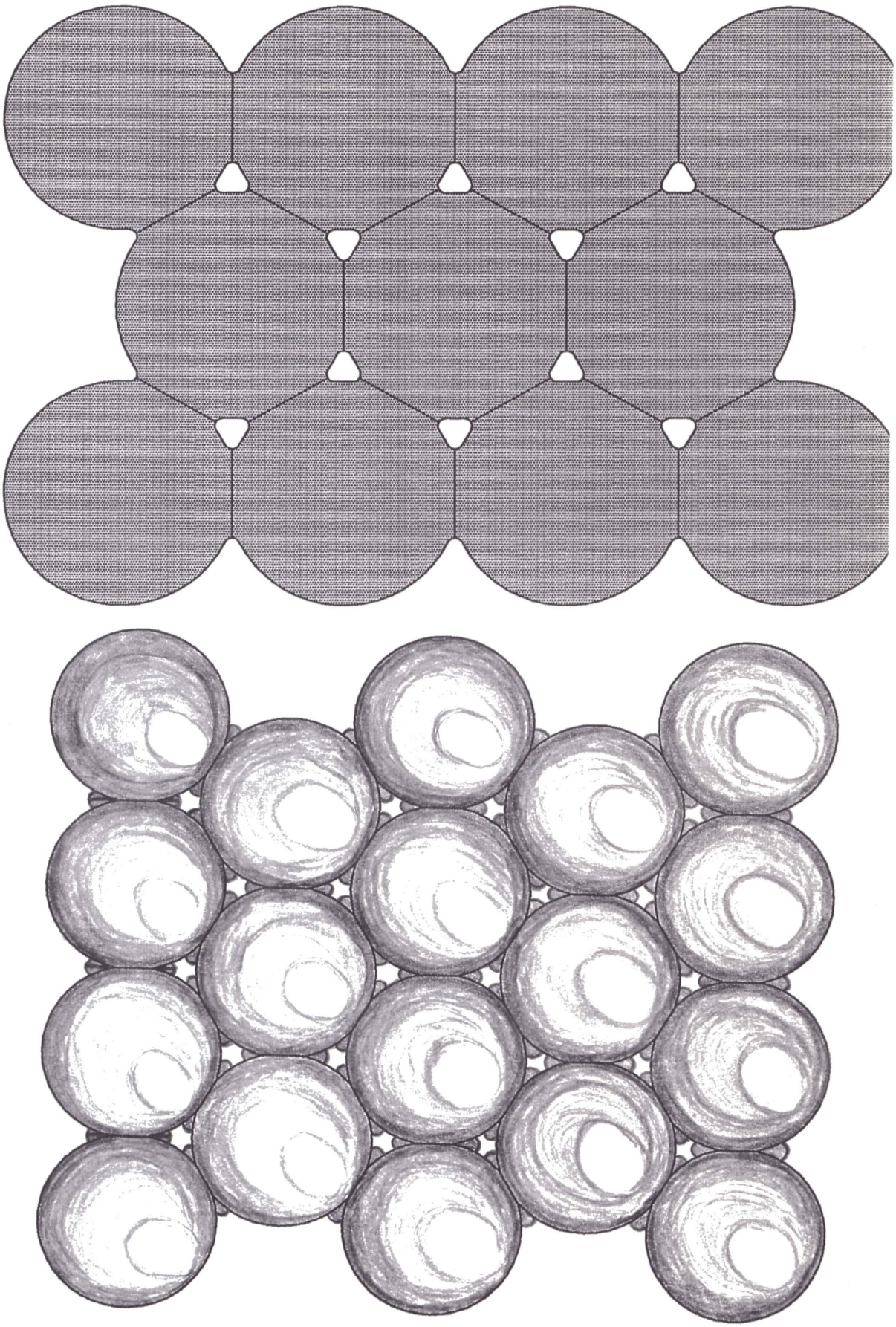

Fig 6.6 Schematic Representations of Particle Deformation.

Agglomerates of Di-Pac Sugar

Spheroid Particles of Copper

Fig 6.7 Micrographs of Loose Powder Particles

Fig 6.8 'As Compacted' Structure of Spherical Copper Powder (-140 + 200 mesh)

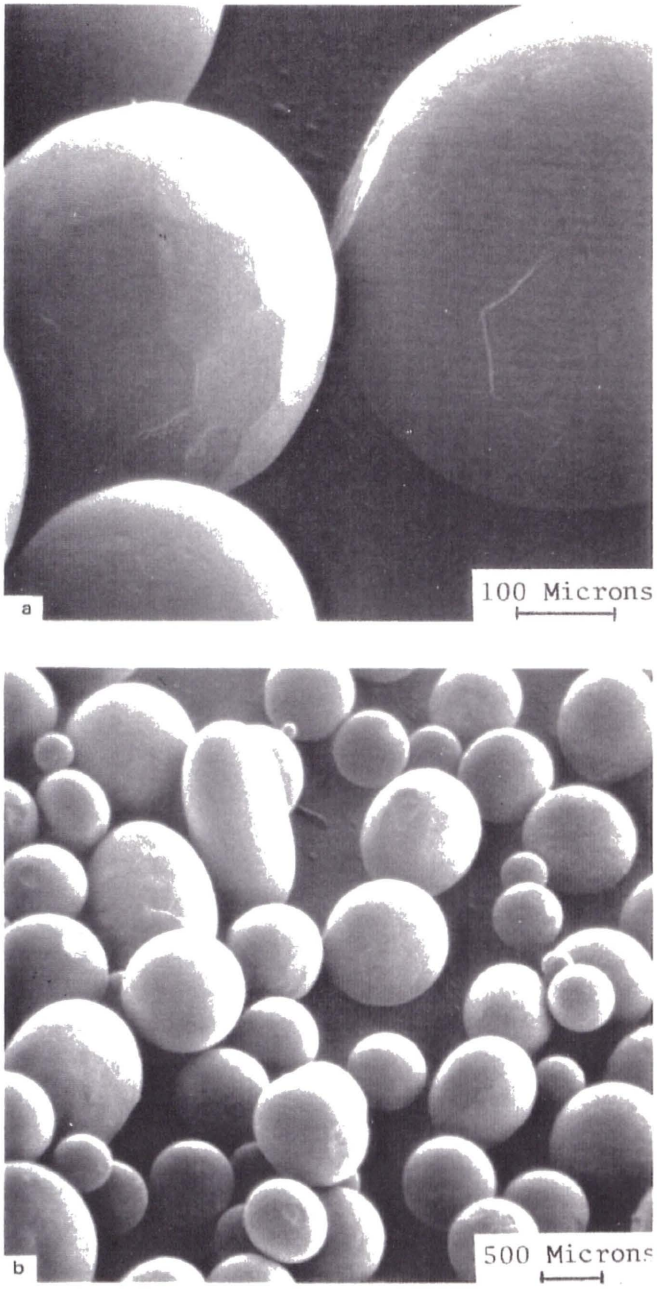

Fig 6.9 Photo-Micrographs of Loose Titanium Alloy Powder.

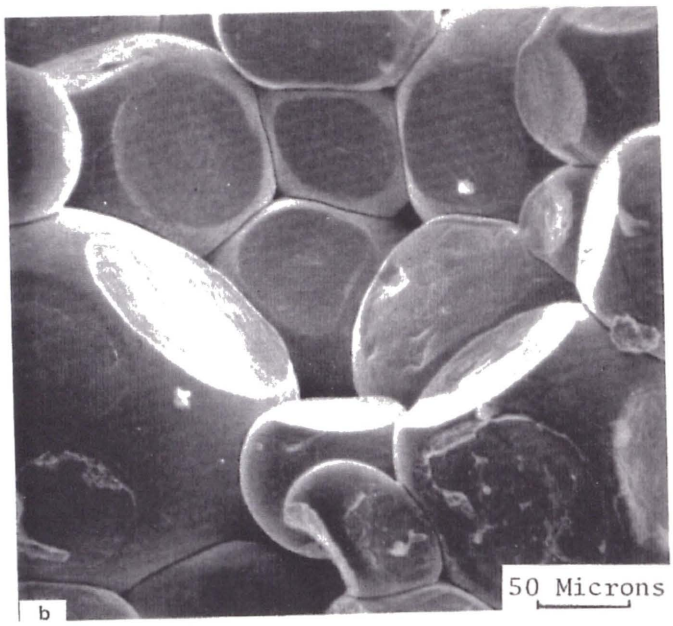

Fig 6.10 (a) Photo-Micrograph of Titanium Alloy Powder Compacted at Low Pressure.

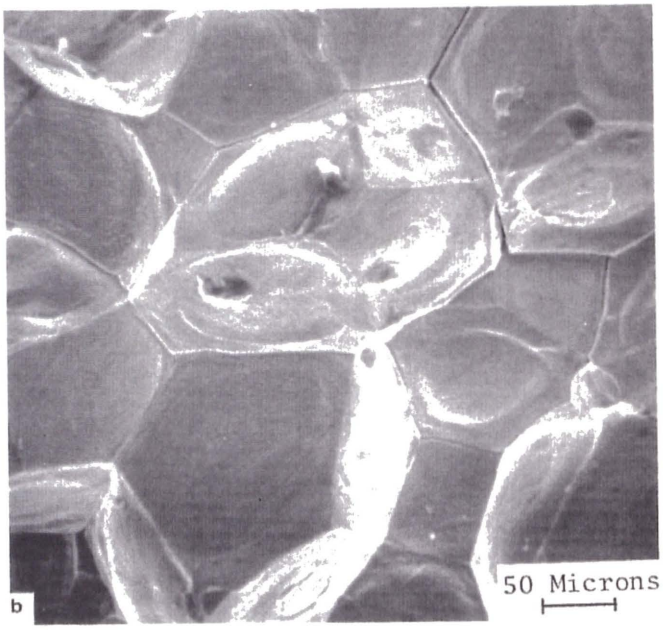

Fig 6.10 (b) Photo-Micrograph of Titanium Alloy Powder Compacted to Near Full Density.

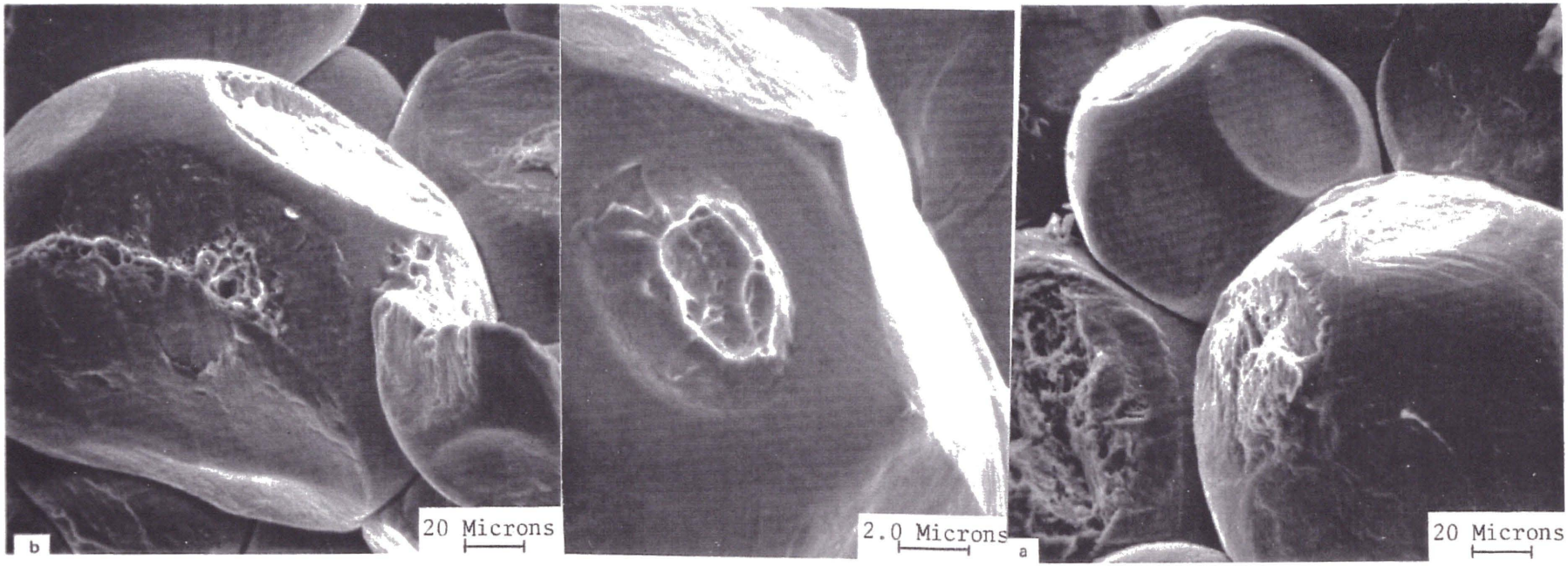

Fig 6.11 Photo-Micrographs Showing Evidence of Inter-Particle Bonding.

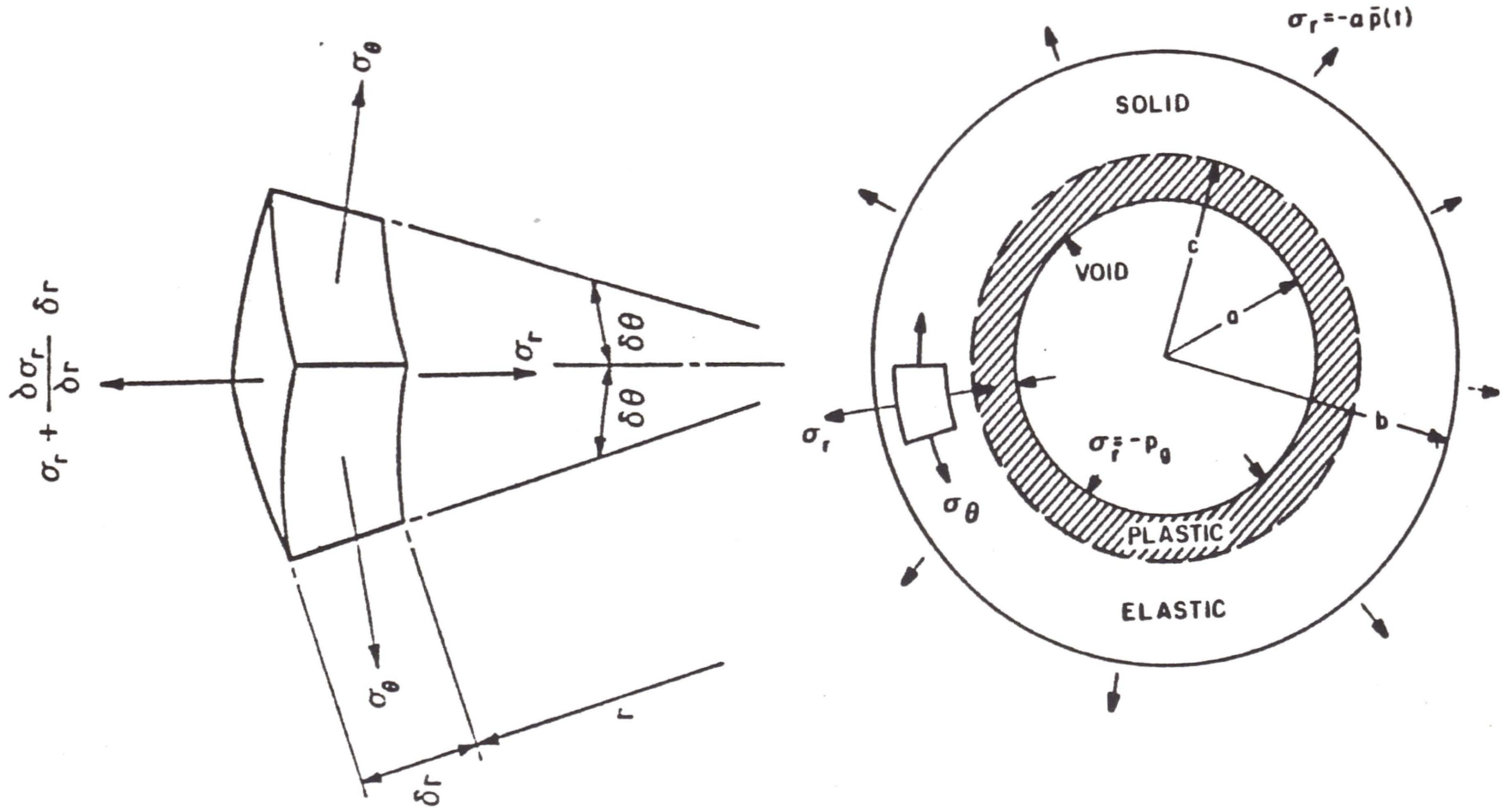

Fig 6.12 The Porous Element.

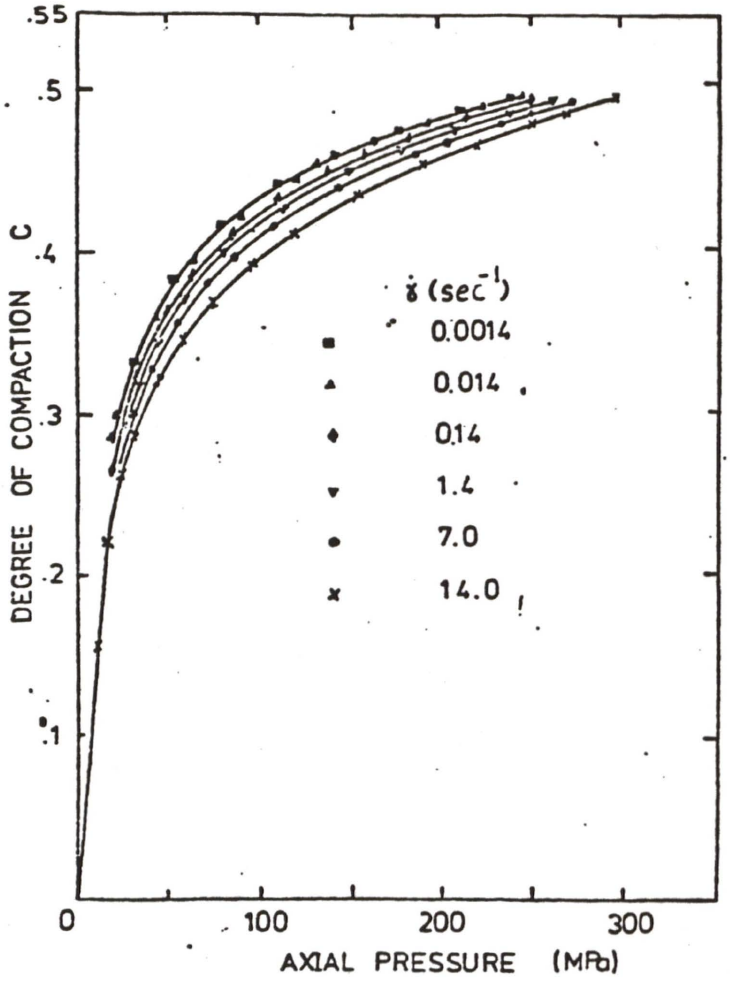

Fig 6.13 Constant Compression Rate Curves for Di-Pac Sugar.

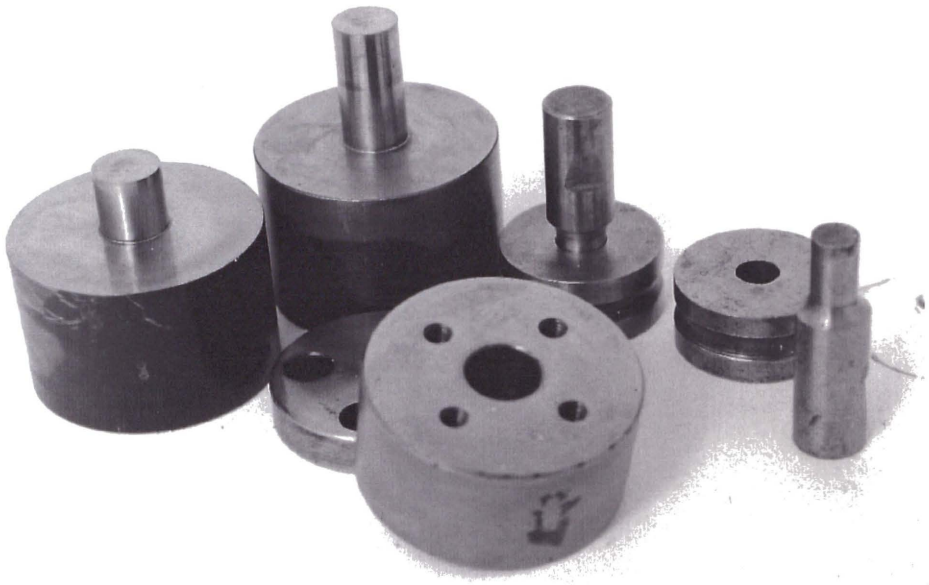

Fig 6.14 Die and Punch Set.

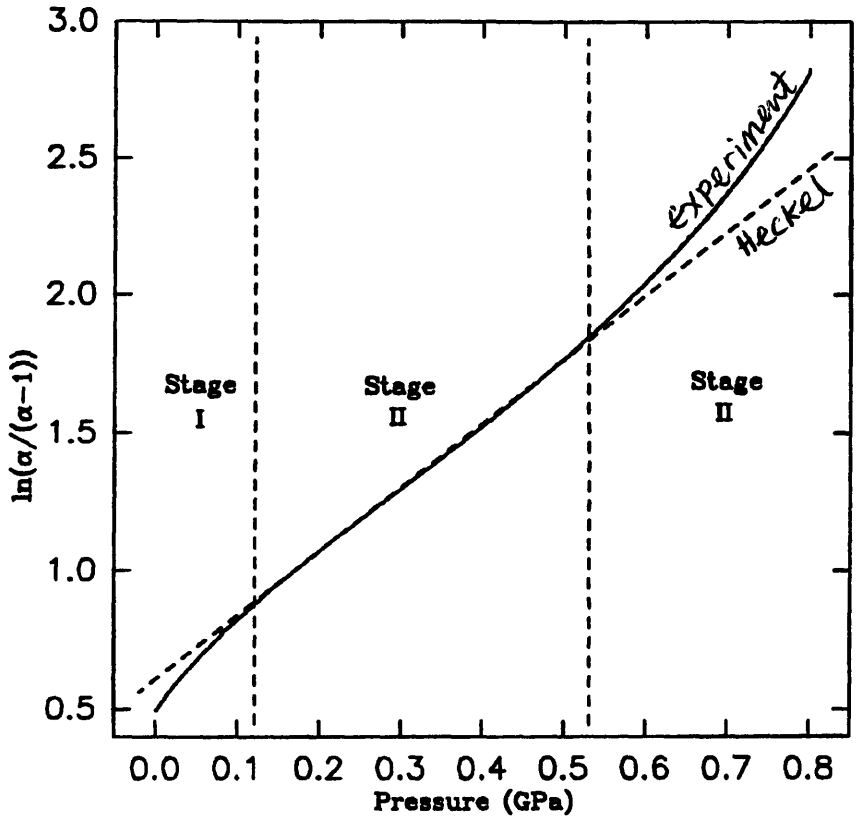

Fig. 6.15(a) Compaction Stages for Steel Powder

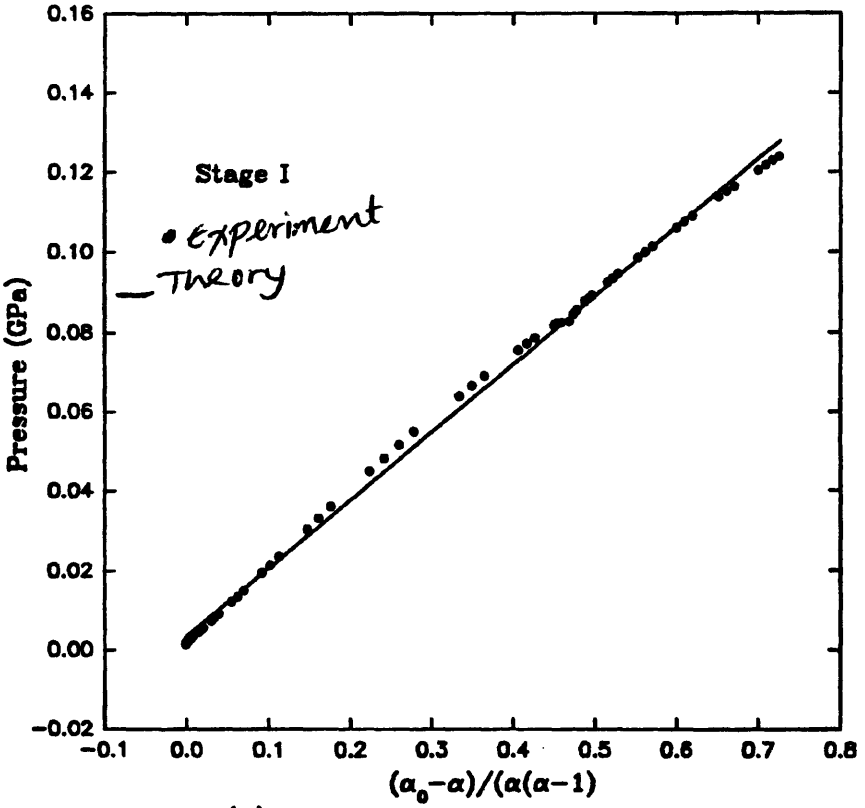

Fig. 6.15(b) Comparing Experimental data with Model for Stage I

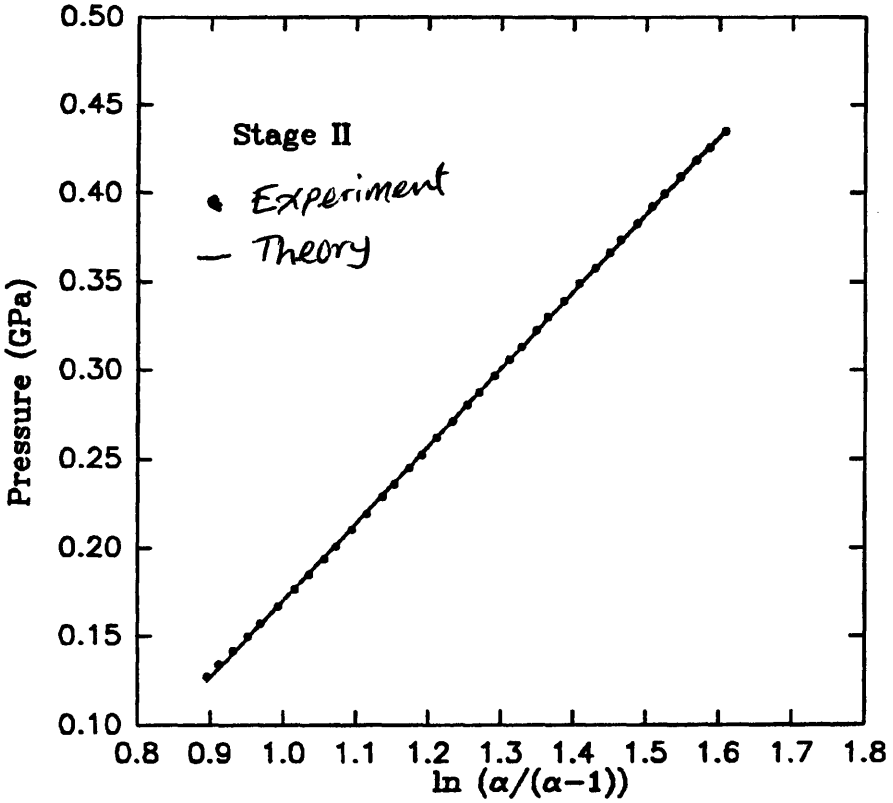

Fig. 6.15(c) Comparing Experimental Data with Model fir Stage II For stainless steel powder

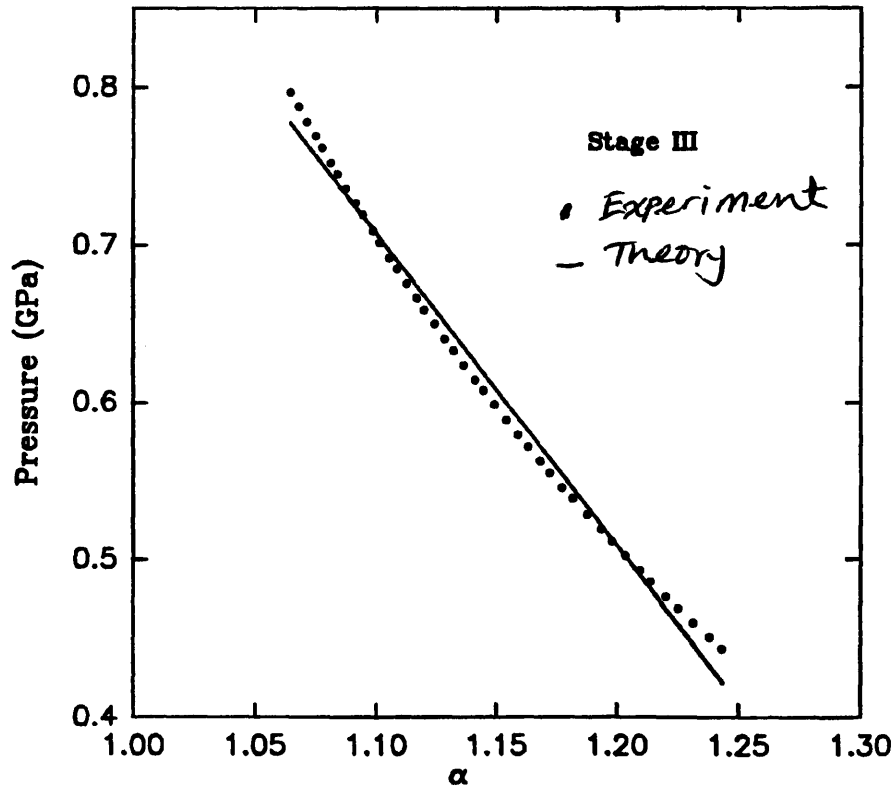

Fig. 6.15(d) Comparing Experimental Data with Model for Stage III

CHAPTER SEVEN

GENERAL DISCUSSIONS AND CONCLUSIONS

DYNAMIC COMPACTION OF POWDERS

It can be argued that a powder mass undergoing compaction is a substance which continuously changes its properties as the compaction process progresses. The analogy is that of a chemical substance undergoing chemical reaction. The product(s) bears no resemblance, in chemical terms, to the original substance. So is a powder mass undergoing compaction, the compact bears no resemblance to the original loose powder in terms of mechanical properties. For a substance which continuously changes into a different substance, in mechanical terms, we should not expect a simple linear relation to characterise its mechanical behaviour, nor adequately describe the process it has gone through.

As explained in Chapter Six, several physical processes have been identified as being responsible for the various stages of the compaction process, from the re-arrangement of the loose powder particles to plastic deformation, fragmentation and bonding during cold working at high pressures. A reason why we should not expect a simple linear relation to describe the compaction process fully. No surprises therefore that the most widely used equations, including those of Heckles and Kawakita are not wholly successful in describing the complete compaction process. However, as pointed out earlier, they have been very useful in providing a means of characterising the behaviour of powders undergoing compaction, albeit partially, mainly because one of the processes in the compaction process predominates in the range of compaction pressure most relevant to various industrial compaction operations.

It is logical, therefore, that any proposed model should recognise the changing mechanical properties of the powder undergoing compaction, and the different physical processes that constitute various stages of the compaction process. Two models have been proposed in this thesis, and each in their own way meet this requirement.

The staircase method relies on the triaxial test result to provide complete information about the changing mechanical behaviour of the powder mass undergoing compaction. It is expected that once the triaxial test data, described in Chapter Three, has been obtained, the numerical method, described in Chapter Four, can be used to simulate the desired compaction process.

On the other hand, the analytical method presented in Chapter Six, provides an equation to describe the different stages of the compaction process. All the parameters and constants required can easily be obtained, experimentally, for the particular granular substance of interest.

It is often necessary to determine the strength of a powder compact. The stress-wave technique of the Hopkinson Pressure Bar, presented in Chapter Five, provides a simple means of determining the mechanical quality of a powder compact.

CONCLUSIONS

The conclusions reached at the end of the Chapters are summarised here.

Chapter Two: High Pressure Triaxial Cell

A new high pressure split triaxial test system is designed and constructed. Tests carried out with it show that it is operating satisfactorily.

An important feature of the system is the flexibility built into it to accommodate

transducers within the cell. This proved to be very successful.

Preliminary tests carried out show that the system is reliable and the experiments are repeatable.

Chapter Three: The Staircase Method

In this chapter, the theoretical basis for the staircase method is presented. It shows that non-linearly varying hypoelastic properties can be obtained or a given powder mass using the split cell triaxial system.

Experimental results obtained for Avicel are presented.

Chapter Four: Numerical Simulation

Three different attempts to simulate the compaction process, using the experimental results from triaxial tests, were presented. Although these were successful to different extent, they demonstrated that such an approach is feasible.

Results obtained for the simulation of die compaction of di-pac sugar showed a very good agreement.

Chapter Five: Stress-wave Technique

An objective of this work was to devise a simple but cost effective and acceptable method of measuring the elastic tension and compression moduli for powder compacts and their tensile fracture strength. Specimen tablets have proved easy to make, handle and install in the stress wave bar system. This technique requires further refinement

by controlling the input pulse, positioning the strain gauges and alignment of the bars and bonding the tablet to the bars.

Chapter Six: Analytical Model

Four stages for the compaction process have been identified and described. Different equations to describe each stage of the process, and methods to experimentally obtain the constants were suggested. The transition points between the various stages were identified.

Stage I: Initial Stage

$$p(t) = K_1 \frac{(\alpha_o - \alpha)}{\alpha(\alpha - 1)}$$

K_1 may be constant or a simple function of α. It may be related to the limiting shear stress.

The transition pressure to stage II is:

$$p_c = \frac{2\sigma_o}{3\alpha_{1,2}}$$

Stage II: Elastic-Plastic Stage.

$$p(t) - p_c = K_2 \ln\left(\frac{\alpha}{\alpha - 1}\right)$$

K_2 is a constant and is related to the yield stress. The transition between this stage and stage III is given by:

$$p_g = p_c + K_2 \ln\left(\frac{\alpha_{2,3}}{\alpha_{2,3}-1}\right)$$

Stage III: Rate dependent cold working

$$P(t) - Pg = F(\ddot{\alpha},\dot{\alpha},\alpha)$$

The transition to stage IV is marked by a critical porosity ϕ_c, appropriate for the material Typical value of ϕ_c is about 0.03.

Stage IV: Solid Stage

$$P(t) = K_4\alpha$$

K_4 can be related to bulk modulus.

We carried out experimental tests, for several powder types, to illustrate the applicability of the above equations. We obtained very good agreement between the results and the equations.

PART TWO

SPALL FRACTURE IN SOLIDS

CHAPTER EIGHT

SPALL FRACTURE IN SOLIDS

8.1 SUMMARY

Engineering, particularly Mechanical Engineering, is a problem solving occupation. A clear definition of the problem one is attempting to solve is therefore essential. This section begins with a brief statement of the problem and a short introduction before considering the general background of the subject.

The physical mechanisms of the spallation phenomenon is considered in general terms, particularly the microfracture processes: namely the nucleation of micro-flaws, the growth of the flaws and their eventual coalescence, which completes the failure process.

The proposed solutions include the presentation of microscopic and macroscopic models for ductile and brittle spallations. A simple unified model applicable to both ductile and brittle spallations is also presented. The applicability of these models to everyday practical engineering materials is illustrated with the simulations of examples of one dimensional plane plate impact tests.

Two dimensional plane plate impact and explosive impact on plates are considered as further examples of the application of the models presented. An overall discussion of the methodologies presented is followed by a brief conclusion.

8.2 A STATEMENT OF THE PROBLEM

The term spallation refers to a special case of dynamic fracture. In this phenomenon, fracture takes place by planar separation of material subjected to dynamic stresswave. The process can be a brittle one in which microcracks are nucleated and propagated dynamically with plastic deformation confined to the small region around the crack tips. These eventually coalesce to form the spall plane. On the other hand ductile spallation is dominated by the nucleation of microvoids which grow elasto-plastically and finally coalesce to form the spall plane. In both cases the process involves nucleation of microfractures, their growth and coalescence. It is also understood that a threshold pressure is required to initiate the spallation process.

The problem, therefore, is how to predict reliably the threshold pressure that will initiate the spallation fracture in a given material and the extent to which spallation will occur as a result of a given stress history.

To a considerable extent this problem has been solved in many different ways. But the methodologies used thus far are essentially complicated and require the evaluation

of many parameters. This is not a trivial task for the vast majority of engineering materials. We therefore pose a new problem of whether it is possible to establish a simple methodology that can easily be applied to practical engineering materials. The heart of the matter, therefore, is the development of simple models to describe the average continuum behaviour of the spall processes. Namely, brittle and ductile spallations.

But what constitutes an adequate description or prediction of the extent of spallation in a material by a given stress history? After all, there is an infinite number of stress histories that can conceivably be imposed on a given material. Any solution to the problem posed must answer two key questions. Is a given stress history enough to cause spallation in a given material? If so, what will be the extent of the spallation fracture?

The former requires a careful but concise and simple definition of the threshold pressure, spall strength, consistent with the proposed model, as well as a means of estimating and verifying its value experimentally or otherwise. The latter, on the other hand, requires an agreeable and understandable measure of the extent of spallation fracture.

Fortunately, there is already a consensus on the measure of spallation fracture in this field of study. The free surface velocity of the target in a plane plate impact test,

sometimes referred to as pull-back velocity or the spall signal, is widely accepted as a good measure for spallation. Therefore, any proposed models should be capable of predicting the spall signal reasonably accurately.

8.3 INTRODUCTION

In general, all fracture is essentially dynamic by nature. It is a rate dependent process in which material bonds are broken and voids created in previously intact solid material. It is, therefore, imperative to understand both the threshold conditions that trigger the process and the governing kinetics by which the fracture proceeds.

In the main there are two major types of fracture. The first is one in which a single or a few macrocracks propagate until fracture is complete, usually in a brittle material. The other is one in which several microfractures dominate, these grow until they coalesce resulting in separation. The former is covered by the traditional "fracture mechanics." Mathematical attempts to gain an understanding of this process is centred upon the energy method. Here a macroscopic crack is treated as a stress-free boundary in a mathematical boundary value problem. The threshold condition for crack instability is assumed to be a critical energy density, stress intensity factor, or other measure of the stress and strain fields near the crack tip. The growth kinetics of the crack are handled as part of a dynamic boundary value problem. The method was pioneered by Griffith and Irwin [1] (1968), and has been extremely successful in

cases where the behaviour of a single large crack in fairly brittle material is of prime interest.

This Griffith energy method is often differentiated into one in which the plastic zone at the macrocrack tip is very small compared with the specimen dimensions and crack size, this is termed "Linear Elastic Fracture Mechanics" LEFM, as the dynamics is almost wholly elastic. The other is one in which the plastic zone is larger but still contained at the crack tip. It is referred to as "Elastic Plastic Fracture Mechanics" EPFM, as there is an appreciable plastic deformation at the tip of the crack.

However, there are many cases in which neither the linear elastic fracture mechanics nor the elastic plastic fracture mechanics will apply. In general, these are cases in which a large number of microfractures dominate the process. A good example is the necking of a smooth metallic ductile bar in tension. This will fail by the nucleation, growth and eventual coalescence of millions of microscopic voids in the necking region. In such cases, the treatment of each individual microcrack or void is virtually impossible and an alternative methodology is required. The spallation of either a brittle or ductile material falls into this category.

The term spallation or scabbing is used to describe the phenomenon of planar separation of material subjected to dynamic stress wave. The separation is parallel to the incident and reflected plane wave fronts generated by impact and it is a result

of the dynamic tensile stress components carried by the reflected wave.

Although a comprehensive review of the literature in this field is provided by the works of Curran [2] (1982), Meyers and Aimone [3] (1983) and Curran et al [4] (1987), we shall look at the general background including the main mechanisms involved in the spallation process. Namely, nucleation, growth and coalescence of microfractures.

8.4 GENERAL BACKGROUND

It was Hopkinson [5] in 1912 who first used the term scabbing and developed the famous Hopkinson Pressure Bar for measuring transient waves. The bar was later modified by Davies [6] (1948) who introduced electronic measuring devices. In the early 1950s, Rinehart [7-9] (1951 to 1952) detailed spall fractures by experiments and started the crystallographic examination of the spall damage as well as attributing the cause of scabbing to the tensile stresses resulting from the reflection of the compressive wave at the free surface. In 1960, Broberg [10] (1960) attributed the spallation phenomena to the development of microfractures. He postulated that when the tensile stress reaches some critical value, microfractures start to grow, the number of which depends on the stress level, and that scabbing is produced when the microfractures join together. These provided a good basis for the work carried out in the following years.

However, despite the link with the growth of microfractures to explain scabbing, the early quantitative theoretical work done in this area took a macroscopic viewpoint in formulating the criteria for spallation. These include the works of Butcher et al [11] (1964), Floyd et al [12] (1968) etc. Later refinements in microscopic examination techniques, and particularly the advancement in computational technology, led to the development of microscopic models to simulate spallation using advanced computers.

Refined microscopic theories were put forward to explain the phenomenon. These were incorporated into hydrodynamic programs in order to predict spallation. There is now a consensus on the physics of the spallation process and there is ample experimental data to back up the microscopic explanation.

In keeping with Broberg, it is now accepted that spallation in ductile materials is dominated by localized elasto-plastic deformation around existing and nucleated microvoids which dynamically grows and coalesces to form the spall plane. On the other hand, spallation in brittle materials is controlled by dynamic microcrack propagation with plastic deformation confined to the small region around the crack tips. The cracks eventually coalesce to form the spall plane.

Mathematical approaches have been developed which treat some key measures of average microscopic void behaviour as internal state variables in the constitutive relations for the material. In other words, the microvoid concentration as well as

orientation and size distribution functions, in the description of the current state of a material particle, are specified in addition to strain entropy and temperature. In this methodology, the fracture kinetics involves the microvoid behaviour, and this introduces rate dependence into the constitutive relations. A scale size or void spacing is also introduced in the constitutive relations. This approach is sometimes generally referred to as "microstatistical fracture mechanics."

The constitutive relations describing micro-statistical fracture processes are non-linear and significantly more complicated in terms of analysis. Furthermore, a lack of accurate data for the nucleation, growth and coalescence of the microscopic voids and cracks meant a rather slow development in the formulation of analytical models in this area. However, in recent years, there have been tremendous advances in the development of computers, making it feasible and economical to implement highly non-linear computational models. In the same period, there has been a significant increase in the sophistication of micro-structure examination technology. It is now possible to devise controlled impact experiments and interrupted quasi-static tests, and correlate observed microfractures with known stress and strain histories, thus "freezing in" the microfracture kinetics at various stages of development and making it possible to obtain accurate kinetics data. This has led to increased activity in the development of analytical models of microfracture processes, combining theory with experimental data and computer modelling, to make increasingly realistic descriptions and predictions of dynamic microfracture failure in solid materials. For example, Curran

and co-workers [13-15] (1971-1973) put forward their nucleation and growth (NAG) model of spall fracture after a series of experiments involving detailed microscopic observations before and after shockwave loading of both ductile and brittle solid materials.

As mentioned earlier, comprehensive literature reviews on this subject, covering experimental, theoretical and computational aspects, were carried out by Curran [2] (1982), Meyers and Aimone [3] (1983) and Curran et al [4] (1987). Since then further work has been done on the fundamental mechanisms of spall nucleation and growth kinetics [16-22] (1988-1993). We shall take a closer look at some of these developments later, especially those that have a significant impact in the formulation of this contribution.

Many of these recent works include visco-plastic constitutive modelling of high strain rate deformation and material damage. Such models, and others that rely on the inclusion of average microstatistical values in to the constitutive models are essentially complicated. They have the disadvantage of requiring a large number of material parameters, upwards of twenty in some cases, many of which are to be determined experimentally. Although such models provide a reasonable description and prediction of the spallation phenomenon, they are cumbersome to apply in practice as many of the parameters required are simply unobtainable for many practical engineering materials.

For example, Rajendran et al [17] (1988) developed a model for "A Void Growth Based Failure Model to Describe Spallation." They used the constitutive/failure model approach, employing the Bodner and Parton (BP model) constitutive equation, modified to include the effect of void nucleation and growth. Although a very good agreement of the spall signal simulated was obtained as compared with experimental record for OHFC copper, some nineteen parameters were required in the model. Another example, Eftis and Nemes [20] (1992), used the visco-plastic constitutive equation of Perzyna in their "Modelling of Impact-induced Spall Fracture and Post Spall Behaviour of Circular Plate." Their model required twenty material parameters for OHFC copper. In their own words "The material parameters and functions needed for void volume growth rate equation are considerably more difficult to determine because micrographic evaluation is required." Some of the parameters they used were assumed, others they obtained from their previous work and the rest were "determined from the work of Curran et al and Johnson."

Addessio and Johnson [22] (1993) required thirteen material parameters for their "Rate Dependent Ductile Failure Model." Nemes et al [19] (1990) on the other hand required twenty one parameters in their "Viscoplastic Constitutive Modelling of High Strain-rate Deformation, Material Damage, and Spall Fracture." The fact that a large number of parameters are often required in such models did not diminish their significance nor the immense contribution made by their authors. It merely illustrates the complexity of such models and how difficult it would be to apply them to

everyday practical engineering materials.

Hence, the case for simpler models, easily applicable to practical engineering materials. In this work, we consider relatively simpler microscopic models for brittle and ductile spallation. These models were incorporated into a one dimensional finite difference code to demonstrate their applicability.

Frequently in applications a full detailed knowledge of material microstructure during spalling is not necessary. There is evidence that spall properties are not very sensitive to microstructural details of the material [23] (1988). It is therefore reasonable to stand back and consider the collective response of the material. In this light, models taking a macroscopic view of the spall process are presented in this work for both ductile and brittle spallation.

By "macroscopic viewpoint" we do not imply macroscopic cracks or voids as in the traditional fracture mechanics. Rather, instead of average microstructural statistical functions of size, distribution and orientation, we consider the collective material response in characterizing the average continuum behaviour of the spall process, while keeping faith with the microstructural nature of the physics of the process.

Further, a simple unified model applicable to both brittle and ductile spallation is considered. A major advantage of this model is that it only requires commonly used

equations of state and constitutive models. Furthermore, only two other parameters are required to simulate the spallation process in a special purpose or commercially available hydrodynamic codes. The applicability of the model is demonstrated by the use of practical examples of spallation with available experimental data.

A further chapter considers the case of two dimensional plate impact and explosive impact on plates. A brief discussion on the models presented and conclusions round up this section of the thesis.

8.5 THE PHYSICAL MECHANISMS OF THE SPALLATION PROCESS

As mentioned above, the physics of the spallation process is essentially a microstructural one. The phenomenon is dominated by the nucleation, growth and eventual coalescence of millions of microvoid in the case of ductile spallation, or microcrack in the case of brittle spallation. Although it is generally available in material science literature, it will provide for greater understanding of the phenomenon to consider the physical process in a little more detail.

8.5.1 Microfracture Nucleation

As will be expected, microfractures, namely microvoids and microcracks in a solid material, take place at locations of heterogeneities. That is sites where the material

no longer appears as a continuum. As a consequence, the scale of nucleated microfractures vary from atomic dimensions in pure single crystals to a few micrometers in typical polycrystalline solids. For example, the typical heterogeneity sites in pure single crystals are vacancy clusters and dislocation pileups. These will show up under microscopic examination as the limit of the continuum of the crystals. Their sizes are therefore on a scale which is comparable to the "graininess" of the crystal, ie atomic in size. On the other hand, flaws in polycrystalline solids will nucleate at heterogeneity sites such as weak grains boundaries and at intergranular inclusions. The size of these are also in accordance with the graininess of the material, ie up to a few micrometers.

Although we can readily identify sites where the nucleation of micro-flaws can take place, the nucleation itself must have a history. That is to say, a flaw that becomes visible on the microscopic level will have a history on the sub-microscopic level. For example, a flaw that develops at a weak grain boundary in a polycrystalline solid must have been encouraged by a stress field before it becomes established as a nucleated microcrack or void and therefore visible and comparable in size to the grainness or continuum limit of the material. Therefore, at what stage in its "infant" history is a microfracture considered to be nucleated? In other words, how do we define nucleation?

It will not be implausible to define nucleation as the creation of a void large enough

to grow under an applied continuum stress field. For example, when a void formed by vacancy clustering reaches a size for which the applied triaxial tensile stress can overcome the surface tension, nucleation has occurred. However, such a definition will create a potential problem. It is recognised by researchers eg Raj and Ashby [24] (1975) and Argon et al [25] (1981), that the void sizes at which such a "nucleation" occurs are often sub-microscopic in size and very difficult to observe. They are, therefore, often below the "continuum limit" as defined by grain size.

Continuum mechanics cannot easily be applied to events of a scale much smaller than the continuum limit, as it will be difficult to prescribe local stresses and strains for such events. A better definition of nucleation should therefore take into account the order of size of the material heterogeneities that determine the continuum limit for the material of interest. Thus nucleation, as it should be defined, will often have sub-microscopic growth but will be taken into account only when they attain sizes of the order of the continuum limit under consideration.

Nucleation of microscopic fracture is therefore defined as "the appearance in a material element of microscopic voids or cracks with sizes comparable to that of the grainness that defines the continuum limit of the material" [4] (1987). For example, in polycrystalline metals with grains of a few micrometers in size, the appearance of voids with sizes of about a micrometer in the grain boundaries or within the grains would constitute nucleation.

8.5.2 Typical Nucleation Sites

It would be helpful to clarify such a careful definition of nucleation by illustrating it with typical practical examples of nucleation sites, the associated nucleation mechanism and the governing load parameters. We shall consider pre-existing flaws, inclusions, grain boundaries and subgrain structure.

Pre-existing flaws and voids are found in some metals such as beryllium, plastics and composites. A population of pre-existing flaws can also be found in many naturally occurring geological materials such as quartzite rock. Evidently, very weak or debonded grain boundaries in a material can be considered as inherent or pre-existing flaws. A growth of such flaws, under the influence of tensile stress and plastic strain, can cause the nucleation of a microfracture if such pre-existing flaws are very small compared to the continuum limit under consideration.

Inclusions and second phase particles are common in many metals most of which are due to the manufacturing processing. Nucleation of microfractures at inclusion and second phase particles is commonly observed at all loading rates. This occurs by the fracture of the inclusions, debonding at the interface, or fracture of the matrix adjacent to a stronger inclusion. Such nucleation can take place as a result of a tensile stress field and plastic strain.

Grain boundaries are favourable sites for nucleation as mentioned in some of the examples above. Some of the mechanisms include vacancy clustering on grain boundaries, grain boundary sliding, and brittle cracks at grain boundaries, especially due to impact loading.

In materials that are free of inclusions, such as OHFC copper, high purity aluminium and copper, researchers have consistently found that they were unable to correlate observed microscopic voids with any inclusions or grain boundary nucleation sites. The work of Cottrell [26] (1958) and Gilman [27] (1958) are examples. They concluded that nucleation must occur at sub-microscopic heterogeneities where dislocation motion can be impeded. The resultant dislocation pileups can cause the nucleation of microvoids due to plastic flow under the influence of shear strain.

8.5.3 Microfracture Growth

Once nucleated, micro-flaws can grow in several different modes depending on the matrix material properties and the stress and strain environments. The growth mode can be by atomic diffusion processes, ductile processes, such as plastic or viscous flow, brittle crack extension, or by shear slippage and extension. In the case of spallation, growth occurs chiefly by ductile plastic flow and/or brittle crack extension.

Growth of microscopic cracks or voids is essentially a continuation of the nucleation

process at pre-existing flaws, inclusion, second-phase particles, grain boundary junctions, or at sub-microscopic sites. Once nucleated, the flaws will grow if the applied load exceeds the growth threshold. In some cases, the growth threshold will be identical to the nucleation threshold. For example, when vacancy diffusion has formed a cluster large enough so that the applied tractions can overcome the surface tension. But in other cases such as debonding of inclusions, subsequent growth may occur by a different mechanism, and growth threshold can be higher or lower than the nucleation threshold.

In polycrystalline solids the microscopic void or crack growth can be conveniently classified into two modes, namely ductile void growth and brittle crack propagation. Either mode can occur intergranularly (in the grain boundaries) or trans-granularly (inside the grains). Generally, low temperatures or high loading rates encourage the brittle mode as plastic flow is inhibited: on the other hand, high temperatures and low loading rates encourage ductile void growth because the dislocation processes responsible for plastic flow are more likely. For example, Argon [25] (1981) and co-workers found that Armco Iron fractures through growth of ductile voids under quasi-static conditions at room temperature, but Shockey et al [28] (1973) found that under impact loading at room temperature, damage in the same material appears as microcracks. Whereas if the impact occurs on the specimen at 300^0C, voids appear and grow just as under the static room temperature conditions of Argon et al.

At some temperatures and loading rates (the specific temperature and loading rates depend on the material), "mixed mode" growth is observed. In this case the fracture surface consists of a mixture of coalesced ductile voids and brittle cracks. If brittle cracks occur trans-granularly, cleavage cracks are observed where weak crystallographic planes have separated. If brittle cracks occur inter-granularly, the grain boundary separates as a weak surface. As an illustration, Shockey et al [28] (1973) found that detailed observations of room temperature impact fractures in Armco iron show that voids were nucleated at inclusions, then cleavage cracks grew out of these voids. Fig 8.1 shows some range of fracture types a single material may undergo.

Many students of traditional fracture mechanics will recognise the growth processes so far described as being that of a quasi-static fracture mechanism. In fact Ashby and his co-workers [29] (1979) defined "dynamic fracture" as a separate mechanisms from "static fracture." However, many researchers have observed that the processes are basically the same. To quote from Curran et al [4] (1987);

> "...we have reached the following conclusions:"
>
> * "Fracture under high rate loading conditions may involve several different ductile and brittle processes, depending on the strain rate, temperature, and loading conditions (state of stress and strain)."
>
> * "These dynamic fracture processes are not basically different from those that

can occur under quasi-static conditions."

Observations of ductile fracture processes have generally shown that nominally spherical voids grow in the damage region. Such observations have been made by several researchers, eg Hancock and MacKenzie [30] (1976), on specimens tested quasi-statically. Under impact conditions, similar approximately spherical voids have been observed in aluminium, copper and heated Armco Iron, Barber et al [31] (1972). This is a very important point as we shall see later, most theoretical models of ductile void growth assume a spherical shape for the microvoids.

However, void growth described by diffusion or plastic flow would require that the voids be less spherical than those observed experimentally. MacKenzie et al [32] (1977) have suggested that the void growth may have occurred by a combination of plastic flow and nucleation processes. Plastic flow would require the void to elongate in the direction of maximum tensile stresses. But there are maximum tensile stresses in the material near the equator of this elongated void. Therefore, small voids in those regions might nucleate and coalesce with the main void to produce an enlargement at the equator. Thus a balance of plastic flow and nucleation of very small voids could maintain a nearly spherical void.

At very low stresses and fracturing rates (ie creep), the dominant ductile void growth mechanism is diffusion., Ghandi and Ashby (33) (1979). At higher stresses, plastic

flow becomes more important. At very high stresses (above the nominal yield strength), inertia and viscous mechanism become significant. For very high rate of fracture, viscous flow is the most probable void growth mechanism.

Although the study of micro-crack growth precedes that of micro-void growth, micro-crack growth is much less understood. At a macroscopic level, crack growth occurs by the extension of a single large crack through the material. But at a microscopic level, the process is much more complex. In more brittle materials smaller microcracks often form around the tip of the bigger crack. This then grows by linking up with the microcrack that best match the normal to the external tensile field. In the case of more ductile material, a larger crack may have microvoids forming around the tip. These grow, linking up with the crack, Shockey et al (34) (1980).

Several variations of other processes have been reported by researchers. Sometimes several non-coplanar microcracks, with the same orientation, are linked along 45^0 lines between their tips by a shear banding process. The microcrack growth process is very complex, and the process can involve a combination of cleavage across grains and between grains, ductile rupture by void linkage, shear slip along inclined planes, debonding around inclusion etc.

8.5.4 Microfracture Coalescence

After sufficient growth, the microscopic flaws coalesce to form fragments. At this stage an element of the material may be defined as completely failed. In spallation, this will result in the separation of the material along a plane that is parallel to the plane wave front responsible for the spall.

Coalescence is one of the least understood procedures. Curran et al [4] (1987) have, for the sake of simplicity, grouped observed coalescence process into two broad categories: direct impingement and localisation between voids.

Direct impingement of voids or cracks is often observed in pure ductile metals such as copper. Nearly spherical voids may grow to near impingement before localised ligaments stretch to complete the coalescence process.

Localisation between voids have been observed in structural steel and other polycrystalline solids, Cox and Low [35] (1974). The voids grow until strain localisation occurs in sheets between voids. Smaller voids will nucleate in the sheet until the main voids are linked, thus completing the coalescence process. Cox and Low presented a photomicrograph of fracture surface of 4340 steel, in which large voids can be seen to be connected by sheets of smaller voids.

8.6 REFERENCES

1 H Lielowitz ed. "Fracture" (Academic, New York, 1968) Vol. 1

2 D R Curran, "Dynamic Fracture in Impact Dynamics" (Edited by J A Zukas, T Nicholas, H F Swift, L B Greszczvk and D R Curran) John Wiley & sons, New York (1982)

3 M A Meyers and C T Aimone, Prog. Matters, Sci. 88,1, (1988) 99

4 D R Curran, L Seaman and D A Shockey, Physics Reports, V. 147, (1987) 253

5 B Hopkinson, Phil. Trans, A212 (1914), 437

6 R M Davies, Phil. Trans., A240, (1948), 375

7 J S Rinehart, J. Appl. Phys, 22, (1951) 555

8 J S Rinehart, J. Appl. Phys, 22, (1951) 1178

9 J S Rinehart, J. Appl. Phys, 23, (1952) 1229

10 K B Broberg, Int. Symp. on Stresswave propagation in Materials, Penn. State University, 1959, p1, InterScience, New York (1960)

11 B M Butcher et al, AIAA Journal, Vol, 2, (1964), 977-990

12 R Floyd et al, Int. Journal for Fracture Mechanics, Vol. 4, No. 4, 91968) 431

13 T W Barber, L Seaman,R C Crowdson and D R Curran, J. Matter. 7, (1972), 393

14 D R Curran, D A Shockey, L Seaman, J. Appl. Phys., 44, (1973), 4025

15 D R Curran, L Seaman and D A Shockey, Physics Today, 30, (1977), 46

16 J N Johnson et al, J. Appl. Phys. V.64, (1988) 6699

17 A M Rajendran et al, J. Appl. Phys. V.65, (1989) 1521

18 F L Addessio et al, J. Appl. Phys. V.67 (1990) 3275

19 J A Nemes et al, J. Appl. Mech. V.57, (1990) 283

20 J Effis et al, Int. J. Fract, V.52 (1992) 301

21 R Cortes, Int. J. Solids Structures, V.29, (1992) 1339

22 F L Addessio et al, J. Appl. Phys. V.74, (1993) 1640

23 D E Grady, J. Mech. Phys. Solids, V.36, (1988) 353

24 R Raj and M F Ashby, AFCA Metall, 23, (1975) 653

25 A S Argon, I W Chen and C W Law, "Creep and Fatigue Fracture", eds RMN Pelloux and N Stoloff (AIME, New York, 1981)

26 A H Cottrell, "Theory of Brittle Fracture in Steel and Similar Metals", Trans. AIME 212 (1958) 192

27 J J Gilman, "Fracture of Zinc-Monocrystals and Bicrystals," Trans. AIME 212 (1958) 783

28 D A Shockey, L Seaman, D R Curran, "Metallurgical Effects at High Strain Rates," eds R W Rohde, BM Butcher, J R Holland and C H Carnes, Plenum, New York, (1973) 473

29 M F Ashby, C Gandhi and D M R Taplin, Acta Metall. 27 (1979), 699

30 J W Hancock and A C McKenzie, J. Mech. & Phys. Solids, 24, (1976)

147

31 T W Barbee Jr., L Seaman, R C Crewdson and D R Curran, J. Mater. 7, (1972) 393

32 A C Mackenzie, J W Hancock and D K Brown, Eng. Fract. Mech. 9, (1977) 167

33 C Gandhi and M F Ashby, Acta Metall 27, (1979) 1565

34 D A Shockey, L Seaman, K C Dao and D R Curran, Trans ASME, J. Pressure Vessel Tech. 102, (1980) 14

35 T B Cox and J R Low Jr., Metall. Trans. 5, (1974) 1457

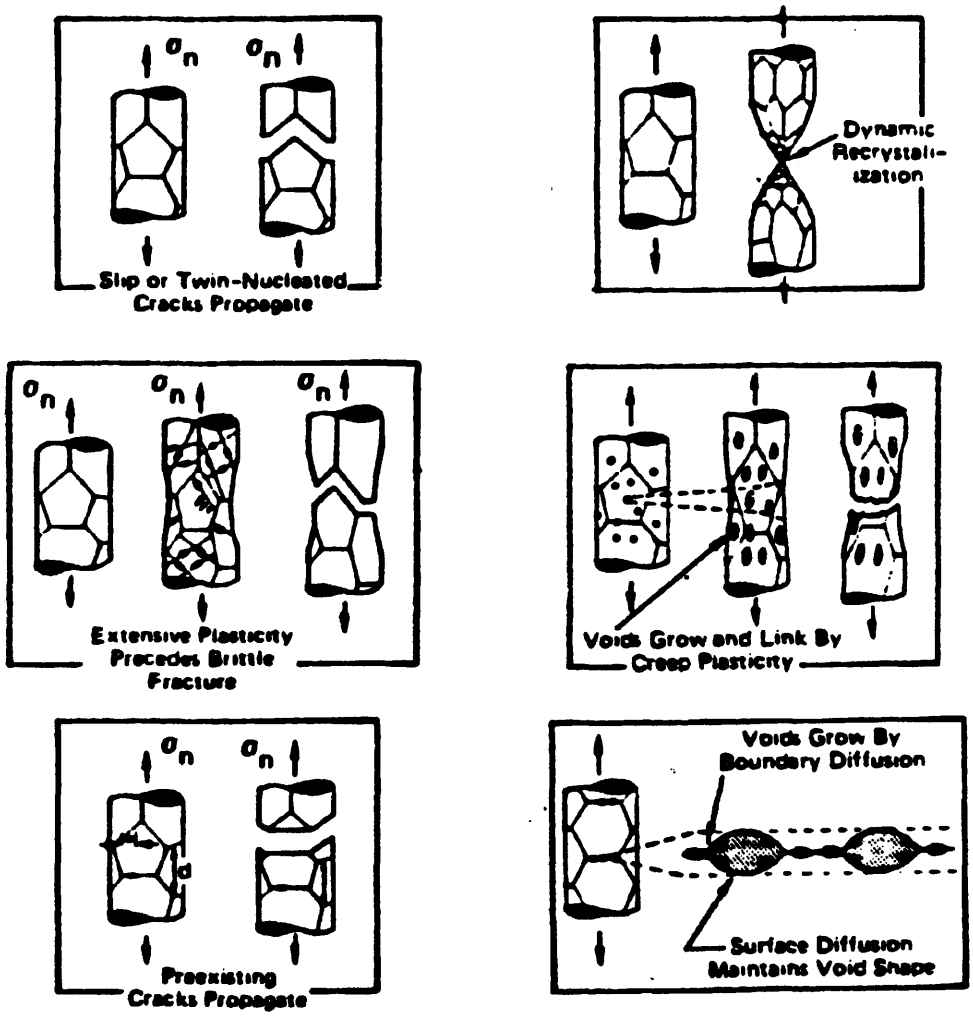

Fig. 8.1 Fracture Types

CHAPTER NINE

ENGINEERING MODELS

FOR DUCTILE SPALLATION

9.1 SUMMARY

After a brief introduction, we present the theoretical basis for a simplified microscopic model for ductile spallation. This is followed by the presentation of another model taking a macroscopic view of the spallation process by pondering the collective response of material in characterising the average continuum behaviour of the phenomenon. The applicability of the models were demonstrated by incorporating them into a finite difference code and modelling a typical impact problem resulting in spallation. The results of the simulations were compared with the experimental data of the impact test simulated. The chapter was rounded up with a brief discussion and conclusion.

9.2 INTRODUCTION

In the previous chapter the physical processes involved in the phenomenon of spallation was discussed in the context of the general microfracture mechanism. The

nature of the solution to the description and prediction of spallation in practical engineering situations was hinted at in the 'statement of the problem'. As we have seen earlier, there are essentially two types of spallation processes. Namely, ductile and brittle spallation. The aim here is to present simplified models to describe ductile spallation.

Ductile spallation, or ductile micro-fracture failure in general, is better understood in comparison to brittle microfracture failure which has been studied for much longer. On the whole, the various models presented for ductile microfracture have been successful. The problem has been that, such models are not easily applicable to practical engineering materials, because large numbers of parameters are often required. As exemplified in the last chapter, some of these models require in excess of twenty parameters, many of which are simply not obtainable even for the special materials commonly used for such studies. None-the-less the available models present a solid foundation for any future research in the field and are immensely useful. This chapter presents a simplification of a previous microscopic void growth model applying it to the simulation of spallation. Later, a macroscopic model for ductile spallation is also presented. The applicability of the two models were tested by incorporating them into a numerical hydrocode and simulating a typical spallation example. The result, of the numerical simulations were compared with experiment. The chapter ends with a brief discussion and conclusion.

9.3 MODELLING VOID GROWTH BY PLASTIC FLOW

There are two main mechanisms of ductile void growth. Namely, diffusion and plastic flow. Under the condition of moderate triaxial (mean) tensile stress and high temperatures, void growth tends to occur on grain boundaries by vacancy diffusion, Raj and Ashby, [1] (1975). But at the extreme of high mean tensile stress and lower temperatures, void growth tends to occur by localised plastic flow around the void, Gurson [2] (1977), and Johnson [3] (1981). Therefore, a successful continuum constitutive model must adequately describe the change in growth mode with changes in the stress and strain environment. The phenomenon of spallation belongs to the latter, i.e. void growth by plastic flow.

When mean tensile stresses are high, as is often the case in spallation events, the voids grow by microscopic plastic flow around their surfaces. The growth of ellipsoidal voids in a plastically deforming matrix has been studied intensely, both experimentally and analytically.

Berg [4] (1962), analysed the growth of an ellipse in a two-dimensional field of viscous material, finding equations governing the rate of volume and shape change. McClintock [5] (1968), transformed Berg's viscous solution into a plastic analysis and applied it to structural materials using an equivalence of shear flow. Rice and Tracey, [6] (1969) dealt with the case of spherical void in a three dimensional flow.

They derived a growth law that depends on both plastic strain and mean tensile stress. Their model pertains to a single void in an infinite medium, therefore the void growth does not affect the imposed stress field.

Later Gurson [2] (1977) extended Rice and Tracey's model to spherical void in an infinite block of material. His growth law also depends on plastic strain and mean tensile stress but he allowed for stresses to be altered by void growth. Gurson's model also allows for void interaction via intersecting plastic strain fields, since the finite volume is defined by void spacing. More recently Gurson and Hutchinson [7] (1981), extended Berg's analysis by considering an ellipsoid in a three-dimensional stress field. They were able to follow the shape changes of the ellipsoid through a complete loading history.

Spallation has been modelled as a case of void growth by plastic flow under spherical tension. The treatment of the growth of voids under a spherically symmetric tensile field has been studied by several investigators and is fairly comprehensive. Chadwick [8] (1959) presented one of the notable early works in this field. But the work of Carroll and Holt, [9-10], (1972), on "Static and Dynamic Pore-Collapse Relations for Ductile Porous Materials" has proved to be an important landmark. Their study encompasses static and dynamic compressive and tensile, elastic-plastic and rigid-plastic cases. Many of the more recent works have used and adapted the basic model presented by Carroll and Holt. These include the work of Johnson [3] (1981) and

Cortes [11] (1992).

In their basic analysis, Carroll and Holt treated a single void contained in a sphere of elastic-plastic material. Under a uniform tensile stress p, applied to the external surface of the sphere, the material first yields at the inner surface, adjacent to the void, see Fig 9.1. With continued loading, the elastic-plastic boundary at $r = r_p$ gradually moves from $r_p = a$ (the void radius) to $r_p = b$ (the external radius of the sphere of material). Eventually the entire sphere of material is at yield. We start from this basic model before looking at others based on it.

9.4 MICROSCOPIC MODEL

Consider the case of spallation in a ductile material. The process is initiated when dynamic plane tensile stress exceeds a threshold value appropriate for the material. Spherical voids are nucleated and grow under the influence of the stress field. These eventually coalesce forming the spall plane as the material separates.

Fig 9.2 shows a rectangular volume element containing a representative distribution of voids. This is subjected to a uniform hydrostatic tension, $\bar{p}$, acting over the surface of the element ($\bar{p}$ being a macroscopic pressure averaged over the entire element, voids and all). Since the cross-sectional area occupied by the voids supports none of the stress, mechanical equilibrium requires that;

$$A_s \bar{p}_s = A\bar{p} \tag{9.1}$$

where $\bar{p}_s$ is the mean stress (spatial average) in the solid material which subtends an average area A_s on a plane of total area A.

For a random distribution of hole shapes and sizes:

$$A_s/A = V_s/V \tag{9.2}$$

and according to Carroll and Holt [9-10] (1972), the mean stress in the solid constituent is;

$$\bar{p}_s = \alpha\bar{p} \tag{9.3}$$

where α is the distention ratio:

$$\alpha = V/V_s \geq 1 \tag{9.4}$$

Therefore, around each of the voids in the distended material there is an average mean stress $\alpha\bar{p}$. If this stress is big enough in tension (depending on the size of the holes), the voids will grow by plastic deformation in the surrounding solid matrix.

Fig 9.3 shows a graphical representation of the simplification made in the Carroll and Holt model. Now we home in on a single porous element, that is a hole and its radius of influence in the solid material matrix. This porous element has a single spherical

hole of radius a, in a sphere of radius b, subjected to an external tensile stress σ_r, see Fig. 9.1,

$$\sigma_r = -\alpha\bar{p}$$

The essential point to the Carroll and Holt model is that; relative values of a and b define the average porosity of the material and a_o (the average initial hole size) becomes a material parameter. In previous models of ductile hole growth, eg Barber and Seaman, [12] (1971), it was assumed that the applied tensile loading stress was applied at infinite external radius. One of the important consequences of the present assumption is that it leads naturally to a $\bar{p}$, α threshold relationship for fully plastic hole growth.

Now, a, b and α are related as follows:

From (9.4) above

$$\alpha = V/V_s = \frac{(\pi b^3)/8}{\pi(b^3 - a^3)/8}$$

or

$$\therefore \alpha = \frac{b^3}{b^3 - a^3} \qquad (9.5)$$

$$(b/a)^3 = \alpha/(\alpha - 1)$$

The porosity is therefore,

$$\phi = \frac{(\alpha - 1)}{\alpha} = (1 - 1/\alpha) \tag{9.6}$$

The relationship between distention α (or porosity, ϕ) and the applied pressure α $\bar{p}(t)$ on the boundary, is obtained by assuming that void expansion takes place with spherical symmetry such that the surrounding material does not change volume. In the spallation (void growth) process nearly all the volume change is associated with void growth and very little with density changes in the solid constituent. That is, the solid matrix is incompressible. This assumption was also made by Curran et al [13] (1987), and Cochran and Banner [14] (1977).

From this conservation of volume;

$$4\pi r^2 dr = 4\pi r_o^2 dr_o$$

at each instance of time, t,

where r is the radius at an element, see fig 9.1.

Which upon integration gives,

$$r^3 = r_o^3 - B(t) \tag{9.7}$$

where B(t) is a function related to the rate of void growth.

If we introduce ψ such that

where

$$\dot{r} = \frac{\partial \psi}{\partial r} \tag{9.8}$$

Then

$$\Psi\ (r,t) \equiv \frac{\ddot{B}(t)}{3r} + \frac{[\dot{B}(t)]^2}{18r^4} \tag{9.9}$$

and using equation (9.5)

$$B(t) = a_o^3\ (\alpha_o - \alpha)\ /\ (\alpha_o - 1) \tag{9.10}$$

Thus when,

B(t)>0, for $\alpha<\alpha_o$ (void compaction)

and when,

B(t)<0, for $\alpha>\alpha_o$ (void growth)

It can be shown that;

$$\frac{B(t)}{a^3} = \frac{\alpha_o - \alpha}{\alpha - 1} \tag{9.11}$$

and

$$\frac{B(t)}{b^3} = \frac{\alpha_o - \alpha}{\alpha} \tag{9.12}$$

Now, the equation of motion for material surrounding the void is given by:

$$\rho \ddot{r} = \frac{\partial \sigma_r}{\partial r} + \frac{2(\sigma_r - \sigma_\theta)}{r} \tag{9.13}$$

where ρ is the solid density and σ_r and σ_θ are radial and circumferential deviatoric stresses, see Fig 9.1.

In accordance with the usual convention, $\bar{p}$ is positive and σ_r, σ_θ are negative in compression. Stress and strain variables with a bar over them are macro-quantities averaged over the whole of the element including the voids, whereas those without a bar are micro-quantities in the material surrounding the voids.

Substituting equation (9.8) into equation (9.13) gives

$$\rho \frac{\partial \psi}{\partial r} = \frac{\partial \sigma_r}{\partial r} + \frac{2\Delta S}{r} \tag{9.14}$$

where $\Delta S \equiv (\sigma_r - \sigma_\theta)$.

We integrate equation (9.14) from a to b with the boundary conditions; σ_r (a,t) = 0 and σ_r (b,t) = - $\alpha \bar{p}$. This gives:

$$\rho\,[\psi_a(t) - \psi_b(t)] = -\alpha\bar{p} + 2\int_a^b \frac{\Delta S}{r}\,dr \qquad (9.15)$$

Using equations (9.8), (9.9) and (9.10), equation (9.15) can be written as:

$$\tau^2\, Y_0\, Q(\ddot{\alpha},\dot{\alpha},\alpha) = -\alpha\bar{p} + 2\int_a^b \frac{\Delta s}{r}\,dr$$

where Y_0 is the yield stress of the solid

$$\tau^2 \equiv \rho a_o^2/3Y_o(\alpha_o - 1)^{2/3}$$

$$Q(\ddot{\alpha},\dot{\alpha},\alpha) \equiv -\ddot{\alpha}[(\alpha-1)^{-1/3} - \alpha^{-1/3}] + 1/6\dot{\alpha}^2[(\alpha - 1)^{-4/3} - \alpha^{-4/3}]$$

Thus we have the following general relationship for dynamic void growth:

$$\sigma + 2\int_a^b \frac{\Delta S}{r} = \frac{\rho a_o^2}{3(\alpha_0 - 1)^{2/3}} Q(\ddot{\alpha},\dot{\alpha},\alpha) \qquad (9.16)$$

where $\sigma = \alpha\bar{p}$.

When specific expression is substituted for ΔS in the integrand on the left hand side, the above equation gives the rate dependent response of void growth in spalling ductile solids.

Johnson [3] (1981) has shown that the period of the sphere deformation process in which the material near the void is plastic and the further material is still elastic is in practice sufficiently brief to be ignored. Therefore, we can reasonably assume that the solid region of the porous element will be at a fully plastic stage from the very beginning of the deformation process.

Hence, for a growing void we will have;

$$\Delta = - \sigma_e$$

where the yield strength σ_e is determined by the particular constitutive equation of the material. For a perfectly plastic material, for instance, where σ_e equals a constant value σ_0, equation (9.16) becomes:

$$\sigma - \frac{2\sigma_0}{3} \ln\left(\frac{\alpha}{\alpha - 1}\right) = \frac{\rho a_0^2}{3(\alpha_0 - 1)^{2/3}} Q(\ddot{\alpha},\dot{\alpha},\alpha) \qquad (9.17)$$

This was the expression derived by Carroll and Holt, [9] (1972), for the case of

shrinking pores.

The above derivation of Carroll and Holt model have been truncated, a detailed derivation is given in Chapter 6.

Johnson, [3], (1981), used the following constitutive equation in his adaptation of the Carroll and Holt model to ductile spallation;

$$\sigma_e = \sigma_0 + \eta\dot{\varepsilon} \tag{9.18}$$

where

σ_e is the equivalent yield stress

σ_0 is the yield stress

$\dot{\varepsilon}$ is the equivalent plastic strain rate

η is the material viscosity $\eta = \frac{2D}{3b^2N}$

D is the material drag co-efficient

b is the Burgers vector

N is the mobile dislocation density

Therefore, ΔS in equation (9.16) is:

$$\Delta S = -\sigma_0 + \eta\dot{\varepsilon} \tag{9.19}$$

Now, displacement, $u = r - r_o$

using equation (9.7),

$$u = r - [r^3 + B(t)]^{1/3}$$

strain

$$\epsilon = \frac{\partial u}{\partial r} - \frac{u}{r}$$

$$= -\left(1 + \frac{B(t)}{r^3}\right)^{-2/3} + \left(1 + \frac{B(t)}{r^3}\right)^{1/3}$$

$$\frac{\dot{\epsilon}}{r} = \frac{\dot{B}(t)}{r^4}\left[\frac{2}{3}\left(1 + \frac{B(t)}{r^3}\right)^{-5/3} + \frac{1}{3}\left(1 + \frac{B(t)}{r^3}\right)^{-2/3}\right] \qquad (9.20)$$

substituting equation (9.20) into equation (9.19) and using equation (9.5);

$$\left(\frac{b}{a}\right)^3 = \alpha/(\alpha - 1)$$

We have;

$$2\int_a^b \frac{\Delta s}{r}\,dr = -\frac{2}{3}\ln\left(\frac{\alpha}{\alpha - 1}\right) - \eta\frac{\dot{B}(t)}{B(t)} \cdot \int_a^b \left[\frac{2}{3}\left(1 + \frac{B(t)}{r^3}\right)^{-5/3} + 1/3\left(1 + \frac{B(t)}{r^3}\right)^{-2/3}\right] d\left(1 + \frac{B(t)}{r^3}\right)$$

using equation (9.10)

$$\frac{\dot{B}(t)}{B(t)} = -\dot{\alpha}/(\alpha_0 - \alpha)$$

Therefore,

$$2\int_a^b \frac{\Delta s}{r}\,dr = -\frac{2}{3}\sigma_0 \ln\left(\frac{\alpha}{\alpha - 1}\right) + \eta.\left(\frac{\dot{\alpha}}{\alpha_0 - \alpha}\right)$$
$$.\left(\left[-(1 + \frac{B(t)}{r^3})^{-2/3}\right]_a^b + \left[(1 + \frac{B(t)}{r^3})^{1/3}\right]_a^b\right)$$

using equations (9.11) and (9.12)

$$= \frac{-2\sigma_0}{3} \ln\left(\frac{\alpha}{\alpha - 1}\right) + \eta\frac{\dot{\alpha}}{\alpha_0 - \alpha}\left[\left(\frac{\alpha_0 - 1}{\alpha - 1}\right)^{-2/3}\right.$$
$$\left.\left(1 - (\frac{\alpha_0 - 1}{\alpha - 1})^{1/3}(\frac{\alpha_0 - 1}{\alpha - 1})^{2/3}\right) - (\frac{\alpha_0}{\alpha})^{2/3}\left(1 - (\frac{\alpha_0}{\alpha})^{1/3}(\frac{\alpha_0}{\alpha})^{2/3}\right)\right]$$

$$= -\frac{2\sigma_0}{3} \ln\left(\frac{\alpha}{\alpha - 1}\right) + \eta.\frac{\dot{\alpha}}{\alpha_0 - \alpha}\left[\left(\frac{\alpha_0 - 1}{\alpha - 1}\right)^{-2/3} \cdot \frac{\alpha - \alpha_0}{\alpha - 1} - \left(\frac{\alpha_0}{\alpha}\right)^{-2/3} \cdot \frac{\alpha - \alpha_0}{\alpha}\right]$$

$$= \frac{2\sigma_0}{3} \ln\left(\frac{\alpha}{\alpha - 1}\right) + \eta\frac{\dot{\alpha}}{\alpha(\alpha - 1)} F(\alpha_1, \alpha_0)$$

where

$$F(\alpha_1,\alpha_0) = \alpha\left(\frac{\alpha - 1}{\alpha_0 - 1}\right)^{2/3} - (\alpha - 1)\left(\frac{\alpha}{\alpha_0}\right)^{2/3}$$

since

$$(\alpha_0 - 1) << 1$$

$$F(\alpha,\alpha_0) \approx \alpha\left(\frac{\alpha - 1}{\alpha_0 - 1}\right)^{2/3}$$

Therefore equation (9.16) becomes:

$$\alpha p - \frac{2\sigma_0}{3}\ln\left(\frac{\alpha}{\alpha - 1}\right) + \eta\frac{\dot{\alpha}}{\alpha(\alpha - 1)}.F(\alpha,\alpha_0) = \frac{\rho a_0^2}{3(\alpha_0 - 1)^{2/3}}.Q(\ddot{\alpha},\dot{\alpha},\alpha)$$

Ignoring the inertia term (ie the right hand side) the distention growth rate $\dot{\alpha}$ is given by:

$$\dot{\alpha} = \frac{(\alpha_0 - 1)^{2/3}}{\eta}\alpha(\alpha - 1)^{1/3}\Delta P \qquad (9.21)$$

where

$$\Delta P = \bar{p} + \frac{2}{3}\frac{\sigma_0}{\alpha}\ln\left(\frac{\alpha}{\alpha - 1}\right)$$

and

$$\alpha = \frac{V}{V_s}$$

V, V_s are the total volume and the specific volume of the solid constituent, respectively.

$\bar{p}$ is the averaged pressure in the composite of solid and voids.

For typical materials, viscosity η (ie the maximum resolved shear stress divide by the plastic shear strain rate in state of rapid plastic deformation) is usually about 10^3 to 10^5 dyne s/cm^2. However, to reproduce spallation data, a much lower value of viscosity was required and Johnson chose it as 10 dyne s/cm^2 for OHFC copper. While acknowledging that such a low value is unexpected, he argued that the usual values of viscosity are for conditions of homogeneous compressive deformation. Johnson further explained that for heterogeneous plastic deformation (as is the case in spallation void growth) there exists substantial localised heating effects due to very high plastic shear strains, of the order of several thousand percent, developed at the expanding pore walls. He reckoned that the corresponding temperature change at the pore wall can be a substantial fraction of the melting temperature of the material. In his own words, "It is not quantitatively known what effect this (ie the high temperature) has on the relationship between plastic shear strain rate and applied shear stress..." The only justification he offered for the unexpected value of viscosity is that "there presently exists no data that precludes the possibility" of such a low value of viscosity in the heterogeneous spallation void growth process, [3], (1981).

On the other hand, Curran et al [13] 91987) used the following expression for the growth rate of void radius in their DFRACT (ductile fracture) model:

$$\dot{R} = \frac{R}{4\eta} (P_s - P_g) \qquad (9.22)$$

where p_s is the pressure in the solid material

p_g is the void growth threshold

and

η is the material viscosity

Curran et al (13) envisaged the spallation void growth process as being a high loading rate one, in which inertial and viscous effects dominate, and that the above expression is predicted theoretically and observed experimentally.

However, Curran et al also found that a much lower value of viscosity was required to simulate experimental spall data. They chose a value of 75 dyne s/cm^2 for OHFC copper and aluminium instead of the usual values of 10^3-10^5 dyne s/cm^2. Unlike Johnson [3] (1981) they did not speculate on the reasons for such a low value of viscosity.

Like Johnson, Raul Cortes [11] (1992) started from the relation obtained by Carroll and Holt, equation (9.15). Employing the usually used constitutive equations for engineering materials, as substitution for ΔS in equation (9.16), he considered the

cases of:

(a) constant yield stress:

$$\sigma_e = \sigma_0$$

(b) strain rate dependence of yield stress:

$$\sigma_e = \sigma_0 (1+ B\dot{\epsilon}^m) \tag{9.23}$$

and of the type

$$\sigma_e = \sigma_0 [1+\beta \ln (\dot{\epsilon} /\dot{\epsilon}_0)] \tag{9.24}$$

(c) strain hardening dependence of yield stress:

$$\sigma_e = \sigma_0 (1+H\epsilon) \tag{9.25}$$

(d) Strain rate and strain hardening dependence of yield stress;

$$\sigma_e = \sigma_0 (1+ H\epsilon) (1+B\dot{\epsilon}^m) \tag{9.26}$$

and a dependence of the type

$$\sigma_e = \sigma_0(1 + H\epsilon)\left[1 + \beta \ln(\frac{\dot{\epsilon}}{\dot{\epsilon}_0})\right] \tag{9.27}$$

where

σ_0 is yield stress

H,B, m and β are material parameters and ϵ is the equivalent plastic strain;

$$\epsilon = 2 \ln\left(\frac{R}{R_0}\right)$$

The Cortes model has not been used to simulate the spallation phenomenon, it was developed to describe the growth of single spherical microvoid in an incompressible medium due to intense dynamic loading. Here a simplified Cortes model is proposed, to describe the spallation phenomenon.

Let us consider the more general case of strain rate and strain hardening dependence of yield stress, equation (9.26).

$$\sigma_e = \sigma_0(1 + H\epsilon)(1 + B\dot{\epsilon}^m) \tag{9.26}$$

where $\epsilon = 2 \ln (r/r_0)$

From equation (9.7):

$$\frac{r_o}{r} = \left(1 + \frac{B(t)}{r^3}\right)^{1/3}$$

sub r = aR

Therefore

$$\frac{r_0}{r} = \left(1 + \frac{B(t)}{a^3R^3}\right)^{1/3}$$

using

$$\ln \frac{r_0}{r} = -\ln \frac{r}{r_0}$$

we have,

$$\epsilon = \frac{2}{3}\left(1 - \frac{B(t)}{a^3R^3}\right)$$

Using the incompressibility of material as represented in equation (9.11); we have

$$\epsilon = 2/3 \ln\left(1 + \frac{\alpha_0 - \alpha}{(\alpha_0 - 1)R^3}\right)$$

$$= -\frac{2}{3}\ln\left(1 - \frac{(\alpha - \alpha_0)}{(\alpha_0 - 1)R^3}\right) \qquad (9.28)$$

and

$$\dot{\epsilon} = \frac{2}{3(\alpha - 1)} \frac{\dot{\alpha}}{R^3} \tag{9.29}$$

Substituting equation (9.26), for ΔS in equation (9.16), and ignoring the inertia term, the differential equation for the dynamic void growth is given by:

$$\sigma + 2\int_1^{b/a} \sigma_0(1 + H\epsilon)(1 + B\,\dot{\epsilon}^m)/R\, dR = I_1 + I_2 = 0 \tag{9.30}$$

where

$$I_1 = 2\int_a^{b/a} \sigma_0(1 + H\epsilon)/R\, dR$$

using the relationship;

$$\ln(1 - x) = \sum_1^{\infty} x^n/n$$

equation (9.28) becomes:

$$\epsilon = \frac{2}{3}\sum_{n=1}^{\infty} \left[\frac{(\alpha - \alpha_0)}{(\alpha - 1)R^3}\right]^n /n \tag{9.31}$$

using equation (9.31) and (9.5)

$$I_1 = \frac{2\sigma_0}{3}\ln\left(\frac{\alpha}{\alpha - 1}\right) + \frac{\sigma_0 H}{3}\sum_{n=1}^{\infty}\left[\frac{\alpha - \alpha_0}{(\alpha - 1)^n n}.\int_1^{b/a} R^{-3n-1}dr\right]$$

$$= \frac{2\sigma_0}{3}\ln\left(\frac{\alpha}{\alpha - 1}\right) + \frac{4\sigma_0 H}{9}\sum_{n=1}^{\infty}\frac{(\alpha - \alpha_0)^n}{(\alpha - 1)^n n^2}.\left(1 - \left(\frac{\alpha - 1}{\alpha}\right)^n\right)$$

$$I_2 = 2\int_1^{b/a}\sigma_0(1 + H\epsilon)B\dot{\epsilon}^m/R\ dr = I_3 + I_4$$

where,

$$I_3 = 2\int_1^{b/a}\sigma_0 B\dot{\epsilon}^m/R\ dR$$

using equation (9.29)

$$I_3 = 2\sigma_0 B.\left[\frac{2\dot{\alpha}}{3(\alpha - 1)}\right]^m.\int_1^{b/a} R^{-3m-1}\ dr$$

$$= 2\sigma_0 B.\left[\frac{2\dot{\alpha}}{3(\alpha - 1)}\right]^m.\frac{1}{3^m}.\left(1 - \left(\frac{\alpha - 1}{\alpha}\right)^m\right) \qquad (9.33)$$

and

$$I_4 = 2\int_1^{b/a} \sigma_0 HB\epsilon\dot{\epsilon}^m / R \, dr$$

using equations (9.31) and (9.29)

$$I_4 = \frac{4\sigma_0 HB}{3} \sum_{n=1}^{\infty} \left[\frac{\alpha - \alpha_0}{(\alpha - 1)R^3}\right]^n / n \left(\frac{2}{3(\alpha - 1)} \cdot \frac{\dot{\alpha}}{R^3}\right)^m \frac{dR}{R}$$

$$= \frac{4\sigma_0 HB}{3} \left(\frac{2\dot{\alpha}}{3(\alpha - 1)}\right)^m \cdot \sum_{n=1}^{\infty} \left[\frac{(\alpha - \alpha_0)}{(\alpha - 1)}\right]^n \cdot \frac{1}{n} R^{-3m-3n-1} dr$$

$$= \frac{4\sigma_0 HB}{3} \left(\frac{2\dot{\alpha}}{3(\alpha - 1)}\right)^m \cdot \sum_{n=1}^{\infty} \frac{(\alpha - \alpha_0)^n}{(\alpha - 1)^n n(n + m)} \cdot \left(1 - \left(\frac{\alpha - 1}{\alpha^{m+n}}\right)\right) \qquad (9.34)$$

equation (9.30) can be rewritten as:

$$\bar{p} + \frac{2\sigma_0}{3} \ln\left(\frac{\alpha}{\alpha - 1}\right) + \frac{4\sigma_0}{9} HF_1(\alpha, \alpha_0) + \frac{2\sigma_0 B}{3m} (2\dot{\alpha}/(3(\alpha - 1)))^m.$$

$$(1 - ((\alpha - 1)/\alpha)^m) + \frac{2\sigma_0 BH}{3} (2\dot{\alpha}/(3(\alpha - 1)))^m F_2(\alpha, \alpha_0) = 0 \qquad (9.35)$$

where,

$$F_1(\alpha,\alpha_0) = \sum_{n=1}^{\infty} \frac{(\alpha - \alpha_0)^n}{(\alpha - 1)^n n^2}.(1 - ((\alpha - 1)/\alpha)^n) \tag{9.36}$$

and

$$F_2(\alpha,\alpha_0) = \sum_{n=1}^{\infty} \frac{(\alpha - \alpha_0)^n}{(\alpha - 1)^n n(n+m)}.(1 - ((\alpha - 1)/\alpha)^n) \tag{9.37}$$

Similarly, for a dependence of equivalent flow stress of the type:

$$\sigma_e = \sigma_0(1 + H\epsilon)\left[1 + \beta \ln(\frac{\dot{\epsilon}}{\dot{\epsilon}_0})\right] \tag{9.27}$$

the corresponding dynamic void growth relation is given by;

$$\bar{p} + \frac{2\sigma_0}{3}\ln(\frac{\alpha}{\alpha - 1}) + \frac{2\sigma_0\beta}{3}\ln(\frac{2\dot{\alpha}}{3(\alpha - 1)\dot{\epsilon}_0})\ln(\frac{\alpha}{\alpha - 1}) - \frac{\beta\sigma_0}{3}.$$

$$[\ln(\alpha/(\alpha - 1))]^2 + \frac{4\sigma_0}{9} HF_1(\alpha,\alpha_0) + \frac{4\sigma_0\beta H}{9}\ln(\frac{2\dot{\alpha}}{3(\alpha - 1)\dot{\epsilon}_0}).$$

$$F_1(\alpha,\alpha_0) - \frac{4\sigma_0\beta H}{9}F_3(\alpha,\alpha_0) = 0 \tag{9.38}$$

where

$$F_3(\alpha,\alpha_0) + \sum_{n=1}^{\infty} \frac{(\alpha - \alpha_0)^n}{(\alpha - 1)^n n} \cdot \left[\frac{1 - ((\alpha - 1)/\alpha)^n}{n^2} - \frac{((\alpha - 1)/\alpha)^n \ln(\alpha/(\alpha - 1))}{n}\right] \tag{3.39}$$

It should be noted that special choice of the material parameters in equations (9.26) and (9.27) were also required to produce experimental spallation data. Nemes et al [15] (1990) for example, presented the following non-linear strain hardening dependence of the yield stress,

$$K = q + (K_0 - q)e^{-\beta_1 \epsilon} \tag{9.40}$$

where K_0 and β_1 are material hardening parameters and q is the saturation hardening stress, instead of, $K = \sigma_0 (1 + H \varepsilon)$.

This allowed Nemes et al a (15) greater flexibility in the careful choice of material parameters in their "Visco-plastic Modelling of High Strain Rate Deformation, Material Damage, and Spall Fracture."

It is essential to emphasise that, unlike Raul Cortes, we are primarily concerned with the description of the spallation void growth process rather than the general initial boundary value problem of the void growth in the incompressible media. We, therefore, make a very important assumption that; the total volumetric strain rates are sufficiently small and the void growth rates are sufficiently large that the tensile

pressure remains near the threshold pressure for void growth. An assumption which was also made by Curran et al [13] (1987), and later by Johnson et al [3] (1988). Thus the void growth equations given above (equations (9.35) and (9.38)) can be simplified, by ignoring the second order terms in the distention rate, as follows.

For equation (9.35), distension rate is given by,

$$d\alpha = \left[\frac{2\sigma_0}{3\alpha(\alpha - 1)} - \frac{4\sigma_0 H}{9} dF_1(\alpha,\alpha_0)\right]^{-1} d\bar{p} \tag{9.41}$$

For equation (9.38), we have,

$$d\alpha = \left[\frac{2\sigma_0}{3\alpha(\alpha - 1)} \frac{- 2\beta\sigma_0}{3\alpha(\alpha - 1)} \ln\frac{\alpha}{\alpha - 1} - \frac{4\sigma_0}{9} H dF_1(\alpha,\alpha_0) + \frac{4\sigma_0\beta H}{9} dF_3(\alpha,\alpha_0)\right]^{-1} d\bar{p} \tag{9.42}$$

where

$$dF_1(\alpha,\alpha_0) = \sum_{n=1}^{\infty}\left[\left[\frac{1 - (\frac{\alpha - 1}{\alpha})^n}{n}\right].[(\alpha - \alpha_0)^{n-1}(\alpha-1)^n - (\alpha - \alpha_0)^n(\alpha - 1)^{-n}\right.$$

$$+\left[\frac{(\alpha - \alpha_0)^n}{n}\right]\left[-\alpha^{-n}(\alpha - 1)^{-1} - \alpha^{-n-1}\right]\Bigg] \qquad (9.43.a)$$

$$dF_3(\alpha,\alpha_0) = \sum_{n=1}^{\infty}\left[\frac{(\alpha - \alpha_0)^n}{(\alpha - 1)^n\, n}\left[-\left(\frac{\alpha - 1}{\alpha}\right)^{n-1}\frac{1}{n\alpha^2} - \ln\frac{\alpha}{\alpha - 1}.\left(\frac{\alpha - 1}{\alpha}\right)^{n-1}.\frac{1}{\alpha^2} + \right.\right.$$

$$\left.\frac{1}{n}\left(\frac{\alpha - 1}{\alpha}\right)^n\frac{1}{\alpha(\alpha - 1)}\right] + \left[\frac{1 - \left(\frac{\alpha - 1}{\alpha}\right)^n}{n^2} - \frac{\left(\frac{\alpha - 1}{\alpha}\right)^n \ln\frac{\alpha}{\alpha - 1}}{n}\right]$$

$$\left.\left.\cdot\left[(\alpha - \alpha_0)^{n-1}(\alpha - 1)^{-n} - (\alpha - \alpha_0)^n(\alpha - 1)^{-n-1}\right]\right]\right] \qquad (9.43.b)$$

Now, the parameter H in the above two equations is the hardening parameter. In some materials, like Aluminium, the effect of this parameter is small and therefore negligible, Cortes [11] (1992). The effect of yield stress is quite significant as expected and Cortes, Johnson and Curran et al showed that the effect of viscosity (parameter β in the equations) can be quite significant. If we omit the hardening parameter in equations (9.41) and (9.42), we get a further simplification of the distention rate. Also, the implication of the assumption made above is that dp is quite small.

For equation (9.41) we have,

$$d\alpha = \frac{2\sigma_0}{3\alpha(\alpha - 1)} \qquad (9.44)$$

For equation (9.42) we have,

$$d\alpha = \left[\frac{2\sigma_0}{3\alpha(\alpha - 1)} - \frac{2\beta\sigma_0}{3\alpha(\alpha - 1)}\ln\frac{\alpha}{\alpha - 1}\right] \tag{9.45}$$

If, however, we are to consider the non-linear strain hardening dependence of yield stress, presented by Nemes et al [15] (1990), equation (9.40) above, the threshold pressure p for void growth is given by,

$$P_g = -\frac{1}{\sqrt{3}}(1 - \phi) \ln\left(\frac{1}{\phi}\right) [2q + (k_o - q)\, F_4\, (\phi, \phi_o) \tag{9.46}$$

where, porosity $\phi = (1 - 1/\alpha)$

ϕ_o being the initial porosity.

$$F_4 = (\phi,\phi_o) = \exp\left[\frac{2}{3}\,\beta_1\,\frac{(\phi_o-\phi)}{\phi(1-\phi_o)}\left(\frac{1-\phi}{1-\phi_o}\right)^{-2/3}\left(\frac{\phi_o}{\phi}\right)^{-2/3}\right] + \exp\left[\frac{2}{3}\,\beta_1\,\frac{(\phi_o-\phi)}{(1-\phi_o)}\left(\frac{1-\phi}{1-\phi_o}\right)^{-2/3}\right] \tag{9.47}$$

and the corresponding void growth equation is given by

$$d\,\phi = [\,\frac{1}{\sqrt{3}}\ln\frac{1}{\phi}\,[\,2q + (k_o - q)\,F_4\,(\phi,\phi_o)] + \frac{1}{\sqrt{3}}\,\frac{(1-\phi)}{\phi}\,[2q + (k_o-q)\,F_4\,(\phi,\phi_o)] + \frac{1}{\sqrt{3}}(1-\phi)\ln\left(\frac{1}{\phi}\right)(k_o-q)\,dF_4\,(\phi,\phi_o)]^{-1}.d\bar{p} \tag{9.48}$$

where

$$dF_4(\phi,\phi_o) = \exp\left[\frac{2}{3}\beta_1\frac{\phi_o-\phi}{\phi(1-\phi_o)}\left(\frac{1-\phi}{1-\phi_o}\right)^{-2/3}\left(\frac{\phi_0}{\phi}\right)^{-2/3}\right]\left[\frac{2}{3}\beta_1\frac{\phi_o}{\phi^2(1-\phi_o)}\right.$$

$$\left.\cdot\left(\frac{1-\phi}{1-\phi_o}\right)^{-2/3}\left(\frac{\phi_o}{\phi}\right)^{-2/3} - \frac{4}{9}\beta_1\frac{(\phi_o-\phi)}{\phi(1-\phi_o)^2}\left(\frac{1-\phi}{1-\phi_o}\right)^{-5/3}\left(\frac{\phi_o}{\phi}\right)^{-2/3} - \frac{4}{9}\beta_1\frac{(\phi_o-\phi)\phi_o}{\phi^3(1-\phi_o)}\right]$$

$$\left[\left(\frac{1-\phi}{1-\phi_o}\right)^{-2/3}\left(\frac{\phi_o}{\phi}\right)^{-5/3}\right] + \exp\left[\frac{2}{3}\beta_1\frac{(\phi_o-\phi)}{(1-\phi_o)}\left(\frac{1-\phi}{1-\phi_o}\right)^{2/3}\right] \qquad (4.49)$$

$$\left[\frac{2}{3}\beta_1\left(\frac{1}{1-\phi_0}\right)\left(\frac{1-\phi}{1-\phi_o}\right)^{-2/3} - \frac{4}{9}\beta_1\frac{(\phi_o-\phi)}{(1-\phi_o)^2}\left(\frac{1-\phi}{1-\phi_o}\right)^{-5/3}\right]$$

This appears complicated, in fact it only involves three material parameters.

It should be noted that dp in equations (9.41), (9.42), and (9.48) should be calculated in accordance with the assumption that the total volumetric strain rates are sufficiently small and the void growth rates are sufficiently large. In other words, void growth is local (or microscopic) and should not significantly affect total volumetric strain.

The pressure of the solid constituent is assumed to be given by:

$$p_s = p_s\,(Vs,\ Es) \tag{9.50}$$

where the subscript s indicates the value of the solid constituent. The condition of mechanical equilibrium requires that;

$$A\,\bar{p} = A_s\,p_s \tag{9.1}$$

where A is the cross-sectional area which transmits pressure. If the voids are distributed at random,

$$\frac{A_s}{A} = \frac{V_s}{V} = \frac{1}{\alpha} \tag{9.52}$$

Therefore,

$$\bar{p} = \frac{1}{\alpha}\,p_s\,(V_s,\ E_s) \tag{9.51}$$

If however, the size of the cells used in finite difference calculation is much larger than the mean void size, V_s in equation (9.51) should not be $\bar{V}/\alpha\ \bar{V}$ where $\bar{V}$ is the specific volume in the composite of solid and voids.

9.5 MACROSCOPIC MODEL

Frequently in application, the full knowledge of the material microstructure, during spallation, is not necessary. Furthermore, there is evidence that, in certain cases, spall properties are not very sensitive to microstructural details of the material [16] (1988). In view of this fact, a macroscopic model to describe ductile spallation is proposed as follows:

Firstly, we define the spall strength (tensile threshold pressure) p_f as such a pressure that when tensile pressure $\bar{p}$ reaches p_f at a time t^*, deforming the solid constituent further is much more difficult than growing voids in the damaged material. This is similar to the assumption made by Cochran and Banner [14] (1977). Secondly, we define the gross porosity $\bar{\phi}$, concerned with gross values rather than the mean void. Furthermore, we assume that spallation is complete when $\bar{\phi}$ reaches a critical value, $\bar{\phi}_c$. While damage is occurring, the tensile pressure is assumed to relax according to a simple rule. The gross damage is evaluated from the whole governing equations based on the collective response of the material rather than the mean void size.

The absolute value of the defined threshold pressure p_f is equal to or greater than the nominal spall strength of the material, and can be estimated by:

$$p_f = - (2\ \rho c_o^2 \sigma_o\ \phi_c\ )^{1/2} \tag{9.52}$$

where ρ density

c_o bulk acoustic velocity

ϕ_c critical porosity

The above equation was given by Grady [16] (1988), using the energy balance analysis.

The spall strength p_f can also be identified as the threshold pressure for void growth given by equation (9.17), (9.35), (9.38) and (9.48). The simplest expression being that obtained from equation (9.17);

$$p_f = - \frac{2\sigma_o}{3} \ln\left(\frac{\alpha}{\alpha - 1}\right) \qquad (9.53)$$

However, there are many experimental data indicating that the ductile spall strength is not a constant material parameter but a function of the loading condition [17] (1989). Where an appropriate value of the spall strength P_f is not available, it would be necessary to obtain a first estimate using one of the equations suggested above (eg equation (9.52) or (9.53)). The determination of the exact value of p_f would depend on the comparison between numerical simulation and appropriate experimental data.

The gross porosity $\bar{\phi}$ is defined, in the numerical calculations, as such material cells that are small enough in the macroscopic view but big enough from the microscopic point of view, and appropriate for the whole finite difference calculation. In

accordance with the definition of the spall strength P_f, the gross distention $\bar{\alpha}$ and porosity $\bar{\phi}$ are expressed by:

$$\bar{\alpha} = \frac{\bar{\rho}^*}{\bar{\rho}} \tag{9.54}$$

and

$$\bar{\phi} = \left(1 - \frac{1}{\bar{\alpha}}\right) \tag{9.55}$$

where $\bar{\rho}$ and $\bar{\rho}^*$ are the gross density of damaged material at the time $t > t^*$ and time t^*, respectively.

While damage is occurring, the tensile pressure $\bar{p}$ is assumed to be relaxed by

$$\bar{p} = p_f \left(1 - \frac{\bar{\phi}}{\bar{\phi}_c}\right) \tag{9.56}$$

The gross porosity $\bar{\ }$ is evaluated from the whole governing equations, including the equation of state for porous material. The equation of state for porous material is given by

$$\bar{p} = \frac{1}{\bar{\alpha}} p_s \left(\bar{\nu} / \bar{\alpha}, E_s\right) \tag{9.57}$$

It should be noted that equations (9.56) and (9.57) are very important in describing the collective response of the damaged material. Obviously, the value of the critical gross porosity $\bar{\phi}_c$ is related to the relaxed rule of tensile pressure, as in equation (9.56). The value of the critical porosity can be determined by a comparison between numerical simulation and experimental data.

It now remains for us to incorporate the above two methods (microscopic and macroscopic) into a finite difference code, and test their applicability to practical engineering problems by comparing the numerical results given by the two methods with experimental data.

9.6 NUMERICAL SIMULATION

A very important advantage of the methodology we have adopted is that the numerical calculations involving the spallation process is separated from the equation of state and constitutive equations. By so doing, the proposed models can be used with any suitable commonly used equations of state and constitutive equations. In commercial general purpose hydrocodes, the models can easily be incorporated via a sub-routine. Even in dedicated codes, the model can be written directly into the code or via a sub-routine. We shall see in later chapters how the model is incorporated into a commercial, general purpose hydrocode, giving it the capability to accurately model problems involving spallation.

In this chapter, the models are written into an in-house one-dimensional finite difference code. A listing of this code is given in Appendix 1. Further, the model can easily be extended into two and three dimensions and coupled to the appropriate numerical code. We shall see how the model has been incorporated into a two dimensional hydrocode in a later chapter.

9.7 APPLICATION

The most widely accepted and effective method for testing spallation models has been through the comparison between experimental and computational velocity history of the free surface of the target in the plane impact of plates of material, the so-called spall signal.

In the numerical simulation of the flat impact of plates of material, equation of state (9.51) or (9.57) for porous material is coupled with the equation of energy conservation to solve for pressure and internal energy. In this exercise, commonly used equations of state and constitutive equations are used with the relatively simple models, presented above, to describe spallation in a practical engineering application. The primary objective of the present study is to develop simple model for ductile spall and to examine the effects of the models on the velocity history of the free surface of the target. No attempt is made to consider the effects of complex constitutive equations on planar spallation.

For the microscopic model, the simplified void growth equation (9.41) contains the parameters σ_0, H and β. The results of numerical simulations indicate that the parameter β, in Johnson-Cook type constitutive equation (9.27), has no appreciable effect on the velocity history of the free surface of the target, while the linear strain hardening parameter H has a significant effect. Introducing non-linear strain hardening, and using the void growth equation (9.48), will necessitate the determination of additional parameters.

Apart from the void growth equation, the stress relaxation rule is a key problem in the numerical simulation of the spallation process. In general, stress relaxation occurs due to two basically different processes. First, the volumetric strain of the matrix material can relax elastically due to the growth of voids, and the associated mean tensile stress also relaxes. Secondly, the decrease of the load-bearing area introduces stress relaxation. Stress relaxation rule is usually connected with the constitutive equation. For example, Rajdendran et al [18] (1989) presented the following yield function to take stress relaxation into account:

$$A(\rho_1)J_2 + B(\rho_1)p^2 = \delta(\rho_1)\sigma_s^2 \tag{9.58}$$

where

$$A(\rho_1) = 2 + \rho_1^2$$

$B(\rho_1) = (1 - \rho_1^2)/3$

$\delta(\rho_1) = \exp^{-\beta_2[(1-\rho_1)/\rho_1]}$

$\rho_1 = 1 - \phi$

J_2 is the second invariant of the deviatoric stress component

β_2 is a material parameter

In order to reproduce a reasonable experimental spall data the function $\partial(\rho_1)$ was modified as

$$\delta(\rho_1) = \left(\frac{g(\rho_1) - g(\rho_{1cr})}{g(1) - g(\rho_{1cr})} \right) \tag{9.59}$$

where

$$g(x) = \left[K_1 - \left(\frac{N}{|N|} \right) (1 - x) \right]^N$$

N, ρ_{1cr} are material parameters.

Furthermore, another parameter β_3 was required.

$$\beta_3 = \dot{\delta}(\rho_1)|_{\rho_1 = 1} \tag{9.60}$$

Thus, Rajendran et al [18] (1989) introduced three material parameters β_3, N and ρ_{1cr} in order to obtain a satisfactory stress relaxation.

By contrast, in the microscopic model, presented above, the volumetric strain relaxation of the matrix material, due to the growth of voids, is ignored in accordance with the assumption that the total volumetric strain rates are sufficiently small during the spall process. Therefore, the associated pressure cannot relax and the spall peak would be overestimated. The pressure relaxation due to the decrease of the load-bearing area, on the other hand, is given by equation (9.51).

The shear modulus is reduced as a function of the developing porosity according to the elastic relations of MacKenzie [19] (1950).

$$\hat{G} = G(1 - \phi F) \tag{9.61}$$

where

G is the shear modulus

$\hat{G}$ the degraded shear modulus

$$F = 15\,\frac{1 - \upsilon}{7 - 5\upsilon}$$

υ is the Poisson's ratio.

Also, the yield strength σ_0 is reduced, as the porosity develops, by,

$$\hat{\sigma}_0 = \sigma_0(1 - \phi) \tag{9.62}$$

where $\hat{\sigma}_0$ is the degraded yield strength of the porous materials.

In the macroscopic model, presented above, we introduced gross porosity $\bar{\phi}$ instead of the microscopic equivalent ϕ, thereby avoiding the additional rate equation of void growth and the complex constitutive equation with the mean void size as internal variable appropriate for localised damaged region. The tensile pressure is assumed to be relaxed by equation (9.56), which would overestimate the pressure relaxation because the voids would not be nearly co-planar unless the spall region is very narrow. The modulus G and yield strength σ_0 are reduced by equations (9.61) and (9.62) respectively, providing ϕ is substituted by $\bar{\phi}$.

9.8 PRACTICAL EXAMPLE

Let us use an example, based on an experiment, to illustrate the effectiveness of the ductile spall models presented in this chapter.

A 9 mm thick copper target plate is impacted by a 2 mm thick plate of the same material at a velocity of 0.185 mm/μs, See fig. 9.4. Fig. 9.5 shows the velocity-time history of the free surface at the target (spall signal) for the experiment, numerical simulation based on the microscopic model, and numerical simulation based on the macroscopic model.

The values of the parameters, for copper, required in the simplified microscopic model were:

$\sigma_0 = 0.22$ GPa

$\alpha_0 = 1.0003$

$H = 0$

$\beta = 0$

$\phi = 0.32$

The values of the parameters used for copper in the macroscopic model were:

$P_f = 1.3$ GPa

$\bar{\phi}_c = 0.02$

The computational results indicate that spallation becomes complete at $t = 2.7\mu s$. The spall shock reflected into the scab at rupture reaches the original free surface at $t = 3.1\mu s$, resulting in the second jump-off of the free surface. At time $t = 2.7\mu s$, ϕ reaches the critical value of 0.32 while the macroscopic equivalent, $\bar{\phi}$ reaches the critical value of 0.02 at the same time. In other words the critical microscopic porosity, $\phi_c = 0.32$, corresponds to the critical macroscopic porosity, $\bar{\phi}_c = 0.02$, at the time of material separation.

However, the relative degree of spall damage calculated by the microscopic and the macroscopic models are different. The spall peak, the second maximum in the free surface velocity history of the target, see Fig. 9.6, depends mainly on the relaxation rule of the tensile pressure. The simplified microscopic model underestimates the pressure relaxation while the simple macroscopic model overestimates the pressure relaxation. Together they give a lower and upper bound of the spall peak, as evident

from Fig. 9.5.

They are quite close to the experimental spall signal, and therefore provide simple and reasonable prediction of the spall behaviour of materials in practical engineering applications.

As a comparison, Fig. 9.7 presents the spall signal for the models described above, the experimental result and the numerical simulation based on the model presented by Rajendran et al. Experimental data is courtesy of Rajendran et al. The figure shows that the results of all three models compare very reasonably with the experimental data. The near-perfect fit of the Rajendran result required some nineteen parameters, most of which were unobtainable for the material modelled and had to be estimated and fine tuned. By contrast, the models presented above require only a handful of parameters available for every day engineering materials.

9.9 CONCLUSION

In this chapter, we have presented a simplified microscopic model for ductile spallation based on existing model for void growth and the assumption that the total volumetric strain rates are sufficiently large that the tensile pressure remains near the threshold pressure for void growth.

By focusing on the collective response of the material and introducing gross porosity,

a macroscopic model to describe ductile spallation was also presented.

The comparisons between experimental data and numerical simulations, based on the model presented, of the free surface velocity of the target plate, in the plane impact of plates, are reasonably good.

The critical porosity in the simplified microscopic model corresponds with the critical porosity in the simple macroscopic model.

The simplified microscopic model gives an upper bound of the spall peak while the simple macroscopic model gives a lower bound.

The models presented require very few parameters, in contrast to existing models, and reasonably characterise the average continuum behaviour of the spall process. Therefore they are expected to provide simple and reasonable prediction of the ductile spall behaviour in practical engineering applications.

REFERENCES

1 R Raj and M F Ashby, Acta Metall. 23 (1975) 653

2 A L Gurson, J.Eng. Mater. Technol. Trans of ASME 99 (1977) 2

3 J N Johnson, J. Appl. Phys, 52 (4) (1981) 2812

4 C A Berg, Proc. Fourth US National Congress Applied Mechanics 2 (1962) 885

5 F A McLintock, J. Appl. Mech. 35 (1968) 363

6 J R Rice and D M Tracey, J. Appl. Mech. Phys. Solids, 17 (1969) 202

7 M Y He and J W Hutchinson, J. Appl. Mech. 12 (1959) 52

8 P Chadwick, J. Mech & Appl. Math. 12 (1959) 52

9 M M Carroll and A C Holt, J. Appl. Phys. 42 (1972) 759

10 M M Carroll and A C Holt, J. Appl. Phys. 43 (1972) 1626

11 R Cortes, Int. J. Solids & Structures, 9 (1992) 1339

12 J W Barber, L Seaman, R C Crewdson and D R Curran, J. Mater. 7 (1972) 393

13 D R Curran, L Seaman & D A Shockey, Physics Reports, 147 (1989) 253

14 S Cochran and D Banner, J. Appl. Phys. 48 (1977) 2729

15 J A Nemes, J.Eftis and P W Randles, J. Appl. Mech. 57 (1990) 283

16 D E Grady, J. Mech. Phys. Solids, 36 (1988) 353

17 K E Froeschner et al. J. Appl. Phys, 65 (1989) 2964

18 A M Rajendran, M A Dietenberger and D J Grove, J. Appl. Phys 65 (4)

(1989) 1521

19 J H MacKenzie, Proceedings of the Physical Society, 63B(2) (1950)2

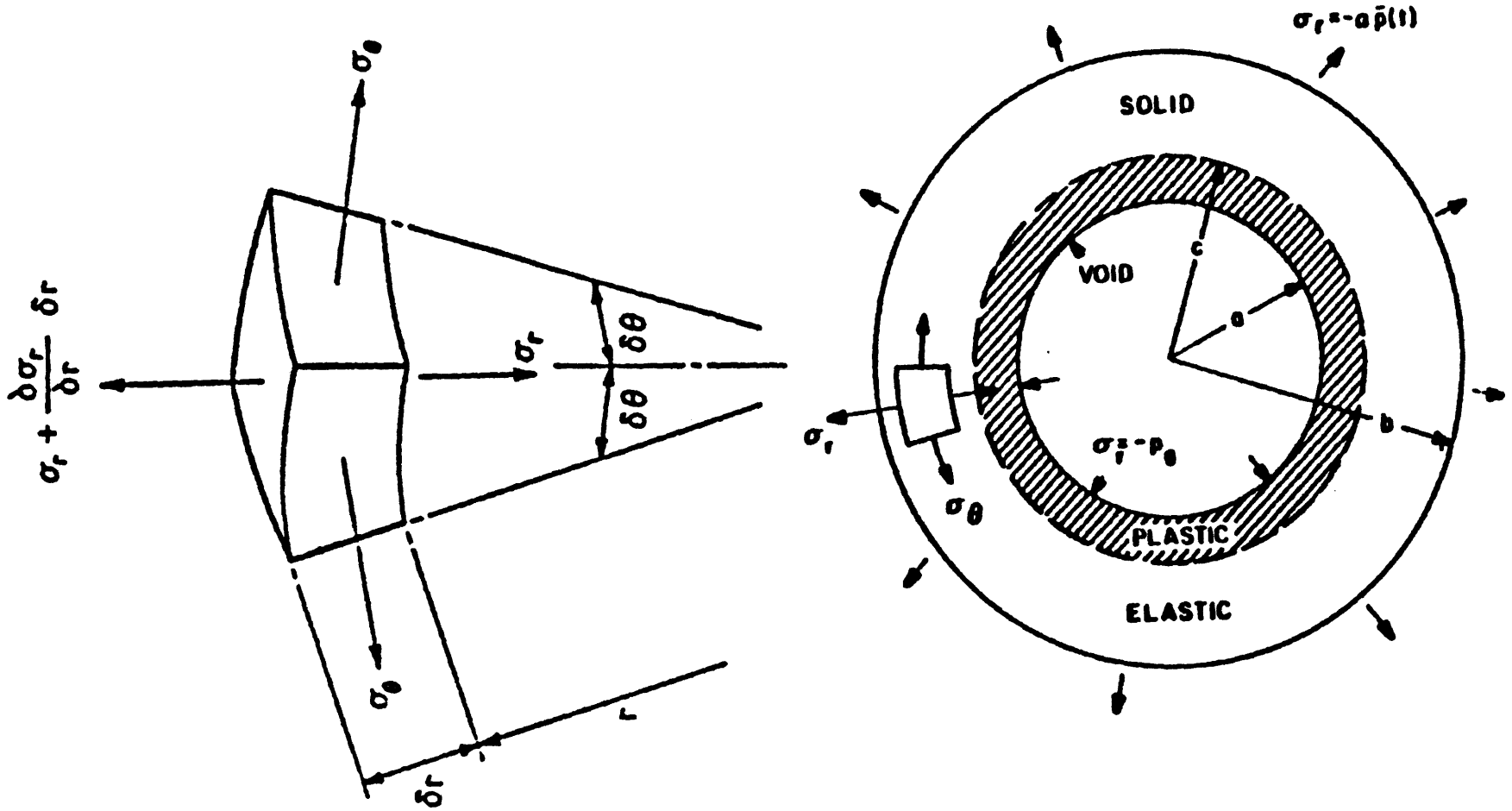

Fig. 9.1 The Porous Element

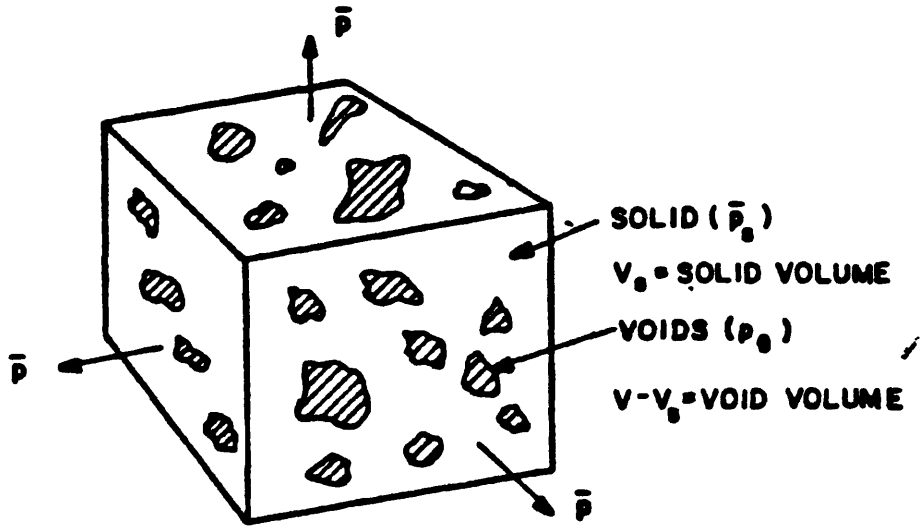

Fig. 9.2 Material Element Containing Voids

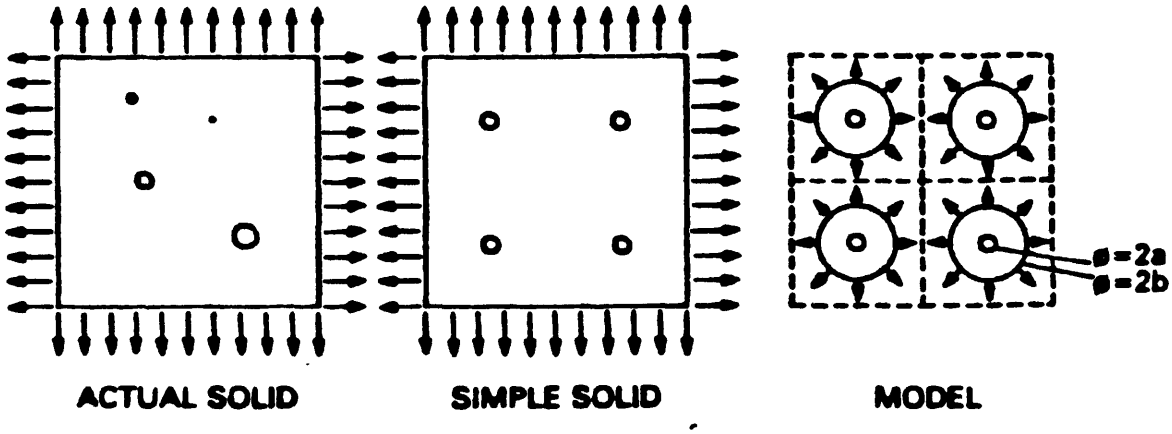

Fig. 9.3 Graphical Representation of the Simplifications of the Model

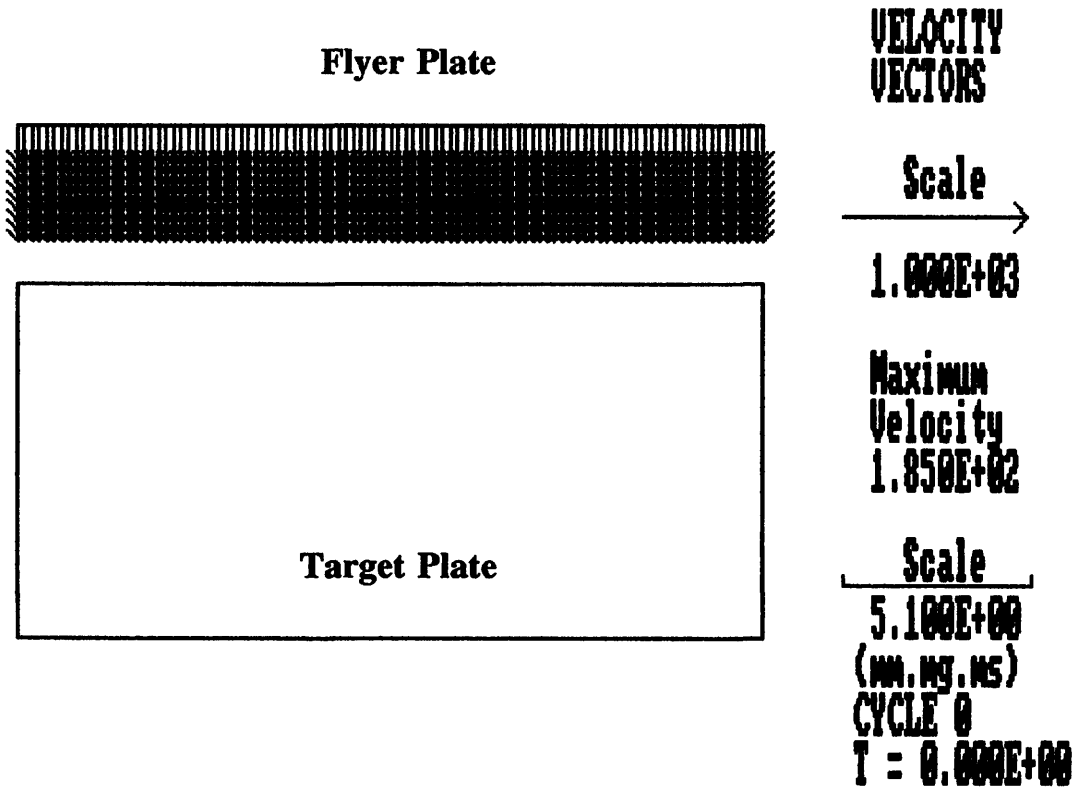

Fig. 9.4 Planar Plate Impact

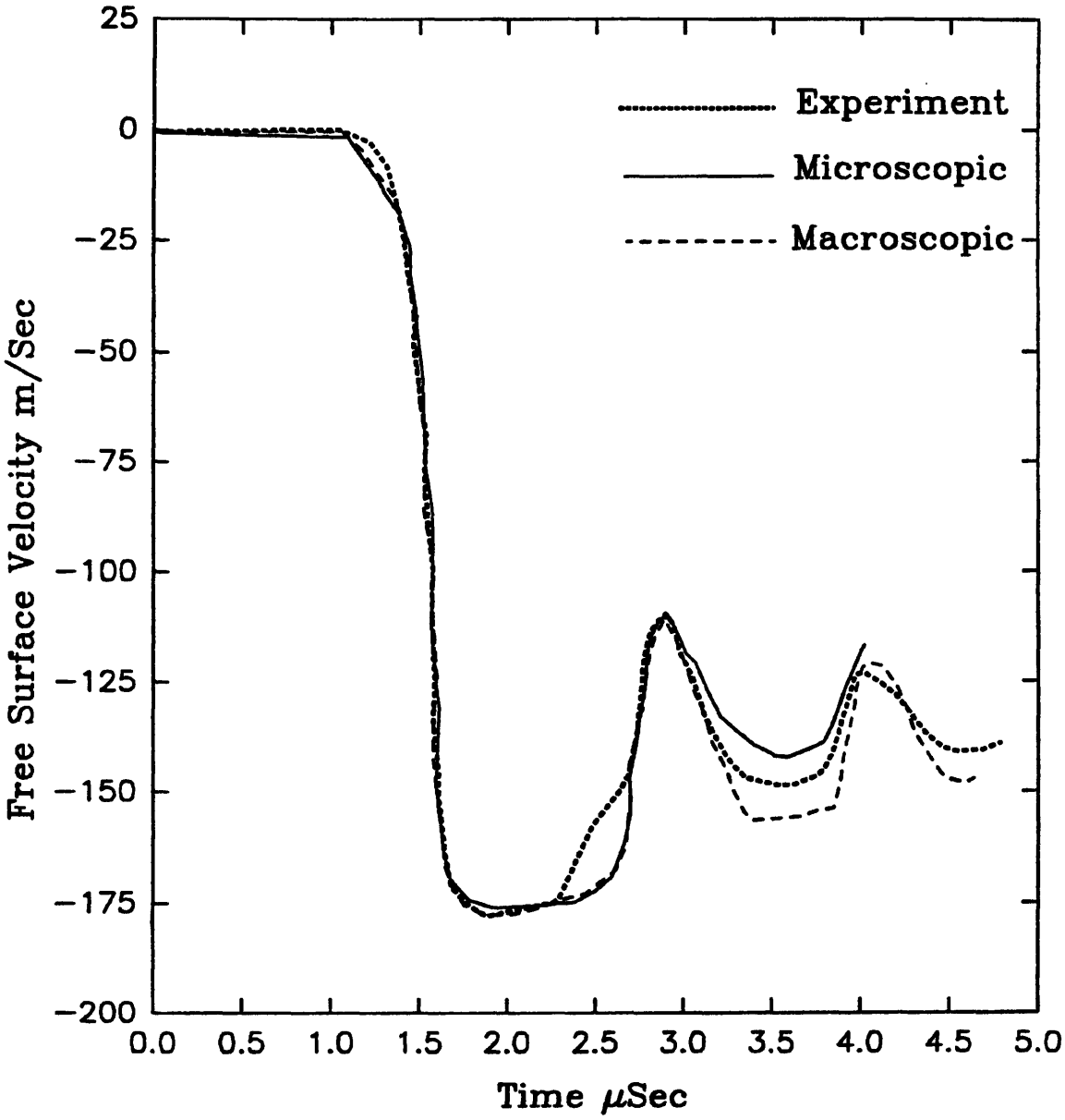

Fig. 9.5 Comparisons Between Experiment and Calculations for OHFC Copper Planar Spall

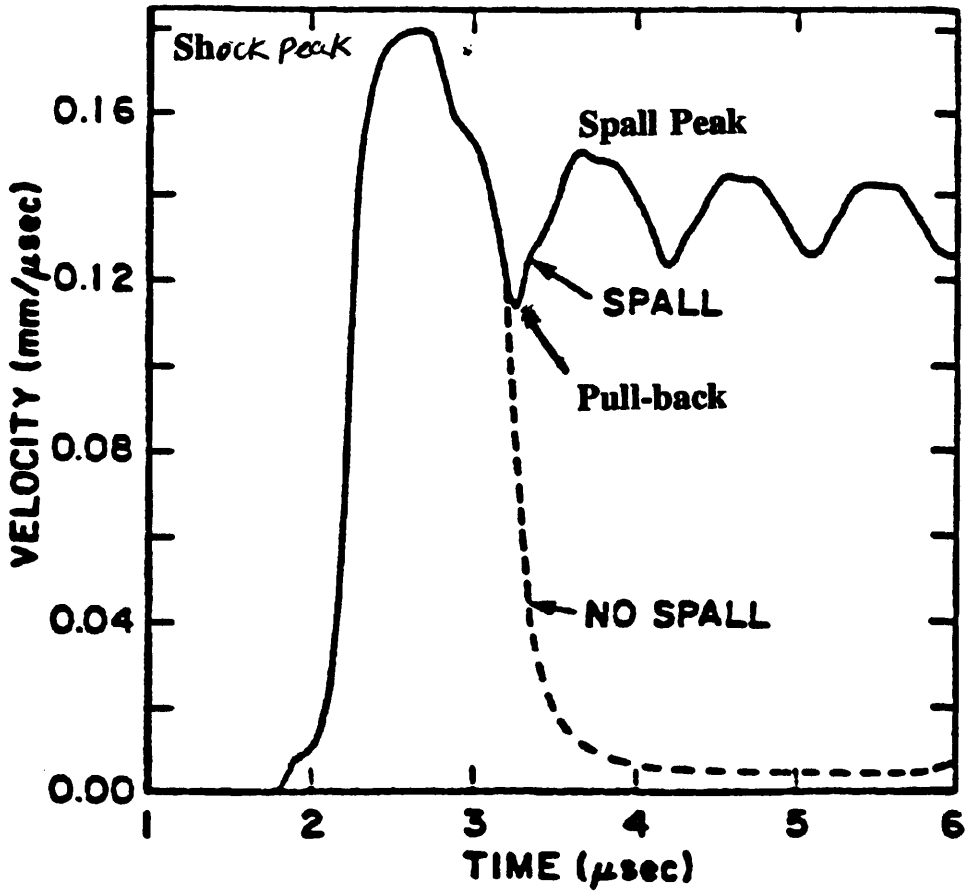

Fig. 9.6 Typical Spall Signal

CHAPTER TEN

ENGINEERING MODELS

FOR BRITTLE SPALLATION

SUMMARY

After a brief introduction, this chapter presents the theoretical basis for a simple microscopic model to describe brittle spall. This is followed by a macroscopic model, based on the collective material response, to characterise the average continuum behaviour of brittle material undergoing spallation. The applicability of these models was demonstrated by incorporating them into a hydrocode and modelling a typical impact problem resulting in spallation. Results of the numerical simulations were compared with experimental data. A brief discussion and conclusion rounds up the chapter.

10.1 INTRODUCTION

There has been a great tradition of the study of brittle macrofracture in material science and other fields of study. Since the pioneering days of Griffiths and Irwin [1] (1968), successful analytical models have been developed to describe brittle macrofracture. Generally, a macroscopic crack is treated as a stress-free boundary in a mathematical boundary value problem. The threshold condition for crack instability is assumed to be a critical energy density, stress intensity factor or other measure of stress and strain fields near the crack tip. The growth kinetics of this macroscopic crack are also handled as part of a dynamic boundary value problem.

This approach is generally referred to as "fracture mechanics" and has been extremely successful in cases where the behaviour of a single, large crack in fairly brittle material is of prime interest. The term "linear elastic fracture mechanics" (LEFM) is used when the plastic zone at the macrocrack tip is very small compared with specimen dimensions and crack size. On the other hand, the term "elastic plastic fracture mechanics" (EPFM) is used when the plastic zone is larger but still contained at the crack tip.

However, there are many cases where neither the LEFM or EPFM applies. A good example is the spallation phenomenon. In this case, failure occurs by the nucleation, growth and coalescence of millions of microfractures. For such a case, the treatment of each microcrack individually becomes forbidding, and a different mathematical approach needs to be adopted.

Instead of treating each microcrack individually, some key measures of average microscopic behaviour are treated as internal state variables in the constitutive relations for the material. For instance, in addition to strain, entropy and temperature, one also specifies the microvoid concentration, orientation and size distribution functions in the description of the current state of a material particle. In this alternative approach, the fracture kinetics involves the microvoid behaviour and introduces specific rate dependence into the constitutive relations. This microstatistical approach is common to both ductile and brittle microfracture. Although brittle microfracture has been studied much longer, it is much less understood than ductile microfracture. Brittle microfracture is much less amenable to analytical and numerical modelling than ductile hole growth. Models for ductile spallation were presented in the last chapter.

Some of the postulated physical mechanisms of brittle microfracture were referred to in Chapter eight. One example is that sometimes several non-planar microcracks with the same orientation will nucleate and grow independently. These are then linked at 45° lines between their tips by a shear banding process. There may be small voids in the shear band which further weaken the material undergoing shear. The resulting fractured surface is then very rough, indicating a combination of cleavage in the original cracks and ductile shearing along the shear planes. It is clear, therefore, that the growth of brittle microfractures occurs by a complex series of processes. As a result, crack growth laws to describe such a process are often complex and require

numerous parameters. Curran et al [2] (1987) published a comprehensive survey of brittle microfracture models including a presentation of their BFRACT model.

Although mean void growth based failure models to describe ductile spall have been very successful, we will indicate that a mean crack growth based failure model for brittle spall seem to be unsuitable.

In this chapter, we present a simple microscopic model to describe brittle spallation in the following manner:

(1) By expressing the solidity evolution using inelastic volumetric strain rate

(2) Determining the inelastic volumetric strain according to the crack opening strain and crack shear strain and

(3) Characterising the complete failure of the material by the use of a critical value of solidity rather than a critical value of damage.

A simple macroscopic model for brittle spall fracture, based on the collective material response, is also presented. The models were incorporated into a numerical finite difference code to demonstrate their applicability. The results of numerical simulation, of a typical brittle spallation problem, were compared with experimental

data.

10.2 SIMPLIFIED MICROSCOPIC MODEL

The simplified microscopic model for brittle spallation was developed as follows:

1 Express the solidity evolution using inelastic volumetric strain rate.

Assuming that the total strain rate $\dot{\varepsilon}_{ij}$ is composed of contributions from the elastic strain rate $\dot{\varepsilon}^e_{ij}$ and inelastic strain rate $\dot{\varepsilon}^c_{ij}$, the expression for the volumetric strain rates $\dot{\varepsilon}_{KK}$ is given by

$$\dot{\varepsilon}_{KK} = \dot{\varepsilon}^e_{KK} + \dot{\varepsilon}^c_{KK} \tag{10.1}$$

The solidity W is defined as

$$W = \frac{V_s}{V} \tag{10.2}$$

where

V total specific volume

V_s specific volume of solid

Differentiating of Equation (10.2) we have;

$$\dot{W} = \frac{V\,\bar{V}_s - V_s\,\bar{V}}{V^2}$$

multiply by

$$\frac{V}{V_s}$$

$$\dot{W}\frac{V}{V_s} = \frac{\dot{V}_s}{V_s} - \frac{\dot{V}}{V}$$

substituting in Equation(10.2)

$$\frac{\dot{V}}{V} = \frac{\dot{V}_s}{V_s} - \frac{\dot{W}}{W} \qquad (10.3)$$

It is also assumed that the elastic changes in W are small in comparison to the inelastic effects of the nucleation, growth and coalescence of cracks. That is, the elastic volume change takes place at constant W. Therefore,

$$\frac{\dot{V}_s}{V_s} = \dot{\varepsilon}^e_{KK} \qquad (10.4)$$

$$\frac{\dot{W}}{W} = - \dot{\varepsilon}^{c}_{KK} \tag{10.4}$$

2 Determine the inelastic volumetric strain according to the crack opening strain and the crack shear strain

Experiments suggest that the number of cracks per volume and orientation with a size greater than R remains approximately exponential during the deformation process [2] (1987). For an exponential distribution, the number density of cracks with radius larger than R is given by

$$N(R,\Omega) = \int_{R}^{\infty} n(R,\Omega)dR = N_o\Omega \exp\left(- \frac{R}{R_m(\Omega)} \right) \tag{10.6}$$

where n (R,Ω) is the number of cracks per volume, size and orientation with a crack radius in the range from R to R + dR and an orientation within the solid angle from Ω to Ω + dΩ. N_o (Ω) and R_m (Ω) are the total number of cracks per volume and the shape parameter for the distribution called the mean crack size, respectively. If it is assumed that the material remains isotropic, then N_o and R_m are independent of orientation Ω.

The cracks are presumed to open under a tensile stress $\sigma_{\phi\theta}$ to the value given by

$$\delta = \frac{4(1 - \upsilon^2)}{\pi} E R\sigma_{\phi\theta} \tag{10.7}$$

where

δ one-half of the maximum separation of the crack faces

$\sigma_{\phi\theta}$ tensile stress normal to the crack plane

E Young's modulus

ν Poisson's ratio

The total volume V_c of crack opened per volume is given by Curran et al [2] (1987) as

$$V_c = \int_0^{\infty} \frac{4\pi R^2 \delta}{3} n dR$$

using equations (10.6) and (10.7)

$$V_c = \frac{16(1 - \upsilon^2)}{3} E\sigma_{\phi\theta} \int_0^{\infty} R^3 \left(\frac{N_o}{R_m}\right) \exp\left(-\frac{R}{R_m}\right) dR$$

$$= \frac{32(1 - \upsilon^2)}{E} \left(\sigma_{\phi\theta} N_o R_m^3\right) \tag{10.8}$$

If the inelastic volumetric strain ε^c_{KK} includes only crack opening strain, the evolution equation of solidity W is obtained from Equation (10.5) and (10.8).

$$\frac{\dot{W}}{W} = -\frac{32(1-\upsilon^2)}{E}\frac{d}{dt}(\sigma_{\phi\theta} N_0 R_m^3) \tag{10.9}$$

However, the inelastic shear strain for a crack in tension is important. The total inelastic volumetric strain ε^c_{KK} per volume including crack opening strain and shear strain is given by F L Addessio et al [3] (1990)

$$\varepsilon^c_{KK} = 15(2-\upsilon)p\beta R_m^3 \tag{10.10}$$

where

$$\beta = \frac{64\pi}{15}\left(\frac{1-\upsilon}{2-\upsilon}\right)\frac{N_o}{G} \tag{10.11}$$

G shear modulus

p pressure

It is of interest to compare ε^c_{KK} given by Equation (10.10) with V_c given by Equation (10.8), Providing $\sigma_{\phi\theta} \sim p$, the ratio;

$$\frac{\varepsilon^c_{KK}}{V_c} = 12.5 \tag{10.12}$$

Indicating that the inelastic crack shear strain is much larger than the inelastic crack opening strain. Thus, the evolution equation of solidity is obtained from Equation

(10.5) and (10.10) thus:

$$\frac{\dot{W}}{W} = -\dot{\varepsilon}^{c}_{KK} \tag{10.5}$$

using equation (10.12) and (10.11)

$$\frac{\dot{W}}{W} = 15(2 - \upsilon).\frac{64\pi}{15G}\left(\frac{1 - \upsilon}{2 - \upsilon}\right)\frac{d}{dt}\left(pN_0R^3{}_m\right)$$

substitute

$$G = \frac{E}{2(1 + \upsilon)}$$

$$\frac{\dot{W}}{W} = \frac{128\pi(1 - \upsilon^2)}{E}\ \frac{d}{dt}\left(pN_0R^3{}_m\right) \tag{10.13}$$

3 Characterise the complete failure of the material by the use of a critical value of solidity W rather than a critical value of damage $N_0R^3{}_m$.

As an example, for Armco iron the number density N(R) of cracks with radius larger than R varies from

$$N(R) = 2x10^5\exp(-R/0.00094) \tag{10.14}$$

to

$$N(R) = 10^7 \exp(-R/0.00016) \tag{10.15}$$

during the process of the nucleation, growth and coalescence of cracks.

Theoretically, a value of unity for $N_0 R^3_m$ approximately corresponds to the complete intersection of cracks with the mean size R_m. However, as shown in Equation (10.15) the value of $N_0 R^3_m$ lower than unity was observed in the elaborate specimen examination, and considered as the failure criterion [2] (1987).

We assume that when the tensile pressure reaches the spall strength, the further decrease of the solidity is mainly due to the crack opening strain, and the crack shear strain caused by the tensile pressure relaxed at a certain value $N_0 R^3_m$. That is

$$dW = -\frac{128\pi(1-\upsilon^2)}{E} N_0 R_m^3 W d\,\bar{p} \tag{10.16}$$

considering both crack opening strain and shear strain, or

$$dW = -\frac{32(1-\upsilon^2)}{E} N_0 R_m^3 W d\bar{p} \tag{10.17}$$

if only the crack opening strain is considered. $\bar{p}$ is the averaged pressure in the composite of solid and cracks. When the solidity reaches a critical value W_c we regard the process of brittle spallation to be complete and separation takes place. By

using this concept, the modelling of brittle spallation is compatible with that of ductile spallation presented in the last chapter.

4 Evaluate the relaxation of tensile stress, ignoring the volumetric strain relaxation of the matrix material due to the cracks opening

In general, the stress relaxation occurs by two basically different processes. First, the volumetric strain of the matrix material can relax elastically due to cracks growing and the associated mean tensile stress also relaxes. Secondly, the decrease of load-bearing area introduces stress relaxation. We assume that the volumetric strain of the matrix material is sufficiently small during the spall process that the associated pressure relaxation due to cracks opening can be omitted, which would overestimate the spall peak. The pressure relaxation due to the decrease of load-bearing area is given by;

$$\overline{p} = W\overline{p_s}\,(\overline{V_s},\overline{e_s}) \tag{10.18}$$

where the subscript s indicates the value of the solid constituent. A bar over a variable indicates one averaged over the cell appropriate for finite difference numerical simulation. $\overline{e}_s$ is the internal energy of the solid constituent and the equation of state for the solid constituent is given by

$$\overline{p_s} = \overline{p_s}(\overline{V_s}, \overline{e_s}) \tag{10.19}$$

10.3 SIMPLE MACROSCOPIC MODEL

In Chapter 9 a macroscopic model for ductile spallation was presented based on the collective response of the material. A macroscopic model for ductile spallation is hereunder presented along the same lines. The theoretical model was developed as follows:

1 Define the critical tensile pressure p_f.

We define p_f as such a tensile pressure that when tensile pressure $\overline{p}$ reaches p_f at the time t*, deforming the solid constituent further is much more difficult than developing microfractures. This definition is similar to the assumption presented by Cochran and Banner [7] (1977). The absolute value of the defined p_f is equal to or greater than the nominal spall strength. It is often necessary to obtain a first estimate of the spall strength before obtaining the actual value by a combination of experimentation and numerical modelling. Such an estimate is obtained by:

$$p_f = (3\rho C_0 K_C^2 \dot{\varepsilon})^{1/3} \tag{10.20}$$

which is given by Grady [5] (1988) using the energy balance analysis.

where

K_c fracture toughness

$\dot{\varepsilon}$ dilational strain rate

C_0 bulk sound speed

ρ density

In the last Chapter, we identified the ductile spall strength as the threshold pressure for a mean void growth, it is interesting to consider whether the brittle spall strength is the threshold pressure for a mean crack growth.

The threshold pressure p_g for crack growth adopted by Curran et al [2] (1987) is

$$p_g = \sqrt{\frac{\pi}{rR}}\, K_c \tag{10.21}$$

If we consider the meaning of mean crack growth, another expression for estimating p_f can be deduced from Equation (10.21) thus,

$$p_f = \sqrt{\frac{\pi}{4R_m}}\, K_C \tag{10.22}$$

In addition, under the assumptions of an exponential size distribution and isotropy,

Addessio et al [5] (1990) indicated that global cracks would grow when;

$$\frac{3}{2}S_{ij}\,S_{ij} + \frac{45}{4(5-\upsilon)}\left((2-\upsilon)p^2 - 2\frac{K}{R_m}\right) \geq 0 \qquad (10.23)$$

where

S_{ij} deviatoric stress components, and

$$K \equiv \frac{\pi}{2}\left(\frac{2-\upsilon}{1-\upsilon}\right)\gamma G \qquad (10.24)$$

γ is the crack surface energy and is given by:

$$\gamma = \frac{K_c^2}{2\rho C_0^2}$$

The quantity ($3/2\ S_{ij}S_{ij}$) is the effective shear stress σ^2_e and an alternative estimate of the threshold pressure p_f for the mean crack growth can be derived from Equation (10.23);

$$p_f = \left(2\frac{K}{R_m(2-\upsilon)} - \frac{4(5-\upsilon)}{45(2-\upsilon)}\,\sigma_e^2\right)^{0.5} \qquad (10.25)$$

In fact,

$$2\frac{K}{(2-\upsilon)R_m} >> \frac{4(5-\upsilon)}{45(2-\upsilon)}\sigma_e^2$$

especially for an isotropic tensile stress state (uniaxial strain), $S_{ij}S_{ij} \sim 0$, the expression (10.25), can therefore be simplified as:

$$p_f = \left(2\frac{K}{(2-\upsilon)R_m^{1/2}}\right)$$

by using Equation (10.24) and substituting for γ;

$$p_f = \sqrt{\frac{3\pi(1-2\upsilon)}{4(1-\upsilon^2)R_m}}\,K_c$$

Therefore,

$$p_f \propto \frac{K_c}{\sqrt{R_m}} \qquad (10.26)$$

On the other hand, Equation (10.20) can also be expressed in terms of the mean crack R_m providing that the fragment size as defined by Grady [4] (1988) is considered as $2R_m$.

$$2R_m = d = 2(\sqrt{3}K_c/\rho C_0\dot{\varepsilon})^{2/3} \tag{10.27}$$

where, we have adopted the same assumption as Curran et al [2] (1987), that the cracks forming the fragment sides have about the same area as the sides, so that the fragment sizes are related to the crack sizes by a factor of near unity. From Equation (10.20) and (10.27), p_f can be expressed as

$$p_f = \sqrt{\frac{3}{R_m}}\, K_c \tag{10.28}$$

Obviously, the p_f given by Equation (10.28) is about two times that given by Equation (10.22) and (10.26). For steel, $K_c = 0.3$ GPa $(cm)^{1/2}$, the p_f given by Equation (10.22) and (10.28) are 2.0 - 4.0 GPa if R_m is 0.017 cm. However, according to the experimental results for Armco iron, described by Equation (10.14) and (10.15), the mean crack size R_m is near 0.001 cm and the p_f given by Equation (10.22), (10.26) and (10.28) are 8.0 ~ 16 GPa, which are much higher than expected.

Therefore, how an appropriate mean crack size R_m is chosen remains to be demonstrated. As a result, a mean crack growth based spallation model may be unsuitable. This is one of the primary reasons why we proposed characterising the completion of brittle spallation (separation of material) by the use of a critical value of the solidity W rather than a critical value of damage $N_0R^3_m$ in the simplified

microscopic model presented earlier in this chapter.

Of course, Equation (10.20) can first be used to estimate the brittle spall strength. There are a lot of experimental data indicating that the brittle spall strength is not a constant material parameter but a function of loading condition [6] (1992). The determination of the value of p_f depends on the comparison between numerical and experimental velocity history of the free surface of the target in the flat impact of plates of material.

2 Define the gross porosity $\bar{\phi}$.

According to the definition of the critical tensile pressure p_f, the gross solidity $\bar{W}$ and porosity $\bar{\phi}$ are defined by

$$\bar{W} = \bar{\rho}/\bar{\rho}* \tag{10.29}$$

$$\bar{\phi} = 1 - \bar{W} \tag{10.30}$$

where $\bar{\rho}$ and $\bar{\rho}*$ are the gross density of the damaged material at the time $t > t*$ and the time $t*$.

3 Assume that when the gross porosity $\bar{\phi}$ reaches a critical value $\bar{\phi}_c$

the spallation becomes complete.

While damage is occurring, the tensile pressure $\bar{p}$ is assumed to be relaxed by

$$\bar{p} = p_f \left(1 - \frac{\bar{\Phi}}{\bar{\Phi}_c} \right) \tag{10.31}$$

4 Evaluate the gross damage from the whole governing equations including the equation of state for porous materials.

The equation of state for porous material is given by

$$\bar{p} = \bar{W}\, \bar{p_s}(\bar{V_s}, \bar{e_s}) \tag{10.32}$$

10.4 APPLICATION

The effective method for verifying the effectiveness of the spall model is through the comparison between experimental and computational velocity history of the free surface of the target in the plane impact of plates of material.

10.4.1 Numerical Simulation

The models presented above were incorporated into a one dimensional finite difference code. It can very easily be extended for use in two and three dimension hydrocodes. An example of two dimensional application is presented in Chapter 12.

The equations for conservation of mass, momentum and energy are:

$$\frac{\overline{V}}{\overline{V}} = \frac{\partial \overline{u}}{\partial x} \tag{10.33}$$

$$\frac{\overline{u}}{\overline{V}} = \frac{\partial \overline{\sigma}}{\partial x} \tag{10.34}$$

$$\overline{e} = \overline{V}\,\overline{s_1}\,\overline{\varepsilon_1} + (\overline{p} + \overline{q})\,\overline{V} = 0 \tag{10.35}$$

where

$\overline{u}$ velocity

x coordinate

$\overline{\sigma}$ $= -(\overline{p} + \overline{q}) + \overline{s}_1$ (total stress)

$\overline{s}_1$ deviatoric stress

$\overline{q}$ artificial viscosity

$\overline{\varepsilon}_1$ $\partial\overline{u}/\partial x$ strain rate

The equation of state for porous material is

$$\bar{p} = W\overline{p_s}(\bar{V}_s, \bar{e}_s) \tag{10.18}$$

for the simplified microscopic model or

$$\bar{p} = \overline{Wp_s}(\bar{V}_s, \bar{e}_s) \tag{10.32}$$

for the simple macroscopic model.

The solidity evolution is given by

$$dW = -\frac{128\pi(1 - \upsilon^2)}{E} N_0 R_m^3 W d\bar{p} \tag{10.16}$$

The gross solidity $\bar{W}$ is given by

$$\bar{W} = \bar{\rho}/\bar{\rho}* \tag{10.29}$$

The modulus is reduced as a function of the developing porosity according to

$$\hat{G} = G(1 - (1 - W)F) \tag{10.36}$$

or

$$\hat{G} = G(1 - (1 - \bar{W})F) \tag{10.37}$$

where $\hat{G}$ is degraded shear modulus and

$$F = 15\frac{1 - \upsilon}{7 - 5\upsilon} \tag{10.38}$$

The primary objective of the present study is to develop simple models for brittle spall and to examine the effects of the models themselves on the velocity history of the free surface of the target. Therefore, no attempt is made to consider the effects of the complex constitutive equation on the planar spallation. The ideal plastic is assumed, and the yield strength σ_0 is reduced as a function of the developing porosity according to

$$\hat{\sigma}_0 = \sigma_0 W \tag{10.39}$$

or

$$\hat{\sigma}_0 = \sigma_0 \overline{W} \tag{10.40}$$

where σ_0 is the degraded yield strength.

In the finite difference calculation, the Equation (10.18) or (10.32) of state for porous material is coupled with the Equation (10.35) of energy conservation to solve the pressure $\overline{p}$ and internal energy $\overline{e}$ which is equal to $\overline{e}_s$ providing surface energy effects

are small.

It is notable that introducing gross solidity $\bar{W}$ instead of W to describe the damage of material has the advantage of avoiding the additional Equation (10.16) of solidity evolution. The correlation between the $\bar{W}$ and W is obviously of interest.

10.4.2 Comparison between experimental and computational results

Let us use an example to explain the effectiveness of the developed brittle spall models.

The plane plate impact experiment is that of a 6 mm thick steel target impacted by a 2 mm thick steel plate at a velocity of 0.4 mm/μs. Details of the experiment are included in Chapter 12.

Fig.10.1 shows a plot of the experimental velocity history of the free surface of the target plate. The two curves in Fig.10.1 are the calculated velocity histories using the simple microscopic model and the macroscopic model. The equation of state used for the solid constituent was that given by Hageman et al [7] (1975).

The numerical results in Fig. 10.1 indicate that the spallation process becomes complete at time t = 1.9μs. The spall shock reflected into the scab at rupture reached

the original free surface of the target at t = 2.3μs, resulting in the free-surface jump off. Comparisons of the computational velocity history of the free surface of the target with the experimental record are reasonably good.

10.4.3 Analysis and discussion

The solidity W and gross solidity $\bar{W}$ both reach the critical value of 0.98 at the time t = 1.9μs for the curve 1 and 2 in Fig. 10.1. Numerical simulation indicates that the values of $\bar{W}$ given by Equation (10.24) and the value of W given by Equation (10.10) are nearly the same during the latter stages of the spall process. The two curves are virtually similar, showing that the two models agree closely with the experimental data.

It is important to note that the value of $N_0R_m^3$ in Equation (10.16) has less effects on the calculated velocity history of the free surface of the target because the solidity W reached the critical value W_c in a short time. W is therefore insensitive to the value of $N_0R^3_m$ since once it reaches W, it remains constant.

It is probably necessary to emphasize that the solidity given by Equation (10.16) is not localised in the mean crack size. For ductile spall, assuming that the total volumetric strain rates are sufficiently small and the void growth rates are sufficiently large, we developed simplified distention growth equations, presented in Chapter 9,

which are localised in the mean void size. Ignoring the strain hardening and strain rate dependence of the yield stress, the distention growth equation is given by;

$$d\alpha = \frac{3(\alpha -)\alpha}{2\sigma_0} d\bar{p} \tag{10.41}$$

where distention α is

$$\alpha = \frac{1}{W} = \frac{b^3}{b^3 - a^3} \tag{10.42}$$

b external radius of the mean void

a internal radius of the mean void

In terms of the distention α, Equation (10.16) is;

$$d\alpha = \frac{128\pi(1 - \nu^2)}{E} N_0 R_m^3 \alpha \, d\bar{p} \tag{10.43}$$

It is apparent that the increase of distention given by Equation (10.41) is faster than the increase of distention given by Equation (10.43).

In fact, the rigorous distention growth equation could be obtained form Equation (10.13);

$$\frac{d\alpha}{\alpha} = \frac{128\pi(1 - \upsilon^2)}{E}(N_0 R_m^3 \, d\bar{p} + 3\bar{p}N_0 R_m^2 dRm + \bar{p}R_m^3 dN_0) \qquad (10.44)$$

However, Equation (10.44) would involve the growth equations of the total number N_0 of cracks per volume and the mean crack size R_m.

The numerical simulations seem to support our assumption that when the tensile pressure reaches the spall strength the further increase of the distention is mainly due to the crack opening strain and the crack shear strain caused by the tensile pressure, relaxed at a certain value of $N_0 R_m^3$. Thus, the simplified microscopic model would avoid involving the details of nucleation and growth of cracks.

10.5 CONCLUSION

1 In contrast with identifying the ductile spall strength as the threshold pressure for a mean void growth, it remains to demonstrate how an appropriate mean crack size R_m is chosen to identify the brittle spall strength as the threshold pressure for a mean crack growth. Therefore, it is difficult to provide a rigorous justification for expressing the brittle spallation in terms of the mean crack size R_m. In other words, although mean void-growth based failure models to describe ductile spall are successful, a mean crack growth-based failure model for brittle spall seems to be unsuitable.

2 The modelling of brittle spall would be compatible with ductile spall modelling providing that the solidity evolution is expressed by the crack opening strain, and the crack shear strain and the complete brittle spallation is characterised by a critical value of the solidity W rather than a critical value of damage $N_0R_m^3$.

3 Under the assumption that when the tensile pressure reaches the spall strength the further decrease of the solidity W is mainly due to the crack opening strain and the crack shear strain caused by the tensile pressure, relaxed at a certain value of $N_0R_m^3$, the simplified microscopic model for brittle spall would avoid involving the details of nucleation and growth of cracks. The numerical simulations appear to support this assumption.

4 The simplified microscopic model for brittle spall and the simple macroscopic model produce basically consistent spallation signal and the critical value of solidity W_c is near the critical value of gross solidity $\bar{W}_c$.

5 The comparisons between experimental and computational velocity history of the free surface of the target in the plane impact of plates of material are reasonably good. Therefore, the simplified microscopic

model for brittle spall and the simple macroscopic model are expected to provide good prediction and analysis of the brittle spall behaviour in engineering application.

REFERENCES

1 H Liebowitz, ed., "Fracture", (Academic, New York, 1968), Vol. 1.

2 D R Curran et al, Physics Reports, V.147 (1987) 253

3 F L Addessio et al, J. Appl. Phys. V.67, (19990) 3275

4 S Cochran et al, J. Appl. Phys. V48, (1977) 2729

5 D E Grady, J. Mech. Phys. Solids, V.36 (1988) 353

6 W Winkler et al, in "Shock compression of condensed matter 1991", p 475, S C Schmidt et al (Editors) Elsevier Science Publishers, B V (1992)

7 L J Hageman et al, Systems, Science and Software SSS-R-75-2654 (1975)

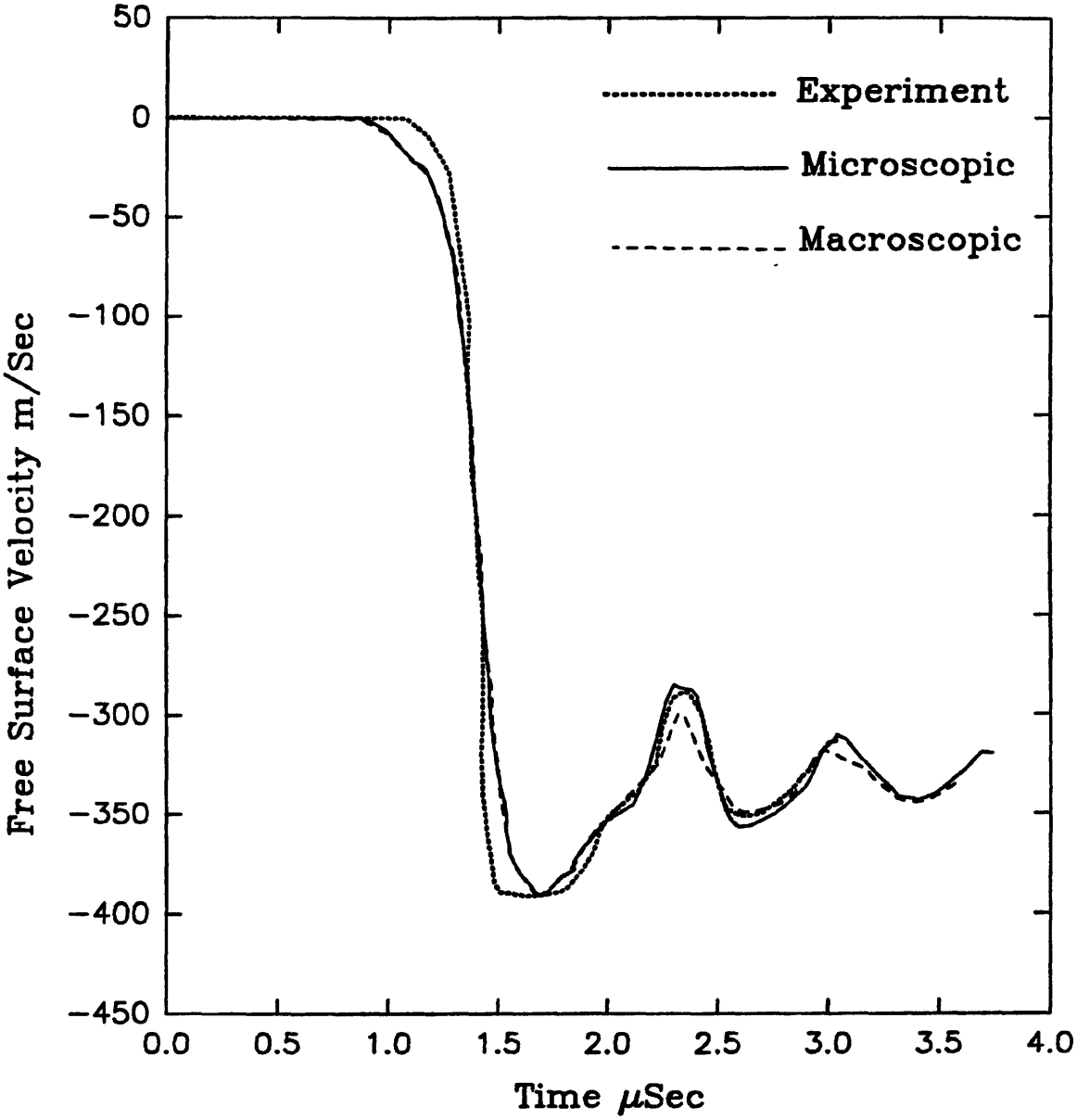

Fig. 10.1 Comparisons Between Experiment and Calculations for Steel Planar Spall

CHAPTER ELEVEN

A SIMPLE UNIFIED SPALLATION FAILURE MODEL

11.1 SUMMARY

This Chapter presents a macroscopic view of the phenomenon of dynamic spallation. A simple new theoretical model was developed to characterise the average continuum behaviour of the spall process and to be applicable to both ductile and brittle spallation. While spallation models often require more than a dozen parameters, the new model requires only two parameters. The model was incorporated into a one dimensional hydrodynamic code to demonstrate its applicability to one dimensional dynamic impact problems. The model can be used with common equations of state and constitutive equations and can be extended to two and three dimensional problems, as will be evident in chapter twelve.

To demonstrate the applicability of the model, the free surface velocity (spall signal) of the target in a plane plate impact experiment was simulated for both ductile and brittle materials. These were compared with experimental data, and show a good agreement.

Plate impact experiments were carried out for ductile and brittle materials recording the free surface velocity history (spall signal). These compare very well with the results of the one dimensional simulations.

11.2 INTRODUCTION

In Chapter nine and Chapter ten microscopic and macroscopic models to describe ductile and brittle spallation, respectively, were presented. There are some similarities between the simple macroscopic model for ductile spall and the simple macroscopic model for brittle spall. This is by no means unexpected or unusual. Several researchers have, in the past, presented models that are essentially based on ductile hole growth but use it to model the spallation of brittle materials, sometimes with some degree of adaptation. For instance, the model presented by Cochran and Banner [1] (1977) and later adapted for strain rate effects by Steinberg [2] (1981) was used in both papers to model the spallation of uranium, and beryllium. The model assumed a statistical distribution of spherical holes. In the last chapter we explained that the process of brittle microfracture occurs by a series of complex processes. Some of these processes are prominent in the mechanism of ductile flaw growth. An example is the shear bending process which links microcracks between their tips.

For very brittle materials, one would expect the microcracks to obey the classical linear elastic fracture mechanics. This would mean an almost instantaneous acceleration of

the cracks to a limiting velocity, the Rayleigh wave speed. Indeed crack speeds close to this value have been reported for glass [3] (1959). However, researchers have reported cleavage crack speeds to be significantly less for structural materials [4] (1973).

Using an energy balance approach for crack growth in elastic materials, Mott [5] (1948) derived the following for crack growth;

$$\dot{R} = V_T (1 - R^*/R)^{1/2} \tag{11.1}$$

where, R^* is the critical crack size for growth of a penny-shaped crack;

$$R^* = \frac{\pi K_{1c}^2}{4\sigma^2}$$

V_T is the terminal velocity, the limiting speed approached as the crack becomes long. K_{1c} is the plane strain fracture toughness.

Berry [6] (1960) presented a more complex form of the above growth law;

$$\dot{R}^2 = V_T^2 (1-R^*/R) [1-(2n^2-1) R^*/R] \tag{11.2}$$

where n is the ratio of the critical stress to applied stress, σ_c/σ.

When the cumulative number of cracks per unit volume is plotted against the evolving crack radius R - see Fig 11.1, it is seen that there is a sudden break at $R = R^*$ and for larger R the curve is concave downwards. In their experimental work with brittle materials, Armco Iron, beryllium, and polycarbonate, Seaman et al [4] (1973) found that the evolution of the cumulative number of cracks ($N\phi(x,t,R)$, did not follow the forms shown in Fig.11.1. Instead of being concave downwards, they found it pivoted out as sketched in Fig 11.2. This, they showed, indicates the same viscous growth relation found for ductile voids. The growth law previously derived by Poritsky [7] (1952) for the expansion of spherical voids in a viscous fluid;

$$\frac{\dot{R}}{R} = \sigma_m - \frac{\sigma_{go}}{4\eta} \tag{11.3}$$

where,

σ_m is mean tensile pressure

σ_{go} is growth threshold

η is viscosity

It is clear that the growth law expected for brittle crack growth is not too dissimilar to that for ductile hole growth. No surprises therefore, that in considering the collective response of material the macroscopic models for brittle and ductile spall, presented in chapters nine, ten, show some similarities.

In this chapter we present a simple failure model applicable to both ductile and brittle materials and based on a macroscopic view of the spallation process while conforming with the microscopic nature of the physics of the phenomenon. It is important however, to distinguish the macroscopic view point from the treatment of a single or a few microcracks as in the method of Griffiths and Irwin in the traditional fracture mechanics. The model was incorporated into a one dimensional and a two dimensional hydrocode and applied to the one dimensional problem of planer plate impact test.

Spallation experiments of planer plate impact were carried out for three different materials and the back-face velocity, the so called spall-signal, was recorded. This was compared with the numerical simulations using our simplified model, and a very good agreement was obtained.

11.3 THE THEORETICAL MODEL

The analytical and computational approaches to the modelling of the spallation phenomenon is almost universally a microscopic one. Various microscopic parameters including microvoid concentration, orientation and size distribution functions, as well as specific rate dependence, were used as internal variables, in constitutive equations, in addition to strain, entropy and temperature. In the last chapter we showed that the use of a mean crack based model to describe brittle spallation may be unsuitable, because the way in which an appropriate mean crack size, is chosen is yet to be

demonstrated. Furthermore, there is evidence that in many cases spall properties are not very sensitive to microstructural details [8] (1988). In our model, we move away from such micro-parameters and consider the collective response of the material by introducing gross parameters to characterize the average continuum behaviour of the spall process. This has the advantage of avoiding the additional rate equation of damage growth and the complex constitutive equation with the mean crack or void size as internal variable appropriate for localised damage. As a result our model can be combined with the usually used equations of state and constitutive equations, making it easy to use with existing hydrocodes.

The Simple Unified Spallation Failure Model was developed as follows:

(1) First we define the critical pressure, p_f, as such a tensile pressure that when the average tensile pressure, $\bar{p}$, reaches p_f at the time t^*, deforming the solid constituent further is much more difficult than growing voids or cracks for the damaged material. This assumption is similar to that which was presented by Cochran and Banner [9] (1977).

(2) We define the gross solidity, $\bar{W}$, as the specific volume of the solid constituent, $\bar{V}_s$, divided by the total specific volume, $\bar{V}$. The gross distention, $\bar{\alpha}$, and porosity, $\bar{\phi}$, are $1/\bar{W}$ and $1-\bar{W}$ respectively. It is necessary to emphasise that $\bar{W}$, $\bar{\alpha}$ and $\bar{\phi}$ are concerned with gross values rather than mean void or crack. According to the definition of critical tensile pressure

P_f, $\bar{W}$, $\bar{\alpha}$ and $\bar{\phi}$ are approximately;

$$\begin{aligned} \bar{W} &= \bar{\rho}/\bar{\rho}^* && (11.4) \\ \bar{\alpha} &= \bar{\rho}^*/\bar{\rho} && (11.5) \\ \bar{\phi} &= 1-\bar{\rho}/\bar{\rho}^* && (116) \end{aligned} \qquad (5)$$

where $\bar{\rho}$ and $\bar{\rho}^*$ are the gross density of damaged material at the time $t > t^*$ and the time t^* respectively. From here on, a bar over a variable indicates one averaged over the cell appropriate for the whole finite-difference numerical simulation.

(3) We assume that the spallation is complete when the gross porosity, $\bar{\phi}$, reaches a critical value, $\bar{\phi}_c$. This critical gross porosity is obviously smaller than the critical mean void volume fraction, ϕ_c, because $\bar{\phi}_c$ is defined over a bigger region than ϕ_c.

(4) We evaluate the gross damage from the whole governing equations based on the collective material response rather than the mean void or crack size.

11.3.1 Estimating the critical pressure:

We define the critical pressure, p_f, as the tensile pressure beyond which further deformation of the solid constituent becomes more difficult than growing voids or cracks for the damaged material. Therefore, the absolute value of p_f is equal to or greater than the usually defined (nominal) spall strength. The determination of the value of p_f depends on the comparison between numerical simulation and experimental data of the planar spall. This is because the minimum free surface velocity (pull back velocity) in the plane impact plate test, is dependent

mainly on p_f, see Fig.11.3. Where spall strength is not available it is necessary to estimate p_f first.

There are several ways of estimating p_f. For example, in using the energy balance analysis to assess the spall strength Grady [8] (1988) estimated spall strength as follows:

For brittle spall (fracture toughness dominated spall),

$$p_f = (3\rho c_0 K_c^2 \dot{\epsilon})^{1/3} \qquad (11.7)$$

where,

- K_c fracture toughness
- $\dot{\epsilon}$ dilational strain rate
- c_0 bulk sound speed

For ductile spall (flow stress dominated spall),

$$P_f = (2\rho c_0^2 Y \phi_c)^{1/2} \qquad (2.8)$$

where,

- Y the flow stress in simple tension
- ϕ_c the critical void volume fraction

Also brittle and ductile spall strength can be derived from the threshold pressure for crack or void growth.

For an exponential distribution, the number density, N, of cracks with radius larger than crack length, C, is given in ref [10] as;

$$N(C,\Omega)dc = \int_{c}^{\infty} n(c,\Omega)dc = N_0(\Omega)\exp\left(-\frac{C}{C_m(\Omega)}\right) \qquad (11.9)$$

for high-velocity impact problems, it is anticipated that the initial distribution N_0 and mean crack size C_m are assumed independent of orientation Ω.

Under the assumptions of an exponential size distribution and isotropy, global cracks will grow when:

$$\frac{3}{2} S_{ij}S_{ij} + \frac{45}{4(5-\upsilon)}\left((2-\upsilon)p^2 - \frac{2K}{C_m}\right) \geq 0 \qquad (11.10)$$

where,

S_{ij} the deviatoric stress components

υ Poisson's ratio

γ the crack surface energy

G the shear modulus and

p tensile pressure

$$K = \frac{\pi}{2}\left(\frac{2-\upsilon}{1-\upsilon}\right)\gamma\, G$$

Equation (11.10) is provided by Addessio et al [11] (1990). The quantity 3/2 $S_{ij}S_{ij}$ is the effective shear stress, σ_e^2 defined in general as:

$$\sigma_e^2 = \frac{3}{2} s_{ij} S_{ij} \qquad (11.11)$$

Now, we can derive the threshold pressure, p_f, for the mean crack growth from Equation (11.10)

$$p_f = \left[\frac{2K}{C_m(2-\upsilon)} - \frac{4(5-\upsilon)}{45(2-\upsilon)} \sigma_e^2 \right]^{1/2} \qquad (11.12)$$

In fact,

$$\frac{2K}{C_m(2-\upsilon)} >> \frac{4(5-\upsilon)}{45(2-\upsilon)} \sigma_e^2$$

especially, for the isotropic tensile stress state (uniaxial strain) $S_{ij}S_{ij} \approx 0$, the threshold pressure p_f is;

$$p_f = \left(\frac{2K}{(2-\upsilon)C_m} \right)^{1/2} \qquad (11.13)$$

On the other hand, we found that Equation (11.7) could also be expressed in terms of the mean crack, C_m, providing that the fragment size, d, as defined by Grady [8] (1988) is

considered as $2C_m$:

$$2C_m = d = 2(\sqrt{3}\ K_c/\rho C_0\dot{\epsilon})^{2/3} \qquad (11.14)$$

From Equation (11.7) and (11.14), p_f is given by;

$$p_f = \sqrt{\frac{3}{C_m}} \qquad (11.15)$$

In addition, the threshold stress, p_g, for crack growth adopted by Curran et al [10] (1987) is given by;

$$p_g = \left(\frac{\pi}{4R}\right)^{1/2} K_c \qquad (11.16)$$

In the meaning of mean crack growth, equation (11.16) is;

$$p_f = \left(\frac{\pi}{4C_m}\right)^{1/2} K_C \qquad (11.17)$$

It is interesting to compare the different values of p_f as determined by Equations (11.17), (11.15) and (11.17). Let us use an example. For steel, K_c = 0.3 GPa $(cm)^{1/2}$, ν = 0.3, then the values of p_f given by Equation (11.3), (11.5) and (11.7) are 2.3 GPa, 3.5 GPa and 2.0 GPa

respectively if C_m is 0.017 cm. However if C_m is 0.001 cm, p_f are 9.6 GPa, 14.6 GPa and 8.35 GPa respectively.

The ductile spall strength can be identified as the threshold pressure for void growth. The threshold for void compaction, given by Carroll et al [12] (1972), is applied to the negative situation deriving the following expression;

$$p_f = 2Y/3 \ln(1/\phi_0) \qquad (11.18)$$

where, ϕ_0 is the initial porosity.

The corresponding equation given by J N Johnson [13] (1981) is;

$$p_f = 2Y/3(1-\phi_0) \ln(1/\phi_0) \qquad (11.19)$$

A general expression of the threshold pressure, p_G, for void growth is given by Nemes et al [14] (1990);

$$p_G = -\frac{K_1}{\sqrt{3}}(1-\phi)\ln(\frac{1}{\phi})[2q + (K_0 - q)F_1(\phi,\phi_0)] \qquad (11.20)$$

where,

$$F_1(\phi,\phi_0) = \exp\left[\frac{2}{3}\beta\left(\frac{(\phi_0 - \phi)}{\phi(1-\phi_0)}\right)\left(\frac{1-\phi}{1-\phi_0}\right)^{-2/3}\left(\frac{\phi_0}{\phi}\right)^{-2/3}\right] +$$

$$\exp\left[\frac{2}{3}\beta\left(\frac{(\phi_0 - \phi)}{(1 - \phi_0)}\right)\left(\frac{(1 - \phi)}{(1 - \phi_0)}\right)^{-2/3}\right] \qquad (11.21)$$

K_1, q, K_0 and β are material parameters.

It is also interesting to compare the p_f determined by Equation (11.8), (11.18) and (11.19). Let us use another example, for OFHC copper, Y = 0.25 GPa, c_0 = 3.9 mm/μs, the p_f given by Equation (11.8), (11.18) and (11.19) are 1.0 GPa, 1.35 GPa and 1.35 GPa respectively; ϕ_c and ϕ_0 are 0.15 and 0.0003 as chosen by Grady and Johnson respectively.

It should be noted that p_f is not a constant material parameter as shown in previous equations. It is dependent on the loading condition. In fact there are numerous experimental data indicating that the spall strength is a function of loading condition, see for example [15] (1989) and [16] (1991).

It is also notable that to obtain an exact spall strength in terms of a mean crack or void size is difficult. This is because the way in which an appropriate mean crack or void size is chosen is yet to be demonstrated, although values obtained for ductile materials are reasonable.

It is also possible to determine the spall strength from measurements of the free surface velocity of the target in a ρlane plate impact test. The first Equation is given by Novikov et al [17] (1982).

$$p_f = \frac{1}{2}\rho_0 C_0 (U_{fo} - U_{fr}) \qquad (11.22)$$

where,

U_{fo} the free-surface jump-off velocity

U_{fr} the minimum surface velocity

Since then, there are a lot of papers discussing, Equations (11.22) [18-21] (1986-1990). The following equation is given by Gathers [20] (1990).

$$p_f = \rho_0 (U_{fo} - U_F)[C_0 + \lambda(U_{fo} + U_F)] \qquad (11.23)$$

where,

λ is the stiffness coefficient in the relation between shock velocity D and mass velocity U

$$U_F = \frac{1}{2}\left[-(C_0/\lambda) + \left((C_0/\lambda)^2 + 2[(C_0/\lambda)(U_{fr} + U_{fo}) + (U_{fr}^2 + U_{fo}^2)]\right)^{\frac{1}{2}}\right] \qquad (11.24)$$

$$D = C_0 + \lambda U$$

The spall strength of uranium, copper and steel determined from Fig. 11.4, 11.5 and 11.6 according to Equation (11.22) and Equation (11.23) respectively, are listed in Table 3.1.

In fact, Equation (11.22) and (11.23) are both derived assuming that the spallation happens instantaneously. However, the assumed instantaneous spallation will occur at a higher value of the velocity, U_{fk}, than the experimental measurement. Therefore, the velocity U_{fk} in Equations (11.22) and (11.23) should not, theoretically, be the experimental spall velocity. It is difficult to provide a simple and reasonable formula for determining the exact spall strength from measurements of the surface velocity of the target.

11.3.2 Simplifying the damage evolution:

Continuum damage models are increasingly being applied to model spall phenomena. Most of the recent investigations of the fundamental mechanisms of spall growth is concerned with the mean crack or void size.

For brittle spall, the growth rate, $\dot{C}_m$, of the mean crack is given by Addessio et al [11] (1990).

$$\dot{C}_m = \frac{6\hat{G}S_{ij}\dot{e}_{ij} + N_p^{-1}(WB_s\dot{\epsilon}_{KK} - 2\hat{G}NsS_{ij}\dot{e}_{ij})\frac{\partial f}{\partial p}}{12\beta^e\hat{G}C_m^2 f + N_p^{-1}(N_c - 4\beta^e\hat{G}C_m^2 N_f)\frac{\partial f}{\partial p} + \frac{\partial f}{\partial C_m}} \qquad (11.25)$$

where,

ε_{ij} the total strain

e_{ij} the deviatoric strain

$\hat{G}$ the degraded shear modulus

W the solidity

$N_p = 1 + \beta^e C_m^3[W B_s - (1 + 2 \Gamma_s) p]$

$N_s = \beta^e \Gamma_s C_m^3$

$Nc=\beta^e C_m^2\{2\Gamma_s f - 3p[wB_s-(1+2\Gamma_s)p]\}$

B_s the bulk modulus for the Solid Constituent

Γ_s the Grüneisen Constant for the Solid Constituent

and

$$\beta^e = (5-\nu)\frac{128\pi}{15}\left(\frac{1-\nu}{2-\nu}\right)\frac{N_0}{G}$$

For ductile spall, the growth rate, $\dot{\phi}$, of the mean void size was given by Nemes et al [14] (1990) as;

$$\dot{\phi} = \frac{1}{\zeta} g(\phi)F(\phi,\phi_0)\,(p - p_G) \qquad (11.26)$$

where,

$$F(\phi,\phi_0) = \frac{\sqrt{3}}{2}\,\phi\left(\frac{1-\phi}{1-\phi_0}\right)^{2/3}\left[\phi - \left(\frac{\phi}{\phi_0}\right)^{2/3}\right]^{-1} \qquad (11.27)$$

$g(\phi)$ a material function to describe the interaction between voids

ζ material parameter

p_G given by Equations (11.20) and (11.21).

It is obvious that the research of growth mechanisms of the mean crack or void is, by definition, a microscopic view of the spall process. It involves an elaborate specimen examination and the complex constitutive modelling of high strain-rate local deformation of the damaged material in the mean crack or void scale. There are too many material parameters to determine and it is difficult to provide a rigorous justification for studying spallations in terms of a mean void or crack size.

Therefore, it is important to step back and ponder the collective response of the material. The material cells that we investigate are small enough from the macroscopic point of view but large enough from the microscopic point of view, and are appropriate for the whole finite difference numerical simulation. The solidity, distention and porosity are concerned with gross values rather than a mean crack or void. Furthermore, according to the definition of critical tensile pressure, p_f, the gross solidity, $\bar{W}$, distention $\bar{\alpha}$ and porosity $\bar{\phi}$ are defined by Equations (11.4), (11.5) and (11.6) respectively. When the gross porosity $\bar{\phi}$ reaches a critical value $\bar{\phi}_c$ the fracture becomes complete. Obviously $\bar{\phi}_c$ is smaller than ϕ_c, the critical mean void volume fraction.

It should be noted that Equation (11.26) for the mean void growth rate is also derived under the assumption that the solid constituent is incompressible. In other words, despite its complexity, the estimation of the mean void growth rate, $\dot{\phi}$, with Equation (11.26) is based on the same assumption as that under which the gross porosity, $\bar{\phi}$, is defined by Equation (11.6).

It is also notable that Equation (11.6) is applicable to both brittle and ductile spallation

through different $\bar{\phi}_c$, thereby avoiding the emphasis on the microscopic processes of spall fracture.

11.3.3 Describe the collective response:

As the damage grows, the stress-free surfaces generated in the material diminish the amount of stress generated by the overall deformation. When the porosity, $\bar{\phi}$, reaches a critical value, $\bar{\phi}_c$, the rapid coalescence of cracks or voids results in complete separation and the magnitude of the tensile pressure drops to zero.

The gross porosity, $\bar{\phi}$, is evaluated from the whole governing equations including the equation of state for porous materials. The pressure of the solid constituent is assumed to be given by:

$$\bar{p}_s = \bar{p}_s(\bar{V}_s, \bar{E}_s) \qquad (11.28)$$

where $\bar{E}$ is the internal energy.

The subscript s indicates the value of the solid constituent.

The condition of mechanical equilibrium requires that;

$$A\bar{p} = A_s \bar{p}_s$$

where,

A is the cross-sectional area which transmits pressure.

If the cracks or voids are distributed at random, then;

$$A_s/A = \bar{V}_s/\bar{V}$$
$$= \bar{\rho}/\bar{\rho}^*$$
$$= 1 - \bar{\phi}$$

Therefore,

$$\bar{p} = (1 - \bar{\phi})\,\bar{p}_s(\bar{V}_s, \bar{E}_s)$$

When surface energy effects are small, it may be assumed that the internal energies of the porous and solid constituent are equal. Consequently, the equation of state for porous materials is given by;

$$\bar{p} = (1 - \bar{\phi})\,\bar{p}_s((1 - \bar{\phi})\bar{V}, \bar{E}) \qquad (11.29)$$

The damage also affects both the yield strength and the effective shear modulus of the material. The modulus is reduced as a function of the developing porosity according to the elastic relations of Mackenzie [22] (1950);

$$\hat{G} = G(1 - \bar{\phi}F) \qquad (11.30)$$

where,

$$F = 15\frac{1 - \upsilon}{7 - 5\upsilon} \qquad (11.31)$$

The yield strength should reduce in the following way;

$$\bar{Y} = Y_0(1 - \bar{\phi}) \qquad (11.32)$$

where,

Y_0 is the yield strength for non-porous material.

It is notable that introducing $\bar{\phi}$ instead of ϕ to describe the damage of material has the advantage of avoiding the additional rate equation of damage growth and the complex constitutive equation with the mean crack or void size as internal variable appropriate for localised damage.

11.4 APPLICATION

A common experimental method for causing spall is through the flat impact of plates of material. The effective method for inspecting the spall model is through the comparison between experimental and computational velocity history of the free surface of the target.

11.4.1 Numerical Simulation

For a one dimensional numerical analysis, the equations for conservation of mass, momentum and energy are:

$$\frac{\dot{\bar{V}}}{\bar{V}} = \frac{\partial \bar{u}}{\partial x} \qquad (11.33)$$

$$\frac{\dot{\bar{u}}}{\bar{V}} = \frac{\partial \bar{\sigma}}{\partial x} \qquad (11.34)$$

$$\dot{\bar{E}} - \bar{V}\,\bar{s}_1\,\dot{\bar{\epsilon}}_1 + (\bar{p} + \bar{q})\,\dot{\bar{V}} = 0 \qquad (11.35)$$

where,

$\bar{u}$ velocity

x co-ordinate

$\bar{\sigma} = -(\bar{p} + \bar{q}) + \bar{s}_1$

$\bar{\sigma}$ total stress

$\bar{s}_1$ deviatoric stress

$\bar{q}$ artificial viscosity

$\bar{\epsilon}_1 = \partial\bar{u}/\partial x$ strain rate

The equation of state for solid constituent is;

$$\bar{p}_s = \bar{p}_s(\bar{V}_s, \bar{E}_s) \qquad (11.28)$$

The corresponding equation of state for damaged material is;

$$\bar{p} = (1 - \bar{\phi})\bar{p}_s((1 - \bar{\phi})\bar{V}, \bar{E}) \qquad (11.29)$$

The gross porosity, $\bar{\phi}$, is given by Equation (11.6). The deviatoric stress components depend on the shear modulus and the yield strength, which are each function of porosity $\bar{\phi}$ given by Equation (11.30) and (11.32) respectively.

Instead of introducing stress relaxation as in the macroscopic models presented in chapters nine and ten, the stress is relaxed by incorporating the damage parameter $\bar{\phi}$ into the equation of state as it is solved simultaneously with the energy equation. Tensile pressure is relaxed formally, when spallation commences, linearly to zero, when separation takes place, by the following relation;

$$\bar{p} = \bar{p}_f\left(1 - \frac{\bar{\phi}}{\bar{\phi}_c}\right) \qquad (11.36)$$

Fig 11.4 and 11.5 show spall signals indicating the different tensile pressure relaxation.

In finite-difference calculation, the Equation (11.28) or Equation (11.29) is coupled with the equation of energy conservation, Equation (11.35), to solve $\bar{p}$ and $\bar{E}$.

The primary objective of the present study is to develop a simplified spall model and to examine the effects of the spall model itself on the velocity history of the free surface of the target in the flat impact of plates. Therefore, no attempt is made to consider the effects of the complex constitutive equation. The most commonly used equation of state and flow surface are adopted.

11.5 COMPARISON BETWEEN EXPERIMENTAL AND COMPUTATIONAL RESULTS;

Let us use some examples to investigate the effectiveness of the present simplified spall model.

11.5.1 Example 1

A 6mm thick Uranium target is impacted by a 3mm thick Uranium plate at the velocity of 0.11mm/μs. The experimental and computational velocity history of the free surface of the target is shown in Fig. 11.6. The experimental data are courtesy of Steinberg [2] (1981). The computational result was obtained using our simplified model with the following value of parameters; p_f = 2.5 GPa, Y_0 = 0.8 GPa, G = 84 GPa, $\bar{\phi}_c$ = 0.02. The equation of state for solid constituent is;

$$\bar{p}_s = K\left(\frac{\bar{\rho}_s}{\bar{\rho}_0} - 1\right) + \bar{\rho}_s \Gamma \bar{E} \qquad (11.37)$$

where,

$\bar{\rho}_0$ the initial density

K the bulk modulus (equals 118 GPa)

Γ the Gruneisen parameter (equals 2.2)

The equation of state used for the damaged material is;

$$\bar{p} = K\frac{\epsilon^e}{1 - \epsilon^e} + \bar{\rho}\,\Gamma\bar{E} \qquad (11.38)$$

where,

$$\epsilon^e = 1 - \bar{\rho}_0/\bar{\rho} + \ln \bar{\rho}^*/\bar{\rho} \qquad (11.39)$$

which is the elastic part of the total strain.

11.5.2 Example 2

A 9mm thick copper target is impacted by a 2mm thick copper plate at the velocity of 0.185mm/μs. The experimental and computational velocity history of the free surface of the target is shown in Fig. 11.7. The experimental data was courtesy of Rajendran et al [23] (1989). The computational result was obtained using our simplified model with the following values for the parameters; p_f = 1.3 GPa, Y_0 = 0.12 GPa, G = 47.7 GPa, $\bar{\phi}_c$ = 0.02. The equation of state used for the solid constituent was given by Hageman et al [24] (1975);

$$\bar{p}_s(=\bar{p}_1) = \left(a + \frac{b}{\frac{\bar{E}}{\bar{E}_0\bar{\eta}^2} + 1}\right)\bar{E}\,\bar{\rho} + A\bar{\mu} + B\bar{\mu}^2 \qquad (11.40)$$

where,

$$\bar{\eta} = \bar{\rho}/\bar{\rho}_0 = \bar{\mu} + 1$$

when,

$$\bar{\rho}/\bar{\rho}_0 < 1 \text{ and } \bar{E} > \bar{E}_0'$$

$$\bar{p}_s(=\bar{p}_2) = a\bar{E}\,\bar{\rho} + \left[\frac{b\bar{E}\,\bar{\rho}}{\frac{\bar{E}}{\bar{E}_0\bar{\eta}^2} + 1} + A\bar{\mu}\,e^{-\alpha_2\left(\frac{\bar{V}}{\bar{V}_0} - 1\right)}\right]\left[e^{-\alpha_1\left(\frac{\bar{V}}{\bar{V}_0} - 1\right)^2}\right] \qquad (11.41).$$

when,

$$\bar{\rho}/\bar{\rho}_0 < 1 \text{ and } \bar{E} < \bar{E}_0'$$

$$\bar{p}_s = \frac{(\bar{E} - \bar{E}_0^*)\bar{p}_2 + (\bar{E}_0' - \bar{E})\,\bar{p}_1}{\bar{E}_0' - \bar{E}_0^*} \qquad (11.42)$$

where, a = 0.5, b = 1.5, A = 139 GPa, B = 110 GPa, $\bar{E}_0 = 32.5 \times 10^{10}$ erg/g, $\alpha_1 = 5$, $\alpha_2 = 5$, $\bar{E}_0^* = 138 \times 10^{10}$ erg/g, $\bar{E}_0' = 690 \times 10^{10}$ erg/g.

The equations of state for damaged material are obtained from Equations (11.29) and (11.40) to (11.41).

11.5.3 Example 3:

A 6mm thick steel target is impacted by a 2mm thick steel plate at the velocity of 0.4mm/μs. The experimental velocity history of the free surface of the target is shown in Fig. 11.8. The experimental result was obtained in the manner discussed in Chapter twelve, and the computational result was obtained using our simplified model. The values of the parameters used are: p_f = 2.5 GPa, Y_0 = 0.34 GPa, G = 77 GPa, $\bar{\phi}_c$ = 0.02. The equation of state used for the solid constituent are Equations (11.40) to (11.42). With the following parameters [24] (1975): a = 0.5, b = 1.5, A = 128 GPa, B = 105 GPa, $\bar{E}_0$ = 9.5 x 10^{10} erg/g, α_1 = 5, α_2 = 5, $\bar{E}_0^*$ = 244 x 10^{10} erg/g, $\bar{E}_0'$ = 1020 x 10^{10} erg/g. The equations of state for damage material are obtained from Equations (2.26) and (3.7) to (3.9).

11.6 DISCUSSION:

The relative degree of spall damage is characterised by the spall peak, that is the second maximum in the free surface velocity history of the target (spall signal). The spall peak is dependent on the critical gross porosity and the equation of state for damaged material.

Despite the simplicity of our model, comparisons of the computational velocity history of the free surface of the target in Figs. 11.6, 11.7 and 11.8 with experimental records are very good.

The model is therefore able to characterise the average continuum behaviour of the spall process and to be applicable to both ductile and brittle spallation of practical engineering materials.

11.7 CONCLUSION

In this paper we present a simple spallation failure model which can be applied to both ductile and brittle spallation; through different p_f and ϕ_c. It requires only two parameters; the critical tensile pressure, p_f and the critical gross porosity, ϕ_c. A reasonable estimate of the two parameters can be obtained and the exact determination of p_f and ϕ_c depends on the comparison between numerical simulation and experimental record of the planer spall test, avoiding the complexities of soft recovery and elaborate specimen examination. The first estimate of p_f can be made by energy balance analysis or in terms of mean crack or void size, although how an appropriate mean crack or void size is chosen is yet to be demonstrated. In general, the minimum free surface velocity, in the plane plate impact test, is mainly dependent on p_f and the spall peak is dependent on ϕ_c.

Because the model can be used with popular equations of state and constitutive models, it can be easily incorporated into a one, two or three dimensional hydrodcode. The spall signal in one dimensional simulation of the planar plate impact was compared with experiments for three materials. These show very good agreement.

The model is therefore able to provide simple and reasonable predictions of the spall behaviour of practical engineering materials.

REFERENCES

[1] S. Cochran and D. Banner, J. Appl. Phys.48(1977) 2729

[2] D J Steinberg and R W Sharp Jr., J. Appl. Phys., 52 (8) (1981) 5072

[3] H. Schardin, in: Proc conf on Fracture, Dwampsott, Mass April 12-24, 1959, sponsored by the National Academy of Science and the national Research Council.

[4] L Seaman, D.A. Shockey and D.R. Curran, Dynamic Crack Propagation, ed. George C. Sih Noordhoff, Leyden, 1973) P.629.

[5] N.F. Mott, Engineering 165 (1948) 16.

[6] J.P. Berry, J. Mech and Phys Solids 8 (1960) 194.

[7]. H Poritsky, Proc First U.S. National Congress of Applied Mech. 34 91967) 847..

[8] D E Grady, J. Mech. Phys, Solids, V.36 (1988) 353

[9] S Cochran et al J. Appl. Phys. V. 48 (1977) 2729

[10] D R Curran et al, Physics Reports, V.147, (1987) 253

[11] F L Addessio et al, J. Appl. Phys, V.67 (1990) 3275

[12] M M Carroll et al, J. Apply. Phys, V.43 (1972) 1626

[13] J N Johnson, J. Appl. Phys, V.52 (1981) 2812

[14] J A Nemes et al, J. Appl. Mech, V.57 (1990) 283

[15] K E Froeschner et al, J. Appl. Phys, V.65 (1989) 2964

[16] W Winkler et al, in "Shock Compression of Condensed Matter" (1991) p 475

[17] S A Novikov et al, J. Mech. Tech. Phys, V.123 (1982) 703

[18] D R Ek et al, in "Shock waves in Condensed Matter" (1986) p 413

[19] J E Osher et al, UCRL -98804 (1989)

[20] G R Gathers, J. Appl. Phys, V.67 (1990) 4090

[21] L C Chhabildas et al, Int. J. Impact Energy, V.10 (1990) 107

[22] J H Mackenzie, Proceedings of the Physical Society 63B, No. 2 (1950) 2

[23] A M Rajendran et al, J. Appl. Phys, V.65 (1989) 1521

[24] L J Hageman et al, SSS-R-75-2654 (1975)

Table 11.1 - Spall strength determined from target surface motion according to Equation (11.22) and (11.23) respectively.

Material	Spall Strength (GPa) Det. by Equation (11.22)	Spall Strength (GPa) Det. by Equation (11.23)
Uranium	1.9	2.0
Copper	1.2	1.4
Steel	1.8	2.2

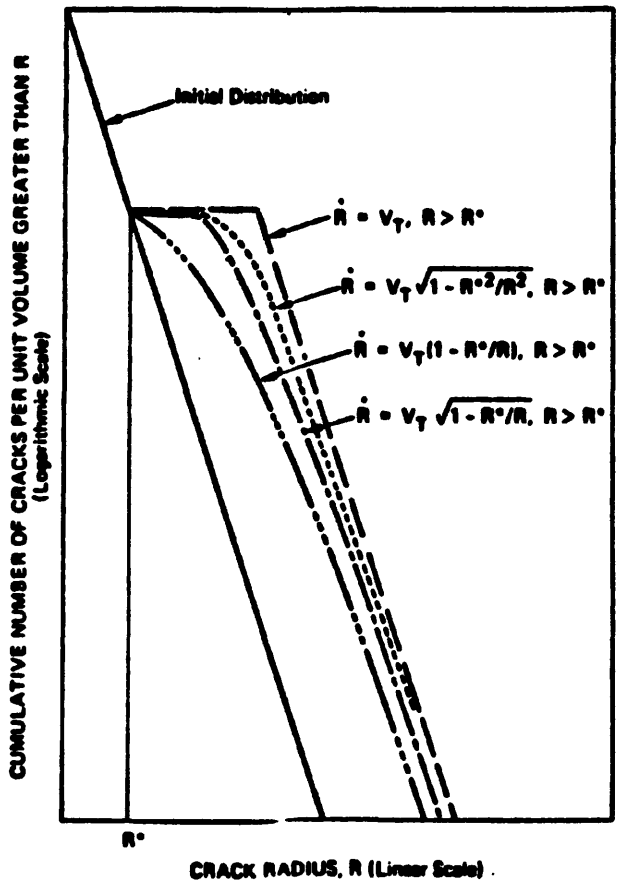

Fig. 11.1 Crack Size Distribution For Different Growth Laws

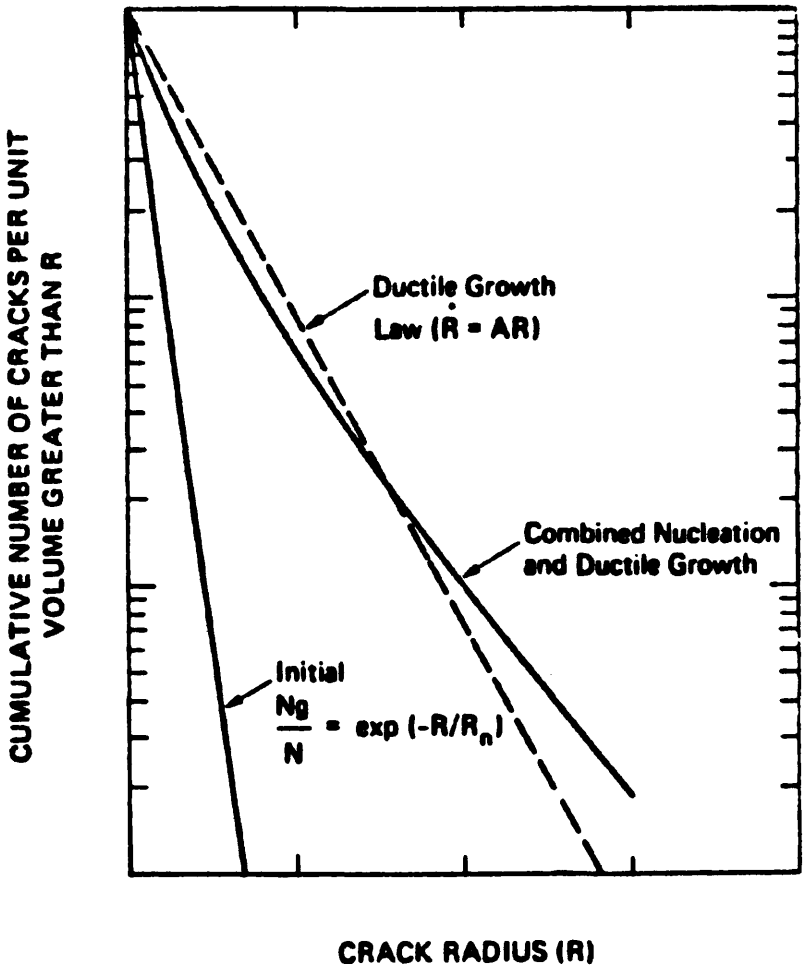

Fig. 11.2 Void Size Distribution From a Ductile Growth Law

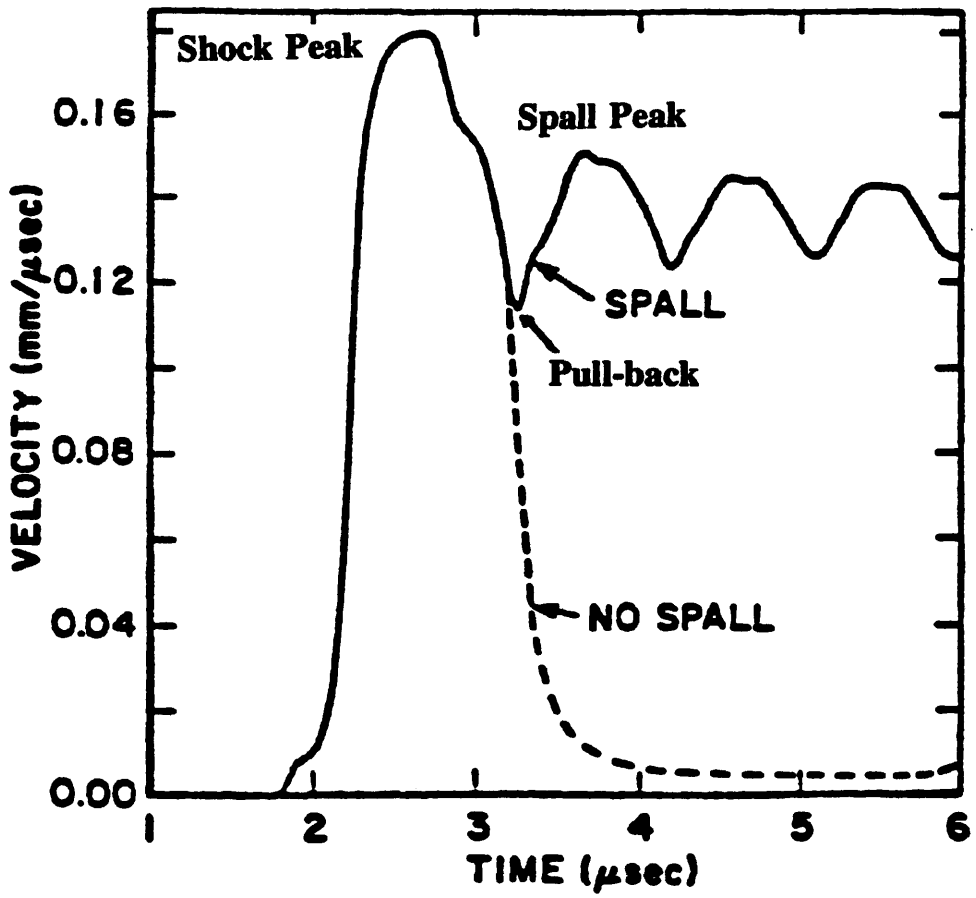

Fig. 11.3 Typical Spall Signal

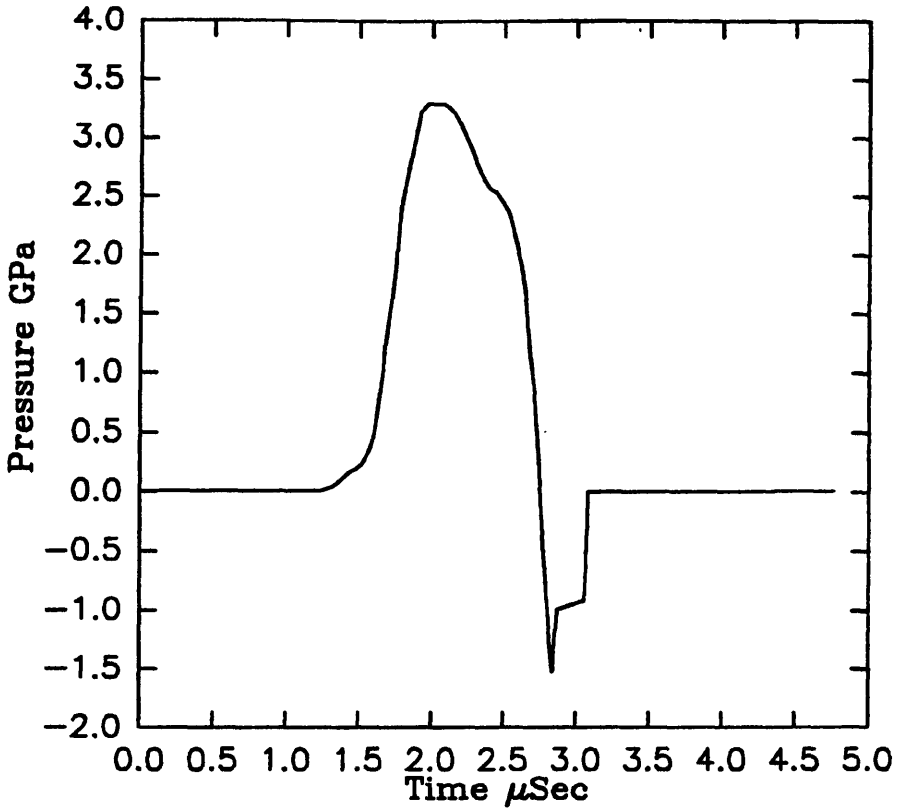

Fig. 11.4 Typical Spall Signal Using Stress Relaxation by a Damage Model

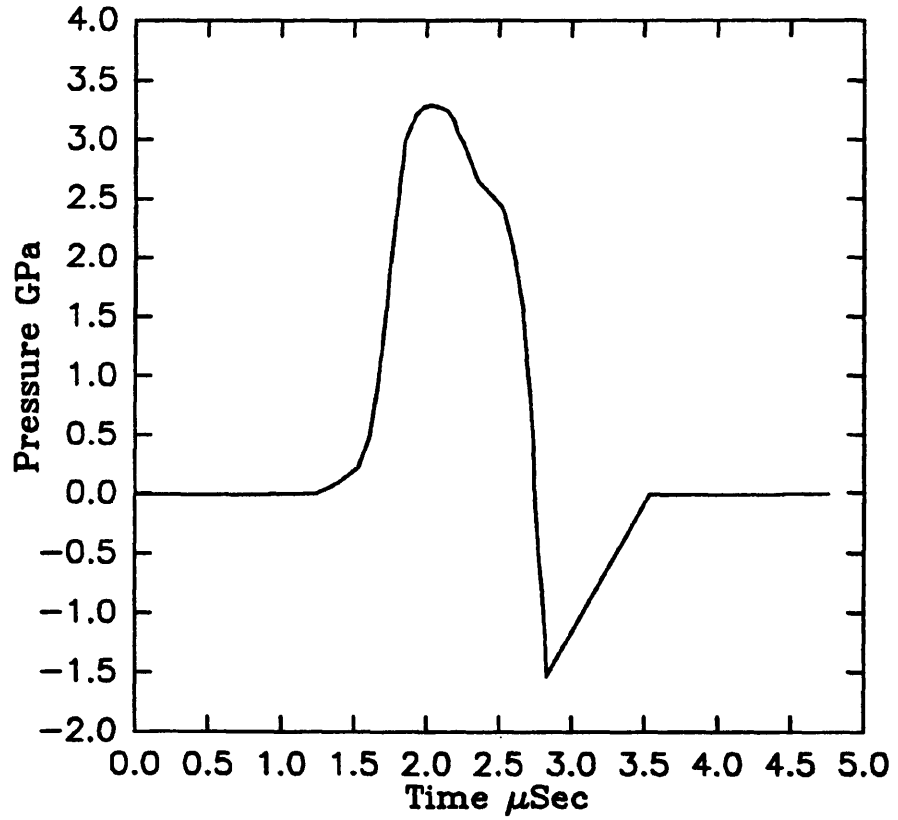

Fig. 11.5 Typical Spall Signal Using Stress Relaxation by Linear Rule

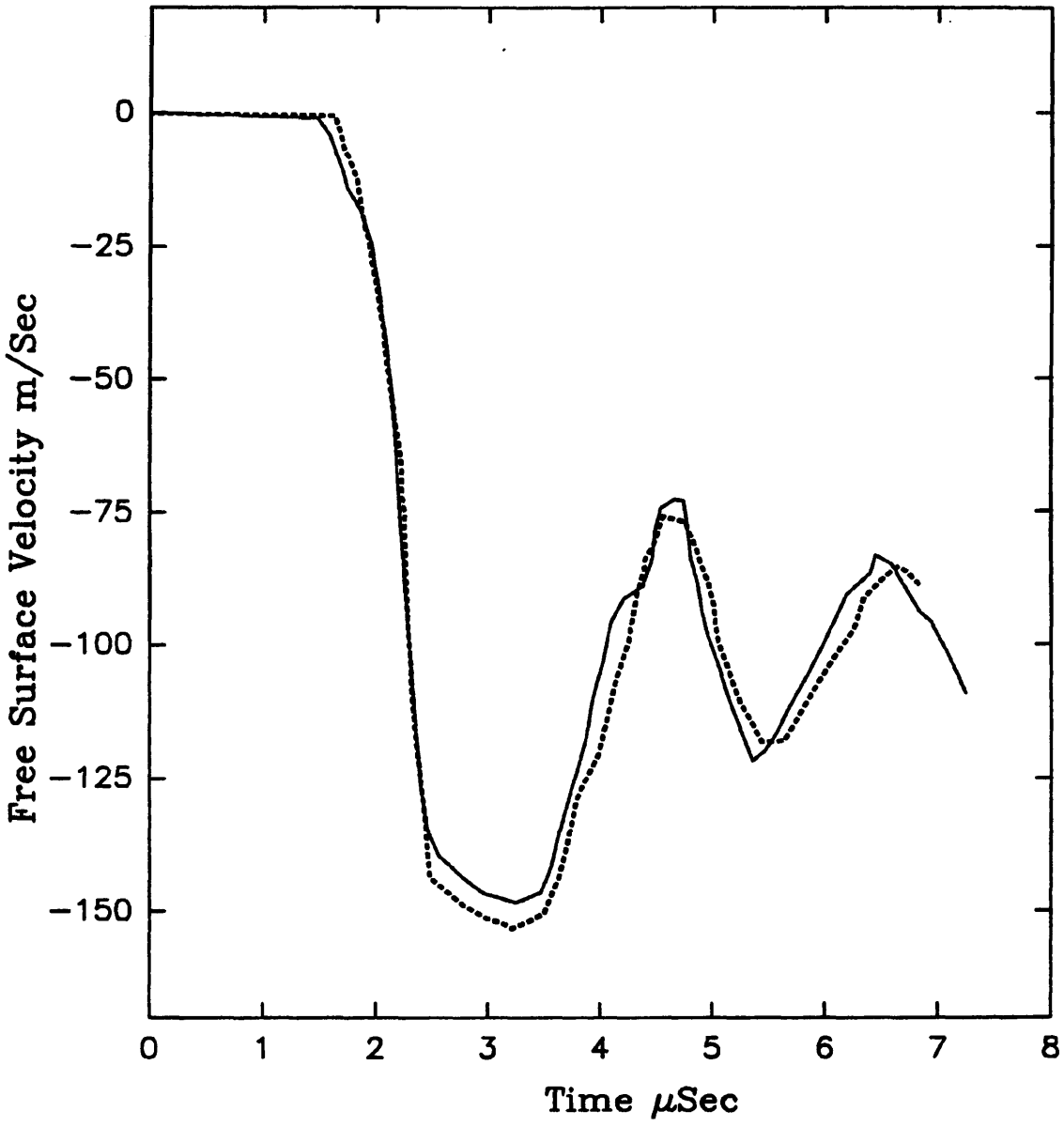

Fig. 11.6 Comparison Between Experiment and Calculation for Uranium Planar Spall

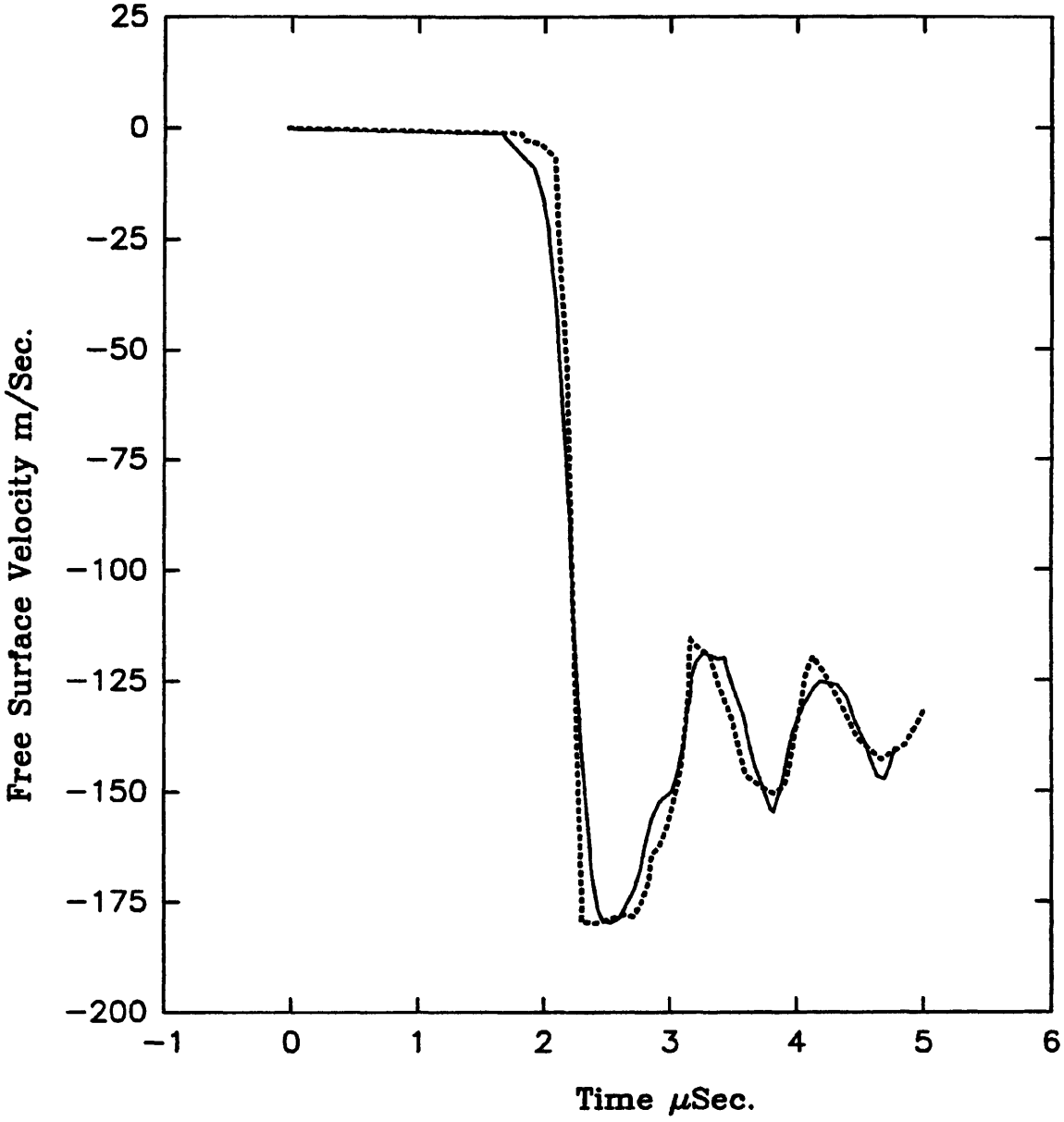

Fig. 11.7 Comparison Between Experiment and Calculation for OHFC Copper Planar Spall

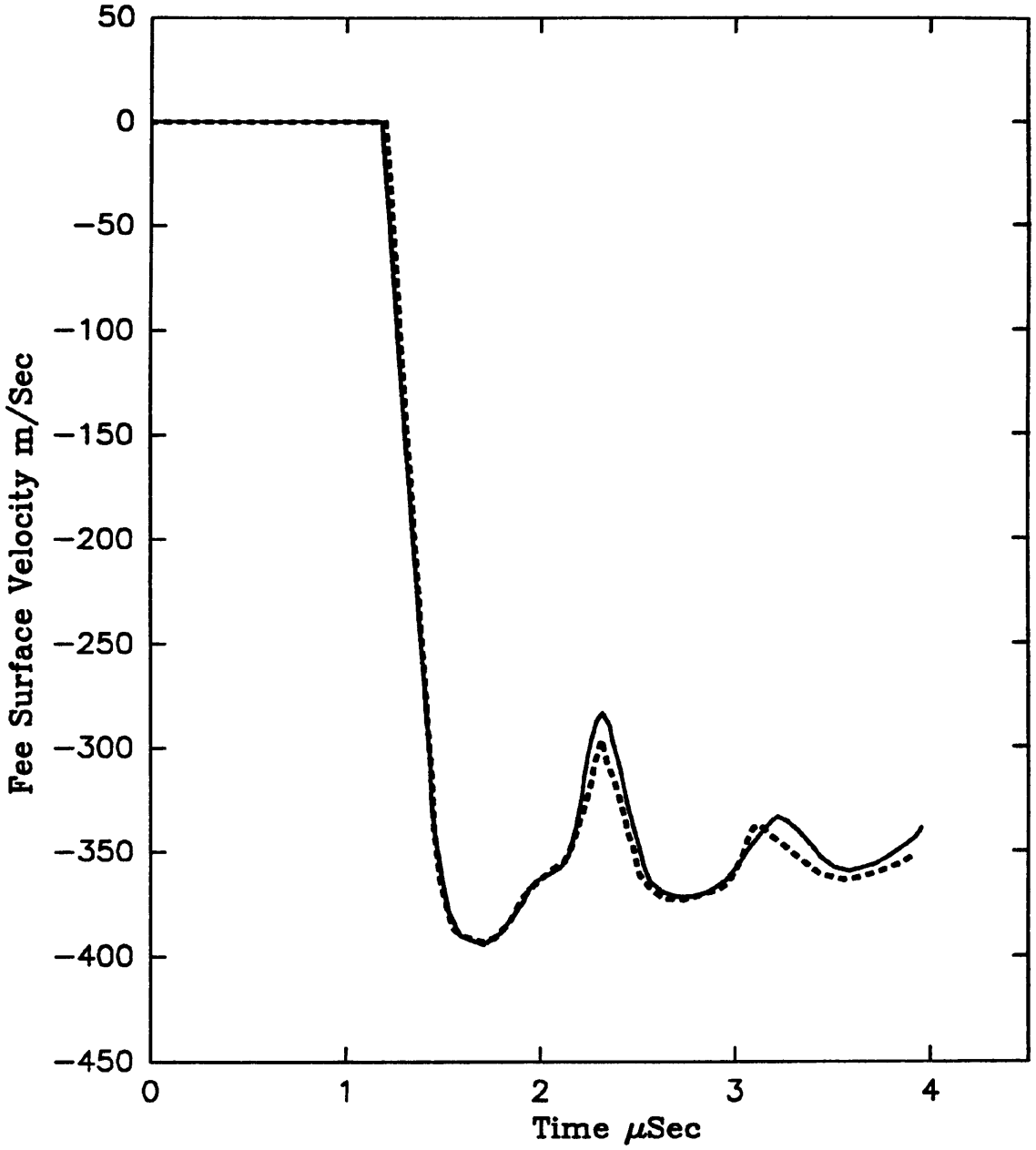

Fig. 11.8 Comparison Between Experiment and Calculation for Steel Planar Spall

CHAPTER TWELVE

EXPERIMENT AND SOME APPLICATION OF THE SPALLATION MODELS

12.1 INTRODUCTION

In Chapters Eight to Eleven, details of the spallation phenomenon were presented. Various models were formulated to describe ductile and brittle spallations, including a simple unified model. The result of the various simulations carried out were compared with experimental data.

In this Chapter, we present the experimental technique of the plane impact of plates and the measurement of the free surface velocity of the target, the so-called spall signal, which is normally used to validate spallation models. Also covered in this Chapter are two dimensional applications of the unified model. The first is a two dimensional plate impact, and the second is explosive impact on thick plate.

12.2 PLATE IMPACT EXPERIMENT

The impact experiments were carried out with the aid of a two chamber gas gun. The details of the gun, instrumentation and method are described below.

12.2.1 The Gas Gun

The gas gun used was a two chamber gun, with a burst disc sandwiched between the two. It is capable of firing projectiles of between 25 to 60 mm diameter at velocities in excess of $400ms^{-1}$. Figure 12.1 shows a schematic drawing of the gas gun, and an assembly drawing is in figure 12.2. The projectile is positioned at the entrance of chamber two, while the burst disc is positioned at the adjacent end of chamber one. The two chambers are then bolted together at the flanges. The target assembly is arranged at the far end of chamber two. Helium gas is let into chamber one, and when the pressure reaches the burst pressure of the disk, it erupts and the projectile is fired at the target.

12.2.2 Projectiles

The projectiles are required to deliver a short compressive stress pulse into the target plate. Ideally the flier disc should hit the target alone, but it must be attached to a sabot for it to be properly projected. After a series of trials [1], the sabot material and its dimensions were decided upon. The flier disc is glued to a sabot of either delrin or balsa wood of about 45 mm long. This length is assured to provide stability during the flight so that a plane impact is ensured.

The delrin sabots were carefully machined hollow to minimise the mass to about 25 g. The balsa sabots, about 8 g, were backed with aluminium discs to prevent them from shattering whilst accelerating in the barrel. Figure 12.3 shows the picture of a typical balsa sabot with the flier disc and backing aluminium plate. The flier discs were ground smooth and parallel. Care was taken in the preparation of the projectiles, particularly the balsa ones, to keep the flier disc perpendicular to the axis.

12.2.3 Projectile Velocity Measurements

The velocity of the projectile was measured with the aid of three laser beams. Figure 12.4 shows a picture of the target area with the three laser devices clearly visible. The lasers were carefully positioned, at known distances apart, near the target. This is so that the impact velocity is measured as accurately as possible, just before impact.

When the projectile cuts the laser beam, a signal is recorded by an oscilloscope. The three lasers provide two separate measure of velocity. These were consistently the same in all our experiments, however, it is valuable to have two records of projectile velocity to check against one another.

12.2.4 Free Surface Velocity Measurement

The velocity of the free surface of the target was measured by a capacitance device. This consists of an insulated disc of about 10 mm diameter mounted parallel to and about 2 to 3 mm away from the free surface of the target. The disc is charged to a high voltage, typically 500 volts. As the free surface moves, the capacitance is altered forcing a redistribution of charge and as a result a current flow in the external circuit. This current is monitored via an amplifier on the transient recorder.

The capacitor consists of a brass button glued into a perspex disc supported off the back surface of the target plate on three nylon pillars. The capacitor gap is set accurately by feeler gauges prior to gluing. Important parts of the circuitry are also mounted directly onto the back of the capacitor to produce a compact unit with minimum noise pick up. The arrangement creates a long path length for stress wave reaching the button and also ensures that mechanical inertia holds the button in place during the time of interest. Figure 12.5 shows a picture of the target assembly with the capacitance device clearly visible. Typical capacitor signal is presented in figure 12.6.

12.2.5 High Speed Photography

In order to validate and check the viability of the velocity and planarity of the flyer plate and also the free surface velocity, a high speed camera was used. An IMACON (Image Converter Camera) was set up at the target area. Figure 12.7 shows a picture of the assembly including the high speed camera. Typical high speed photographs are shown in figure 12.8. An image analysis was used to generate displacement versus time plots from the high speed photographs. The data from the high speed photographs generally confirm the electronic measurements described above.

12.2.6 Plane Wave Generator

In order to achieve velocities of more than 500 ms^{-1}, explosively driven flyer plates were used [1]. Figure 12.9 to 12.11 show the device and the target plate assembly. Similar transducers were used to obtain the various velocity measurements as explained above.

12.2.7 Tests and Results

Most of the tests carried out were on steel targets. The mild steel results were shown in Chapter Eleven. Another of the results is discussed later in this Chapter. Other results shown in Chapters Nine and Ten were obtained from the references to which they were credited in those chapters.

12.3 TWO DIMENSIONAL PLATE IMPACT

The development of spall fracture and the post spall behaviour of a target plate after having been impacted by a flyer plate of smaller diameter travelling at high speed, is described by means of the simple unified spall model presented in Chapter Eleven.

Non-oblique impact of circular plates which have unequal diameters generate multi-dimensional axi-symmetric strain consisting of three normal components and one shear component that vary in the radial direction, as well as along the plate thickness direction.

Because of the edge effect caused by the circumference of the smaller flyer plate, non-planar waves originating from the circumferential edge, complicate the pattern of wave deformation. A schematic illustration of the plate configuration is given in Figure 12.12. Also shown are the initial plane compressive wavefronts propagating across each plate, and the non-planar wave starting from the circular edge of the flyer. The latter wave travelling radially towards the centre of the target, reduces the region of target material that initially will be subjected only to very high mean stress. However, if the plates are relatively thin, that is, if their diameters are more than ten times their thickness, a central region of the target will briefly experience large tensile mean stress arising from superposition of the reflected planar longitudinal stress waves, prior to arrival of the radial wave. When the impact velocity of the flyer is sufficiently large, the induced mean stress in the target reaches intensities that are high enough to cause spall fracture. The physical features of the spall separation, that is the location of the plane of material separation, the diameter of the separated circular region, and whether or not the target will develop a scab or experience fragmentation, depend upon the relative diameters and thicknesses of the colliding plates, as well as the velocity of the flyer.

12.3.1 Numerical Simulation

In the experiment simulated, a 60mm mm diameter, 3 mm thick aluminium flyer plate was propelled by the explosive lens (plane wave generator) on to a 15 mm thick 50D steel target. Figure 12.13 to 12.15 show comparisons of the material status with experiment specimens. Also presented are Velocity vectors and initial mesh used in the simulation. The comparison with experiment specimen seen in the photographs

are very good. The experimental record of the free surface velocity is shown together with the result of the simulation in Figure 12.16. This shows a reasonable agreement between the two.

12.4 Stress-wave Focusing

Johnson [2] (1981) simulated the case of a 25 mm copper plate subjected to explosive impact by 12.7 mm layer of composition B-3. As expected, his model showed two spall planes, as observed in experiment. In commenting on the explosively produced spallation model of Breed et al [3] (1967), he said: "This model has been useful in reproducing the observed spall layers in explosive events, but is not applicable to low pressure-impact experiments." He added that: "Likewise, models developed for plate-impact situations, seem to be inadequate in high pressure regime."

We were, therefore, anxious to test the models presented in Chapters Nine to Eleven, particularly the simple unified models, to see that they can properly predict explosive event as well as they did the plate-impact events.

In this Chapter we demonstrate the effectiveness of the unified model by incorporating it into a two dimensional hydrocode, AUTODYN and simulating the fracture of steel plate by the use of stress wave focusing [4].

This specially designed tool consists of a composite lens of rubber and iron filings. Several layers of explosive are laid on the lens as shown in Figure 12.17 [4]. When the explosive is detonated, focused compressive shock wave is imparted onto the steel target. When this is reflected from the free end of the target plate, tensile mean stress develops to cause fracture in the target plate. Fig 12.17 also shows some contour plots of pressure in the target plate, and figure 12.18 show some velocity vectors of the event.

Depending on the nature of the lens geometry, a significant amount of spallation takes place first before the remaining cross-section is fractured. The High Energy Rate Engineering Group in UMIST, Applied Mechanics, were working on the design of the lens that will increase or decrease the thickness of the spalled scab. Any simulation of this even must therefore take into account the proper modelling of the spallation phenomenon.

We applied the Simple Unified Model presented in Chapter Eleven to this engineering problem. Figure 12.20. shows a photograph of two specimens in which the spall fracture has been frozen by energy absorption devices. The same figure shows the result of the simulation at about the same stage. The similarities between the simulation and the experiment are remarkable. Not only did the model predict the two layers of spall plane observed in the experiment, it also predicted the "lacerations" seen in the specimens.

Also, Figure 12.21 shows a picture of two completely separated specimens. Figure.... shows the corresponding simulation result. The comparison between the experiment and the simulation are excellent.

12.5 CONCLUSION

We presented the experimental techniques of the plane impact of plates.

The two dimensional plate impact modelled, shows very good agreement with experiment.

The simulation of the stress-wave focusing experiments were very good.,

This illustrates that the models presented can be extended to simulate two dimensional problems. Also that the models are suitable to both plate-impact and explosive

spallation.

References

1. P Tennant, MSc Thesis, UMIST, To be published in 1995
2. J N Johnson, J Appl. Phys., 52 (4), (1981)
3. B R Breed, C L Mader, and D Venable, J. Appl. Phys. 38 (1967), 3271
4. A De Joode, PhD Thesis, UMIST, To be published in 1995.

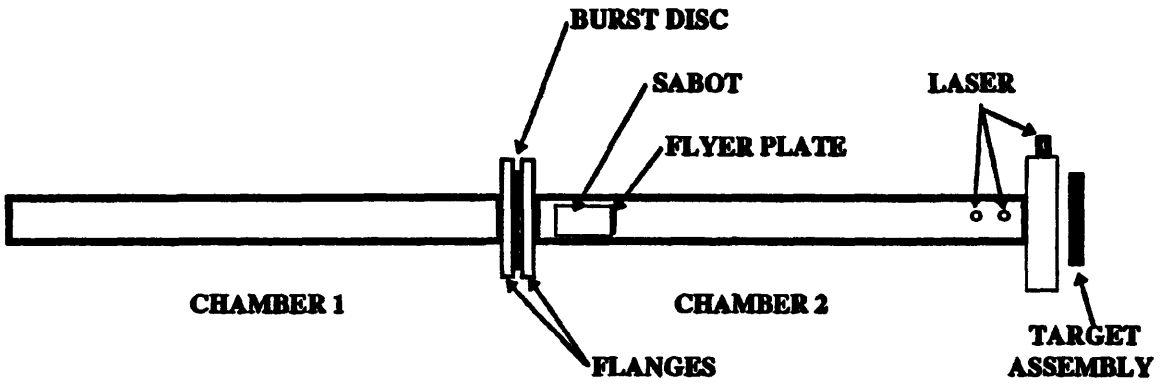

Fig. 12.1 Schematic Diagram of the Air Gun

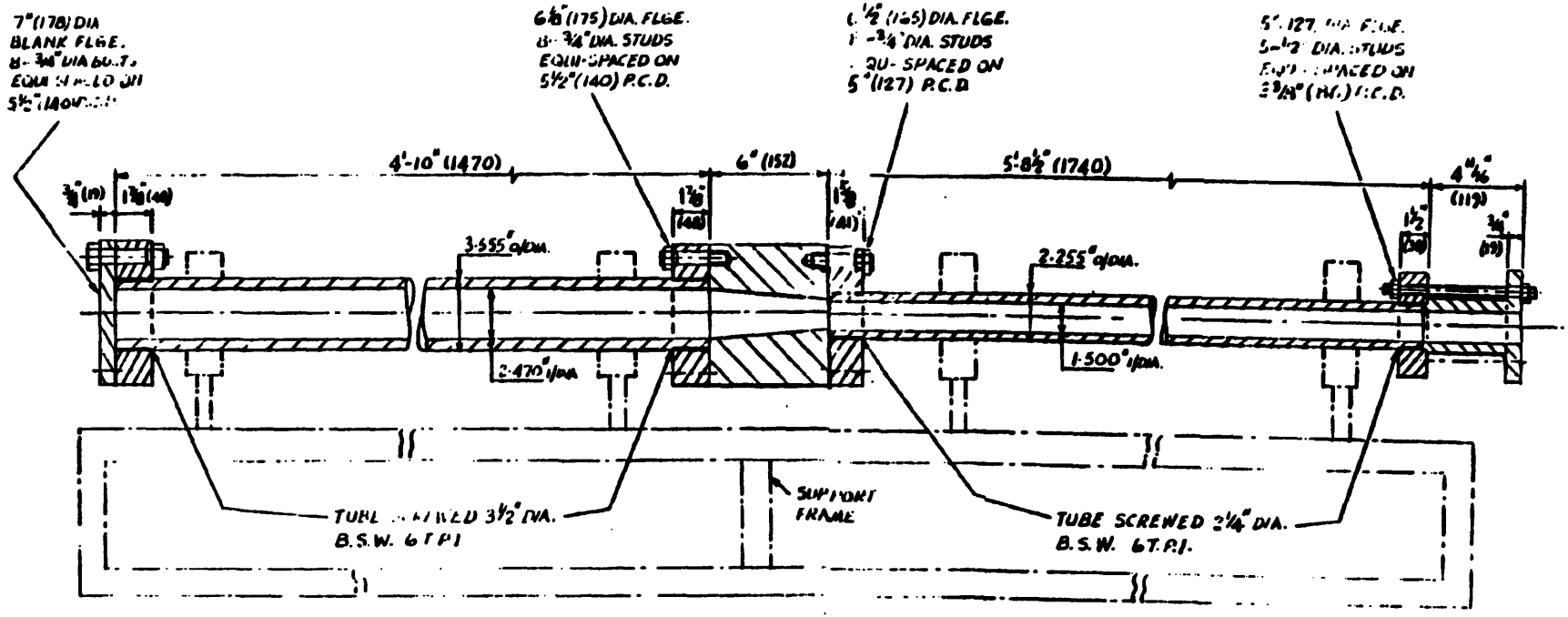

ELEVATION SECTIONAL

Fig. 12.2 Assembly Drawing of the Air Gun

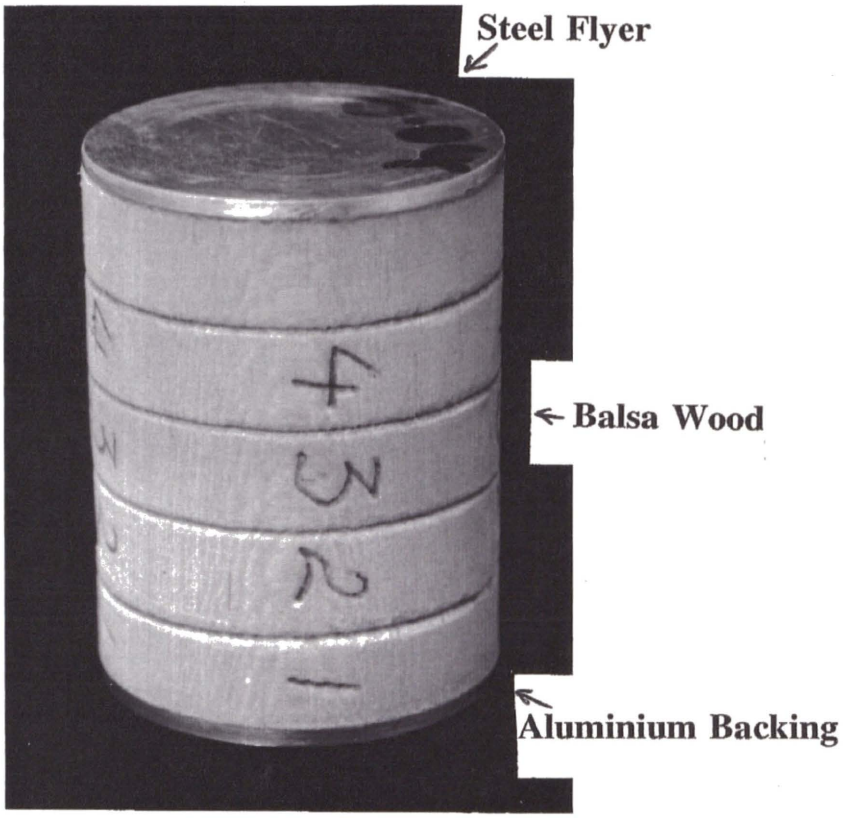

Fig. 12.3 The Balsa Wood Sabot

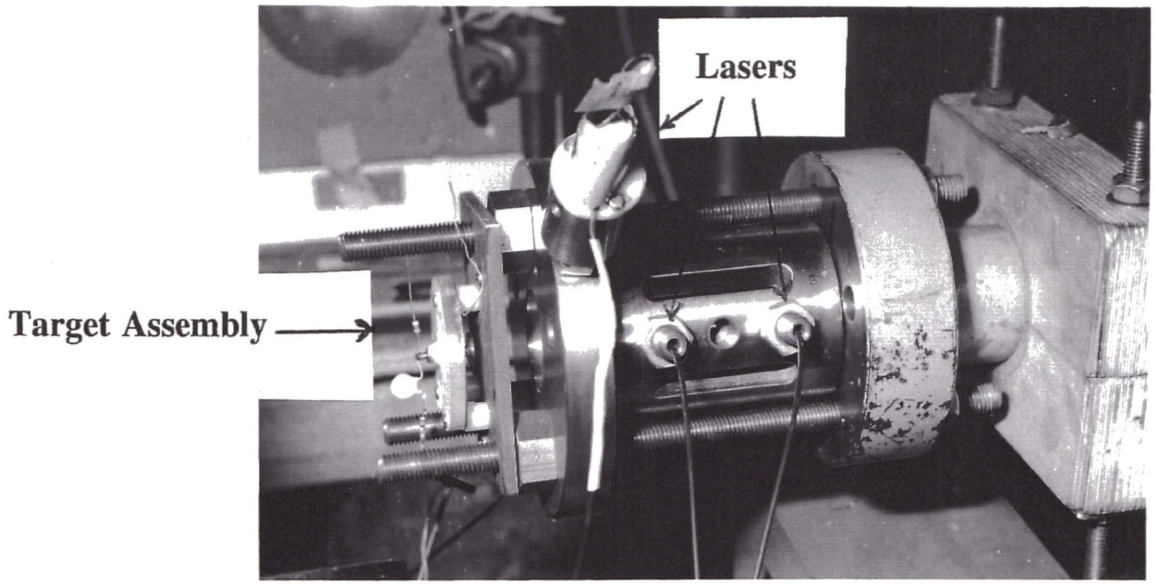

Fig. 12.4 The Target Area

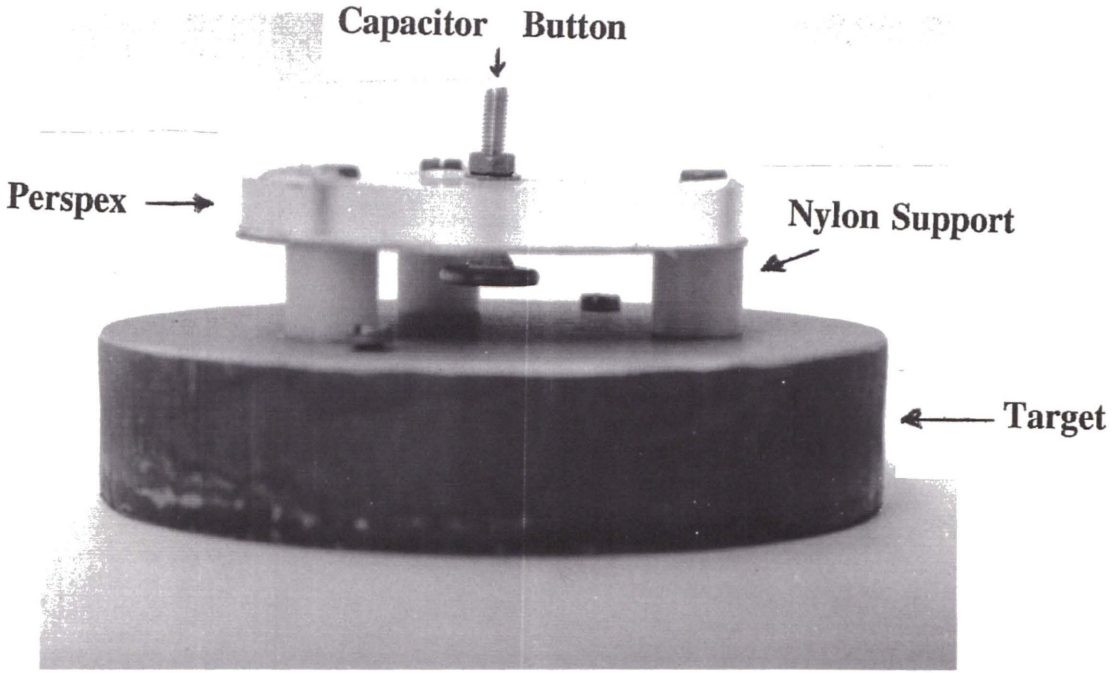

Fig. 12.5 Target Assembly

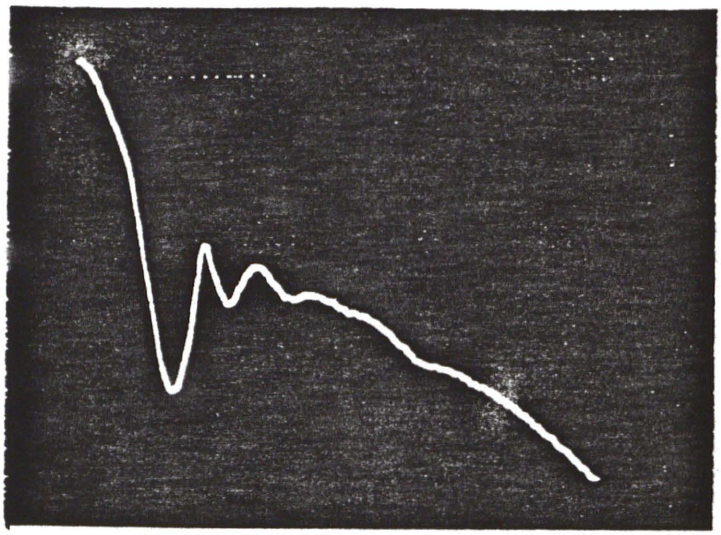

Velocity-Time of Back Face of the Target

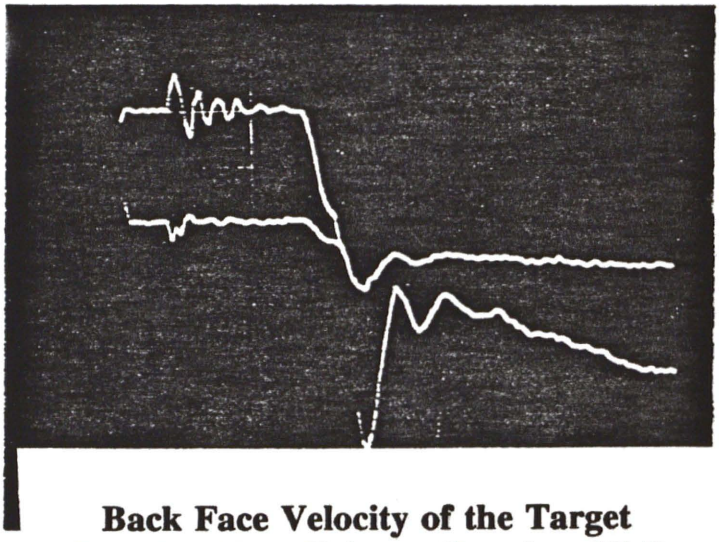

Back Face Velocity of the Target Showing Pure Trigger Signal as Well

Fig. 12.6 Typical Capacitor Signal During Spallation

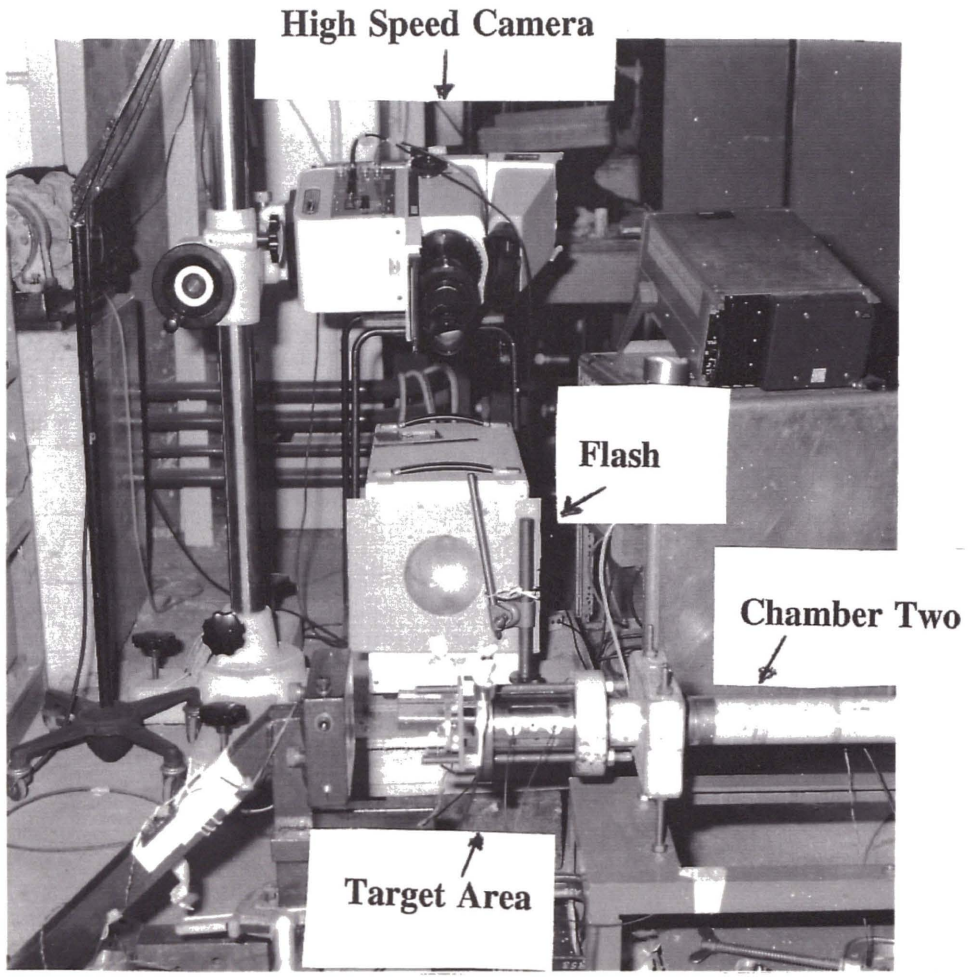

Fig. 12.7 The Target End of the Airgun

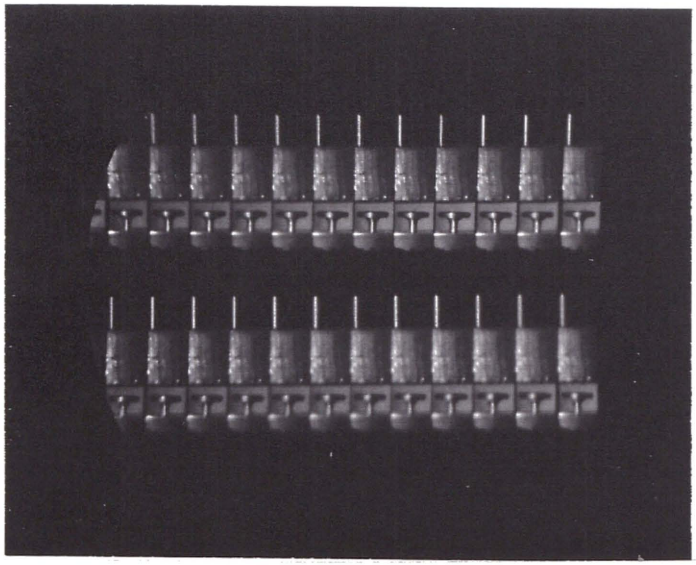

Still Shot of Target and Capacitor Button

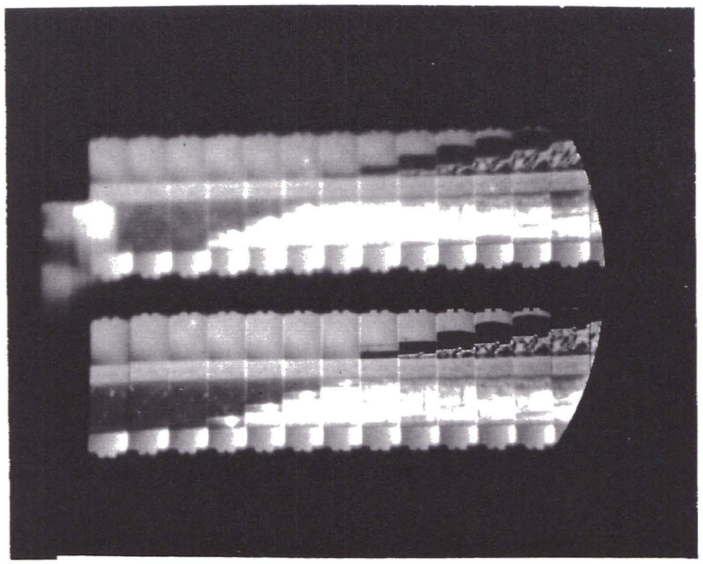

Projectile Impact and Target Spall

Fig. 12.8 Typical High Speed Photographs

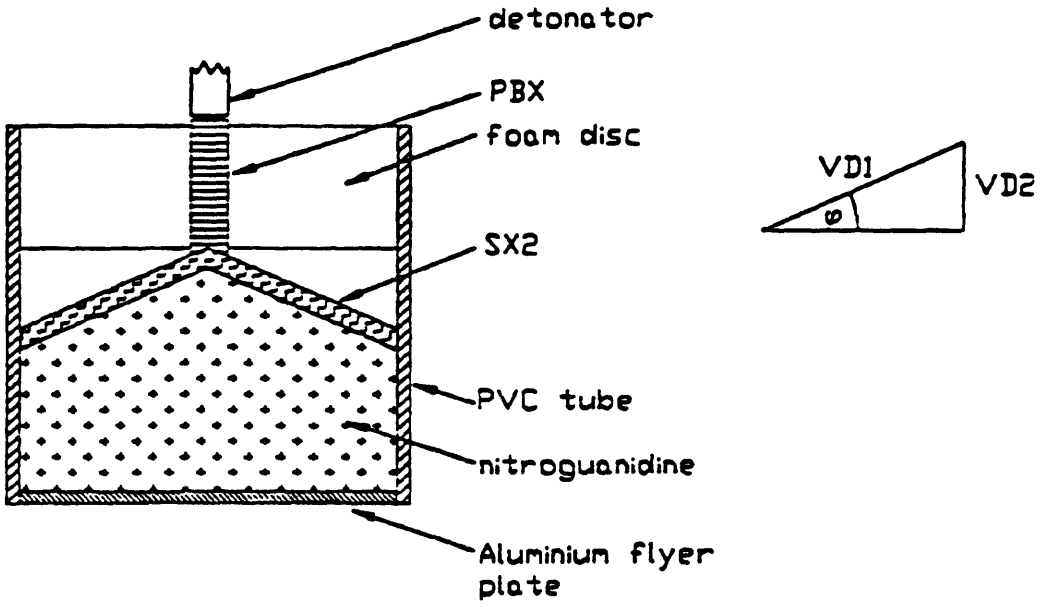

Fig. 12.9 Explosive Lense (Plane Wave Generator) and Flyer Plate

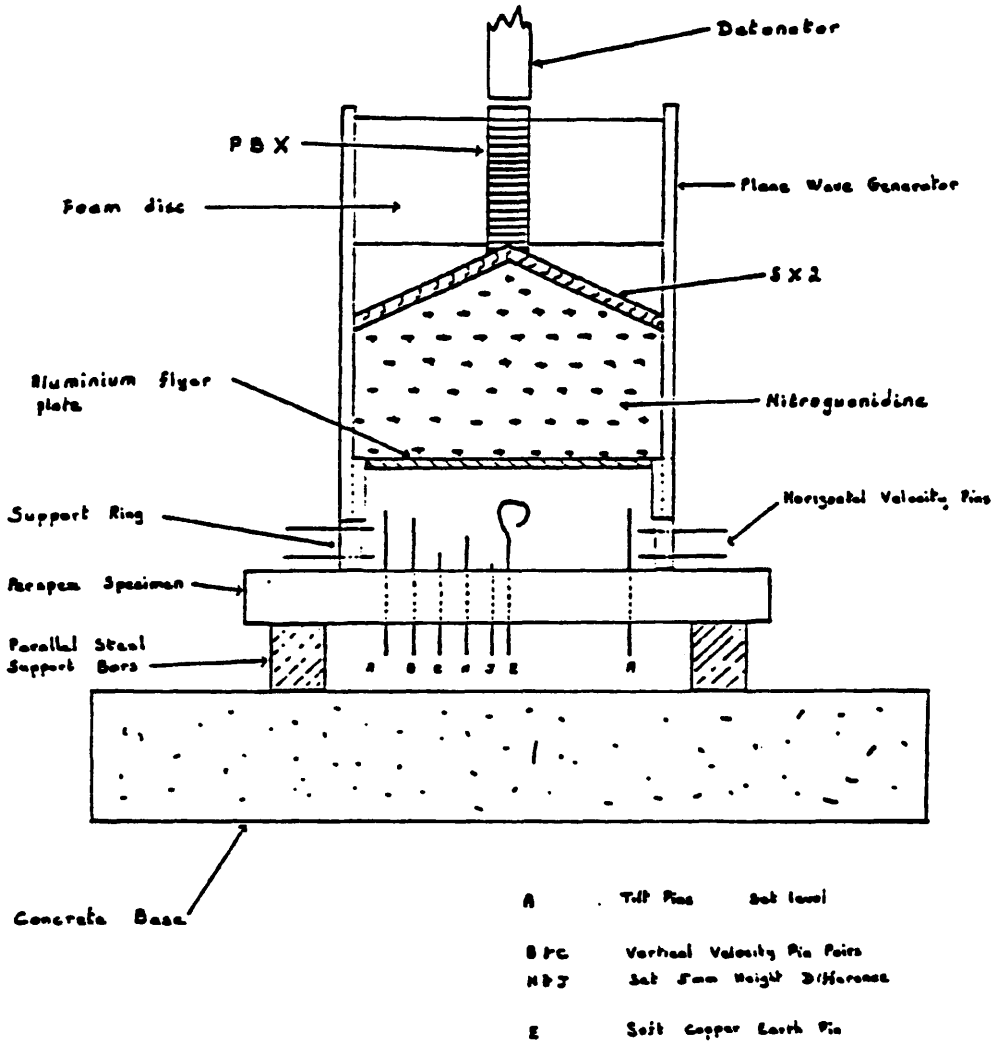

Fig. 12.10 Plane Wave Generator and Flyer Plate Test assembly

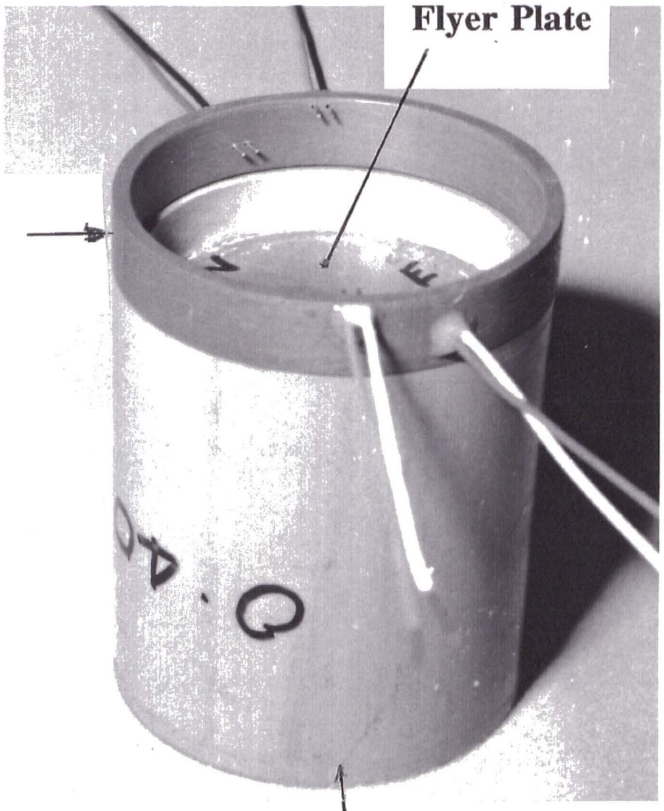

Fig. 12.11 Plane Wave Generator with Planarity Test Device

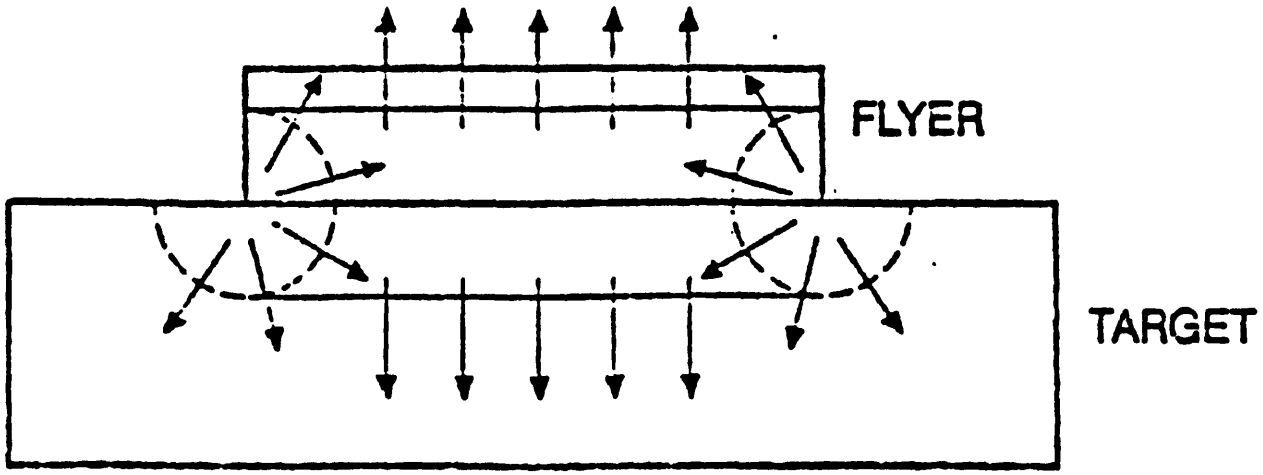

Fig. 12.12 Impact of Circular Flyer Plate with Larger Diameter Target Plate

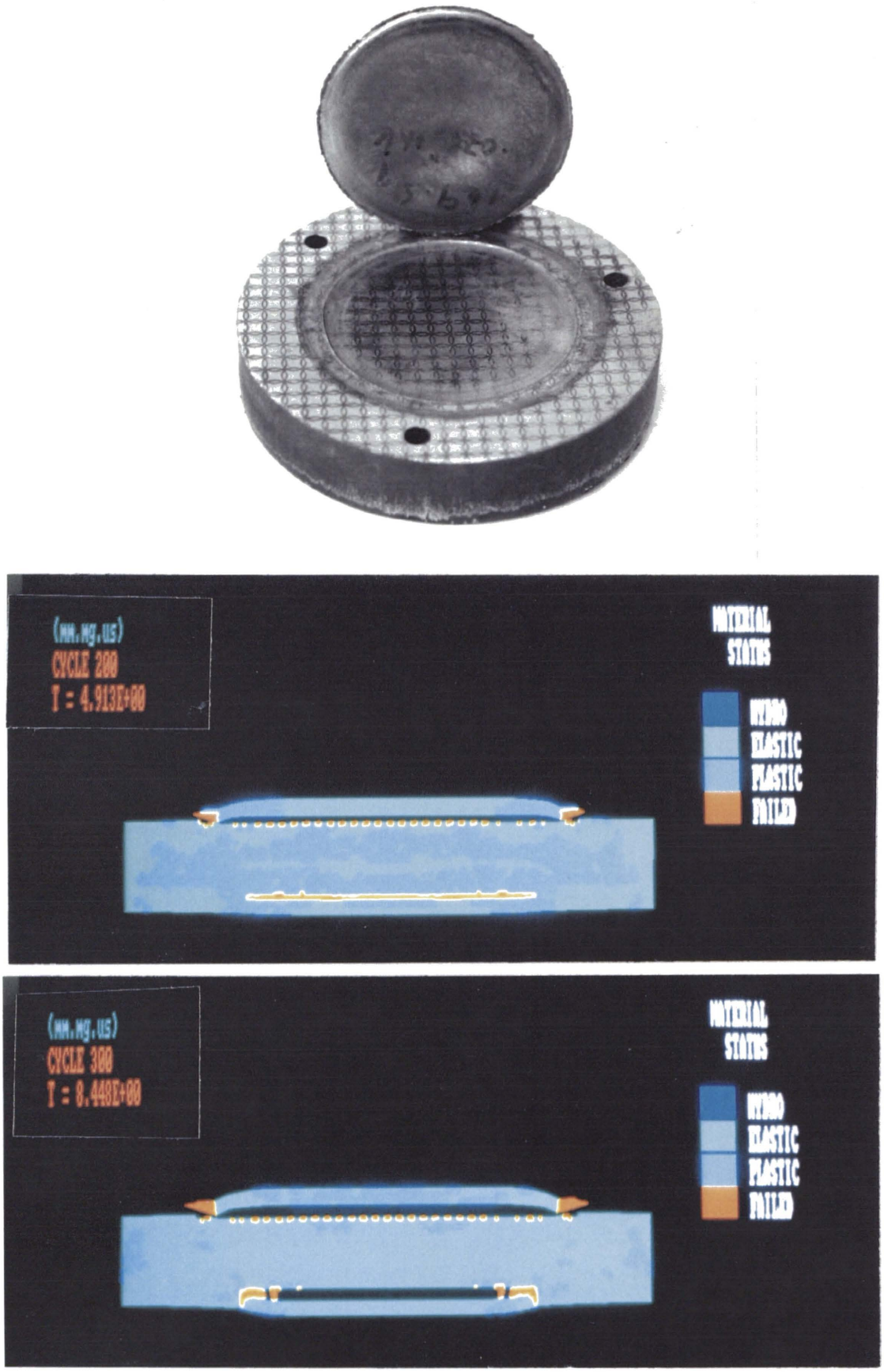

Fig. 12.13 Plane Plate Impact
Experiment and Numerical Material Status

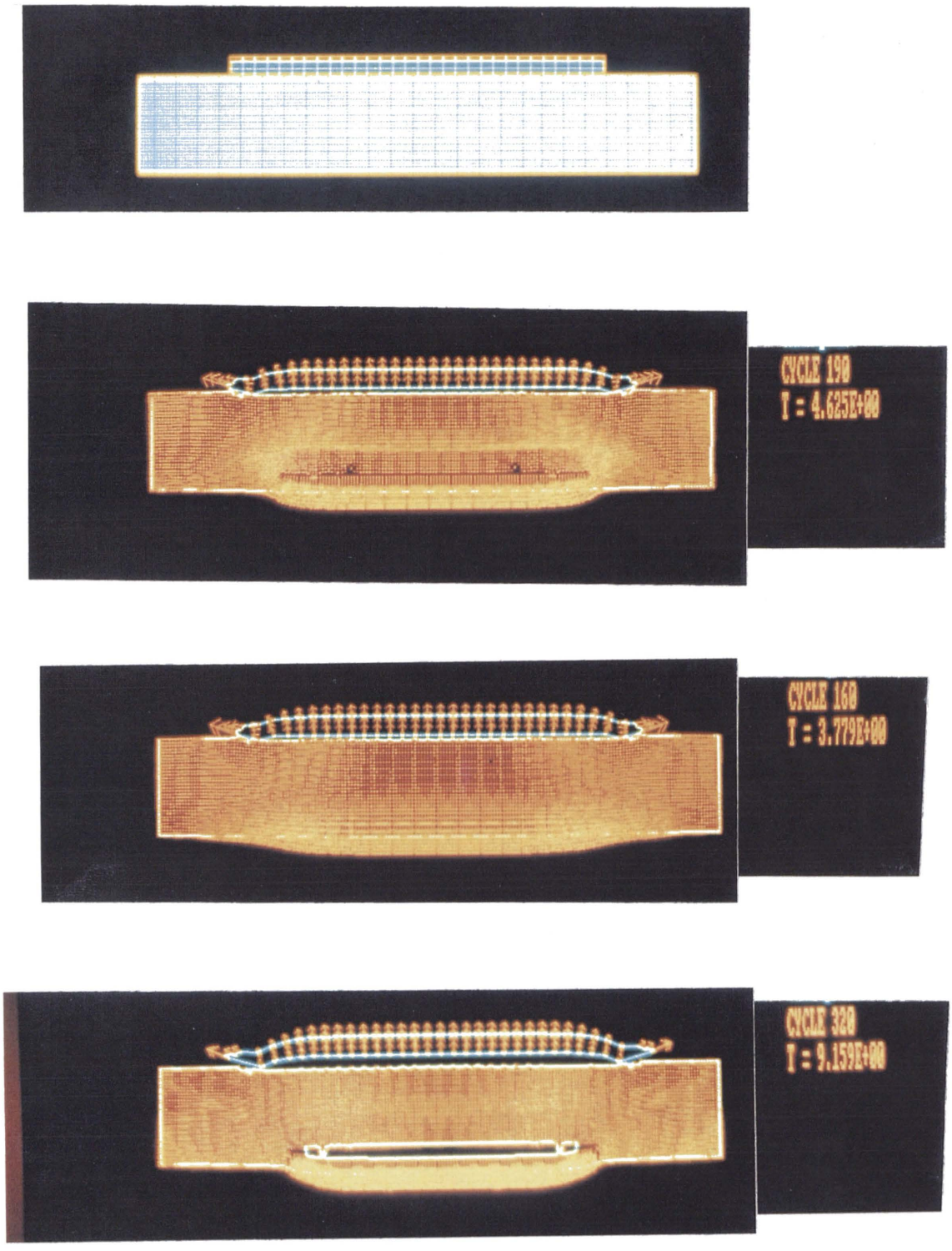

Fig. 12.14 Plane Plate Impact
Mesh and Velocity Vectors

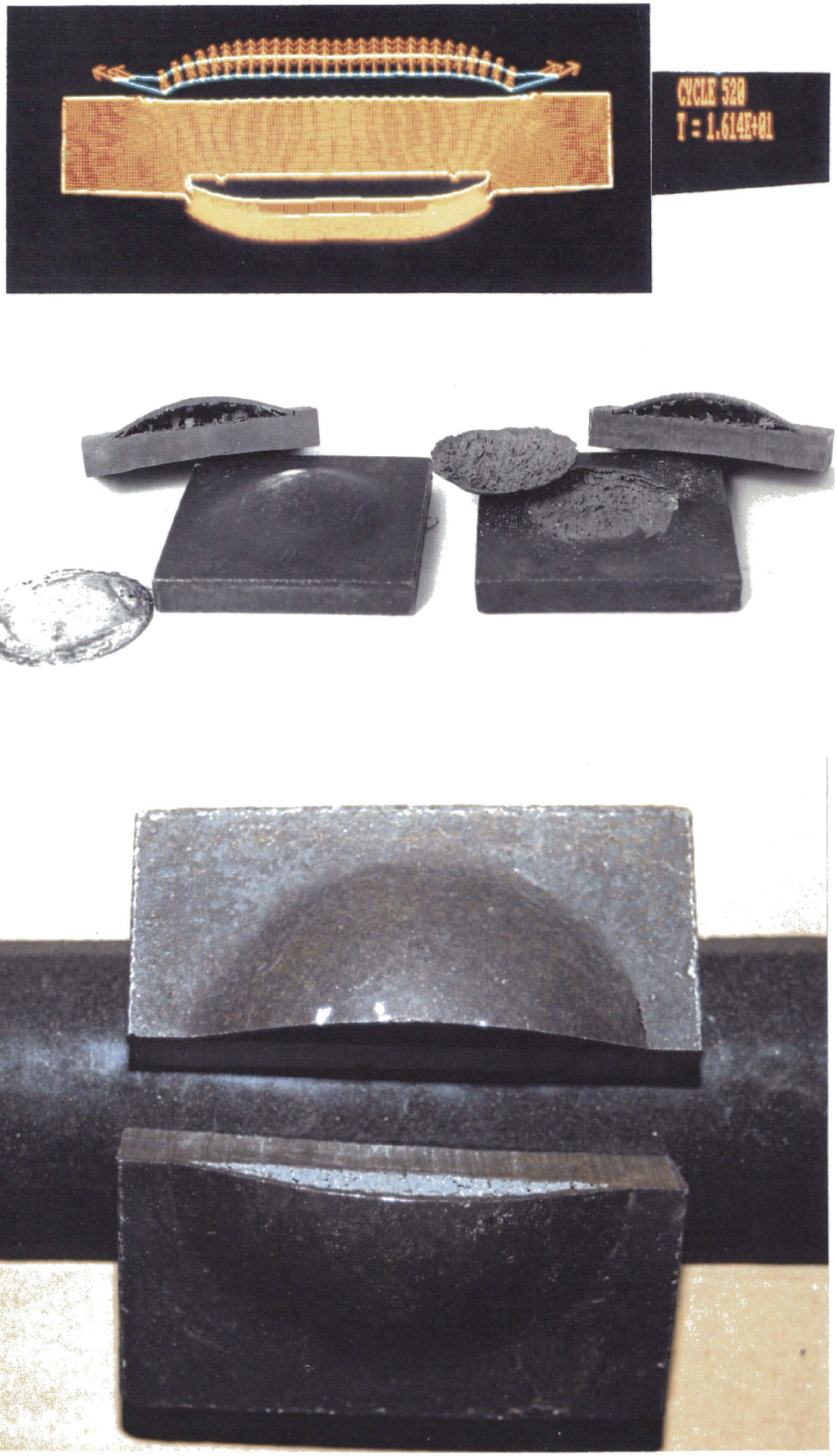

Fig. 12.15 Plane Plate Impact Material Separation Experiment and Numerical Comparisons

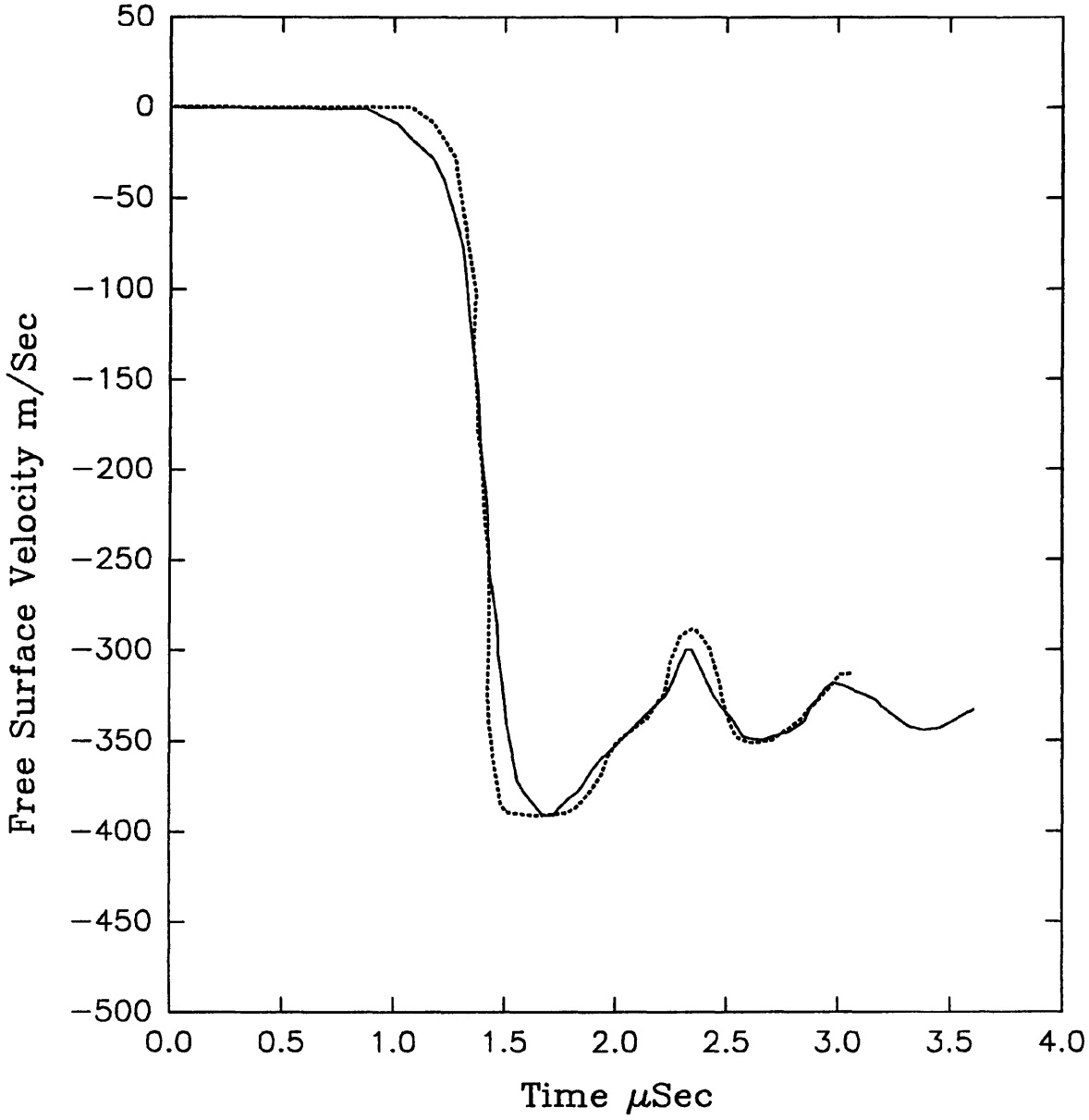

Fig. 12.16 Comparison Between Experiment and Calculation for Steel Planar Spall

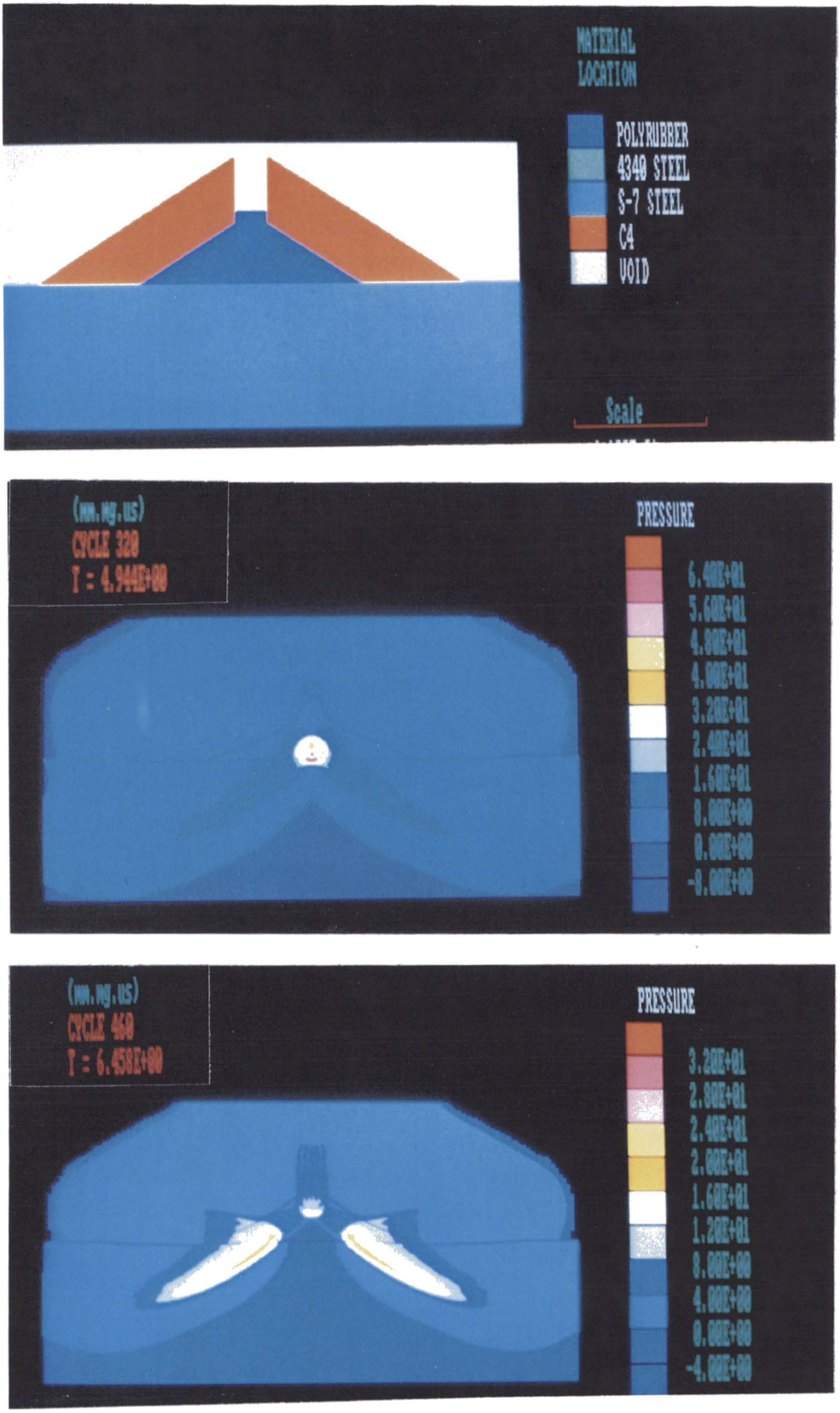

Fig. 12.17 Stress-wave Focussing
Initial Material Location and Pressure Contours

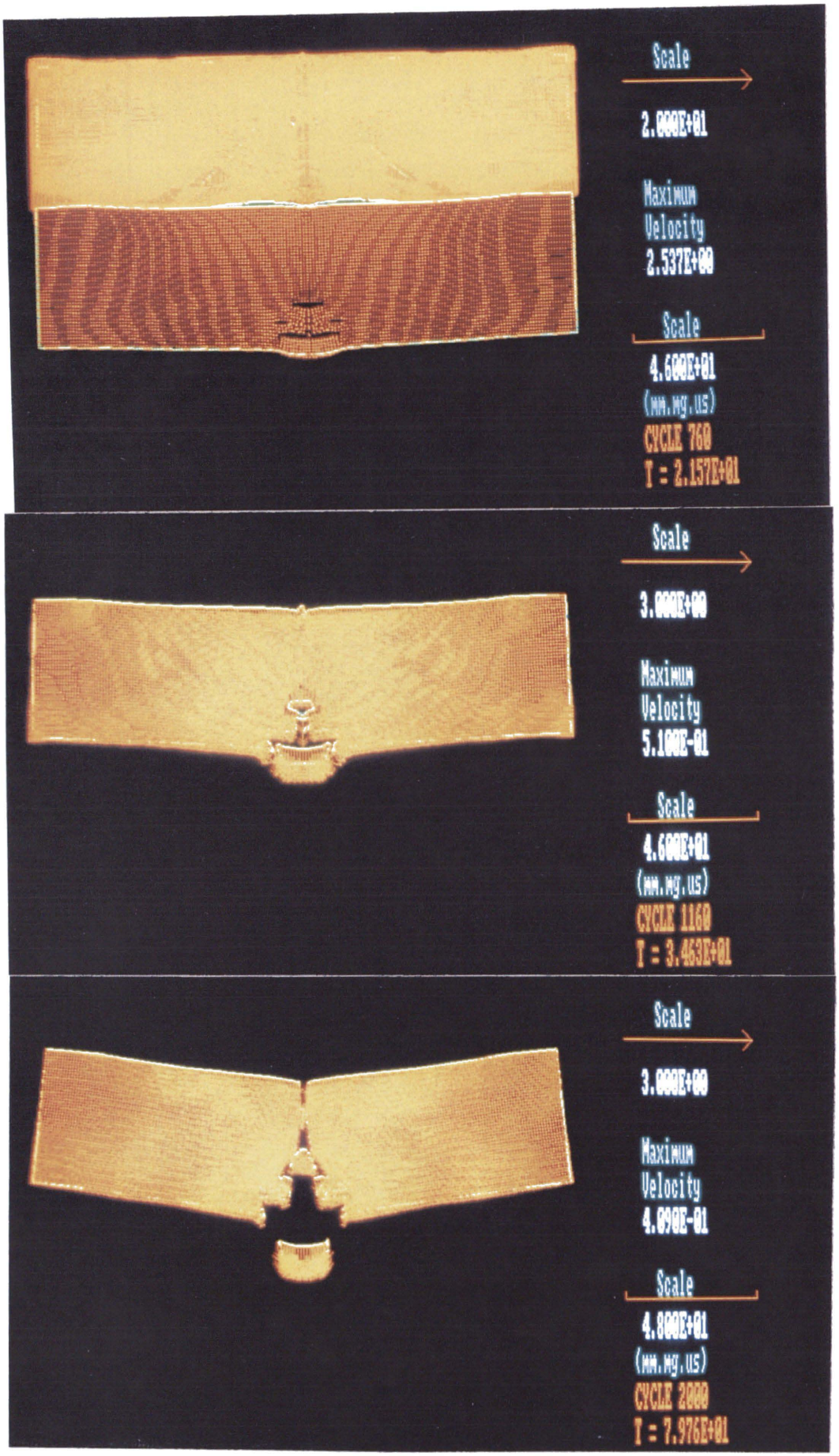

Fig. 12.18 Stress-wave Focussing: Velocity Vectors

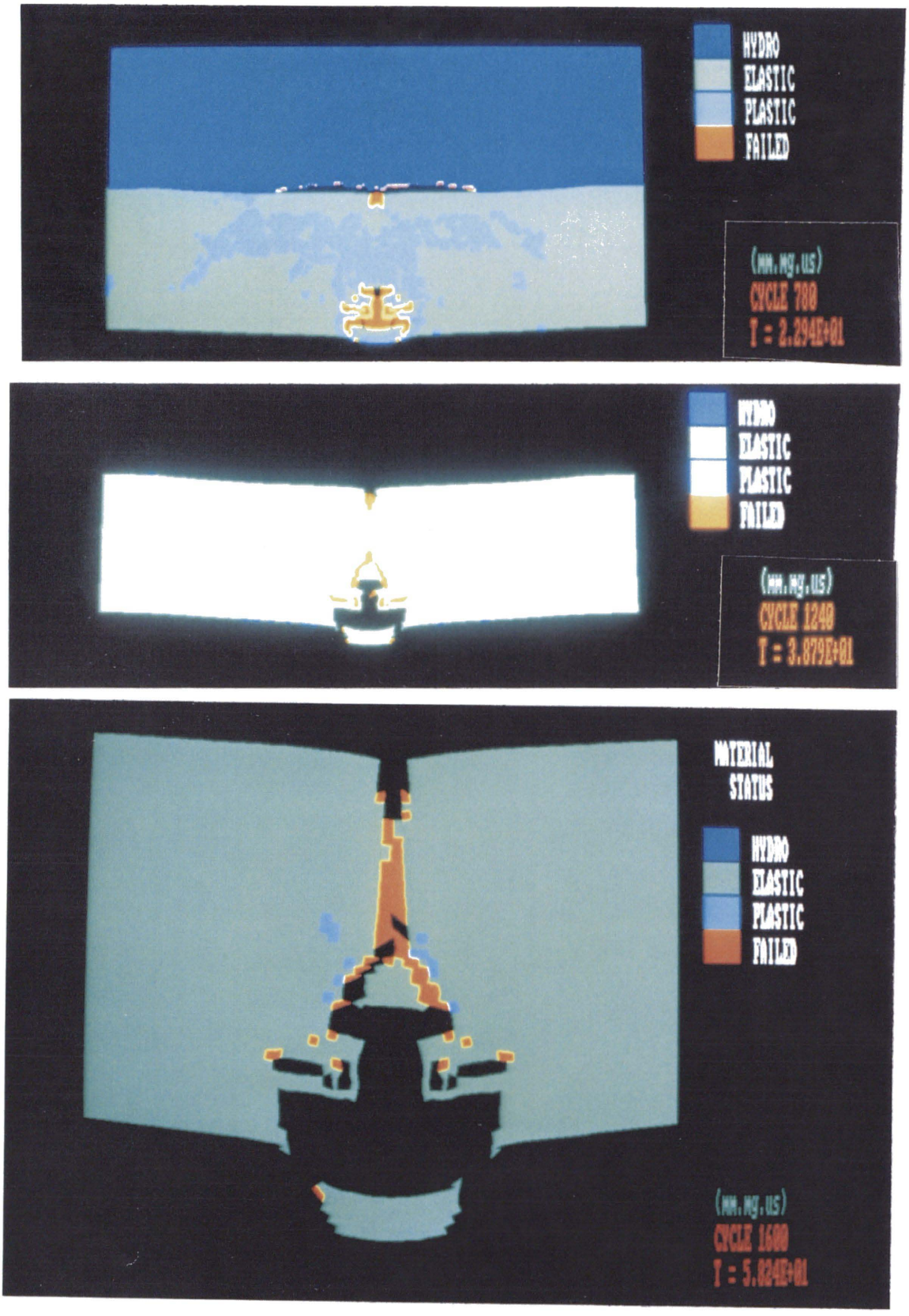

Fig. 12.19 Stress-wave Focussing: Material Status

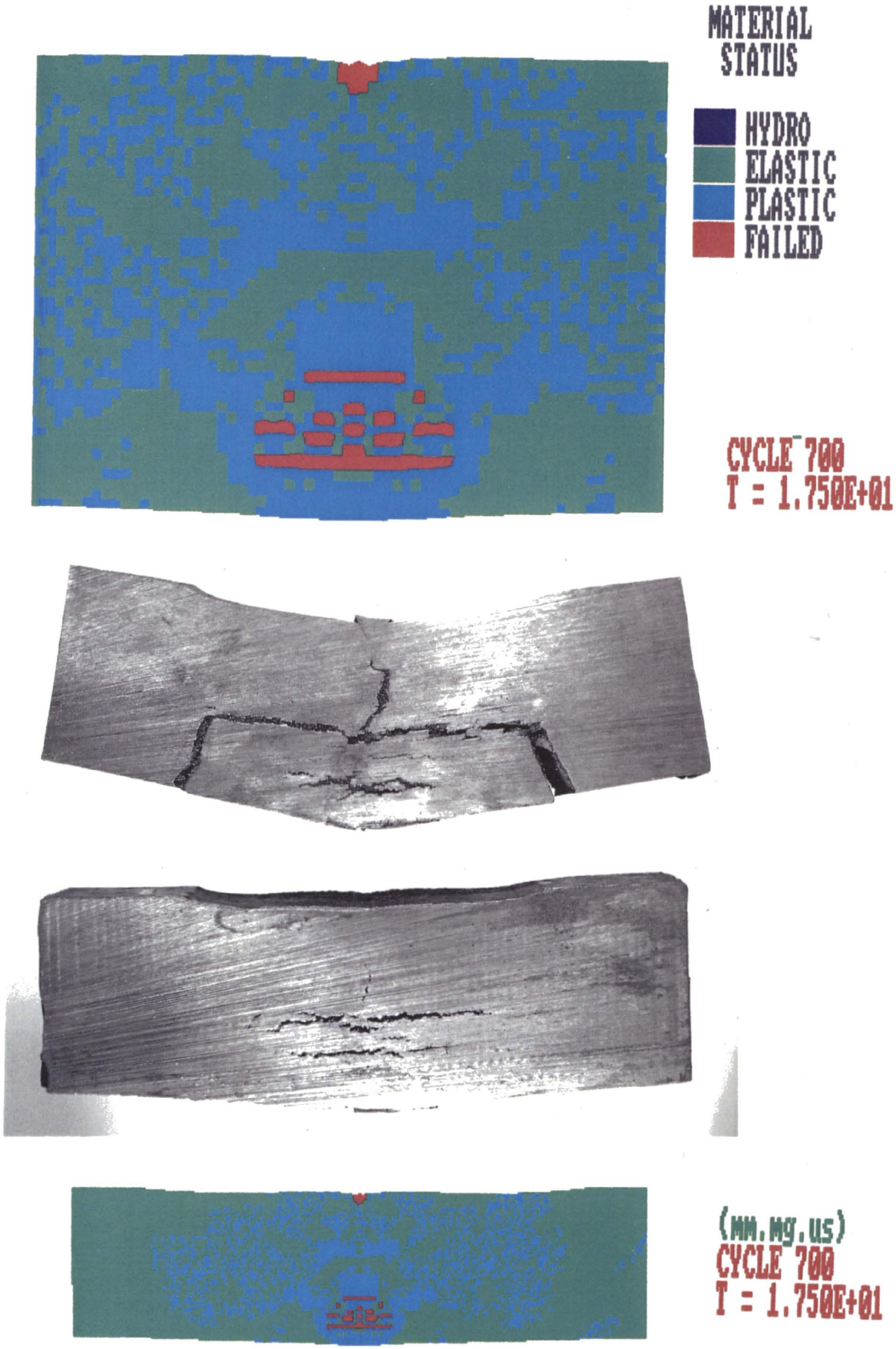

Fig. 12.20 Stress-wave Focussing
Arrested Experimental Spall Compared with Simulation

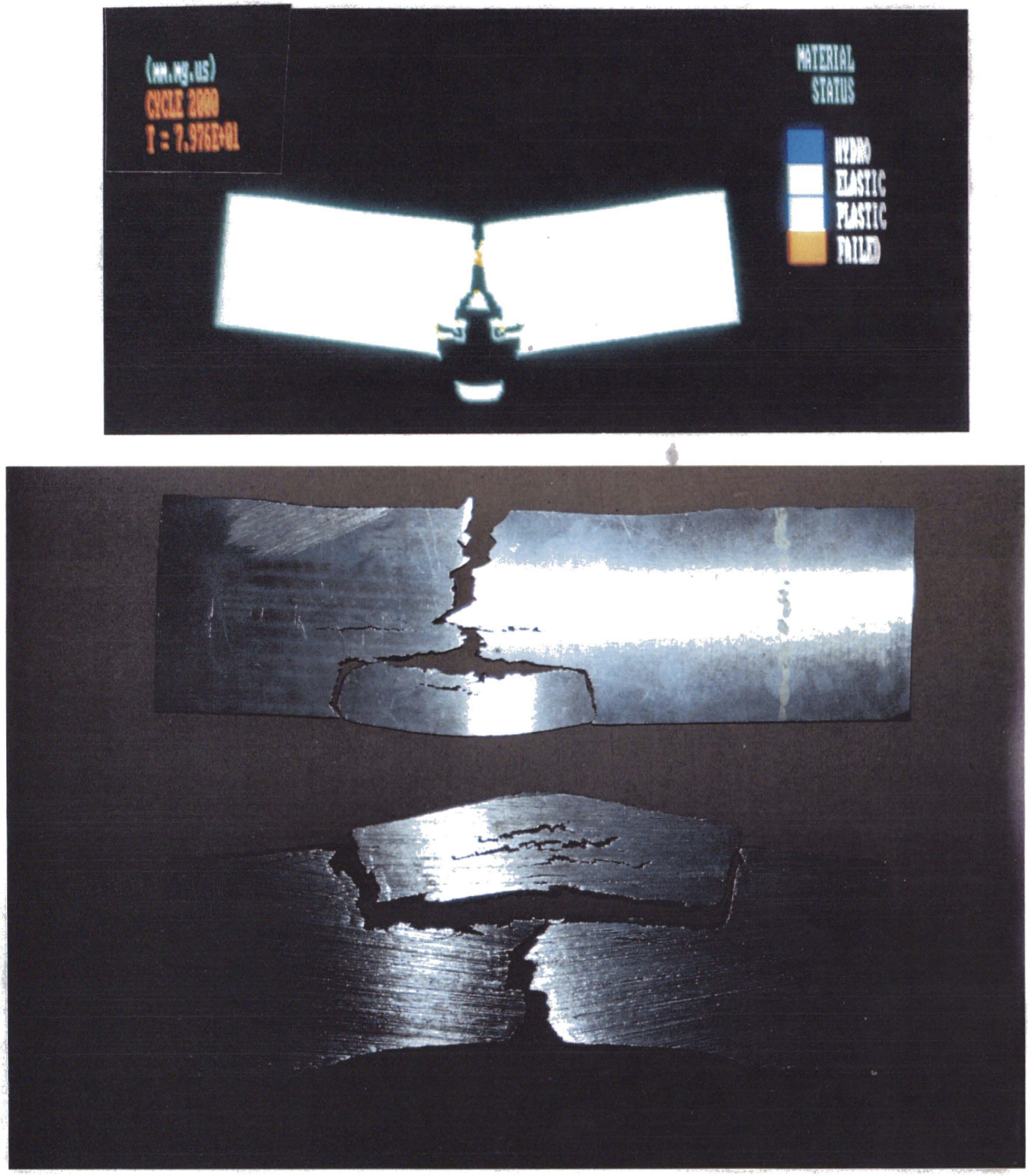

Fig. 12.21 Stress-wave Focussing
Experimental Material Fracture Compared with Simulation

CHAPTER 13

DISCUSSION AND CONCLUSION ON PART TWO

13.1 GENERAL DISCUSSION

Many spallation models have been presented in the past. Although the majority are limited to modelling specific events such as plate-impact,they have been generally successful. Because most of them are based on microscopic view of the spallation process, they are often complicated and require large numbers of parameters which are simply not easily obtainable for practical engineering materials.

We presented two simplified microscopic models, one for ductile spallation and the other to describe brittle spallation. Also presented were two macroscopic models, ductile and brittle. These were later unified into a simple model to describe both ductile and brittle spallations.

All the models were tested by applying them to practical spallation events and comparing the results with experimental data. One of the important features of the models presented is that they can be used with any desired equation of state and constitutive models. This makes them "portable", easily attached to general purpose or special hydrocodes. They can be extend to two or three dimensions and can be applied to plate impact, explosive impact and other spallation events. Because they are essentially very simple, only a handful of parameters are required and these can be obtained experimentally for practical engineering materials or can be reliably estimated by existing analytical methods. Several conclusions were drawn at the end of the presentation of each model.

13.2 CONCLUSIONS

The conclusions reched at the end of the preceding chapters are summarised here.

Chapter Nine: Engineering Models for Ductile Spallation

In this chapter, we have presented a simplified microscopic model for ductile spallation based on existing model for void growth and the assumption that the total volumetric strain rates are sufficiently large that the tensile pressure remains near the threshold pressure for void growth.

By focusing on the collective response of the material and introducing gross porosity, a macroscopic model to describe ductile spallation was also presented.

The comparisons between experimental data and numerical simulations, based on the model presented, of the free surface velocity of the target plate, in the plane impact of plates, are reasonably good.

The critical porosity in the simplified microscopic model corresponds with the critical porosity in the simple macroscopic model.

The simplified microscopic model gives an upper bound of the spall peak while the simple macroscopic model gives a lower bound.

The models presented require very few parameters, in contrast to existing models, and reasonably characterise the average continuum behaviour of the spall process. Therefore they are expected to provide simple and reasonable prediction of the ductile spall behaviour in practical engineering applications.

Chapter Ten: Engineering Models for Brittle Spallation

1 In contrast with identifying the ductile spall strength as the threshold pressure for a mean void growth, it remains to demonstrate how an appropriate mean crack size R_m is chosen to identify the brittle spall strength as the threshold pressure for a mean crack growth. Therefore, it is difficult to provide a rigorous justification for expressing the brittle spallation in terms of the mean crack size R_m. In other words, although mean void-growth based failure models to describe ductile spall are successful, a mean crack growth-based failure model for brittle spall seems to be unsuitable.

2 The modelling of brittle spall would be compatible with ductile spall modelling providing that the solidity evolution is expressed by the crack opening strain, and the crack shear strain and the complete brittle spallation is characterised by a critical value of the solidity W rather than a critical value of damage $N_0R_m^3$.

3 Under the assumption that when the tensile pressure reaches the spall strength the further decrease of the solidity W is mainly due to the crack opening strain and the crack shear strain caused by the tensile pressure, relaxed at a certain value of $N_0R_m^3$, the simplified microscopic model for brittle spall would avoid involving the details of nucleation and growth of cracks. The numerical simulations appear to support this assumption.

4 The simplified microscopic model for brittle spall and the simple macroscopic model produce basically consistent spallation signal and the critical value of solidity W_c is near the critical value of gross solidity $\bar{W}_c$.

5 The comparisons between experimental and computational velocity history of the free surface of the target in the plane impact of plates of material are reasonably good. Therefore, the simplified microscopic

model for brittle spall and the simple macroscopic model are expected to provide good prediction and analysis of the brittle spall behaviour in engineering application.

Chapter Eleven: Simple Unified Spallation Failure Model

In this paper we present a simple spallation failure model which can be applied to both ductile and brittle spallation; through different p_f and ϕ_c. It requires only two parameters; the critical tensile pressure, p_f and the critical gross porosity, ϕ_c. A reasonable estimate of the two parameters can be obtained and the exact determination of p_f and ϕ_c depends on the comparison between numerical simulation and experimental record of the planer spall test, avoiding the complexities of soft recovery and elaborate specimen examination. The first estimate of p_f can be made by energy balance analysis or in terms of mean crack or void size, although how an appropriate mean crack or void size is chosen is yet to be demonstrated. In general, the minimum free surface velocity, in the plane plate impact test, is mainly dependent on p_f and the spall peak is dependent on ϕ_c.

Because the model can be used with popular equations of state and constitutive models, it can be easily incorporated into a one, two or three dimensional hydrodcode. The spall signal in one dimensional simulation of the planar plate impact was compared with experiments for three materials. These show very good agreement.

The model is therefore able to provide simple and reasonable predictions of the spall behaviour of practical engineering materials.

Chapter Twelve: Experiment and Some Applications of the Spallation Models

We presented the experimental techniques of the plane impact of plates.

The two dimensional plate impact modelled, shows very good agreement with experiment.

The simulation of the stress-wave focusing experiments were very good.,

This illustrates that the models presented can be extended to simulate two dimensional problems. Also that the models are suitable to both plate-impact and explosive spallation.

APPENDIX ONE

```
      PROGRAM ODGG
      DIMENSION F(600),F11(600),X(600),X11(600),XS(600),
     1   XS1(600),U(600),U11(600),V(600),W(600),E(600),P(600),
     2   Y(600),Q(600),G(600),S(600),Z(600),C(600),D(600),
     3   Z1(60),Z2(60),Z3(60),Z4(60),Z5(60),Z6(60),Z7(60),
     4   Z8(60),J1(60),W1(60),F22(60),D99(60),Z51(60),
     &  Z11(60),Z12(60),Z13(60),Z44(600),Z55(600),
     1   SM1(600),SM2(600),SM3(600),DD0(60),DD1(600),
     2   DD2(600),TT(600),Z81(60),Z82(60),Z83(60),Z84(60),
     3   Z85(60),Z86(60),Z87(60),Z88(60),Z89(60),VS(60),
     4   Z91(60),Z92(60),Z93(60),Z94(60),Z95(60),Z96(60),Z97(60),
     5  Z98(60),A8(600),A9(600),A99(600),TA(600),EC(600),EM(600),
     6  VS1(600),SE(600),STX(600),MSS(600),US(600),US1(600),
     7   Z71(60),Z72(60),Z73(60),Z74(60),Z75(60),Z76(60),Z77(60),
     8   Z61(60),Z62(60),Z63(60),Z41(60),Z42(60),Z43(60),Z54(60),
     9  Z45(60),Z46(60),Z47(60),Z48(60),Z49(60),Z50(60)
         COMMON F,F11,X,X11,XS,XS1,U,U11,V,W,E,Z51,US,US1,
     1   P,Y,Q,G,S,Z,C,D,Z1,Z2,Z3,Z4,Z5,Z6,
     2   Z7,Z8,W1,F22,D99,J1,D8,D9,W8,W9,M91,
     3   M92,N91,N92,G8,G9,N11,N22,L44,J8,
     4   J9,I1,L9,R2,R3,T,DT,N66,N55,W0,SEM,
     5   EVP,VSC,ECP,BAU,EX0
         COMMON Z11,Z12,Z13,Z44,Z55,SM1,SM2,SM3,
     1   DD0,DD1,DD2,TT,LY,Z81,Z82,Z83,Z84,Z85,Z86,Z87,Z88,Z89,
     2   R111,R112,R113,N8,N9,G1,D1,M9,VS,
     3   Z91,Z92,Z93,Z94,Z95,Z96,Z97,Z98,
     4   A8,A9,A99,TA,EC,EM,VS1,SE,STX,MSS,
     5   Z71,Z72,Z73,Z74,Z75,Z76,Z77,
     6   Z61,Z62,Z63,Z41,Z42,Z43,Z54,Z45,Z46,Z47,Z48,Z49,Z50
         OPEN(1,FILE='INP.DAT',STATUS='OLD')
        open(6,file='kin2',status='new')
         READ(1,*)D8,D9,W8,W9,M91,M92,N91,N92,G8,
     1   G9,N11,N22,L44,LY,R111,R112,R113,SEM,EVP,VSC,ECP,BAU,EX0
         READ(1,*)(Z1(I),Z2(I),Z3(I),Z4(I),Z5(I),Z6(I),Z7(I),Z8(I),
     1  I=1,n11)
         READ(1,*)(W1(I),DD0(I),VS(I),I=1,n11)
         read(1,*)(j1(i),f22(i),i=1,n22)
         READ(1,*)(Z11(I),Z12(I),Z13(I),I=1,n11)
         READ(1,*)(Z81(I),Z82(I),Z83(I),Z84(I),Z85(I),Z86(I),
     4   Z87(I),Z88(I),Z89(I),I=1,n11)
         READ(1,*)(Z91(I),Z92(I),Z93(I),Z94(I),Z95(I),
     1   Z96(I),Z97(I),Z98(I),I=1,n11)
         READ(1,*)(Z71(I),Z72(I),Z73(I),Z74(I),Z75(I),Z76(I),
     1   z77(i),i=1,n11)
         READ(1,*)(Z61(I),Z62(I),Z63(I),Z41(I),Z42(I),Z43(I),I=1,n11)
         READ(1,*)(Z54(I),Z45(I),Z46(I),Z47(I),Z48(I),Z49(I),
     1   Z50(I),Z51(I),I=1,n11)
         close(1)
         WRITE(6,90)EVP,VSC,ECP,BAU,EX0
90       FORMAT(1X,5(E12.5,1X))
```

```
      WRITE(6,100)D8,D9,W8,W9,G8,G9,R111,R112,R113,SEM,
     1 M91,M92,N91,N92,N11,N22,L44,LY
  100 FORMAT(1X,10(E12.5,1X)/8(I10,4X))
      WRITE(6,104)(W1(J),Z1(J),Z2(J),Z3(J),Z4(J),Z5(J),Z6(J),Z7(J),
     1 J=1,N11)
      WRITE(6,101)(Z8(J),DD0(J),Z11(J),Z12(J),Z13(J),Z81(J),
     1 Z82(J),J=1,N11)
  101 FORMAT(1X,7E14.5)
      write(6,105)(j1(i),f22(i),i=1,n22)
  105 format(1x,I10,e14.5)
      WRITE(6,101)(Z83(J),Z84(J),Z85(J),Z86(J),Z87(J),Z88(J),Z89(J),
     1 J=1,N11)
 C102 FORMAT(1X,7E14.5,I10/)
      WRITE(6,103)(VS(J),Z42(J),J=1,N11)
  103 FORMAT(1X,2E14.5)
  104 forMAT(1X,8E14.5)
      T=0.0
      L9=1
      R3=1.0
      DO 110 I22=1,N11
      W0=W1(I22)
      IF(ABS(W0).LT.(1.0E-6))GOTO 110
      J8=J1(I22)
      J9=J1(I22+1)
      I1=I22
      D99(I1)=W0*(F22(I22)-F22(I22+1))/(J9-J8)
      CALL IN
  110 CONTINUE
      R2=.0001
      N55=J1(N22)
      N66=N55-1
      X(N55)=F22(N22)
      X11(N55)=F22(N22)
      U(N55)=.0
      U11(N55)=0.0
      P(N55)=0.0
      DO 210 I22=1,N55
      XS(I22)=X(I22)
      F(I22)=X(I22)
      XS1(I22)=X11(I22)
      F11(I22)=X11(I22)
  210 CONTINUE
      CALL WR
      L9=0
      DT=R2
  220 R3=1.0
  222 T=T+R2
      DO 230 I22=1,N11
      J8=J1(I22)
      J9=J1(I22+1)
      IF(J8.EQ.J9)GOTO 230
      W0=W1(I22)
      I1=I22
```

```
      IF(T.LT.1.0)GOTO 225
      STOP
225   CALL GG
230   CONTINUE
      N66=N55-1
      DO 240 I22=1,N66
      IF(X11(I22+1).LT.X(I22))GOTO 232
      R2=0.5*R2
      GOTO 222
232   V(I22)=W(I22)
      Y(I22)=P(I22)
      Z(I22)=D(I22)
      S(I22)=C(I22)
      XS(I22)=X(I22)
      XS1(I22)=X11(I22)
      STX(I22)=-P(I22)-Q(I22)+C(I22)
      MSS(I22)=C(I22)-D(I22)
      US(I22)=U(I22)
      US1(I22)=U11(I22)
240   CONTINUE
      IF(ABS(X(1)-F(1)).GT.1.0E-6)GOTO 221
      W(1)=W1(1)
      V(1)=W1(1)
      E(1)=0.0
      P(1)=0.0
      Y(1)=0.0
      Q(1)=0.0
      G(1)=0.0
      C(1)=0.0
      S(1)=0.0
      D(1)=0.0
      Z(1)=0.0
     SM1(1)=0.0
     SM2(1)=0.0
     SM3(1)=0.0
     Z44(1)=Z4(1)
     Z55(1)=Z5(1)
      TT(1)=0.0
     DD1(1)=DD0(1)
     DD2(1)=DD0(1)
221   XS(N55)=X(N55)
     XS1(N55)=X11(N55)
     R2=R3*0.1
      IF(ABS(T-DT).LE.(1.0E-1))GOTO 310
      GOTO 220
310   IF(ABS(U11(N55)).GT.(1.0E-4))GOTO 312
      CALL WR1
      GOTO 313
312   CALL WR1
313   DT=DT+0.01
      LMN=0
      GOTO 220
     close(6)
```

```
      END
      SUBROUTINE IN
      DIMENSION F(600),F11(600),X(600),X11(600),XS(600),
     1 XS1(600),U(600),U11(600),V(600),W(600),E(600),P(600),
     2 Y(600),Q(600),G(600),S(600),Z(600),C(600),D(600),
     3 Z1(60),Z2(60),Z3(60),Z4(60),Z5(60),Z6(60),Z7(60),
     4 Z8(60),J1(60),W1(60),F22(60),D99(60),Z51(60)
      DIMENSION Z11(60),Z12(60),Z13(60),Z44(600),Z55(600),
     1 SM1(600),SM2(600),SM3(600),DD0(60),DD1(600),
     2 DD2(600),TT(600),Z81(60),Z82(60),Z83(60),Z84(60),
     3 Z85(60),Z86(60),Z87(60),Z88(60),Z89(60),VS(60),
     4 Z91(60),Z92(60),Z93(60),Z94(60),Z95(60),Z96(60),Z97(60),Z98(60),
     5 A8(600),A9(600),A99(600),TA(600),EC(600),EM(600),VS1(600),
     6 SE(600),STX(600),MSS(600),US(600),US1(600),
     7 Z71(60),Z72(60),Z73(60),Z74(60),Z75(60),Z76(60),Z77(60),
     8 Z61(60),Z62(60),Z63(60),Z41(60),Z42(60),Z43(60),Z54(60),Z45(60),
     9 Z46(60),Z47(60),Z48(60),Z49(60),Z50(60)
      COMMON F,F11,X,X11,XS,XS1,U,U11,V,W,E,Z51,US,US1,
     1 P,Y,Q,G,S,Z,C,D,Z1,Z2,Z3,Z4,Z5,Z6,
     2 Z7,Z8,W1,F22,D99,J1,D8,D9,W8,W9,M91,
     3 M92,N91,N92,G8,G9,N11,N22,L44,J8,
     4 J9,I1,L9,R2,R3,T,DT,N66,N55,W0,SEM,
     5 EVP,VSC,ECP,BAU,EX0
      COMMON Z11,Z12,Z13,Z44,Z55,SM1,SM2,SM3,
     1 DD0,DD1,DD2,TT,LY,Z81,Z82,Z83,Z84,Z85,Z86,Z87,Z88,Z89,
     2 R111,R112,R113,N8,N9,G1,D1,M9,VS,
     3 Z91,Z92,Z93,Z94,Z95,Z96,Z97,Z98,
     4 A8,A9,A99,TA,EC,EM,VS1,SE,STX,MSS,
     5 Z71,Z72,Z73,Z74,Z75,Z76,Z77,
     6 Z61,Z62,Z63,Z41,Z42,Z43,Z54,Z45,Z46,Z47,Z48,Z49,Z50
      IF(ABS(W0-W8).GT.(1.0E-6))GOTO 410
      N8=1
      N9=N91
      G1=G8
      D1=D8
      M9=M91
      CALL EX
      GOTO 430
410   IF(ABS(W0-W9).GT.(1.0E-6))GOTO 420
      N8=1
      N9=N92
      G1=G9
      D1=D9
      M9=M92
      CALL EX
      GOTO 430
420   N8=0
      M9=M91
      CALL IN2
430   RETURN
      END
      SUBROUTINE EX
      DIMENSION F(600),F11(600),X(600),X11(600),XS(600),
```

```
     1  XS1(600),U(600),U11(600),V(600),W(600),E(600),P(600),
     2  Y(600),Q(600),G(600),S(600),Z(600),C(600),D(600),
     3  Z1(60),Z2(60),Z3(60),Z4(60),Z5(60),Z6(60),Z7(60),
     4  Z8(60),J1(60),W1(60),F22(60),D99(60),Z51(60)
        DIMENSION Z11(60),Z12(60),Z13(60),Z44(600),Z55(600),
     1  SM1(600),SM2(600),SM3(600),DD0(60),DD1(600),
     2  DD2(600),TT(600),Z81(60),Z82(60),Z83(60),Z84(60),
     3  Z85(60),Z86(60),Z87(60),Z88(60),Z89(60),VS(60),
     4  Z91(60),Z92(60),Z93(60),Z94(60),Z95(60),Z96(60),Z97(60),Z98(60),
     5  A8(600),A9(600),A99(600),TA(600),EC(600),EM(600),VS1(600),
     6  SE(600),STX(600),MSS(600),US(600),US1(600),
     7  Z71(60),Z72(60),Z73(60),Z74(60),Z75(60),Z76(60),Z77(60),
     8  Z61(60),Z62(60),Z63(60),Z41(60),Z42(60),Z43(60),Z54(60),Z45(60),
     9  Z46(60),Z47(60),Z48(60),Z49(60),Z50(60)
        COMMON F,F11,X,X11,XS,XS1,U,U11,V,W,E,Z51,US,US1,
     1  P,Y,Q,G,S,Z,C,D,Z1,Z2,Z3,Z4,Z5,Z6,
     2  Z7,Z8,W1,F22,D99,J1,D8,D9,W8,W9,M91,
     3  M92,N91,N92,G8,G9,N11,N22,L44,J8,
     4  J9,I1,L9,R2,R3,T,DT,N66,N55,W0,SEM,
     5  EVP,VSC,ECP,BAU,EX0
        COMMON Z11,Z12,Z13,Z44,Z55,SM1,SM2,SM3,
     1  DD0,DD1,DD2,TT,LY,Z81,Z82,Z83,Z84,Z85,Z86,Z87,Z88,Z89,
     2  R111,R112,R113,N8,N9,G1,D1,M9,VS,
     3  Z91,Z92,Z93,Z94,Z95,Z96,Z97,Z98,
     4  A8,A9,A99,TA,EC,EM,VS1,SE,STX,MSS,
     5  Z71,Z72,Z73,Z74,Z75,Z76,Z77,
     6  Z61,Z62,Z63,Z41,Z42,Z43,Z54,Z45,Z46,Z47,Z48,Z49,Z50
        U11(M9)=-D1/(G1+1.0)
        U(M9)=-D1/(G1+1.0)
        W(M9)=(G1/(G1+1.0))**N9/W0
        V(M9)=(G1/(G1+1.0))**N9/W0
        E(M9)=G1/(G1+1.0)/(G1+1.0)/(G1-1.0)*D1*D1*N9
        E(M9)=E(M9)+(D1*D1/(G1*G1-1.0)/2.0)*(1-N9)
        P(M9)=W0*D1*D1/(G1+1.0)*N9
        Q(M9)=0.0
        G(M9)=N9
        IF(L9.EQ.0)GOTO 510
        CALL IN2
  510   RETURN
        END
        SUBROUTINE IN2
        DIMENSION F(600),F11(600),X(600),X11(600),XS(600),
     1  XS1(600),U(600),U11(600),V(600),W(600),E(600),P(600),
     2  Y(600),Q(600),G(600),S(600),Z(600),C(600),D(600),
     3  Z1(60),Z2(60),Z3(60),Z4(60),Z5(60),Z6(60),Z7(60),
     4  Z8(60),J1(60),W1(60),F22(60),D99(60),Z51(60)
        DIMENSION Z11(60),Z12(60),Z13(60),Z44(600),Z55(600),
     1  SM1(600),SM2(600),SM3(600),DD0(60),DD1(600),
     2  DD2(600),TT(600),Z81(60),Z82(60),Z83(60),Z84(60),
     3  Z85(60),Z86(60),Z87(60),Z88(60),Z89(60),VS(60),
     4  Z91(60),Z92(60),Z93(60),Z94(60),Z95(60),Z96(60),Z97(60),Z98(60),
     5  A8(600),A9(600),A99(600),TA(600),EC(600),EM(600),VS1(600),
     6  SE(600),STX(600),MSS(600),US(600),US1(600),
```

```
     7  Z71(60),Z72(60),Z73(60),Z74(60),Z75(60),Z76(60),Z77(60),
     8  Z61(60),Z62(60),Z63(60),Z41(60),Z42(60),Z43(60),Z54(60),Z45(60),
     9  Z46(60),Z47(60),Z48(60),Z49(60),Z50(60)
        COMMON F,F11,X,X11,XS,XS1,U,U11,V,W,E,Z51,US,US1,
     1  P,Y,Q,G,S,Z,C,D,Z1,Z2,Z3,Z4,Z5,Z6,
     2  Z7,Z8,W1,F22,D99,J1,D8,D9,W8,W9,M91,
     3  M92,N91,N92,G8,G9,N11,N22,L44,J8,
     4  J9,I1,L9,R2,R3,T,DT,N66,N55,W0,SEM,
     5  EVP,VSC,ECP,BAU,EX0
        COMMON Z11,Z12,Z13,Z44,Z55,SM1,SM2,SM3,
     1  DD0,DD1,DD2,TT,LY,Z81,Z82,Z83,Z84,Z85,Z86,Z87,Z88,Z89,
     2  R111,R112,R113,N8,N9,G1,D1,M9,VS,
     3  Z91,Z92,Z93,Z94,Z95,Z96,Z97,Z98,
     4  A8,A9,A99,TA,EC,EM,VS1,SE,STX,MSS,
     5  Z71,Z72,Z73,Z74,Z75,Z76,Z77,
     6  Z61,Z62,Z63,Z41,Z42,Z43,Z54,Z45,Z46,Z47,Z48,Z49,Z50
        IF(I1.GE.N11)GOTO 605
        IF(ABS(W1(I1+1)).GT.(1.0E-6))GOTO 605
        X11(J9)=F22(I1+1)
605     X(J8)=F22(I1)
        IF(J8.EQ.M9)GOTO 607
        U11(J8)=0.0
        U(J8)=0.0
607     IF(J9.EQ.M9)GOTO 608
        U11(J9)=0.0
        U(J9)=0.0
608     J81=J8+1
        J91=J9-1
        DO 620 J=J81,J91
        X11(J)=X(J-1)-D99(I1)/W0
        X(J)=X(J-1)-D99(I1)/W0
        IF(J.EQ.M9)GOTO 620
        U11(J)=0.0
        U(J)=0.0
        GOTO 620
620     CONTINUE
        DO 610 J=1,20
        U11(J)=-0.4
        U(J)=-0.4
610     CONTINUE
        U11(21)=-0.2
        U(21)=-0.2
        P(20)=6.4
        P(21)=6.4
        IF(I1.EQ.1)GOTO 623
        IF(ABS(W1(I1-1)).LE.(1.0E-6))GOTO 625
623     X11(J8)=X(J8)
625     DO 660 J=J8,J91
        IF(J.EQ.M9)GOTO 626
        W(J)=1.0/W0
        V(J)=1.0/W0
       E(J)=0.0
        P(J)=0.0
```

```
      Y(J)=0.0
      Q(J)=0.0
      G(J)=0.0
      C(J)=0.0
      S(J)=0.0
      D(J)=0.0
      Z(J)=0.0
      SM1(J)=0.0
      SM2(J)=0.0
      SM3(J)=0.0
      Z44(J)=Z4(I1)
      Z55(J)=Z5(I1)
      TT(J)=0.0
      DD1(J)=DD0(I1)
      DD2(J)=DD0(I1)
      A8(J)=0.0
      A9(J)=0.0
      A99(J)=0.0
      TA(J)=300.0
      EC(J)=0.0
      EM(J)=0.0
      SE(J)=0.0
      VS1(J)=VS(I1)
      GOTO 660
626   C(J)=0.0
      S(J)=0.0
      D(J)=0.0
      Z(J)=0.0
      TT(J)=0.0
      SM1(J)=0.0
      SM2(J)=0.0
      SM3(J)=0.0
      Z44(J)=Z4(I1)
      Z55(J)=Z5(I1)
627   IF(ABS(P(M9)).LE.(1.0E-6))GOTO 660
630   X2=0.5*SQRT(G1)/1.5*ABS(X11(J+1)-X(J))
      X2=X2/SQRT(G1*P(J)*V(J))
      IF(R3.LE.X2)GOTO 660
      R3=X2
660   CONTINUE
      RETURN
      END
      SUBROUTINE GG
      DIMENSION F(600),F11(600),X(600),X11(600),XS(600),
     1 XS1(600),U(600),U11(600),V(600),W(600),E(600),P(600),
     2 Y(600),Q(600),G(600),S(600),Z(600),C(600),D(600),
     3 Z1(60),Z2(60),Z3(60),Z4(60),Z5(60),Z6(60),Z7(60),
     4 Z8(60),J1(60),W1(60),F22(60),D99(60),Z51(60)
      DIMENSION Z11(60),Z12(60),Z13(60),Z44(600),Z55(600),
     1 SM1(600),SM2(600),SM3(600),DD0(60),DD1(600),
     2 DD2(600),TT(600),Z81(60),Z82(60),Z83(60),Z84(60),
     3 Z85(60),Z86(60),Z87(60),Z88(60),Z89(60),VS(60),
     4 Z91(60),Z92(60),Z93(60),Z94(60),Z95(60),Z96(60),Z97(60),Z98(60),
```

```
     5   A8(600),A9(600),A99(600),TA(600),EC(600),EM(600),VS1(600),
     6   SE(600),STX(600),MSS(600),US(600),US1(600),
     7   Z71(60),Z72(60),Z73(60),Z74(60),Z75(60),Z76(60),Z77(60),
     8   Z61(60),Z62(60),Z63(60),Z41(60),Z42(60),Z43(60),Z54(60),Z45(60),
     9   Z46(60),Z47(60),Z48(60),Z49(60),Z50(60)
         COMMON F,F11,X,X11,XS,XS1,U,U11,V,W,E,Z51,US,US1,
     1   P,Y,Q,G,S,Z,C,D,Z1,Z2,Z3,Z4,Z5,Z6,
     2   Z7,Z8,W1,F22,D99,J1,D8,D9,W8,W9,M91,
     3   M92,N91,N92,G8,G9,N11,N22,L44,J8,
     4   J9,I1,L9,R2,R3,T,DT,N66,N55,W0,SEM,
     5   EVP,VSC,ECP,BAU,EX0
         COMMON Z11,Z12,Z13,Z44,Z55,SM1,SM2,SM3,
     1   DD0,DD1,DD2,TT,LY,Z81,Z82,Z83,Z84,Z85,Z86,Z87,Z88,Z89,
     2   R111,R112,R113,N8,N9,G1,D1,M9,VS,
     3   Z91,Z92,Z93,Z94,Z95,Z96,Z97,Z98,
     4   A8,A9,A99,TA,EC,EM,VS1,SE,STX,MSS,
     5   Z71,Z72,Z73,Z74,Z75,Z76,Z77,
     6   Z61,Z62,Z63,Z41,Z42,Z43,Z54,Z45,Z46,Z47,Z48,Z49,Z50
         IF(ABS(W0-W8).GT.(1.0E-6))GOTO 710
         N8=1
         G1=G8
         D1=D8
         CALL GGA
         GOTO 730
710      IF(ABS(W0-W9).GT.(1.0E-6))GOTO 720
         N8=1
         G1=G9
         D1=D9
         CALL GGA
         GOTO 730
720      N8=0
         IF(J8.LE.M91)GOTO 722
         IF(J8.LE.M92)GOTO 722
         IF(ABS(X(J8)-F(J8)).GT.(1.0E-6))GOTO 722
         IF(ABS(P(J9)).GT.(1.0E-3))GOTO 722
         GOTO 730
722      CALL GGA
730      RETURN
         END
         SUBROUTINE GGA
         DIMENSION F(600),F11(600),X(600),X11(600),XS(600),
     1   XS1(600),U(600),U11(600),V(600),W(600),E(600),P(600),
     2   Y(600),Q(600),G(600),S(600),Z(600),C(600),D(600),
     3   Z1(60),Z2(60),Z3(60),Z4(60),Z5(60),Z6(60),Z7(60),
     4   Z8(60),J1(60),W1(60),F22(60),D99(60),Z51(60)
         DIMENSION Z11(60),Z12(60),Z13(60),Z44(600),Z55(600),
     1   SM1(600),SM2(600),SM3(600),DD0(60),DD1(600),
     2   DD2(600),TT(600),Z81(60),Z82(60),Z83(60),Z84(60),
     3   Z85(60),Z86(60),Z87(60),Z88(60),Z89(60),VS(60),
     4   Z91(60),Z92(60),Z93(60),Z94(60),Z95(60),Z96(60),Z97(60),Z98(60),
     5   A8(600),A9(600),A99(600),TA(600),EC(600),EM(600),VS1(600),
     6   SE(600),STX(600),MSS(600),US(600),US1(600),
     7   Z71(60),Z72(60),Z73(60),Z74(60),Z75(60),Z76(60),Z77(60),
```

```
     8  Z61(60),Z62(60),Z63(60),Z41(60),Z42(60),Z43(60),Z54(60),Z45(60),
     9  Z46(60),Z47(60),Z48(60),Z49(60),Z50(60)
        COMMON F,F11,X,X11,XS,XS1,U,U11,V,W,E,Z51,US,US1,
     1  P,Y,Q,G,S,Z,C,D,Z1,Z2,Z3,Z4,Z5,Z6,
     2  Z7,Z8,W1,F22,D99,J1,D8,D9,W8,W9,M91,
     3  M92,N91,N92,G8,G9,N11,N22,L44,J8,
     4  J9,I1,L9,R2,R3,T,DT,N66,N55,W0,SEM,
     5  EVP,VSC,ECP,BAU,EX0
        COMMON Z11,Z12,Z13,Z44,Z55,SM1,SM2,SM3,
     1  DD0,DD1,DD2,TT,LY,Z81,Z82,Z83,Z84,Z85,Z86,Z87,Z88,Z89,
     2  R111,R112,R113,N8,N9,G1,D1,M9,VS,
     3  Z91,Z92,Z93,Z94,Z95,Z96,Z97,Z98,
     4  A8,A9,A99,TA,EC,EM,VS1,SE,STX,MSS,
     5  Z71,Z72,Z73,Z74,Z75,Z76,Z77,
     6  Z61,Z62,Z63,Z41,Z42,Z43,Z54,Z45,Z46,Z47,Z48,Z49,Z50
810     DO 1610 J=J8,J9
        IF(J.EQ.1)GOTO 950
        IF(ABS(X11(J8)-X(J8)).GT.(1.0E-4))GOTO 812
        IF(J.EQ.J8)GOTO 1610
812     IF(J.EQ.J1(N22))GOTO 1004
        IF(ABS(X11(J)-X(J)).LT.(1.0E-6))GOTO 830
        IF(X11(J).GT.X(J))GOTO 950
8300    LMN=1
        IF(J.EQ.J1(N22))GOTO 2000
        F100=U(J)
        F101=U11(J)
        IF(J.EQ.J8)GOTO 8220
        IF(J.EQ.J9)GOTO 8220
        GOTO 814
8220    IF(ABS(W1(I1)-W8).GT.(1.0E-6))GOTO 8223
8221    U11(J)=0.0
        U(J)=0.0
        IF(J.EQ.J9)GOTO 1990
        X(J)=X11(J)
        GOTO 1610
1990    X11(J)=X(J)
        GOTO 1610
8223    IF(ABS(W1(I1)-W9).GT.(1.0E-6))GOTO 8224
        GOTO 8221
8224    IF(J.EQ.J8)GOTO 822
        IF(J.EQ.J9)GOTO 824
814     IF(U(J).GT.0.0)GOTO 816
        U11(J)=U(J)+0.5*(U11(J)-U(J))
        U(J)=U(J)+0.5*(U11(J)-U(J))
        GOTO 820
816     U11(J)=U11(J)+0.5*(U(J)-U11(J))
        U(J)=U11(J)+0.5*(U(J)-U11(J))
820     IF(ABS(F101-F100).LT.1.0E-6)GOTO 830
        T100=ABS(XS1(J)-XS(J))/ABS(F101-F100)
        X(J)=XS(J)+F100*T100+(R2-T100)*U(J)
        X11(J)=XS(J)+F100*T100+(R2-T100)*U(J)
        GOTO 1610
822     IF(ABS(W1(I1-1)).GT.(1.0E-6))GOTO 823
```

```
      I5=I1-2
      GOTO 803
823   I5=I1-1
803   IF(ABS(W1(I1)-W1(I5)).LT.(1.0E-6))GOTO 814
      GOTO 825
824   IF(ABS(W1(I1+1)).GT.(1.0E-6))GOTO 805
      I5=I1+2
      GOTO 806
805   I5=I1+1
806   IF(ABS(W1(I5)-W1(I1)).LT.(1.0E-6))GOTO 814
      GOTO 825
825   IF(U(J).LE.0.0)GOTO 826
      UV11=U(J)
      UV=U11(J)
      IF(J.EQ.J9)GOTO 6
      I4=I1
      GOTO 828
6     I4=I5
      I5=I1
      GOTO 828
826   UV11=-U11(J)
      UV=-U(J)
      IF(J.EQ.J9)GOTO 8
      I4=I5
      I5=I1
      GOTO 828
8     I4=I1
828   F17=W1(I4)*Z2(I4)-W1(I5)*Z2(I5)
      F18=W1(I4)*Z1(I4)+W1(I5)*Z1(I5)+2*W1(I4)*Z2(I4)*UV11-
     1 2*W1(I5)*Z2(I5)*UV
      F19=W1(I4)*Z1(I4)*UV11+W1(I4)*Z2(I4)*UV11*UV11-W1(I5)*
     1 Z2(I5)*UV*UV+W1(I5)*Z1(I5)*UV
      IF(U(J).LT.0.0)GOTO 829
      U(J)=(F18+SQRT(F18*F18-4*F17*F19))/2/F17
      U11(J)=(F18+SQRT(F18*F18-4*F17*F19))/2/F17
      GOTO 820
829   U(J)=-(F18+SQRT(F18*F18-4*F17*F19))/2/F17
      U11(J)=-(F18+SQRT(F18*F18-4*F17*F19))/2/F17
      GOTO 820
830   IF(J.EQ.J9)GOTO845
      GOTO 870
845   IF((-P(J)-Q(J)+S(J)-P(J-1)-Q(J-1)+S(J-1))/2.GT.0.)
     1 GOTO 950
      GOTO 1002
870   IF(LY.EQ.1)GOTO 872
      IF((SM1(J)+SM1(J-1))/2.0.LT.Z11(I1))GOTO 880
      SM1(J)=0.0
      SM1(J-1)=0.0
      SM3(J)=0.0
      SM3(J-1)=0.0
      GOTO 1850
872   IF(ABS(DD1(J)-1.0).LT.1.0E-5)DD1(J)=DD0(I1)
      IF(ABS(DD1(J)).LT.1.0E-5)DD1(J)=DD0(I1)
```

```
      F1=Z5(I1)*2./3.*ALOG(1.0/(1.0-1.0/DD1(J)))
     IF((-P(J)).GE.F1)GOTO 1308
880    F1=-P(J)-Q(J)+S(J)+P(J-1)+Q(J-1)-S(J-1)
       F3=(S(J)-Z(J))/(X11(J+1)+X(J))*W(J)+
     1 (S(J-1)-Z(J-1))/(X11(J)+X(J-1))*W(J-1)
       IF(J.EQ.J9)GOTO 966
       GOTO 920
966    F1=2*F1
       GOTO 1620
920    U11(J)=U(J)-R2*F1/D99(I1)*X(J)**(L44-1)
     1 /F(J)**(L44-1)+F3*(L44-1)*R2
       U(J)=U(J)-R2*F1/D99(I1)*X(J)**(L44-1)
     1 /F(J)**(L44-1)+F3*(L44-1)*R2
       X11(J)=XS(J)+R2*U(J)
       X(J)=XS(J)+R2*U(J)
       GOTO 1005
1308   IF(ABS(A9(J)).LT.1.0E-6)GOTO 1382
       IF(VSC.EQ.1.0)GOTO 1380
       IF(VSC.EQ.2.0)GOTO 1384
       IF(VSC.EQ.3.0)GOTO 1386
       VS1(J)=ABS((S(J))/(2.0/3.0*A9(J)))
       GOTO 1382
1380   VS1(J)=VS(I1)*ABS(A9(J)*1.0E+5)**0.
       GOTO 1382
1384   F1=E(J)-EC(J)+Z62(I1)*ABS(S(J)*A9(J))
       VS1(J)=Z61(I1)*EXP(Z63(I1)/F1)*2.0*Z44(J)
       GOTO 1382
1386   F2=ABS(A99(J))
       F1=Z43(I1)+Z46(I1)*F2+Z47(I1)*F2**2.0+Z48(I1)*F2**3.0
       F1=(F1+Z49(I1)*F2**4.0+Z50(I1)**5.0)*0.1
       F1=EXP(Z54(I1)*(Z55(J)/SQRT(3.0)-F1)/Z43(I1))-1
       VS1(J)=ABS(Z55(J)/SQRT(3.0)/F1/Z45(I1))
1382   F1=P(J)+Q(J)+Z5(I1)/DD1(J)*ALOG(DD1(J)/(DD1(J)-1.0))
       f1=-F1*DD1(J)*(DD1(J)-1.0)**(1.0/3.0)*(DD0(I1)-1.0)**(2/3)
     1 /VS1(J)
      f1=z5(i1)*2./3.*alog(1./(1.-1./dd1(j)))
      DD1(J)=DD1(J)+3.*dd1(j)*(dd1(j)-1.)*abs(p(j)+f1)/2./z5(i1)
5555   F1=(DD1(J)-1.0)/DD1(J)
      IF(F1.LE.0.0001)GOTO 880
       SM3(J)=0.0
      DD1(J)=DD0(I1)
1850   goto 950
950    IF(J.EQ.J1(N22))GOTO 1004
       F1=2*(-P(J)-Q(J)+S(J))
       F3=(S(J)-Z(J))/(X11(J+1)+X(J))*W(J)*2
       U(J)=U(J)-R2*F1/D99(I1)*X(J)**(L44-1)/F(J)
     1 **(L44-1)+F3*(L44-1)*R2
       U11(1)=U(1)
       X(J)=XS(J)+R2*U(J)
       X11(1)=X(1)
       IF(J.EQ.J8)GOTO 1005
960    F1=-2*(-P(J-1)-Q(J-1)+S(J-1))
       F3=(S(J-1)-Z(J-1))/(X11(J)+X(J-1))*W(J-1)*2
```

```
      U11(J)=U11(J)-R2*F1/D99(I1)*X11(J)**(L44-1)
     1 /F11(J)**(L44-1)+F3*(L44-1)*R2
      X11(J)=XS1(J)+R2*U11(J)
      U(N55)=U11(N55)
      X(N55)=X11(N55)
      GOTO 1005
 1002 IF(ABS(X11(J-1)-X(J-1)).LT.1.0E-6)GOTO 1013
      GOTO 880
 1013 IF(ABS(X11(J+1)-X(J+1)).LT.1.0E-6)GOTO 1003
      GOTO 880
 1003 F1=3.0*(-P(J)-Q(J)+S(J)+P(J-1)+Q(J-1)-S(J-1))
      F1=F1-1.0/3.0*(-P(J+1)-Q(J+1)+S(J+1)+P(J-2)+
     1 Q(J-2)-S(J-2))
      F3=(S(J)-Z(J))/(X11(J+1)+X(J))*W(J)+
     1 (S(J-1)-Z(J-1))/(X11(J)+X(J-1))*W(J-1)
 1620 IF(ABS(W1(I1+1)).GT.(1.0E-6))GOTO 1622
      I7=I1+2
      GOTO 1624
 1622 I7=I1+1
 1624 U11(J)=U(J)-R2*F1/(D99(I1)+D99(I7))*
     1 X(J)**(L44-1)/F(J)**(L44-1)+F3*(L44-1)*R2
      U(J)=U(J)-R2*F1/(D99(I1)+D99(I7))*
     1 X(J)**(L44-1)/F(J)**(L44-1)+F3*(L44-1)*R2
      X11(J)=XS(J)+R2*U(J)
      X(J)=XS(J)+R2*U(J)
      GOTO 1005
 1710 IF(L44.EQ.1)GOTO 1701
      IF(J.EQ.J8)GOTO 1701
      IF(J.EQ.J9)GOTO 1701
      F1=ABS(X11(J+1)**L44-X(J-1)**L44-XS1(J+1)**
     1 L44+XS(J-1)**L44)
      F3=((X11(J+1)+XS1(J+1))/2.0)**(L44-1)
      F3=ABS(F3-((X(J-1)+XS(J-1))/2.0)**(L44-1))
      F2=(4.0/3.0)**(L44-2)*F1/F(J)*D99(I1)/W1(I1)
      DD2(J)=DD2(J)+F2/(3.1416**(L44-2))/F3
      F2=1.0-(DD2(J)/DD0(I1))**(2.0/3.0)
      IF(F2.LE.(1.0E-4))F2=0.0
      F2=F2*Z8(I1)
      IF(F2.GT.(1.0E-3))GOTO 1701
      SM3(J)=0.0
      DD2(J)=DD0(I1)
      GOTO 1701
 1004 IF(L44.EQ.1)GOTO 960
      U(J)=0.0
      X(J)=F(J)
      IF((-P(J-1)-Q(J-1)+S(J-1)).GT.Z8(I1))GOTO 960
      U11(J)=0.0
      X11(J)=F11(J)
      GOTO 1005
 2000 IF(L44.EQ.1)GOTO 960
      U(J)=0.0
      X(J)=F(J)
      U11(J)=0.0
```

```
      X11(J)=F11(J)
1005  IF(ABS(Q(J)).GT.1.0E-6)GOTO 1701
      IF(LY.EQ.1)GOTO 1740
      IF(SM2(J).LT.Z11(I1))GOTO 1701
      SM2(J)=0.0
      SM3(J)=0.0
1740  IF((-P(J)-Q(J)+Z(J)).GE.Z8(I1))GOTO 1710
1701  IF(J.EQ.1)GOTO 1610
      IF(X11(J).GE.X(J))GOTO 1610
      IF(ABS(U11(J)-U(J)).LT.1.0E-3)GOTO 1610
1610  CONTINUE
      IF(N8.EQ.0)GOTO 1006
      E9=G1/(G1+1)/W0
1006  DO 1020 J=J8,J9
1061  IF(J.EQ.J9)GOTO 1020
      IF(ABS(W0-W8).GT.(1.0E-6))GOTO 6543
      IF(N8.EQ.1)TT(J)=ABS(F(M9)-(F(J)+F11(J+1))/2.0)/D1
6543  IF(ABS(X11(J+1)-F11(J+1)).LE.(1.0E-6))GOTO 1070
      GOTO 1062
1070  IF(ABS(X(J)-F(J)).LE.(1.0E-6))GOTO 1020
1062  W(J)=ABS(X11(J+1)**L44-X(J)**L44)/
     1  ABS(F11(J+1)**L44-F(J)**L44)/W0
      IF(N8.EQ.0)GOTO 1007
      IF(E9.LT.W(J))GOTO 1007
      E9=W(J)
1007  IF(W(J).LT.V(J))GOTO 1008
      Q(J)=0.0
      GOTO 1020
1008  IF(ABS(W0-W8).LT.(1.0E-6))GOTO 1009
      IF(ABS(W0-W9).LT.(1.0E-6))GOTO 1009
      H1=2.0
      GOTO 1015
1009  H1=2.0
1015  F1=2*h1*h1/(W(J)+V(J))
      Q(J)=F1*(U11(J+1)-U(J))*(U11(J+1)-U(J))
      IF(P(J).LT.0.0)GOTO 1020
      F2=P(J)*0.5*(V(J)+W(J))
     Q(J)=Q(J)+1.6/(W(J)+V(J))*SQRT(F2)*
     1  ABS(U11(J+1)-U(J))
1020  CONTINUE
      IF(W0.LT.(3.0E-2))GOTO 1100
      IF(N8.EQ.0)GOTO 1205
1100  J91=J9-1
      DO 1119 J=J8,J91
      IF(ABS(W(J)-1.0/W0).LE.(1.0E-6))GOTO 1119
      IF(W0.GT.(3.0E-2))GOTO 1101
      G(J)=1.0
      G1=1.4
1101  IF(ABS(G(J)-1.0).LE.(1.0E-6))GOTO 1116
      IF(J.EQ.M9)GOTO 1102
      IF(ABS(W0-W8).GT.(1.0E-6))GOTO 6542
      IF(T.LT.TT(J))GOTO 1106
      IF(ABS(0.5*(X(J+1)-X(J))).LE.(D1*(T-TT(J))))GOTO1102
```

```
      F5=0.4*D1*(T-TT(J))/(ABS(X(J+1)-X(J)))
6542  IF(ABS(X11(J9)-F11(J9)).LT.(1.0E-6))GOTO6541
      IF(ABS(G(J91)-1.0).LT.(1.0E-6))GOTO6541
      J92=J91-1
      G(J91)=1.0
      J101=J92
      P(J91)=W0*D1*D1/(G1+1.0)
      E(J91)=G1/(G1+1.0)/(G1+1.0)/(G1-1.0)/D1*D1
      W(J91)=(G1/(G1+1.0))/W0
      P(J92)=P(J91)
      E(J92)=E(J91)
      W(J92)=W(J91)
6541  E5=G1/(G1+1.0)/W0
      IF(W(J).LT.E5)GOTO1102
      GOTO1110
1102  G(J)=1.0
      GOTO1116
1106  G(J)=0.0
      GOTO1116
1110  F1=(ABS(1.0/W0-W(J)))**2.1
      G(J)=F1/(ABS(1.0/W0-E9))**2.1
      IF(G(J).GT.0.99)G(J)=1.0
      IF(G(J).LT.0.01)G(J)=0.0
1116  F1=(E(J)-(0.5*P(J)+Q(J))*(W(J)-V(J)))
      E(J)=F1/(1+0.5*(G1-1)*G(J)/W(J)*(W(J)-
     1  V(J)))
      P(J)=(G1-1)*G(J)*E(J)/W(J)
      F1=G1*P(J)*W(J)
      IF(F1.LT.(1.0E-6))GOTO 1119
      X2=0.5*SQRT(G1)/1.5*ABS(X11(J+1)-X(J))/
     1  SQRT(F1)
      IF(R3.LE.X2)GOTO 1119
      R3=X2
1119  CONTINUE
      GOTO 1350
1205  J91=J9-1
      DO 1319 J=J8,J91
      IF(ABS(W(J)-1/W0).LE.(1.0E-6))GOTO 1319
      F1=0.5*(X11(J+1)+XS1(J+1)-X(J)-XS(J))
      A9(J)=(U11(J+1)+US1(J+1)-U(J)-US(J))*0.5/F1
      A99(J)=A99(J)+A9(J)*R2
      F1=0.50*(X11(J+1)+XS1(J+1)+X(J)+XS(J))
      A8(J)=0.0
      IF(EVP.EQ.1.0)GOTO 1207
      F1=1.0/3.0*(W(J)-V(J))/(0.5*(W(J)+V(J)))
      GOTO 1209
1207  F3=(E(J)-EC(J))+Z62(I1)*ABS(S(J)*A9(J))
      IF(ABS(F3).LT.1.0E-1)GOTO 1299
      F2=Z61(I1)*EXP(Z63(I1)/F3)
      IF(ABS(F2).LT.1.0E-10)GOTO 1299
      IF(ABS(SE(J)).GE.(2.0/3.0*(Z55(J))))GOTO 1208
      F1=(S(J)-SE(J))/F2
      GOTO 1209
```

```
1208    F1=(S(J)-2.0/3.0*Z55(J))/F2
        GOTO1209
1299    F1=0.0
1209    IF(LY.EQ.1)GOTO 1210
        IF((-P(J)-Q(J)+S(J)).GE.Z5(I1))GOTO 1220
        GOTO 1240
1210    IF(DD1(J).GT.DD0(I1))GOTO 1222
        GOTO1240
1220    F3=ABS(X11(J+1)**L44-X(J)**L44-XS1(J+1)
     1  **L44+XS(J)**L44)
        SM3(J)=SM3(J)+F3/(ABS(XS1(J+1)**L44-XS(J)
     1  **L44))
        GOTO 1223
1222    SM3(J)=(DD1(J)-1.0)/DD1(J)
1223    F3=15.0*(1.0-Z13(I1))/(7.0-5.0*Z13(I1))
        Z44(J)=Z4(I1)*(1.0-SM3(J)*F3)
        Z55(J)=Z5(I1)*(1.0-4.0*SM3(J))
        GOTO 1250
1240    IF(ECP.EQ.1.0)GOTO 1241
1244    Z44(J)=Z4(I1)
        Z55(J)=Z5(I1)
        GOTO 1250
1241    IF(E(J).LT.EM(J))GOTO 1242
        Z44(J)=0.0
        Z55(J)=0.0
        GOTO 1250
1242    F91=P(J)/(1.0/W0/W(J))**(1.0/3.0)
        F92=Z95(I1)*(TA(J)-300.00)
        F93=(1.0+Z94(I1)*F91-F92)
        F94=Z5(I1)*ABS(1.0+Z92(I1)*A99(J))**Z93(I1)
        Z44(J)=Z4(I1)*F93
        Z55(J)=F94*F93
        IF(F94.LT.Z91(I1))GOTO 1250
        Z55(J)=Z91(I1)*F93
1250    SE(J)=SE(J)+2.0*Z44(J)*A9(J)*R2
        C(J)=S(J)+2.0*Z44(J)*(A9(J)*R2-F1)
        D(J)=Z(J)+2.0*Z44(J)*(A8(J)*R2-F1)
        DC9=-C(J)-D(J)
        DK8=C(J)*C(J)+D(J)*D(J)+DC9*DC9
        DK9=DK8-2.0/3.0*Z55(J)*Z55(J)
        IF(ABS(DK8).LE.(1.0E-6))GOTO 1228
        IF(DK9.LT.0.0)GOTO 1228
        C(J)=C(J)*SQRT(2.0/3.0)*Z55(J)/SQRT(DK8)
        D(J)=D(J)*SQRT(2.0/3.0)*Z55(J)/SQRT(DK8)
1228    IF(BAU.EQ.1.0)GOTO 1229
        GOTO 1270
1229    IF(C(J).LE.S(J))GOTO 1270
        F3=2.0/3.0*Z55(J)
        IF(ABS(F3).LT.1.0E-6)GOTO 1271
        IF(C(J).GE.0.0)GOTO 1246
        Z44(J)=Z41(I1)-C(J)/F3*(Z4(I1)-Z41(I1))
        GOTO 1248
1246    Z44(J)=(1.0-C(J)/F3)*Z41(I1)
```

```
1248   IF(Z44(J).GT.(Z4(I1)*F93))GOTO 1270
       Z44(J)=Z4(I1)*F93
       GOTO 1270
1271   Z44(J)=0.0
1270   X1=0.5*(W(J)+V(J))*0.5*(C(J)+S(j))*A9(J)*R2
       Y1=0.5*(W(J)+V(J))*0.5*(D(J)+Z(j))*A8(J)*R2
     1 *(L44-1)
       A1=0.5*(V(J)-W(J))/DD1(J)
       B1=E(J)+(0.5*P(J)+Q(J))*(V(J)-W(J))
       W(J)=W(J)/DD1(J)
       W1(I1)=W1(I1)*DD0(I1)
       IF(SEM.EQ.2.0)GOTO 1280
       IF(SEM.EQ.3.0)GOTO 1285
       IF(SEM.EQ.4.0)GOTO 1290
       F31=(1.0/W1(I1)/W(J))**2.0*Z85(I1)
       F32=F31-A1*Z81(I1)*F31/W(J)-A1*Z82(I1)*F31/W(J)
       F33=(1.0/W1(I1)/W(J))-1.0
       F34=F32-A1*(Z83(I1)*F33+Z84(I1)*F33*F33)-B1-X1-Y1
       F35=F31*(Z83(I1)*F33*A1+Z84(I1)*F33*F33*A1+B1+X1+Y1)
       F36=1.0-Z81(I1)*A1/W(J)
       E(J)=(-F34+SQRT(F34*F34+4.0*F36*F35))/2.0/F36
       P(J)=E(J)/W(J)*(Z81(I1)+Z82(I1)/(E(J)/F31+1.0))
     1 +Z83(I1)*F33+Z84(I1)*F33*F33
       PC=P(J)
       IF(W(J).LT.1.0/W1(I1))GOTO 1305
       F37=W(J)*W1(I1)-1.0
       F38=F31-A1*F31/W(J)*(Z81(I1)+
     1 Z82(I1)*EXP(-Z86(I1)*F37*F37))
       F41=A1*Z83(I1)*F33*EXP(-Z87(I1)*F37-Z86(I1)*F37*F37)
       F38=F38-F41-B1-X1-Y1
       F39=F31*(F41+B1+X1+Y1)
       E(J)=(-F38+SQRT(F38*F38+4.0*F36*F39))/2.0/F36
       P(J)=Z81(I1)*E(J)/W(J)+(Z82(I1)*E(J)/W(J)/
     1 (E(J)/F31+1.0)+Z83(I1)*F33*EXP(-Z87(I1)*F37))
     2 *EXP(-Z86(I1)*F37*F37)
       PE=P(J)
       IF(E(J).GT.Z89(I1))GOTO 4321
       E(J)=(B1+X1+Y1)*(Z89(I1)-Z88(I1))-A1*Z88(I1)*PE
       E(J)=(E(J)+A1*Z89(I1)*PC)/(Z89(I1)-Z88(I1)-
     1 A1*PE+A1*PC)
       P(J)=(E(J)-Z88(I1))*PE+(Z89(I1)-E(J))*PC
       P(J)=P(J)/(Z89(I1)-Z88(I1))
       GOTO 4321
1280   Y7=W0*Z1(I1)*Z1(I1)*(1-W0*W(J))
       Y7=Y7/(1-Z2(I1)*(1.0-W0*W(J)))
       Y7=Y7/(1-Z2(I1)*(1.0-W0*W(J)))
       F1=0.5*Y7*(1/W0-W(J))
       E(J)=A1*Y7-Z3(I1)*A1*F1*W0+B1+X1+Y1
       E(J)=E(J)/(1-Z3(I1)*A1*W0)
       P(J)=Y7+Z3(I1)*W0*(E(J)-F1)
       GOTO1282
1285   TA(J)=3.0E-4
       F1=1.0/W(J)/W1(I1)
```

```
      F2=42.83-100.11*F1**(1.0/3.0)+51.88*F1**(2.0/3.0)
      F2=F2+39.56*F1-49.84*F1**(4.0/3.0)+15.66*F1**(5.0/3.0)
      F3=-15.804/F1+55.406*F1**(-2.0/3.0)-57.431*F1**(-1.0/3.0)
      F3=F3+64.326-55.168*F1**(1.0/3.0)+8.6712*F1**(2.0/3.0)
      F3=F3+14.6*ALOG(F1)
      F4=-0.6657*F1**(-2.0/3.0)+0.6901*F1**(-1.0/3.0)
      F4=F4+0.7894-1.3257*F1**(1.0/3.0)+0.5207*F1**(2.0/3.0)
1286  F5=4.624*TA(J)*(2.0*F4+TA(J))/(F4+TA(J))
      F6=8.355*F1*TA(J)*(3.0*F4+TA(J))/(F4+TA(J))
      F7=281.36*F1**(1.0/2.0)*TA(J)**2.0
      F111=(F2+F6+F7)*0.01
      F111=A1*F111+B1+X1+Y1
      F8=207.65*F1**(-1.0/2.0)*TA(J)**2.0
      F111=F111-(F8+F3)*0.01
      IF(ABS(F5*0.01-F111).LT.1.0E-6)GOTO1287
      TA(J)=TA(J)+1.0E-6
      GOTO 1286
1287  P(J)=(F2+F6+F7)*0.01
      E(J)=(F3+F5+F8)*0.01
      TA(J)=TA(J)*1.0E+6
      GOTO 1282
1290  F40=1.0/W(J)/W1(I1)
      F41=-1.989+11.3*F40-5.433*F40**2.0+0.7943*F40**3.0
      F41=F41+0.657E-7*F40**4.0
      F42=-209.69+402.5*F40-279.59*F40**2.0+85.99*F40**3.0
      F43=0.0
      F44=0.0
      B1=B1+X1+Y1
      FS1=1.0-F41*A1
      FS2=F41*B1+F42+F41*(X1+Y1)
      P(J)=FS2/FS1
      E(J)=A1*P(J)+B1
1282  IF(P(J).GE.0.0)GOTO 1305
      F1=B1+X1+Y1-Z3(I1)*W0*Z6(I1)/Z7(I1)/3
     1 *A1*(W(J)*W0-1)
      E(J)=F1/(1-A1*Z3(I1)*W0)
      P(J)=Z3(I1)*W0*(E(J)-Z6(I1)/Z7(I1)/3.0*
     1 (W(J)*W0-1))
4321  IF((-P(J)-Q(J)+C(J)).LT.Z5(I1))GOTO 1420
      SM1(J)=SM1(J)+ABS(Z55(J)+P(J)+Q(J)-C(J))**
     1 (Z12(I1))*R2
1420  IF((-P(J)-Q(J)+D(J)).LT.Z5(I1))GOTO 1305
      SM2(J)=SM2(J)+ABS(Z55(J)+P(J)+Q(J)-D(J))**
     1 (Z12(I1))*R2
1305  W(J)=W(J)*DD1(J)
      W1(I1)=W1(I1)/DD0(I1)
      p(j)=p(j)/dd1(j)
     IF(EX0.EQ.2.0)GOTO 1306
      F1=1.0/W(J)/Z71(I1)
      F2=1.0/Z74(I1)*(EXP(Z74(I1)*(1.0-F1**(-1.0/3.0)))-1.0)
      EC(J)=3.0/Z71(I1)*Z73(I1)*(1.0-F1**(1.0/3.0)+F2)
      GOTO 1307
1306  F1=1.0/W(J)/W1(I1)
```

```
      F2=Z71(I1)/F1+Z72(I1)/F1**(2.0/3.0)+Z73(I1)/F1**(1.0/3.0)
      F2=F2+Z74(I1)+Z75(I1)*F1**(1.0/3.0)+Z76(I1)*F1**(2.0/3.0)
      EC(J)=(F2+Z77(I1)*ALOG(F1))*0.01
1307  TA(J)=(E(J)-EC(J))/Z51(I1)
      F1=1.0/W0/W(J)
      F2=F1**(2.0*(Z97(I1)-Z98(I1)-1.0/3.0))
      EM(J)=EC(J)+Z51(I1)*Z96(I1)*EXP(2.0*Z98(I1)*(1.0-1.0/F1))*F2
      IF(ABS(V(J)-W(J)).LE.(1.0E-6))GOTO 1315
      F1=ABS(W(J)*W(J)*(Y(J)-P(J))/(V(J)-W(J)))
      F1=F1/W(J)/W(J)*0.5*(V(J)+W(J))*0.5*
     1(V(J)+W(J))
      IF(F1.LE.(1.0E-6))GOTO 1315
      F1=ABS(X11(J+1)-X(J))*0.5/SQRT(F1)
      IF(R3.LE.F1)GOTO 1315
      R3=F1
1315  F1=ABS(U11(J+1)-U(J))
      IF(F1.LT.(1.0E-6))GOTO 1319
      X2=0.5*ABS(X11(J+1)-X(J))/4.0/3.0/3.0/F1
      IF(LMN.EQ.1)X2=0.00001
      IF(R3.LE.X2)GOTO 1319
      R3=X2
      IF(ABS(W(J)-1.0/W1(I1)).GT.1.0E-6)GOTO 1319
      E(J)=0.1702
      P(J)=0.0
     Y(J)=0.0
      Q(J)=0.0
     G(J)=0.0
      C(J)=0.0
     S(J)=0.0
      D(J)=0.0
     Z(J)=0.0
      SM1(J)=0.0
      SM2(J)=0.0
      SM3(J)=0.0
      Z44(J)=Z4(I1)
      Z55(J)=Z5(I1)
      TT(J)=0.0
     DD1(J)=DD0(I1)
     DD2(J)=DD0(I1)
1319  CONTINUE
1350  RETURN
      END
      SUBROUTINE WR
      DIMENSION F(600),F11(600),X(600),X11(600),XS(600),
     1 XS1(600),U(600),U11(600),V(600),W(600),E(600),P(600),
     2 Y(600),Q(600),G(600),S(600),Z(600),C(600),D(600),
     3 Z1(60),Z2(60),Z3(60),Z4(60),Z5(60),Z6(60),Z7(60),
     4 Z8(60),J1(60),W1(60),F22(60),D99(60),Z51(60)
      DIMENSION Z11(60),Z12(60),Z13(60),Z44(600),Z55(600),
     1 SM1(600),SM2(600),SM3(600),DD0(60),DD1(600),
     2 DD2(600),TT(600),Z81(60),Z82(60),Z83(60),Z84(60),
     3 Z85(60),Z86(60),Z87(60),Z88(60),Z89(60),VS(60),
     4 Z91(60),Z92(60),Z93(60),Z94(60),Z95(60),Z96(60),Z97(60),Z98(60),
```

```
     5   A8(600),A9(600),A99(600),TA(600),EC(600),EM(600),VS1(600),
     6   SE(600),STX(600),MSS(600),US(600),US1(600),
     7   Z71(60),Z72(60),Z73(60),Z74(60),Z75(60),Z76(60),Z77(60),
     8   Z61(60),Z62(60),Z63(60),Z41(60),Z42(60),Z43(60),Z54(60),Z45(60),
     9   Z46(60),Z47(60),Z48(60),Z49(60),Z50(60)
         COMMON F,F11,X,X11,XS,XS1,U,U11,V,W,E,Z51,US,US1,
     1   P,Y,Q,G,S,Z,C,D,Z1,Z2,Z3,Z4,Z5,Z6,
     2   Z7,Z8,W1,F22,D99,J1,D8,D9,W8,W9,M91,
     3   M92,N91,N92,G8,G9,N11,N22,L44,J8,
     4   J9,I1,L9,R2,R3,T,DT,N66,N55,W0,SEM,
     5   EVP,VSC,ECP,BAU,EX0
         COMMON Z11,Z12,Z13,Z44,Z55,SM1,SM2,SM3,
     1   DD0,DD1,DD2,TT,LY,Z81,Z82,Z83,Z84,Z85,Z86,Z87,Z88,Z89,
     2   R111,R112,R113,N8,N9,G1,D1,M9,VS,
     3   Z91,Z92,Z93,Z94,Z95,Z96,Z97,Z98,
     4   A8,A9,A99,TA,EC,EM,VS1,SE,STX,MSS,
     5   Z71,Z72,Z73,Z74,Z75,Z76,Z77,
     6   Z61,Z62,Z63,Z41,Z42,Z43,Z54,Z45,Z46,Z47,Z48,Z49,Z50
         WRITE(6,151)T,R2
151      FORMAT(1X,2HT=,E12.5,4X,3HR2=,E12.5/)
         WRITE(6,155)(X(J),X11(J),U(J),U11(J),E(J),
     1   W(J),P(J),STX(J),C(J),D(J),J=1,N66)
155      FORMAT(1X,10(E12.5,1X))
         WRITE(6,157)X11(N55),U11(N55)
157      FORMAT(1X,2(E12.5,4X)/)
         WRITE(6,158)(A9(J),A99(J),EM(J),TA(J),Z44(J),Z55(J),VS1(J),
     1   J=1,N66)
158      FORMAT(1X,7(E12.5,1X))
         RETURN
        END
         SUBROUTINE WR1
         DIMENSION F(600),F11(600),X(600),X11(600),XS(600),
     1   XS1(600),U(600),U11(600),V(600),W(600),E(600),P(600),
     2   Y(600),Q(600),G(600),S(600),Z(600),C(600),D(600),
     3   Z1(60),Z2(60),Z3(60),Z4(60),Z5(60),Z6(60),Z7(60),
     4   Z8(60),J1(60),W1(60),F22(60),D99(60),Z51(60)
         DIMENSION Z11(60),Z12(60),Z13(60),Z44(600),Z55(600),
     1   SM1(600),SM2(600),SM3(600),DD0(60),DD1(600),
     2   DD2(600),TT(600),Z81(60),Z82(60),Z83(60),Z84(60),
     3   Z85(60),Z86(60),Z87(60),Z88(60),Z89(60),VS(60),
     4   Z91(60),Z92(60),Z93(60),Z94(60),Z95(60),Z96(60),Z97(60),Z98(60),
     5   A8(600),A9(600),A99(600),TA(600),EC(600),EM(600),VS1(600),
     6   SE(600),STX(600),MSS(600),US(600),US1(600),
     7   Z71(60),Z72(60),Z73(60),Z74(60),Z75(60),Z76(60),Z77(60),
     8   Z61(60),Z62(60),Z63(60),Z41(60),Z42(60),Z43(60),Z54(60),Z45(60),
     9   Z46(60),Z47(60),Z48(60),Z49(60),Z50(60)
         COMMON F,F11,X,X11,XS,XS1,U,U11,V,W,E,Z51,US,US1,
     1   P,Y,Q,G,S,Z,C,D,Z1,Z2,Z3,Z4,Z5,Z6,
     2   Z7,Z8,W1,F22,D99,J1,D8,D9,W8,W9,M91,
     3   M92,N91,N92,G8,G9,N11,N22,L44,J8,
     4   J9,I1,L9,R2,R3,T,DT,N66,N55,W0,SEM,
     5   EVP,VSC,ECP,BAU,EX0
         COMMON Z11,Z12,Z13,Z44,Z55,SM1,SM2,SM3,
```

```
     1  DD0,DD1,DD2,TT,LY,Z81,Z82,Z83,Z84,Z85,Z86,Z87,Z88,Z89,
     2  R111,R112,R113,N8,N9,G1,D1,M9,VS,
     3  Z91,Z92,Z93,Z94,Z95,Z96,Z97,Z98,
     4  A8,A9,A99,TA,EC,EM,VS1,SE,STX,MSS,
     5  Z71,Z72,Z73,Z74,Z75,Z76,Z77,
     6  Z61,Z62,Z63,Z41,Z42,Z43,Z54,Z45,Z46,Z47,Z48,Z49,Z50
        WRITE(6,161)T,R2
161     FORMAT(1X,2HT=,E12.5,4X,3HR2=,E12.5/)
        DO 166 I22=1,N11
        N99=J1(I22)
        WRITE(6,165)X(N99),F(N99),X11(N99),
     1  F11(N99),U(N99),U11(N99)
        WRITE(6,165)E(N99),W(N99),P(N99),Q(N99),C(N99),D(N99)
165     FORMAT(1X,6(E12.5,4X))
166     CONTINUE
        WRITE(6,168)X(N55),X11(N55),U(N55),U11(N55)
168     FORMAT(1X,4(E12.5,4X)/)
        RETURN
        END
```

APPENDIX THREE

```
*HEADING
 PUNCH
**
**
**
***NODE AND NODE SET DEFINITION AND GENERATION
**
**
*NODE
 101,,,
 107,6.0E-3,0.0
 111,10.0E-3,,
 255,0.0,70.0E-3
 265,10.0E-3,70.0E-3
 299,0.0,73.0E-3
 305,6.0E-3,73.0E-3
 309,10.0E-3,71.0E-3
 311,0.0,73.0E-3
 317,6.0E-3,73.0E-3
 395,0.0,79.0E-3
 401,6.0E-3,79.0E-3
 411,0.0,79.0E-3
 417,6.0E-3,79.0E-3
 421,10.0E-3,79.0E-3
 455,0.0,81.0E-3
 461,6.0E-3,81.0E-3
 465,10.0E-3,81.0E-3
 471,0.0,81.0E-3
 477,6.0E-3,81.0E-3
 499,0.0,84.0E-3
 505,6.0E-3,84.0E-3
**
*NGEN,NSET=BODYC
 101,299,11
*NGEN,NSET=BODYS
 111,309,11
*NGEN,NSET=BODYM
 107,305,11
*NFILL,BIAS=1.4,NSET=BODYR
 BODYC,BODYM,6,1
*NFILL,BIAS=1.467,NSET=BODYL
 BODYM,BODYS,4,1
*NSET,NSET=BASE,GENERATE
 101,111,1
*NGEN,NSET=NECKS
 317,401,7
```

```
*NGEN,NSET=NECKC
 311,395,7
*NFILL,BIAS=1.4,NSET=NECK
 NECKC,NECKS,6,1
*NGEN,NSET=PROTS
 421,465,11
*NGEN,NSET=PROTC
 411,455,11
*NGEN,NSET=PROTM
 417,461,11
*NFILL,BIAS=1.4,NSET=PROTL
 PROTC,PROTM,6,1
*NFILL,BIAS=1.467,NSET=PROTR
 PROTM,PROTS,4,1
*NGEN,NSET=TOPS
 477,505,7
*NGEN,NSET=TOPC
 471,499,7
*NFILL,BIAS=1.4,NSET=TOP
 TOPC,TOPS,6,1
*NSET,NSET=CENTER
 BODYC,NECKC,PROTC,TOPC
*NSET,NSET=MPCA1,GENERATE
 299,305,1
*NSET,NSET=MPCA2,GENERATE
 311,317,1
*NSET,NSET=MPCB1,GENERATE
 395,401,1
*NSET,NSET=MPCB2,GENERATE
 411,417,1
*NSET,NSET=MPCC1,GENERATE
 455,461,1
*NSET,NSET=MPCC2,GENERATE
 471,477,1
**
**
***ELEMENT AND ELEMENT DEFINITION AND GENERATION
**
**
*ELEMENT,TYPE=CAX8R
 1,101,103,125,123,102,114,124,112
 50,311,313,327,325,312,320,326,318
 70,411,413,435,433,412,424,434,422
 80,471,473,487,485,472,480,486,478
**
*ELGEN,ELSET=BODYT
 1,5,2,1,9,22,5,1,,,
*ELGEN,ELSET=NECK
 50,3,2,1,6,14,3,1,,,
```

```
*ELGEN,ELSET=PROTR
 70,5,2,1,2,22,5,1,,,
*ELGEN,ELSET=TOP
 80,3,2,1,2,14,3,1,,,
*ELSET,ELSET=ELTOP
 83,84,85
*ELSET,ELSET=PARTB
 31,32,33,34,35,36,37,38,39,40,41,42,43,44,45
*ELSET,ELSET=PART
 PARTB,NECK,PROTR,TOP
*ELSET,ELSET=PROTT
 78,79
*ELSET,ELSET=PROTB
 73,74
*ELSET,ELSET=ELPRES
 25,30,35,40,45,52,55,58,61,64,67,74,79,82,85
*ELSET,ELSET=ALLEL
 BODYT,NECK,PROTR,TOP
**
*SOLID SECTION,ELSET=ALLEL,MATERIAL=SSTEEL
**
*MATERIAL,NAME=SSTEEL
*ELASTIC
 200.0E9,0.3
**
**
***BOUNDARY CONDITIONS
**
**
*BOUNDARY
 BASE,2
 CENTER,1
**
*MPC
 5,MPCA1,MPCA2
 5,MPCB1,MPCB2
 5,MPCC1,MPCC2
**
*PLOT
 PUNCH
*DRAW
*DETAIL,ELSET=PART
*DRAW
**
**
*STEP,AMPLITUDE=RAMP
 LOADING PUNCH
*STATIC,PTOL=10.
 0.1E-3,1.E-3
```

```
*NODE FILE
 COORD,U
*EL FILE
 S,E
*DLOAD
 ELPRES,P2,150E6
 ELTOP,P3,150E6
 PROTT,P3,150E6
 PROTB,P1,150E6
 16,P2,15E6
*PRINT,FREQUENCY=5
*EL PRINT,FREQUENCY=5
 S,PRIN
 E
*NODE PRINT,FREQUENCY=5
 U
*PLOT,COLORS=6,FREQUENCY=5
*PLOT MODE,FILL=YES
*DETAIL,ELSET=ALLEL
*CONTOUR
 U1
 U2
 E11
 E22
 E33
 S11
 S22
 S33
*DETAIL,ELSET=PART
*CONTOUR
 U1
 U2
 E11
 E22
 E33
 S11
 S22
 S33
*END STEP
```

APPENDIX TWO

```
*HEADING
 POWDER COMPACTION
**
**
***NODE AND NODE SET DEFINITION AND GENERATION
**
**
**
*NODE
101,,,
109,2.E-2,,
173,0.,2.E-2
181,2.E-2,2.E-2
**
201,,,
209,2.E-2,,
273,0.,2.E-2
281,2.E-2,2.E-2
**
301,,,
309,2.E-2,,
373,0.,2.E-2
381,2.E-2,2.E-2
**
401,,,
409,2.E-2,,
473,0.,2.E-2
481,2.E-2,2.E-2
**
10,0.,2.E-2
18,2.E-2,2.E-2
46,0.,2.5E-2
54,2.E-2,2.5E-2
**
2000,2.001E-2,0.0E-2
2004,2.5E-2,0.0E-2
2040,2.001E-2,2.0E-2
2044,2.5E-2,2.0E-2
**
*NGEN,NSET=BNSL1
101,109,1
*NGEN,NSET=TNSL1
173,181,1
*NGEN,NSET=BNSL2
201,209,1
*NGEN,NSET=TNSL2
```

```
273,281,1
*NGEN,NSET=BNSL3
301,309,1
*NGEN,NSET=TNSL3
373,381,1
*NGEN,NSET=BNSL4
401,409,1
*NGEN,NSET=TNSL4
473,481,1
**
*NGEN,NSET=PTOPN
46,54,1
*NGEN,NSET=PBOTN
10,18,1
**
*NGEN,NSET=ALNL1
101,173,9
102,174,18
103,175,9
104,176,18
105,177,9
106,178,18
107,179,9
108,180,18
109,181,9
**
*NGEN,NSET=ALNL2
201,273,9
202,274,18
203,275,9
204,276,18
205,277,9
206,278,18
207,279,9
208,280,18
209,281,9
**
*NGEN,NSET=ALNL3
301,373,9
302,374,18
303,375,9
304,376,18
305,377,9
306,378,18
307,379,9
308,380,18
309,381,9
**
*NGEN,NSET=ALNL4
```

```
401,473,9
402,474,18
403,475,9
404,476,18
405,477,9
406,478,18
407,479,9
408,480,18
409,481,9
**
*NGEN,NSET=ALPNS
10,46,9
11,47,18
12,48,9
13,49,18
14,50,9
15,51,18
16,52,9
17,53,18
18,54,9
**
*NGEN,NSET=DIEB
2000,2004,1
*NGEN,NSET=DIET
2040,2044,1
*NGEN,NSET=DIEF
2000,2040,5
*NGEN,NSET=DIES
2004,2044,5
*NFILL,NSET=DIEN
DIEB,DIET,8,5
*NSET,NSET=MPCN1
112,114,116,120,121,122,123,124,125,126,130,132,134,138,
139,140,141,142,143,144,148,150,152,156,157,158,159,160,
161,162,166,168,170
**
*NSET,NSET=MPCN2
212,214,216,220,221,222,223,224,225,226,230,232,234,238,
239,240,241,242,243,244,248,250,252,256,257,258,259,260,
261,262,266,268,270
**
*NSET,NSET=MPCN3
312,314,316,320,321,322,323,324,325,326,330,332,334,338,
339,340,341,342,343,344,348,350,352,356,357,358,359,360,
361,362,366,368,370
**
*NSET,NSET=MPCN4
412,414,416,420,421,422,423,424,425,426,430,432,434,438,
439,440,441,442,443,444,448,450,452,456,457,458,459,460,
```

```
461,462,466,468,470
**
*NSET,NSET=BCNL1
BNSL1
*NSET,NSET=BCNL2
BNSL2
*NSET,NSET=BCNL3
BNSL3
*NSET,NSET=BCNL4
BNSL4
**
*NSET,NSET=EQL1C
110,119,128,137,146,155,164
*NSET,NSET=EQL1W
118,127,136,145,154,163,172
**
*NSET,NSET=EQL2C
210,219,228,237,246,255,264
*NSET,NSET=EQL2W
218,227,236,245,254,263,272
**
*NSET,NSET=EQL3C
310,319,328,337,346,355,364
*NSET,NSET=EQL3W
318,327,336,345,354,363,372
**
*NSET,NSET=EQL4C
410,419,428,437,446,455,464
*NSET,NSET=EQL4W
418,427,436,445,454,463,472
**
**NSET,NSET=PTOPN
**46,47,48,49,50,51,52,53,54
*NSET,NSET=EQPMB
10,11,12,13,14,15,16,17,18
*NSET,NSET=EQL1T
173,174,175,176,177,178,179,180,181
*NSET,NSET=EQL2T
273,274,275,276,277,278,279,280,281
*NSET,NSET=EQL3T
373,274,375,376,377,378,379,380,381
*NSET,NSET=EQL4T
473,474,475,476,477,478,479,480,481
**
*NSET,NSET=FIXL1
101,110,119,128,137,146,155,164,173,
**109,118,127,136,145,154,163,172,181
*NSET,NSET=FIXL2
201,210,219,228,237,246,255,264,273,
```

```
**209,218,227,236,245,254,263,272,281
*NSET,NSET=FIXL3
301,310,319,328,337,346,355,364,373,
**309,318,327,336,345,354,363,372,381
*NSET,NSET=FIXL4
401,410,419,428,437,446,455,464,473,
**409,418,427,436,445,454,463,472,481
**
**
***ELEMENT AND ELEMENT DEFINITION AND GENERATION
**
*ELEMENT,TYPE=CAX8R
111,101,103,121,119,102,112,120,110
211,201,203,221,219,202,212,220,210
311,301,303,321,319,302,312,320,310
411,401,403,421,419,402,412,420,410
**
*ELGEN,ELSET=LAYR1
111,4,2,1,4,18,4,1,,,
*ELGEN,ELSET=LAYR2
211,4,2,1,4,18,4,1,,,
*ELGEN,ELGEN=LAYR3
311,4,2,1,4,18,4,1,,,
*ELGEN,ELSET=LAYR4
411,4,2,1,4,18,4,1,,,
**
*ELSET,ELSET=ELTL1
123,124,125,126
*ELSET,ELSET=ELTL2
223,224,225,226
*ELSET,ELSET=ELTL3
323,324,325,326
*ELSET,ELSET=ELTL4
423,424,425,426
**
*ELSET,ELSET=REST
LAYR2,LAYR3,LAYR4
**
*SOLID SECTION,ELSET=LAYR1,MATERIAL=POWDER1
*SOLID SECTION,ELSET=LAYR2,MATERIAL=POWDER2
*SOLID SECTION,ELSET=LAYR3,MATERIAL=POWDER3
*SOLID SECTION,ELSET=LAYR4,MATERIAL=POWDER4
**
*MATERIAL,NAME=POWDER1
*ELASTIC
36.8E6,0.21
*MATERIAL,NAME=POWDER2
*ELASTIC
6.5E6,0.21
```

```
*MATERIAL,NAME=POWDER3
*ELASTIC
7.3E6,0.21
*MATERIAL,NAME=POWDER4
*ELASTIC
9.8E6,0.21
**
*ELEMENT,TYPE=CAX8R
11,10,12,30,28,11,21,29,19
*ELGEN,ELSET=PUNCH
11,4,2,1,2,18,4,1,,,
**
*ELEMENT,TYPE=CAX8R
20,2000,2002,2012,2010,2001,2007,2011,2005
*ELGEN,ELSET=DIE
20,2,2,1,4,10,2,1,,,
**
*ELSET,ELSET=METAL
PUNCH,DIE
**
*SOLID SECTION,ELSET=METAL,MATERIAL=STEEL
*MATERIAL,NAME=STEEL
*ELASTIC
204.E9,0.3
**
***INTERFACE ELEMENTS BETWEEN PUNCH AND POWDER
*ELEMENT,TYPE=INTER3A,ELSET=INTFACE
31,173,174,175,10,11,12
*ELGEN,ELSET=INTFACE
31,4,2,1
*INTERFACE,ELSET=INTFACE
*FRICTION
0.
**
**
***INTERFACE ELEMENTS BETWEEN THE DIE AND POWDER
*ELEMENT,TYPE=INTER3A,ELSET=IFPD
41,109,118,127,2000,2005,2010
42,127,136,145,2010,2015,2020
43,145,154,163,2020,2025,2030
44,163,172,181,2030,2035,2040
**
*INTERFACE,ELSET=IFPD
*FRICTION
 0.4,40.0E6
**
**
*MPC
5,MPCN1,MPCN2
```

```
5,MPCN2,MPCN3
5,MPCN3,MPCN4
**
*EQUATION
2
EQL2C,2,-1,EQL1C,2,1
2
EQL3C,2,-1,EQL1C,2,1
2
EQL4C,2,-1,EQL1C,2,1
2
EQL2W,2,-1,EQL1W,2,1
2
EQL3W,2,-1,EQL1W,2,1
2
EQL4W,2,-1,EQL1W,2,1
2
TNSL1,2,-1,EQPMB,2,1
2
TNSL2,2,-1,EQPMB,2,1
2
TNSL3,2,-1,EQPMB,2,1
2
TNSL4,2,-1,EQPMB,2,1
**
**
***BOUNDARY CONDITIONS
*BOUNDARY
BCNL1,2
BCNL2,2
BCNL3,2
BCNL4,2
FIXL1,1
FIXL2,1
FIXL3,1
FIXL4,1
DIEB,2
DIES,1
**
**
*AMPLITUDE,NAME=DISAMP
.1,.2,.2,.48,.3,.62,.4,.74,
.5,.84,.6,.90,.7,.95,.8,.98,
.9,.99,1.,1.
**
*PLOT
POWDER COMPACTION
*DRAW,ELNUM,NODENUM
**
```

```
*STEP,INC=10
MODEL CHANGE 1
*STATIC,PTOL=10.
.1E-4,1E-4
*MODEL CHANGE,REMOVE
REST
*NODE FILE
COORD,U
*EL FILE
S,E
*EL PRINT,FREQUENCY=50
S,PRIN
E
*NODE PRINT,FREQUENCY=50
U
*PLOT,FREQUENCY=50
MODEL CHANGE 1
*DISPLACED
U,1.0
*END STEP
**
*STEP,INC=10
LOADING LAYER 1
*STATIC,PTOL=100
.1,1.
*NODE FILE
COORD,U
*EL FILE
S,E
*PRINT,FREQ=5
**BOUNDARY
**BNSL1,2
**DLOAD,AMPLITUDE=DISAMP
**ELTL1,P3,40.E6
*BOUNDARY,AMPLITUDE=DISAMP
PTOPN,2,2,-2.5E-3
*EL PRINT,FREQ=50
S,PRIN
E
*NODE PRINT,FREQ=50
U
*PLOT,FREQUENCY=50
LAYER 1
*DISPLACED
U,1.0
*END STEP
**
*STEP,INC=10
MODEL CHANGE 2
```

```
*STATIC,PTOL=10.
1E-4,1E-3
*MODEL CHANGE,INCLUDE
LAYR2
*NODE FILE
COORD,U
*EL FILE
S,E
*EL PRINT,FREQUENCY=50
S,PRIN
E
*NODE PRINT,FREQUENCY=50
U
*PLOT,FREQUENCY=50
MODEL CHANGE 2
*DISPLACED
U,1.0
*END STEP
**
*STEP,INC=10
LOADING LAYER 2
*STATIC,PTOL=100
.1E-3,1.E-3
*NODE FILE
COORD,U
*EL FILE
S,E
*PRINT,FREQ=5
**BOUNDARY,OP=MOD
**BNSL2,2
***DLOAD,AMPLITUDE=DISAMP
**ELTL1,P3,90.E6
*BOUNDARY,AMPLITUDE=DISAMP
PTOPN,2,2,-5.E-3
*EL PRINT,FREQ=50
S,PRIN
E
*NODE PRINT,FREQ=50
U
*PLOT,FREQUENCY=50
LAYER 1,2
*DISPLACED
U,1.0
*END STEP
**
*STEP,INC=10
MODEL CHANGE 3
*STATIC,PTOL=10.
.1E-6,1.E-6
```

```
*MODEL CHANGE,INCLUDE
LAYR3
*NODE FILE
COORD,U
*EL FILE
S,E
*EL PRINT,FREQUENCY=50
S,PRIN
E
*NODE PRINT,FREQUENCY=50
U
*PLOT,FREQUENCY=50
MODEL CHANGE 3
*DISPLACED
U,1.0
*END STEP
*STEP,INC=10
LOADING LAYER 3
*STATIC,PTOL=100
.1E-3,1.E-3
*NODE FILE
COORD,U
*EL FILE
S,E
*PRINT,FREQ=5
**BOUNDARY,OP=MOD
**BNSL3,2
**DLOAD,AMPLITUDE=DISAMP
**ELTL1,P3,140.E6
*BOUNDARY,AMPLITUDE=DISAMP
PTOPN,2,2,-7.5E-3
*EL PRINT,FREQ=50
S,PRIN
E
*NODE PRINT,FREQ=50
U
*PLOT,FREQUENCY=50
LAYER 1,2,3
*DISPLACED
U,1.0
*END STEP
**
*STEP,INC=10
MODEL CHANGE 4
*STATIC,PTOL=10.
.1E-6,1.E-6
*MODEL CHANGE,INCLUDE
LAYR4
*NODE FILE
```

```
COORD,U
*EL FILE
S,E
*EL PRINT,FREQUENCY=50
S,PRIN
E
*NODE PRINT,FREQUENCY=50
U
*PLOT,FREQUENCY=50
MODEL CHANGE 4
*DISPLACED
U,1.0
*END STEP
*STEP,INC=10
LOADING LAYER 4
*STATIC,PTOL=100
.1E-3,1.E-3
*NODE FILE
COORD,U
*EL FILE
S,E
*PRINT,FREQ=5
**BOUNDARY,OP=MOD
**BNSL4,2
**DLOAD,AMPLITUDE=DISAMP
**ELTL1,P3,300.E6
*BOUNDARY,AMPLITUDE=DISAMP
PTOPN,2,2,-1.E-2
*EL PRINT,FREQ=50
S,PRIN
E
*NODE PRINT,FREQ=50
U
*PLOT,FREQUENCY=50
LAYER 1,2,3,4
*DISPLACED
U,1.0
*CONTOUR
S11
S22
S33
E11
E22
E33
*END STEP
```